



HAL
open science

Une approche générique pour l'analyse et le filtrage des signaux bivariés

Julien Flamant

► **To cite this version:**

Julien Flamant. Une approche générique pour l'analyse et le filtrage des signaux bivariés. Traitement du signal et de l'image [eess.SP]. Ecole Centrale de Lille, 2018. Français. NNT : 2018ECLI0008 . tel-01926941

HAL Id: tel-01926941

<https://theses.hal.science/tel-01926941>

Submitted on 19 Nov 2018

HAL is a multi-disciplinary open access archive for the deposit and dissemination of scientific research documents, whether they are published or not. The documents may come from teaching and research institutions in France or abroad, or from public or private research centers.

L'archive ouverte pluridisciplinaire **HAL**, est destinée au dépôt et à la diffusion de documents scientifiques de niveau recherche, publiés ou non, émanant des établissements d'enseignement et de recherche français ou étrangers, des laboratoires publics ou privés.

Centrale Lille

Thèse

Présentée en vue
d'obtenir le grade de

Docteur

En

Spécialité : **Automatique, Génie informatique, Traitement du signal et image**

Par

JULIEN FLAMANT

Doctorat délivré par Centrale Lille

Titre de la thèse:

A general approach for the analysis and filtering of bivariate signals

*Une approche générique pour l'analyse et le filtrage
des signaux bivariés*

Soutenue le 27 Septembre 2018 devant le jury d'examen:

Président

Patrick FLANDRIN Directeur de Recherche CNRS, École Normale Supérieure de Lyon

Rapporteurs

Tülay ADALI Distinguished University Professor, University of Maryland, Baltimore County

Gabriel PEYRÉ Directeur de Recherche CNRS, École Normale Supérieure

Examineurs

Marianne CLAUSEL Professeure des Universités, Université de Lorraine

Philippe RÉFRÉGIER Professeur des Universités, Centrale Marseille

Membre invité

Eric CHASSANDE-MOTTIN Directeur de Recherche CNRS, Université Paris Diderot

Directeurs de thèse

Pierre CHAINAIS Professeur des Universités, Centrale Lille

Nicolas LE BIHAN Chargé de Recherche CNRS, Université Grenoble Alpes

Thèse préparée dans le Laboratoire

Centre de Recherche en Informatique Signal et Automatique de Lille

Université de Lille, Centrale Lille, CNRS, UMR 9189 - CRISTAL

École Doctorale SPI 072

Remerciements

Je souhaiterais tout d'abord remercier très sincèrement les membres du jury. Merci à Tülay Adalı et Gabriel Peyré, qui ont accepté d'être les rapporteurs de ce manuscrit, ainsi qu'à Marianne Clausel, Patrick Flandrin et Philippe Réfrégier d'avoir bien voulu examiner cette thèse. J'en suis profondément honoré.

Cette thèse n'aurait pu se dérouler sans les conseils avisés et les encouragements constants de mes directeurs de thèse, Pierre Chainais et Nicolas Le Bihan. J'ai énormément appris à vos côtés et je mesure aujourd'hui la chance qui a été la mienne durant ces trois années. Merci de m'avoir fait confiance. En particulier, merci Pierre d'avoir accepté cette aventure il y a un peu plus de trois ans. Enfin merci Nicolas d'être présent depuis le début, depuis cette année de master à Melbourne qui a tout lancé.

Merci à Eric Chassande-Mottin de m'avoir offert l'opportunité de travailler autour de ce sujet si excitant des ondes gravitationnelles. J'ai hâte de continuer notre collaboration. Merci aussi pour ta présence tout au long de la thèse, de la fin de la première année jusqu'au jour de la soutenance.

Merci à l'équipe SigMA, membres présents et passés: Amine, Ayoub, Clément, Christelle, François, Guillaume, Jean-Michel, Jérémie, John, Mahmoud, Nouha, Patrick, Pierre, Philippe, Phuong, Quentin, Rémi, Rémy, Théo, Victor, Vincent, Wadih. Vous avez su créer un environnement unique où chacun, qu'il soit doctorant ou permanent, a la possibilité de s'épanouir dans une ambiance inégalable. Merci pour ces trois belles années.

Merci à Patrick et Ingrid, pour leur incomparable hospitalité héritée, je pense, d'un savant mélange entre Alpes, Méditerranée et Scandinavie dont eux seuls ont le secret. Merci à Rémi pour cette folle aventure autour des zéros, en attendant le passage à la vitesse de la lumière. Les pauses café(s) à rallonge entre l'histoire de Lille et la filmographie de Bruno Dumont me manqueront.

Merci à Clément et Phuong, co-bureau les plus gourmands que je connaisse. Il y aura toujours des bouteilles de Saint Bé au frais pour vous. Merci à Guillaume, pour ton soutien indéfectible lors de cette dernière année si particulière. Je n'oublierai pas tes pas de danse Noirmoutrins – *Dream Machine*.

Merci aux amis Melbourniens, Vincent et Géraldine, pour votre incroyable gentillesse lors de mon passage en Octobre. Merci à Jeanne, pour avoir continué sur le chemin si particulier de la thèse. J'espère que ton année en Australie t'apportera autant qu'elle m'a apportée.

Merci à Germain, compagnon de route depuis de longues années déjà. Que de chemins (de montagne, mais pas seulement) parcourus ensemble depuis nos vertes années Strasbourgeoises et Cachanaises. Merci à Loic et Lucie, ainsi qu'à Thomas, qui nous ont rejoint en chemin. Merci aussi à Lucile et Nathan pour leur fidèle amitié.

Merci à Brigitte et Marc, pour leur goût des bonnes choses. Merci de m'avoir toujours accueilli si chaleureusement, et même hébergé sur la fin.

Merci à mes parents, qui m'ont toujours soutenu et encouragé. Vous avez su me donner ce goût de la curiosité, à mon sens si important dans le monde de la recherche. Merci à Lucas, qui, malgré ses études chronophage, a toujours su être présent.

Enfin, par-dessus tout, merci à Laura, sans qui cette aventure Lilloise n'aurait jamais pu exister, et sans qui l'avenir serait bien trop différent.

Contents

CONTENTS	7
NOTATIONS	13
o INTRODUCTION	15
o.1 A first example: the monochromatic bivariate signal	16
o.1.1 <i>Vector and complex representations</i>	16
o.1.2 <i>The concept of polarization: Stokes parameters and Poincaré sphere</i>	17
o.1.3 <i>Expressions for ellipse parameters</i>	17
o.1.4 <i>Natural descriptors for bivariate signals</i>	18
o.2 An overview of signal processing for bivariate signals	18
o.2.1 <i>Random bivariate signals in the vector representation</i>	19
o.2.2 <i>Random bivariate signals in the complex representation</i>	19
o.2.3 <i>LTI filtering in the vector representation: matrix-valued filters</i>	21
o.2.4 <i>LTI filtering in the complex representation: widely linear filters</i>	21
o.2.5 <i>Instantaneous ellipses and time-frequency analysis</i>	22
o.3 An ideal framework for bivariate signal processing?	23
o.3.1 <i>Limitations of existing methods</i>	23
o.3.2 <i>Summary of requirements</i>	25
o.4 Contributions and outline	25
1 QUATERNION FOURIER TRANSFORM FOR BIVARIATE SIGNALS	31
1.1 Quaternions	32
1.1.1 <i>Definition</i>	32
1.1.2 <i>Quaternion operations</i>	33
1.1.3 <i>Complex subfields</i>	34
1.1.4 <i>Polar forms</i>	34
1.1.5 <i>Quaternions and 3D rotations</i>	35
1.2 Quaternion Fourier transform	35
1.2.1 <i>Definition, existence, inversion</i>	35
1.2.2 <i>Properties of the Quaternion Fourier transform</i>	36
1.3 Processing bivariate signals with the quaternion Fourier transform	39
1.3.1 <i>Bivariate signals</i>	40

1.3.2	<i>Choice of the axis of the QFT</i>	40
1.3.3	<i>Monochromatic bivariate signals</i>	41
1.4	Conclusion	42
APPENDICES		
1.A	Euler polar form computation	44
1.B	Hilbert spaces over quaternions	44
1.C	Discretization of the quaternion Fourier transform	45
1.C.1	<i>Discrete-time quaternion Fourier transform</i>	46
1.C.2	<i>Discrete quaternion Fourier transform</i>	46
1.D	Proofs of quaternion Fourier transform properties	46
1.D.1	<i>Convolution properties (1.34) and (1.35)</i>	47
1.D.2	<i>Theorem 1.1 (Parseval-Plancherel)</i>	47
1.D.3	<i>Theorem 1.2 (Gabor-Heisenberg uncertainty principle)</i>	47
2	SPECTRAL ANALYSIS OF BIVARIATE SIGNALS	49
2.1	Quaternion spectral density for deterministic bivariate signals	50
2.1.1	<i>Finite energy signals</i>	50
2.1.2	<i>Finite power signals</i>	51
2.2	Stationary random bivariate signals	51
2.2.1	<i>Spectral representation theorem</i>	52
2.2.2	<i>Quaternion power spectral density</i>	53
2.2.3	<i>Quaternion autocovariance</i>	54
2.2.4	<i>Cross-covariances and cross-spectral densities</i>	55
2.3	The quaternion spectral density in practice	56
2.3.1	<i>Stokes parameters</i>	57
2.3.2	<i>Degree of polarization. Unpolarized and polarized parts decomposition.</i>	58
2.3.3	<i>Poincaré sphere representation</i>	59
2.3.4	<i>Examples</i>	61
2.4	Nonparametric spectral estimation	64
2.4.1	<i>Conventional spectral estimators</i>	65
2.4.2	<i>Estimation of polarization parameters</i>	67
2.4.3	<i>Illustration</i>	68
2.5	Conclusion	70
APPENDICES		
2.A	Circularity of spectral increments	72
2.B	Expressions for the quaternion power spectral density and the quaternion autocovariance	72
2.C	Unpolarized signals and non-Gaussianity	73
2.D	Proofs	74
2.D.1	<i>Proof of the spectral representation Theorem 2.1</i>	74

2.D.2 *Proof of Theorems 2.2 and 2.3* 76

3 LINEAR-TIME INVARIANT FILTERS 77

3.1 From matrix to quaternion representation of LTI filters 78

3.1.1 *LTI filtering of bivariate signals using linear algebra* 78

3.1.2 *From matrices to quaternions* 79

3.1.3 *Quaternions and physics* 80

3.2 Quaternion filters for bivariate signals 80

3.2.1 *Unitary filters* 81

3.2.2 *Hermitian filters* 82

3.2.3 *General form of LTI filters* 85

3.3 Some applications of quaternion filters 86

3.3.1 *Spectral synthesis by Hermitian filtering* 86

3.3.2 *Whitening and unpolarizing filter* 88

3.3.3 *Wiener filtering* 89

3.3.4 *Some decompositions of bivariate signals* 90

3.3.5 *Modeling Polarization Mode Dispersion* 94

3.4 Conclusion 97

APPENDICES

3.A Output-input cross-spectral properties 98

3.B Filter identification using unpolarized white Gaussian noise 98

3.C Linear algebra and quaternion equivalence 99

3.C.1 *Matrix-vector and quaternion operations* 99

3.C.2 *Unitary transforms* 100

3.C.3 *Hermitian transforms* 100

3.D Wiener filter derivation 101

4 TIME-FREQUENCY REPRESENTATIONS 103

4.1 Quaternion embedding of bivariate signals 104

4.1.1 *Definition* 105

4.1.2 *Instantaneous parameters* 106

4.1.3 *Examples* 107

4.2 Spectrograms and scalograms for bivariate signals 109

4.2.1 *Quaternion short-term Fourier transform* 109

4.2.2 *Quaternion continuous wavelet transform* 112

4.3 Asymptotic analysis and ridges 115

4.3.1 *Ridges of the quaternion short-term Fourier transform* 115

4.3.2 *Ridges of the quaternion continuous wavelet transform* 116

4.3.3 *Ridge extraction* 117

4.4	Generic time-frequency-polarization representations	117
4.4.1	<i>Quaternion Wigner-Ville distribution</i>	118
4.4.2	<i>Cohen class for bivariate signals</i>	121
4.5	An application to seismic data	124
4.6	Conclusion	125
APPENDICES		
4.A	Canonical quadruplet of bivariate signals	127
4.B	Stationary phase approximation	128
4.C	Proofs	129
4.C.1	<i>Proof of Theorem 4.1</i>	129
4.C.2	<i>Proof of Theorem 4.2.</i>	130
5	NONPARAMETRIC CHARACTERIZATION OF GRAVITATIONAL WAVES POLARIZATIONS	133
5.1	Gravitational waves and precessing binaries	133
5.2	Modeling the emitted gravitational waveform	134
5.3	Stokes parameters characterization of precession	136
5.4	Application to precession diagnosis	137
5.5	Conclusion	138
APPENDICES		
5.A	Harmonic analysis in spherical coordinates	140
5.A.1	<i>Spin weighted spherical harmonics</i>	140
5.A.2	<i>Wigner-D functions</i>	140
5.B	Gravitational waveform in the inertial frame	140
5.B.1	<i>Calculation of the emission modes in the inertial frame</i>	140
5.B.2	<i>Waveform expression</i>	141
5.C	Instantaneous Stokes parameters	142
5.C.1	<i>Quaternion embedding of the emitted waveform</i>	142
5.C.2	<i>Stokes parameters expressions</i>	143
CONCLUSION 145		
A general approach for the analysis and filtering of bivariate signals 145		
Perspectives 148		
RÉSUMÉ EN FRANÇAIS 153		
BIBLIOGRAPHY 168		
APPENDIX: REPRODUCTION OF THE ARTICLE		
“ON THE ZEROS OF THE SPECTROGRAM OF WHITE NOISE”, R. BARDENET, J. FLAMANT, P. CHAINAIS 169		

Notations

Generic notations

$x(t), X(\nu)$	scalar (complex or quaternion-valued) signals in time and frequency domains
$\mathbf{x}(t), \mathbf{X}(\nu)$	vector signals in time and frequency domains
$\uparrow\mathbf{x}(t), \uparrow\mathbf{X}(\nu)$	augmented vector signals in time and frequency domains
$\underline{\mathbf{m}}(t), \underline{\mathbf{M}}(\nu)$	matrices in time and frequency domains
$\uparrow\underline{\mathbf{m}}(t), \uparrow\underline{\mathbf{M}}(\nu)$	augmented matrices in time and frequency domains

Spaces

$\mathbb{R}, \mathbb{C}, \mathbb{H}$	Real, complex and quaternions numbers
$U(2), SU(2)$	Sets of unitary and special unitary 2-by-2 complex matrices
$SO(3)$	Special orthogonal group, <i>i.e.</i> rotations matrices of \mathbb{R}^3
$L^p(\mathbb{R}; \mathbb{H})$	L^p space of functions $x : \mathbb{R} \rightarrow \mathbb{H}$
$H^2(\mathbb{R}; \mathbb{H})$	Hardy space of square integrable functions $x : \mathbb{R} \rightarrow \mathbb{H}$

p. 105

Quaternion calculus

<i>Assumption</i>	Let $q = a + \mathbf{i}b + \mathbf{j}c + \mathbf{k}d \in \mathbb{H}$ and $\boldsymbol{\mu} \in \mathbb{H}$ s.t. $\boldsymbol{\mu}^2 = -1$.
$\text{Re}, \text{Im}_i, \text{Im}_j, \text{Im}_k$	real and imaginary parts operators
$\mathcal{S}(q), \mathcal{V}(q)$	scalar (real) and vector (imaginary) parts of $q = \mathcal{S}(q) + \mathcal{V}(q)$
$\bar{q} = a - \mathbf{i}b - \mathbf{j}c - \mathbf{k}d$	Conjugate of q . For $p, q \in \mathbb{H}$, $\overline{pq} = \bar{q}\bar{p}$
$\bar{q}^\boldsymbol{\mu} = -\boldsymbol{\mu}q\boldsymbol{\mu}$	Involution by $\boldsymbol{\mu}$
$e^{\boldsymbol{\mu}\alpha} = \cos \alpha + \boldsymbol{\mu} \sin \alpha$	Quaternion exponential, $\boldsymbol{\mu} \in \mathbb{H}$ s.t. $\boldsymbol{\mu}^2 = -1$ and $\alpha \in \mathbb{R}$
$q = q e^{i\theta}e^{-k\chi}e^{j\varphi}$	Euler polar form of q
$\mathbb{C}_\boldsymbol{\mu} = \text{span}\{1, \boldsymbol{\mu}\}$	complex subfield of \mathbb{H} isomorphic to \mathbb{C}
$\text{Proj}_{\mathbb{C}_i}\{q\} = \frac{q+\bar{q}^i}{2}$	Projection of q onto \mathbb{C}_i

p. 35

Polarization related quantities

a, θ, χ	Amplitude, orientation and ellipticity of the polarization ellipse	p. 16
S_0, S_1, S_2, S_3	Stokes parameters	p. 17
Φ	Degree of polarization	p. 58
s_1, s_2, s_3	Normalized Stokes parameters $s_i \triangleq S_i/S_0, i = 1, 2, 3$	p. 60

Spectral analysis

<i>Assumption</i>	$x(t) = u(t) + \mathbf{i}v(t)$ is a second-order stationary random bivariate signal.
$R_{uu}(\tau), R_{uv}(\tau)$	Autocovariance of u , cross-covariance between u and v
$P_{uu}(\tau), P_{uv}(\nu)$	PSD of u , cross-PSD between u and v
$R_{xx}(\tau), \tilde{R}_{xx}(\tau)$	Autocovariance of x , complementary-covariance of x
$P_{xx}(\nu), \tilde{P}_{xx}(\nu)$	PSD of x , complementary-PSD of x

$\gamma_{xx}(\tau), \gamma_{xy}(\tau)$	Quaternion autocovariance of x , quaternion cross-covariance between x and y	p. 54, 55
$\Gamma_{xx}(\nu), \Gamma_{xy}(\nu)$	Quaternion PSD of x , quaternion cross-PSD between x and y ,	p. 53, 55
$\hat{\Gamma}_{xx}^{(p)}(\nu), \hat{\Gamma}_{xx}^{(mt)}(\nu)$	periodogram and multitaper estimates of the quaternion PSD of x	p. 65, 66

Time-frequency analysis

$x_+(t)$	Quaternion embedding of the bivariate signal x	p. 105
$\mathcal{H}\{x\}$	Hilbert transform of x	p. 106
$F_x^g(\tau, \nu)$	Quaternion Short-Term Fourier Transform of x using a window g	p. 110
$W_x(\tau, s)$	Quaternion Continuous Wavelet Transform of x	p. 113
$WV_x(\tau, \nu)$	Quaternion Wigner-Ville transform of x	p. 118

Acronyms

C-PSD	Complementary Power Spectral Density
LTI	Linear Time-Invariant
PSD	Power Spectral Density
Q-CWT	Quaternion Continuous Wavelet Transform
Q-STFT	Quaternion Short-Term Fourier Transform
QFT	Quaternion Fourier Transform

Introduction



In many areas of science there is the need to jointly analyze two observed real-valued signals: eastward and northward velocities of oceans currents (Gonella, 1972; Thomson and Emery, 2014) and winds (Hayashi, 1982; Tanaka and Mandic, 2007); polarized waves in optics (Brosseau, 1998; Born and Wolf, 1980) and seismology (Samson, 1983; Pinnegar, 2006); pairs of electrode recordings in EEG or MEG (Sakkalis, 2011; Sanei and Chambers, 2013); gravitational waves (Misner, Thorne, and Wheeler, 1973) and many more. Fig. 1 depicts three examples of bivariate signals.

A bivariate signal can be either modeled as a vector signal $\mathbf{x} : \mathbb{R} \rightarrow \mathbb{R}^2$ or as a complex-valued signal $x : \mathbb{R} \rightarrow \mathbb{C}$ such that

$$\mathbf{x}(t) = \begin{bmatrix} u(t) \\ v(t) \end{bmatrix} \quad \text{or} \quad x(t) = u(t) + iv(t) \quad (1)$$

where $u(t)$ and $v(t)$ are real-valued signals corresponding *e.g.* to eastward and northward ocean current velocities. The vector and complex representations equivalently encode trajectories in the 2D plane, see Fig. 2. The choice of one over the other representation usually depends on the application area: vector-valued signals are more common in optics and geophysics. The complex representation is more common in oceanography (Gonella, 1972; Mooers, 1973), which has popularized a decomposition of bivariate signals into counter-rotating components known as *rotary components*. Many recent methods developed in the signal processing literature (Schreier, 2008; Lilly and Olhede, 2010a; Walden, 2013; Sykulski, Olhede, and Lilly, 2016) also use the complex representation. It shall be noted that perhaps the first to recognize the potential of the complex representation to study bivariate signals were Blanc-Lapierre and Fortet (1953).

The use of the complex representation over the vector representation has often been advocated for in the signal processing community. While this has sparked some heated debates, see for instance the discussion between Picinbono (1996) and Johnson (1996), this choice seems to be well accepted today by the signal processing community. The often quoted advantages of the complex representation include: a preserved relation between the two real univariate components, simplified expressions, the direct availability of fundamental notions such as amplitude and phase and the geometric insights offered by complex numbers. See *e.g.* the recent books of Mandic and Goh (2009) and Schreier and Scharf (2010) for a detailed discussion of these advantages.

This thesis aims at providing an unifying framework for the processing of bivariate signals. For this purpose, Section 0.1 introduces key concepts thanks to the very first example of the monochromatic bivariate signal. Then Section 0.2 reviews the usual vector and complex approaches for processing bivariate signals. Section 0.3 presents the limitations of these two approaches and discusses the requirements that an *ideal* framework should satisfy. Section 0.4 outlines the contributions of this thesis on a chapter-by-chapter basis.

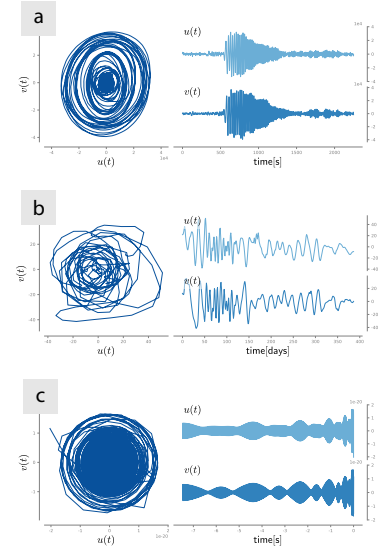


Figure 1: Three examples of bivariate signals. The time-evolution of the two components $u(t)$ and $v(t)$ as well as the trace in the $u - v$ plane are represented. (a) polarized seismic wave (b) horizontal current velocities measured by an oceanic drifter (c) gravitational wave polarizations emitted by a precessing coalescing binary.

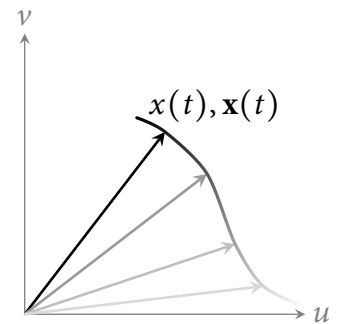


Figure 2: A bivariate signal defined by (1) corresponds to a trajectory in the 2D plane.

0.1 A FIRST EXAMPLE: THE MONOCHROMATIC BIVARIATE SIGNAL

The simplest example of bivariate signal is the *monochromatic* bivariate signal: it carries a single frequency ν_0 . Still, it enables the introduction of many key concepts related to the study and understanding of bivariate signals.

0.1.1 Vector and complex representations

A monochromatic bivariate signal is given in its vector representation by

$$\mathbf{x}(t) = \begin{bmatrix} u(t) \\ v(t) \end{bmatrix} = \begin{bmatrix} a_u \cos(2\pi\nu_0 t + \varphi_u) \\ a_v \cos(2\pi\nu_0 t + \varphi_v) \end{bmatrix}, \quad (2)$$

where $a_u, a_v \geq 0$ and $\varphi_u, \varphi_v \in [0, 2\pi)$ are the amplitudes and phases of the respective components. The complex representation of this signal writes

$$\begin{aligned} x(t) &= a_u \cos(2\pi\nu_0 t + \varphi_u) + i a_v \cos(2\pi\nu_0 t + \varphi_v) \\ &= a_+ e^{i\theta_+} e^{i2\pi\nu_0 t} + a_- e^{-i\theta_-} e^{-i2\pi\nu_0 t} \end{aligned} \quad (3)$$

where $a_+, a_- \geq 0$ and $\theta_+, \theta_- \in [0, 2\pi)$ are the amplitude and phase of each *phasor*¹, respectively. Eq. (3) describes the signal $x(t)$ as a sum of two counter-rotating phasors at frequencies ν_0 and $-\nu_0$. These are also called the *rotary components* of the signal (Schreier and Scharf, 2010).

1. A *phasor* is here understood as a signal of the form $t \mapsto e^{i2\pi\nu t}$, where $\nu \in \mathbb{R}$.

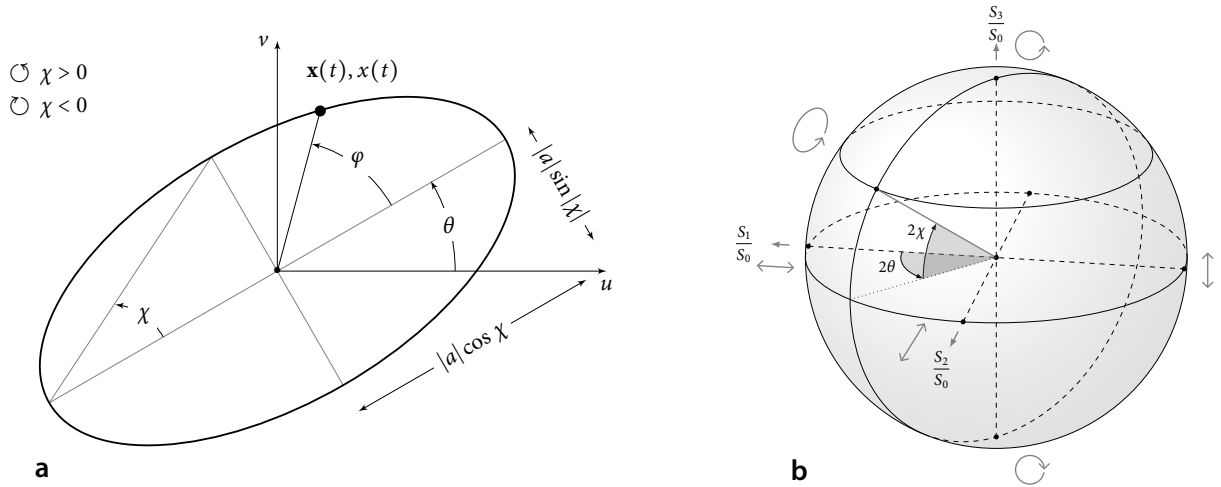


Fig. 3a depicts the elliptical trajectory in the 2-dimensional plane defined by the monochromatic bivariate signal (2). This trajectory is described by four natural parameters. Two of them encode the *geometry* of the ellipse. The orientation $\theta \in [-\pi/2, \pi/2]$ gives the angle between the major axis of the ellipse and the horizontal axis. The ellipticity $\chi \in [-\pi/4, \pi/4]$ characterizes the shape of the ellipse: it is directly related to the ratio between minor and major axes. For $\chi = 0$ the ellipse degenerates into a line segment, while for $\chi = \pm\pi/4$ it becomes a circle. Importantly the sign of χ gives the running direction within the ellipse: counter-clockwise if $\chi > 0$ and clockwise for $\chi < 0$. The two remaining parameters are classical: the amplitude $a \geq 0$ controls the size of the ellipse and the phase $\varphi \in [0, 2\pi)$ gives the initial position of the signal within the ellipse.

Figure 3: (a) The monochromatic bivariate signal describes an elliptical trajectory in the 2-dimensional plane. (b) Poincaré sphere of polarization states. To any point on the sphere is associated a unique polarization state either described by spherical angular coordinates $(2\theta, 2\chi)$ or normalized Stokes parameters $S_1/S_0, S_2/S_0$ and S_3/S_0 .

0.1.2 The concept of polarization: Stokes parameters and Poincaré sphere

In optics the signal $\mathbf{x}(t)$ defined by (2) or $x(t)$ defined by (3) would describe the instantaneous position of the electric field in the transverse plane, *i.e.* in the plane orthogonal to the direction of propagation of the light. As it describes an elliptical trajectory, the electric field is said to be *elliptically polarized*. Polarization is a fundamental concept related to wave propagation, which can be found in various domains such as optics and electromagnetics (Born and Wolf, 1980), seismology (Aki and Richards, 2002) or gravitational wave theory (Misner, Thorne, and Wheeler, 1973).

The *polarization ellipse* is usually described in optics by *Stokes parameters*. They form a set of four real-valued parameters S_0, S_1, S_2 and S_3 which are experimentally accessible via intensity measurements. They are related to ellipse parameters a, θ and χ like

$$S_0 = a^2 \quad (4)$$

$$S_1 = a^2 \cos 2\theta \cos 2\chi \quad (5)$$

$$S_2 = a^2 \sin 2\theta \cos 2\chi \quad (6)$$

$$S_3 = a^2 \sin 2\chi. \quad (7)$$

The first parameter S_0 is purely energetic; remaining parameters S_1, S_2 and S_3 describe the polarization state of the monochromatic bivariate signal. Being a phase term, φ does not appear in Stokes parameters.

Fig. 3b depicts the Poincaré sphere, first introduced by Poincaré (1892). This powerful geometric representation of polarization states directly connects Stokes parameters to the natural parameters a, θ and χ of the ellipse. To any point on the surface of the 2-dimensional unit sphere one associates a unique polarization state. Its spherical angular coordinates $(2\theta, 2\chi)$ give the geometric parameters of the ellipse. Its Cartesian coordinates provide the corresponding normalized Stokes parameters $S_1/S_0, S_2/S_0$ and S_3/S_0 . The north and south pole of the Poincaré sphere describe counter clockwise and clockwise circular polarization, respectively. The equator describes linearly polarized states: the orientation θ evolves with the longitude. As one moves towards the poles, the ellipticity χ increases in absolute value and one tends to circular polarization.

Expressions (4)–(7) correspond to the particular case where the signal is *fully polarized*. The case of *partially polarized* or *unpolarized* signals will be discussed in more detail in Chapter 2.

0.1.3 Expressions for ellipse parameters

It is natural to search for the expression of the ellipse trajectory parameters a, θ, χ and φ in terms of the standard parameterization of each representation (vector or complex). Starting from Eq. (2) the amplitude a and phase φ read

$$a = \sqrt{a_u^2 + a_v^2} \quad \text{and} \quad \varphi = \frac{\varphi_u + \varphi_v}{2}. \quad (8)$$

The orientation θ and ellipticity χ are given by

$$\tan 2\theta = \frac{2a_u a_v}{a_u^2 - a_v^2} \cos(\varphi_u - \varphi_v) \quad \text{and} \quad \sin 2\chi = \frac{2a_u a_v}{a_u^2 + a_v^2} \sin(\varphi_u - \varphi_v) \quad (9)$$

when $a_u \neq a_v$. The case $a_u = a_v$ corresponds to circular polarization: it follows that $\chi = \pm\pi/4$ and θ is undefined for this case.

The amplitude a and phase φ are obtained from the complex representation (3) as

$$a = \sqrt{2}\sqrt{a_+^2 + a_-^2} \quad \text{and} \quad \varphi = \frac{\theta_+ + \theta_-}{2}. \quad (10)$$

The orientation θ and ellipticity χ write

$$\theta = \frac{\theta_+ - \theta_-}{2}, \quad \text{and} \quad \tan \chi = \frac{a_+ - a_-}{a_+ + a_-}. \quad (11)$$

If one compares expressions (9) and (11) for θ and χ we see that (11) decouples the contribution from the amplitude and phases from each rotary component. This apparent simplicity is sometimes used as an argument supporting the use of the complex representation (11) over the vector representation (9), see *e.g.* Schreier and Scharf (2010).

0.1.4 Natural descriptors for bivariate signals

One could argue whether or not a , θ , χ and φ represent *natural* parameters for the elliptical trajectory depicted in Fig. 3a. These parameters appear traditionally in optics (Brosseau, 1998; Born and Wolf, 1980) thanks to the Poincaré sphere representation and the associated Stokes parameters expressions. Moreover they also appeared as quantities of interest in the signal processing literature, see *e.g.* Schreier (2008) and Walden (2013). These parameters are natural in the sense that they directly embody the *joint structure* of the two univariate signals that constitute the monochromatic bivariate signal. One associates a common amplitude a , a common phase φ and two geometric parameters θ and χ to the signal $\mathbf{x}(t)$ or $x(t)$. This contrasts with parameterizations $(a_u, a_v, \varphi_u, \varphi_v)$ or $(a_+, a_-, \varphi_+, \varphi_-)$ which involve two amplitudes and two phases. In fact Eqs. (2) and (3) can be interpreted as the decomposition of the signal into, respectively, horizontal and vertical linearly polarized components and counter-clockwise and clockwise circularly polarized components. The natural or canonical parameters $(a, \theta, \chi, \varphi)$ are very generic in the sense that they are not attached to any particular representation, *i.e.* to any choice of orthogonal polarizations decomposition.

0.2 AN OVERVIEW OF SIGNAL PROCESSING FOR BIVARIATE SIGNALS

Now we review the two usual approaches for the processing of generic bivariate signals. They are based either on the use of vector representation $\mathbf{x}(t)$ or the complex representation $x(t)$ of bivariate signals.

Section 0.2.1 and Section 0.2.2 first consider the case of second-order stationary random bivariate signals: they form an important category of random bivariate signals whose second-order statistical properties (*i.e.* mean and covariances functions) are invariant to any given time-shift. In this setting, at any given frequency the spectral contribution of the signal takes the form of a random ellipse (Walden, 2013): its orientation, ellipticity, or amplitude vary over realizations. In particular we put the emphasis on the notion of (*im*)*properness* of random complex signals.

Section 0.2.3 and Section 0.2.4 then describe one of the most fundamental signal processing task, *i.e.* linear time-invariant (LTI) filtering, in both representations.

Finally, Section 0.2.5 presents existing methods towards the characterization of instantaneous attributes of bivariate signals, and how it relates to time-frequency analysis techniques.

0.2.1 Random bivariate signals in the vector representation

For sake of simplicity, second-order stationarity is simply referred to as *stationarity* in what follows, and signals are assumed to be zero-mean. Consider a stationary random bivariate signal $\mathbf{x}(t) = [u(t), v(t)]^\top$ where $u(t)$ and $v(t)$ are jointly stationary real-valued signals and where $^\top$ is the transpose operator. The covariance matrix function of the vector signal $\mathbf{x}(t)$ is (Priestley, 1981)

$$\underline{\mathbf{R}}_{\mathbf{xx}}(\tau) = \mathbf{E} \{ \mathbf{x}(t) \mathbf{x}^\top(t - \tau) \} = \begin{bmatrix} R_{uu}(\tau) & R_{uv}(\tau) \\ R_{vu}(\tau) & R_{vv}(\tau) \end{bmatrix} \quad (12)$$

where R_{uu} , R_{vv} denote the autocovariances of u and v , and where R_{uv} denotes the cross-covariance between u and v . These are defined like

$$R_{uu}(\tau) = \mathbf{E} \{ u(t)u(t - \tau) \}, \quad R_{vv}(\tau) = \mathbf{E} \{ v(t)v(t - \tau) \}, \quad R_{uv}(\tau) = \mathbf{E} \{ u(t)v(t - \tau) \}. \quad (13)$$

Note that R_{uu} and R_{vv} are even functions of τ , and that for all τ , $R_{vu}(\tau) = R_{uv}(-\tau)$. The entry-wise Fourier transform (denoted symbolically by \mathcal{F}) of the covariance matrix function $\underline{\mathbf{R}}_{\mathbf{xx}}(\tau)$ defines the power spectral density (PSD) matrix of $\mathbf{x}(t)$

$$\underline{\mathbf{P}}_{\mathbf{xx}}(\mathbf{v}) = \mathcal{F} \underline{\mathbf{R}}_{\mathbf{xx}}(\mathbf{v}) = \begin{bmatrix} P_{uu}(\mathbf{v}) & P_{uv}(\mathbf{v}) \\ P_{vu}(\mathbf{v}) & P_{vv}(\mathbf{v}) \end{bmatrix}, \quad (14)$$

where P_{uu} and P_{vv} are the PSD of u and v and where P_{uv} is the cross-PSD between u and v . The PSD matrix $\underline{\mathbf{P}}_{\mathbf{xx}}$ is Hermitian positive semidefinite since PSDs P_{uu} and P_{vv} are real-valued nonnegative and $P_{vu}(\mathbf{v}) = \overline{P_{uv}(\mathbf{v})}$ for every \mathbf{v} . See e.g. Priestley (1981) for more details on spectral analysis using the vector representation.

0.2.2 Random bivariate signals in the complex representation

Complex-valued random variables and random signals have been widely studied in the signal processing literature (Picinbono, 1994; Amblard, Gaeta, and Lacoume, 1996a, 1996b; Picinbono and Bondon, 1997; Ollila, 2008; Adali, Schreier, and Scharf, 2011). Many simulation procedures of such signals have been also proposed (Rubin-Delanchy and Walden, 2007; Chandna and Walden, 2013; Sykulski and Percival, 2016).

The complete statistical characterization of the second-order properties of a stationary complex signal $x(t)$ involves two quantities: the usual autocovariance function $R_{xx}(\tau)$ and the complementary or pseudo-covariance $\tilde{R}_{xx}(\tau)$. They are defined as

$$\text{(autocovariance)} \quad R_{xx}(\tau) \triangleq \mathbf{E} \left\{ x(t) \overline{x(t - \tau)} \right\}, \quad (15)$$

$$\text{(complementary-covariance)} \quad \tilde{R}_{xx}(\tau) \triangleq \mathbf{E} \{ x(t)x(t - \tau) \}. \quad (16)$$

Remark that the pseudo-covariance $\tilde{R}_{xx}(\tau)$ is simply the covariance function between $x(t)$ and its conjugate $\overline{x(t)}$.

The autocovariance function is Hermitian $R_{xx}(-\tau) = \overline{R_{xx}(\tau)}$ and the com-

plementary covariance is even $\tilde{R}_{xx}(\tau) = \tilde{R}_{xx}(-\tau)$. In the spectral domain one defines the PSD and complementary PSD (C-PSD) of the signal x as

$$\text{(PSD)} \quad P_{xx}(\nu) = \mathcal{F}R_{xx}(\nu), \quad (17)$$

$$\text{(C-PSD)} \quad \tilde{P}_{xx}(\nu) = \mathcal{F}\tilde{R}_{xx}(\nu). \quad (18)$$

The PSD $P_{xx}(\nu)$ is real nonnegative but not necessarily even $P_{xx}(-\nu) \neq P_{xx}(\nu)$ as x is complex-valued. The C-PSD is complex-valued $\tilde{P}_{xx}(\nu) \in \mathbb{C}$ and even $\tilde{P}_{xx}(-\nu) = \tilde{P}_{xx}(\nu)$.

Usually (Schreier and Scharf, 2003b) one introduces the augmented complex vector signal $\uparrow \mathbf{x}(t) = [x(t), \bar{x}(t)]^\top$. Then the corresponding augmented covariance matrix reads

$$\uparrow \mathbf{R}_{xx}(\tau) \triangleq \mathbf{E} \left\{ \uparrow \mathbf{x}(t) \uparrow \mathbf{x}^\dagger(t - \tau) \right\} = \begin{bmatrix} R_{xx}(\tau) & \tilde{R}_{xx}(\tau) \\ \tilde{R}_{xx}(\tau) & R_{xx}(\tau) \end{bmatrix}, \quad (19)$$

with \dagger the conjugate-transpose operator. Its entry-wise Fourier transform defines the augmented PSD matrix

$$\uparrow \mathbf{P}_{xx}(\nu) = \begin{bmatrix} P_{xx}(\nu) & \tilde{P}_{xx}(\nu) \\ \tilde{P}_{xx}(\nu) & P_{xx}(-\nu) \end{bmatrix}. \quad (20)$$

Note that the augmented PSD matrix involves expressions of the PSD at both positive and negative frequencies. The augmented PSD matrix is directly related to the PSD matrix (14) of the real vector $\mathbf{x}(t)$ like

$$\uparrow \mathbf{P}_{xx}(\nu) = \mathbf{T} \mathbf{P}_{xx}(\nu) \mathbf{T}^\dagger \quad (21)$$

where \mathbf{T} is defined as

$$\mathbf{T} = \begin{bmatrix} 1 & \mathbf{i} \\ 1 & -\mathbf{i} \end{bmatrix}. \quad (22)$$

A signal $x(t)$ is said to be second-order circular or *proper* if its complementary covariance vanishes, i.e. $\tilde{R}_{xx}(\tau) = 0$ for all τ . Otherwise $x(t)$ is said to be *improper*. The term *proper* may refer to the fact that *proper* complex-valued signals behave very similarly to real-valued signals (Schreier and Scharf, 2003b). Equivalently, a *proper* signal is characterized by a null C-PSD $\tilde{P}_{xx}(\nu) = 0$ for all ν . Using (21), we found that a *proper* signal is characterized by

$$P_{uu}(\nu) = P_{vv}(\nu) \quad \text{and} \quad \text{Re } P_{uv}(\nu) = 0 \quad \text{for all } \nu \quad (23)$$

Or equivalently in the time-domain:

$$R_{uu}(\tau) = R_{vv}(\tau) \quad \text{and} \quad R_{uv}(-\tau) = -R_{uv}(\tau) \quad \text{for all } \tau. \quad (24)$$

Stationary analytic signals without a DC component are examples of proper complex signals, see for instance Schreier and Scharf (2010, p. 57).

Remark: random ellipses The contribution of a single frequency to a stationary random bivariate signal takes the form of a random ellipse. The statistical properties of random ellipses have been widely investigated in the signal processing community (Walden and Medkour, 2007; Rubin-Delanchy and Walden, 2008; Medkour and Walden, 2008; Chandna and Walden, 2011; Walden, 2013). See also Barakat (1985) and Brosseau (1995) for similar results regarding the statistical properties of Stokes parameters. These results will be reviewed in Section 2.4.2 in our discussion on the estimation of polarization parameters.

0.2.3 LTI filtering in the vector representation: matrix-valued filters

Back to the vector representation of bivariate signals, consider the input $\mathbf{x}(t)$ and the output $\mathbf{y}(t)$ of an arbitrary LTI filter. Such a filter is described by its matrix impulse response $\underline{\mathbf{m}}(t)$, a real-valued 2-by-2 matrix such that

$$\mathbf{y}(t) = \underline{\mathbf{m}} * \mathbf{x}(t) \quad (25)$$

where $*$ denotes entry-wise convolution. If

$$\underline{\mathbf{m}}(t) = \begin{bmatrix} m_{11}(t) & m_{12}(t) \\ m_{21}(t) & m_{22}(t) \end{bmatrix} \quad \text{and} \quad \mathbf{x}(t) = \begin{bmatrix} x_1(t) \\ x_2(t) \end{bmatrix} \quad (26)$$

then the matrix-vector LTI filtering relation (25) reads explicitly

$$\mathbf{y}(t) = \begin{bmatrix} m_{11} * x_1(t) + m_{12} * x_2(t) \\ m_{21} * x_1(t) + m_{22} * x_2(t) \end{bmatrix}. \quad (27)$$

The filtering relation (25) can be rewritten in the frequency domain as the simple matrix-vector relation

$$\mathbf{Y}(\nu) = \underline{\mathbf{M}}(\nu)\mathbf{X}(\nu) \quad (28)$$

where \mathbf{Y} , \mathbf{X} and $\underline{\mathbf{M}}$ denote entry-wise Fourier transforms of \mathbf{y} , \mathbf{x} and $\underline{\mathbf{m}}$. Note that (28) describes, for each frequency, a linear relationship between 2 dimensional complex-vectors. Using (28) the relationship between PSD matrices of \mathbf{y} and \mathbf{x} is given by

$$\underline{\mathbf{P}}_{yy}(\nu) = \underline{\mathbf{M}}(\nu)\underline{\mathbf{P}}_{xx}(\nu)\underline{\mathbf{M}}^\dagger(\nu). \quad (29)$$

In optics, the spectral domain relation (28) is usually preferred over the time-domain relation (25). This arises since most light sources (e.g. lasers) can be assumed narrow-band; explicit frequency-dependence is often omitted. The study of linear relationships between 2 dimensional complex-vectors as in (28) is called *Jones calculus*. This formalism permits to describe interactions between polarized light and non-depolarizing linear optical systems (e.g. quarter-wave plates, polarizers, etc.) and is still widely used. See e.g. Gil (2007) and Gil and Ossikovski (2016) for more details.

Jones calculus is named after R. C. Jones, who introduced this formalism in a series of papers published in 1941, see Jones (1941).

0.2.4 LTI filtering in the complex representation: widely linear filters

The most generic LTI filter in the complex representation of bivariate signals takes the form of a *widely linear filter*:

$$y(t) = h_1 * x(t) + h_2 * \bar{x}(t), \quad (30)$$

where $h_1(t)$ and $h_2(t)$ are two complex-valued impulse response functions. The signal $x(t)$ and its conjugate $\bar{x}(t)$ are filtered separately to produce the output signal $y(t)$. This approach was first proposed by Brown and Crane (1969) who coined the term ‘‘conjugate linear filtering’’. Aspects regarding optimum mean-square linear estimation using such filters were developed subsequently by several authors, see Gardner (1993), Picinbono and Chevalier (1995), and Schreier and Scharf (2003b).

The term ‘‘widely linear filtering’’ is due to Picinbono and Chevalier (1995).

The widely linear filtering relation (30) can be rewritten in the augmented vector representation. Introduce the spectral domain augmented matrix of the filter as

$$\mathbf{H}(\mathbf{v}) \triangleq \begin{bmatrix} H_1(\mathbf{v}) & H_2(\mathbf{v}) \\ H_1(-\mathbf{v}) & H_2(-\mathbf{v}) \end{bmatrix} \quad (31)$$

The relation between augmented PSD matrices of $y(t)$ and $x(t)$ then is

$$\mathbf{P}_{yy}(\mathbf{v}) = \mathbf{H}(\mathbf{v}) \mathbf{P}_{xx}(\mathbf{v}) \mathbf{H}^\dagger(\mathbf{v}). \quad (32)$$

From the augmented PSD matrix definition (20) and Eqs. (31)–(32) one sees that the filtering relation in the complex-representation involves simultaneously positive and negative frequencies. The equivalence between the widely linear filtering relation (32) and the matrix-vector filtering relation (29) is readily obtained using transformation (21).

0.2.5 Instantaneous ellipses and time-frequency analysis

In practical situations where a narrowband bivariate signal is acquired, the signal trajectory will in general take the form of a time-varying ellipse. *Instantaneous* ellipse parameters then characterize the nonstationary behavior of the signal. For deterministic signals, Lilly and Gascard (2006) have proposed the modulated elliptical signal model in the complex representation

$$x(t) = e^{i\theta(t)} [c(t) \cos \varphi(t) + \mathbf{i}d(t) \sin \varphi(t)] \quad (33)$$

where $c(t) \geq 0$ and where $d(t)$ can take any sign. The angle $\theta(t) \in [-\pi/2, \pi/2]$ encodes the *instantaneous orientation* of the ellipse; $\varphi(t) \in (-\pi, \pi)$ gives the *instantaneous phase*, *i.e.* the instantaneous position of $x(t)$ around the ellipse. Quantities $c(t)$ and $|d(t)|$ describe the instantaneous major and minor axes of the ellipse, respectively. The sign of $d(t)$ reflects the direction of circulation around the ellipse. As shown by Lilly and Olhede (2010a), these instantaneous parameters can be obtained from pairs of *analytic signals*: either from the analytic signal of the vector $[u(t), v(t)]$ or from the analytic signal of the complex augmented vector $[x(t), \overline{x(t)}]$.

For the characterization of generic, *i.e.* wideband, nonstationary bivariate signals various methods have been proposed. For the nonstationary random case (Hindberg and Hanssen, 2007; Schreier, 2008), it consists in examining suitable correlations or coherences using pairs of time-frequency representations of complex-valued signals. Alternative approaches using the vector representation have been proposed in the deterministic case, mainly by the geophysics community (Diallo et al., 2005; Roueff, Chanussot, and Mars, 2006; Pinnegar, 2006). We also note that bivariate extensions (Rilling et al., 2007; Tanaka and Mandic, 2007) of the empirical mode decomposition (EMD) (Huang et al., 1998) have also attracted much interest in recent years.

0.3 AN IDEAL FRAMEWORK FOR BIVARIATE SIGNAL PROCESSING?

0.3.1 Limitations of existing methods

Existing approaches are based on the use of either the vector $\mathbf{x} = [u(t), v(t)]^T$ or complex $x(t) = u(t) + iv(t)$ representation of bivariate signals. Such approaches exhibit intrinsic limitations which prevent to consider them as an *ideal* framework for processing bivariate signals. Below we detail point-by-point these limitations.

No direct description in terms of natural ellipse parameters As already discussed in Section 0.1 for the simple monochromatic bivariate case, neither the vector nor complex representation permits a direct description of bivariate signals in terms of natural elliptical trajectory parameters a , θ , χ and φ . This issue propagates to even more challenging scenarios, *e.g.* non-stationary or random signals. Parameters must be determined from pairs of amplitude-phase quantities, a procedure which implicitly implies a decomposition of the bivariate signal into a peculiar orthogonal polarizations basis. In the vector representation, natural ellipse parameters are obtained from the amplitude and phase of the linear horizontal (a_u, φ_u) and linear vertical polarization (a_v, φ_v). The complex representation yields amplitude and phase of circularly polarized components, counter-clockwise (a_+, φ_+) and clockwise (a_-, φ_-).

An ideal framework should feature this direct description in terms of natural ellipse parameters, in order not to be subject to a particular orthogonal polarizations decomposition. This would provide straightforward interpretations and greatly simplify the synthesis of bivariate signals with prescribed physical properties.

Interpretability of positive frequencies only in the complex representation For a physicist it is natural to consider positive frequencies only as, per definition, frequency is the number of oscillations per time unit (Cohen, 1995). For real-valued signals this can be mathematically justified thanks to the Hermitian symmetry $X(-\nu) = \overline{X(\nu)}$ of their Fourier transform: “negative frequencies” do not convey any supplementary information to positive ones. This authorizes useful identifications, *e.g.* between the cosine model $\cos(2\pi\nu t)$ and the complex exponential $\exp(i2\pi\nu t)$. It also enables the construction of the *analytic signal of a real signal* (Gabor, 1946; Ville, 1948), which is the foundation for time-frequency analysis (Flandrin, 1998).

To that extent, the complex representation of bivariate signals is not satisfactory as both *positive* and *negative* frequencies have to be considered: the Fourier transform of a complex signal $x(t)$ no longer satisfies Hermitian symmetry. Negative frequencies are associated to clockwise rotating components and positive frequencies are attached to counter-clockwise rotating components. This refers to the so-called *rotary spectrum analysis* popularized by oceanographers (Gonella, 1972). At a given (physical) frequency $|\nu|$ the circulation direction in the ellipse is recovered by comparing amplitudes at $-\nu$ and ν , see Eq. (11).

An ideal framework using the complex representation of bivariate signals should feature a nice correspondence between *mathematical* (positive and negative) and *physical* (positive only) frequencies. This would allow natural

This issue is specific to the complex representation of bivariate signals. The Fourier transform of the vector signal $\mathbf{x}(t)$ exhibits Hermitian symmetry and one can consider only positive frequencies Fourier vectors.

interpretations of the spectral content of bivariate signals.

Physical interpretations of (im)properness The notion of (im)properness of complex-valued variables and signals has been of fundamental importance in the signal processing literature: see *e.g.* Adali, Schreier, and Scharf (2011) for a review. Improperity surely is meaningful when considering complex signals created from real (univariate) signals, *e.g.* analytic signals or complex baseband representation of real signals. It is particularly useful in communications, where improperity arises from in-phase/quadrature imbalance due to receiver or channel imperfections, or when the transmitted signal is non-stationary². Many works (see *e.g.* Schreier and Scharf (2010) for a review) have shown that taking into account improperity of complex signals increases performances of detection and estimation algorithms.

However one could question the physical relevance of this notion for (random) bivariate signals, *i.e.* for signals such as polarized waves, surface wind or ocean currents measurements.

Fig. 4 supports our discussion by depicting three proper signals which however carry very different physical properties. Fig. 4a represents a monochromatic bivariate signal with frequency ν_0 that is fully circularly polarized. Fig. 4b displays this signal corrupted by additive proper white Gaussian noise. The signal is then said to be *partially polarized* at frequency ν_0 . Fig. 4c shows a realization of proper white Gaussian noise, which corresponds to an unpolarized signal (at all frequencies.) As these three examples demonstrate, (im)properness seems not to be the most relevant feature when dealing with physical properties, *e.g.* polarization, of bivariate signals.

In our opinion an ideal framework should provide a direct description of bivariate signals in terms of relevant physical parameters. This should provide a straightforward classification or discrimination of bivariate signals based on physically interpretable properties, such as the *degree of polarization*.

Interpretation of LTI filtering relations A common limitation of both the vector and complex representation is the lack of direct interpretability of filtering relations (25) and (30). Similar issues arise with relations between PSDs (29) and (32). For the univariate case, filters are described in the spectral domain by the usual filtering relation

$$Y(\nu) = G(\nu)X(\nu) \quad (34)$$

where $G(\nu)$ is frequency response of the filter. Its magnitude $|G(\nu)|$ and phase $\arg G(\nu)$ have a natural interpretation in terms of *gain* and *phase delay* of the filter, respectively. Such physical interpretations are lacking in the bivariate case, as shown by LTI filtering expressions in the vector (25) and complex (30) representations.

A ideal framework must be able to provide such interpretations. It will improve the ability to specify desired behavior of filters for bivariate signals, and to tailor their use to the physical properties of bivariate signals.

Systematic time-frequency analysis A comprehensive and generic time-frequency analysis theory for bivariate signals does not exist in the vector setting, neither

2. Analytic signals of nonstationary random real signals are known to be improper (Picinbono and Bondon, 1997; Schreier and Scharf, 2003a).

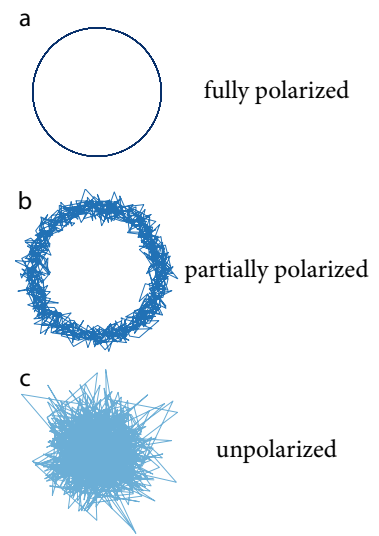


Figure 4: Three *proper* complex signals with very different polarization properties. (a) a fully circularly polarized monochromatic signal with frequency ν_0 . (b) signal in (a) corrupted by additive proper white Gaussian noise. The signal is partially polarized at frequency ν_0 (c) proper white Gaussian noise is unpolarized.

representation does the complex representation. As already mentioned, existing approaches rely on the simultaneous processing of pairs of time-frequency representations (Hindberg and Hanssen, 2007; Schreier, 2008; Roueff, Chanussot, and Mars, 2006; Diallo et al., 2005). Data-driven methods such as bivariate extensions of the EMD (Rilling et al., 2007; Tanaka and Mandic, 2007) have also been proposed. However, fundamental notions such as the *spectrogram* of a bivariate signal are not yet defined.

One foundation for the time-frequency analysis of bivariate signals was described by Lilly and Gascard (2006) and Lilly and Olhede (2010a) with the modulated ellipse model (33). However as pointed out by the authors in Lilly and Olhede (2010a) this model is not able to separate multicomponent bivariate signals, as it is based on pairs of analytic signals. It may also appear that the modulated ellipse model (33) is somehow arbitrary and not completely theoretically grounded.

An ideal framework should provide meaningful and physically interpretable time-frequency representations for bivariate signals. Those should encompass and extend well-known concepts from usual time-frequency analysis such as analytic signals, spectrograms, scalograms as well as generic (*i.e.* bilinear) time-frequency representations.

Note that by *spectrogram* we mean a quadratic or bilinear time-frequency representation based on a short-term Fourier transform.

0.3.2 Summary of requirements

To summarize, an ideal and complete framework for processing bivariate signals should exhibit three distinctive and equally important features:

- ▶ *straightforward physical descriptions*: usual quantities from signal processing *e.g.* power spectral densities, LTI filters or time-frequency representations should be defined directly in terms of meaningful physical parameters. In addition, the framework should feature a desirable correspondence between negative and positive frequencies. These properties would allow direct interpretations and greatly simplify the design of many standard operations, such as filtering.
- ▶ *mathematical guarantees*: the approach should gather all necessary and desirable mathematical properties such as the conservation of energetic quantities or the inversion of time-frequency representations.
- ▶ *computationally fast implementations*: the proposed framework should come with tools that are as numerically efficient as existing approaches.

The last two requirements are crucial factors: the physical interpretability of the framework must preserve mathematical properties and numerical efficiency. Fulfilling these three requirements from, respectively, physics, mathematics and computer science would make the proposed approach a true *signal processing framework* (Flandrin, 2018).

0.4 CONTRIBUTIONS AND OUTLINE

THIS THESIS provides an unifying framework for the processing of bivariate signals. The proposed approach addresses all aforementioned limitations of existing approaches. It relies on two key ingredients. First, just like real-valued or univariate signals are usually embedded in complex numbers for ease of study, we embed bivariate signals – seen as complex-valued signals – in their

natural extension, the set of quaternions \mathbb{H} . Second the definition of a dedicated quaternion Fourier transform offers a meaningful spectral representation to bivariate signals. Thus the approach yields elegant, compact and efficient computations. Physical parameters describing the polarization properties of bivariate signals are naturally embedded in the proposed framework. It enables straightforward generalizations of usual signal processing notions such as spectral densities, filters, analytic signals or spectrograms to the bivariate case.

The proposed framework sheds light upon the physics of bivariate signals. More importantly, it does not sacrifice any fundamental mathematical guarantees nor computationally fast implementations. Any new quantity introduced within the proposed framework is validated by a theorem or a proposition. A companion open-source Python package called BiSPy³ implements our findings for the sake of reproducible research.

The potential of quaternion algebra and its relatives – such as Pauli matrices – has been recognized for long time in optics (Richartz and Hsü, 1949; Marathay, 1965; Whitney, 1971; Pellat-finet, 1984). This stems from its ability to give an insightful geometric treatment of polarization states. Many works, recently reviewed by Tudor (2010a, 2010b), have taken advantage of this fact to provide a pure operatorial, “matrix-free” formalism for the geometric description of polarization states and their interaction with linear (optical) systems. In fact this potential was even recognized long time ago by Hamilton (1844), the inventor of quaternions, in a letter to his friend Graves (17th October, 1843)

“ There seems to me to be something analogous to polarized intensity in the pure imaginary part; and to unpolarized energy (indifferent to direction) in the real part of a quaternion: and thus we have some slight glimpse of a future Calculus of Polarities. ”

As we shall see in Chapter 2, Hamilton’s prediction was almost correct: the only difference is that the real part of the quaternion power spectral density contains the sum of contributions from the unpolarized and polarized parts of the signal, respectively.

However we note that existing results are not directly applicable to the case of bivariate signals. Relations presented by Tudor (2010a, 2010b) and references therein are only given at the power spectral density level. Global phase effects are omitted and no direct or practical filtering relations are available. In addition as it focuses mainly on the monochromatic case, the formalism lacks a nice time-frequency duality which would make easy the handling of generic wideband bivariate signals.

Le Bihan, Sangwine, and Ell (2014) made a first step towards handling bivariate signals (seen as complex numbers) with a quaternion Fourier transform. They studied some of its properties and defined a bivariate analogue to the analytic signal, a key step towards the time-frequency analysis of bivariate signals. Unfortunately, the physical interpretation of their approach was limited to specific cases and thus lacked generality. Nonetheless these preliminary results form the starting point of this thesis.

This manuscript is divided into 5 chapters that describe the systematic construction of a complete framework for the processing of bivariate signals.

3. BiSPy: Bivariate Signal Processing in Python.

Documentation, tutorials and code at

 bispy.readthedocs.io/
 github.com/jflamant/bispy

As pointed out by Karlsson and Petersson (2004), if Hamilton had developed such “calculus of Polarities” he would have preceded Jones (1941) and Mueller (1943) by almost a century.

At the end of each chapter, appendices gather related complementary results and proofs.

CHAPTER 1 introduces the two ingredients of the proposed framework: quaternion algebra and the quaternion Fourier transform (QFT). In particular the properties of the QFT are studied in detail. We provide new results showing that the QFT is a well-defined mathematical object similar to the usual Fourier transform. We notably demonstrate a generalized Parseval-Plancherel theorem, which reveals that the QFT not only preserves energy but also another quadratic geometry-related quantity. The end of this chapter settles our framework for the processing of bivariate signals. The use of the QFT makes it possible to give a meaningful and physically interpretable quaternion-valued spectral representation of bivariate signals seen as complex-valued signals. The material presented in this chapter has been published in an international journal (Flamant, Le Bihan, and Chainais, 2017e).

CHAPTER 2 discusses the spectral analysis of bivariate signals. It focuses mainly on the case of second-order stationary random bivariate signals. We prove a spectral representation theorem for harmonizable signals. This key result introduces the quaternion power spectral density (PSD) of a bivariate signal. Another key quantity, the quaternion autocovariance of a bivariate signal, is defined thanks to a Wiener-Khinchine-like theorem for the QFT. The quaternion PSD has a direct interpretation in terms of polarization features, namely frequency-dependent Stokes parameters. We also discuss the role of the degree of polarization, a natural parameter which quantifies the dispersion of the polarization ellipse at each frequency. Nonparametric spectral estimation is investigated in detail and we show that the estimation of polarization quantities requires special care. Numerical experiments and illustrative examples support our findings. This chapter includes material from publications in an international journal (Flamant, Le Bihan, and Chainais, 2017c) and a contribution to the national conference GRETSI 2017 (Flamant, Le Bihan, and Chainais, 2017a).

CHAPTER 3 deals with the theory of linear time-invariant (LTI) filtering for bivariate signals. Based on an usual decomposition from polarization optics, we decompose LTI filters into *unitary* and *Hermitian* ones. Each class has natural interpretation in terms of fundamental properties of optical media: unitary filters model *birefringence* whereas Hermitian filters model *diattenuation* effects. The proposed framework directly gives filtering relations in terms of the eigenvalues and eigenvectors of the filter. It reveals the physical specificity of each filter and makes it easy to prescribe or design filters for bivariate signals. We demonstrate the relevance of the approach on two standard tasks of signal processing: spectral synthesis of stationary Gaussian signals and Wiener filtering. It also yields original decompositions of bivariate signals in two parts with prescribed properties. These promising results have been accepted for publication in an international journal (Flamant, Chainais, and Le Bihan, 2018a). They were also presented at the international conference SSP 2018 (Flamant, Chainais, and Le Bihan, 2018b) where we received a *Best Student paper award*.

CHAPTER 4 addresses the time-frequency analysis of bivariate signals. We define a bivariate analogue of the analytic signal called the quaternion embedding of a complex signal. It allows for direct identification of instantaneous amplitude and phase, as well as instantaneous polarization attributes. We introduce the short-term quaternion Fourier transform and quaternion continuous wavelet transform to overcome the inherent limitations of the quaternion embedding. Their properties are studied in detail. Two fundamental theorems guarantee their inversion. They also ensure the interpretability of associated time-frequency-polarization representations, namely *polarization spectrogram* and *polarization scalogram*, respectively. An asymptotic analysis ensures that these time-frequency-polarization representations localize meaningfully. The last part of this chapter develops a generic approach to the construction of time-frequency-polarization representation. We define the quaternion Wigner-Ville distribution and provide a construction of the Cohen class of bilinear representations. Numerical experiments from simulated and real-world data support our analysis. The majority of these results has been published in an international journal (Flamant, Le Bihan, and Chainais, 2017e). It was presented at the international conference ICASSP 2017 (Flamant, Le Bihan, and Chainais, 2017b) and at the national conference GRETSI 2017 (Flamant, Le Bihan, and Chainais, 2017d).

CHAPTER 5 explores the potential of the framework for the characterization of the polarization pattern of gravitational waves (GW) emitted by precessing binaries. This work results from a collaboration with Eric Chassande-Mottin and Fangchen Feng. Precession of emitting GW sources induces a modulation of the polarization pattern of the GW. We show that the framework developed in this thesis grants a new nonparametric characterization method for these effects. Importantly the approach does not assume any dynamical model for precession. Hence it is very promising for the future of GW characterization as it has the potential of revealing any dynamical effect that affects the GW polarization pattern. Our findings are illustrated on simulated data in noise-free and in realistic simulated noise contexts. These results have been presented at the international conference EUSIPCO 2018 (Flamant et al., 2018).

THE CONCLUDING CHAPTER, page 145, presents conclusions and discusses some of the prospects triggered by the work presented in this manuscript.

THE APPENDIX, page 169 describes the main results from a collaboration with Rémi Bardenet and Pierre Chainais. This joint work was performed in parallel with the research framework for bivariate signals developed in this thesis. We have studied the distribution of the zeros of the spectrogram of white Gaussian noise when the window is itself Gaussian. Our contributions are threefold: we rigorously define the zeros of the spectrogram of continuous white Gaussian noise, we explicitly characterize their statistical distribution, and we investigate the computational and statistical underpinnings of the practical implementation of signal detection based on the statistics of spectrogram zeros. This appendix reproduces the article “On the zeros of the spectrogram of white noise,” Bardenet, Flamant, and Chainais (2018), currently under review at *Applied and Computational Harmonic Analysis*.

LIST OF PUBLICATIONS

International journals

- 📄 J. Flamant, P. Chainais, and N. Le Bihan. 2018a. “A complete framework for linear filtering of bivariate signals.” *IEEE Transactions on Signal Processing* 66, no. 17 (September): 4541–4552. doi:[10.1109/TSP.2018.2855659](https://doi.org/10.1109/TSP.2018.2855659)
- 📄 J. Flamant, N. Le Bihan, and P. Chainais. 2017c. “Spectral analysis of stationary random bivariate signals.” *IEEE Transactions on Signal Processing* 65 (23): 6135–6145. doi:[10.1109/TSP.2017.2736494](https://doi.org/10.1109/TSP.2017.2736494)
- 📄 J. Flamant, N. Le Bihan, and P. Chainais. 2017e. “Time-frequency analysis of bivariate signals.” In Press, *Applied and Computational Harmonic Analysis*. doi:[10.1016/j.acha.2017.05.007](https://doi.org/10.1016/j.acha.2017.05.007)
- 📄 R. Bardenet, J. Flamant, and P. Chainais. 2018. “On the zeros of the spectrogram of white noise.” *manuscript accepted for publication in Applied and Computational Harmonic Analysis*. eprint: [arXiv:1708.00082](https://arxiv.org/abs/1708.00082)

International peer-reviewed conferences

- 👥 J. Flamant, P. Chainais, E. Chassande-Mottin, F. Feng, and N. Le Bihan. 2018. “Non-parametric characterization of gravitational-wave polarizations.” In *26th European Signal Processing Conference (EUSIPCO), 2018*, 1–5. September
- 👥 J. Flamant, P. Chainais, and N. Le Bihan. 2018b. “Linear filtering of bivariate signals using quaternions.” In *IEEE Statistical Signal Processing Workshop (SSP), 2018, Freiburg*, 1–5. Best Student Paper Award
- 👥 J. Flamant, N. Le Bihan, and P. Chainais. 2017b. “Polarization spectrogram of bivariate signals.” In *IEEE International Conference on Acoustics, Speech, and Signal Processing (ICASSP), 2017, New Orleans, USA*

National peer-reviewed conferences

- 👥 J. Flamant, N. Le Bihan, and P. Chainais. 2017a. “Analyse spectrale des signaux aléatoires bivariés.” In *GRETSI 2017*. Juan-les-Pins, France
- 👥 J. Flamant, N. Le Bihan, and P. Chainais. 2017d. “Spectrogramme de polarisation pour l’analyse des signaux bivariés.” In *GRETSI 2017*. Juan-les-Pins, France

Quaternion Fourier transform for bivariate signals



The purpose of this chapter is to lay the foundations of the proposed framework for the analysis and filtering of bivariate signals. This framework relies on two key ingredients: *quaternions* and the *quaternion Fourier transform*. We will first take a step back to gather the mathematical properties of these two elements in a generic setting. Then we will show that quaternions and the quaternion Fourier transform provide a natural embedding for bivariate signals viewed as complex-valued signals. The overall approach can be compared to the case of real-valued or univariate signals: these are usually embedded in the complex domain thanks to the Fourier transform, leading to many quantities of interest such as amplitude and phase. Here the fruitful combination of quaternions and quaternion Fourier transform yields an efficient, rigorous and easily interpretable framework for the handling of bivariate signals.

Quaternions form a four-dimensional algebra. A quaternion-valued signal can thus convey up to four channels simultaneously, giving rise to many signal processing applications. Examples include three-channel signal processing in geophysics (Le Bihan and Mars, 2004; Miron, Le Bihan, and Mars, 2006; Rehman and Mandic, 2010) and more generic four-channel signal processing (Took and Mandic, 2009, 2010; Vía, Ramírez, and Santamaría, 2010). Quaternions also appear in the representation of the monogenic signal (Felsberg and Sommer, 2001; Clausel, Oberlin, and Perrier, 2015), which is an extension of the analytic signal to the case of (bi-dimensional) images. In contrast to these existing approaches, quaternions are used in this manuscript as a *natural embedding* for bivariate signals viewed as *complex-valued* signals.

The name *quaternion Fourier transform* does not refer to a single mathematical instance. The set of quaternions exhibits two additional dimensions compared to the usual complex field thus providing a large choice of quaternion Fourier transform definitions. Motivated by applications in image processing (Sangwine, 1996; Ell and Sangwine, 2007; Bülow and Sommer, 2001), most definitions concern signals $x : \mathbb{R}^2 \rightarrow \mathbb{H}$, *i.e.* two-dimensional quaternion Fourier transforms. See *e.g.* Hitzer (2007) for possible definitions and their resulting properties. In general, two-dimensional quaternion Fourier transforms lack some usual properties of the complex Fourier transform, which may have hampered their widespread use. In contrast we study here the generic one-dimensional quaternion Fourier transform first introduced by Jamison (1970) in his PhD dissertation. This quaternion Fourier transform exhibits properties similar to the usual complex Fourier transform and enjoys a numerically efficient implementation relying on FFTs only. We demonstrate that the quaternion Fourier transform builds a solid ground for the representation and analysis of bivariate signals by a suitable choice of its free-parameter, its *axis*.

CHAPTER CONTENTS

1.1	Quaternions	32
	Definition • Quaternion operations • Complex subfields • Polar forms • Quaternions and 3D rotations •	
1.2	Quaternion Fourier transform	35
	Definition, existence, inversion • Properties of the Quaternion Fourier transform •	
1.3	Processing bivariate signals with the quaternion Fourier transform	39
	Bivariate signals • Choice of the axis of the QFT • Monochromatic bivariate signals •	
1.4	Conclusion	42
	APPENDICES	
1.A	Euler polar form computation	44
1.B	Hilbert spaces over quaternions	44
1.C	Discretization of the quaternion Fourier transform	45
	Discrete-time quaternion Fourier transform • Discrete quaternion Fourier transform •	
1.D	Proofs of quaternion Fourier transform properties	46
	Convolution properties (1.34) and (1.35) • Theorem 1.1 (Parseval-Plancherel) • Theorem 1.2 (Gabor-Heisenberg uncertainty principle) •	

Quaternion Fourier transforms have been widely used in color image processing, since RGB information can be stored in the vector part (imaginary part) of a quaternion, see Ell, Le Bihan, and Sangwine (2014) and references therein.

The formal construction of the proposed framework has been published in an international journal (Flamant, Le Bihan, and Chainais, 2017e):

- 📖 J. Flamant, N. Le Bihan, and P. Chainais. 2017e. “Time-frequency analysis of bivariate signals.” In Press, *Applied and Computational Harmonic Analysis*. doi:10.1016/j.acha.2017.05.007

In this paper we reviewed some known properties of the quaternion Fourier transform and proved some additional ones, including the generalized Parseval-Plancherel Theorem 1.1 and the Gabor uncertainty principle (Theorem 1.2). This paper also discusses the choice of the axis of the quaternion Fourier transform to efficiently process bivariate signals, as well as the use of a specific quaternion polar form to build meaningful interpretations.

First, we review quaternion algebra in Section 1.1. Then Section 1.2 studies the generic mathematical properties of the quaternion Fourier transform. Section 1.3 combines these two elements to establish a meaningful framework for the spectral description of bivariate signals. Appendices 1.A to 1.C gather complementary elements. Proofs of the main properties of the quaternion Fourier transform are collected in Appendix 1.D.

1.1 QUATERNIONS

In this section we only cover the necessary material on quaternions for this manuscript and refer to dedicated textbooks for more details. References include the original work of Hamilton (1866) and more recent textbooks such as Ward (1997) and Conway and Smith (2003). Historical aspects can be found in Crowe (1967) and Baez (2002). See also Ell (2013) for a recent review on the use of quaternions in signal processing.

Quaternions were first described by Sir William Rowan Hamilton in 1843. Hamilton had understood the tight link between complex numbers and 2-dimensional geometry and has thus tried for many years to find the corresponding algebra to handle 3-dimensional geometry. His quest for a system of *algebraic triplets* however failed until he discovered on the 16th of October 1843 that he needed a fourth dimension to handle them, leading to the quaternions. He immediately carved the rule for quaternion multiplication into the stone of the Brougham bridge in Dublin. This carving has now disappeared and has been replaced by a plaque honoring his discovery. Hamilton devoted his last 20 years to the study of his quaternions which culminated in his book, *Elements of quaternions*. After his death in 1865 quaternions remained fashionable for some time, but they were rapidly superseded by the advent of modern vector calculus through the work of Gibbs and Heaviside. Since the end of the 20th century, quaternions have however regained some attention primarily due to their ability to efficiently represent 3D rotations. They are used in numerous applications, ranging from computer graphics to robotics.

We recommend the musical video of A Capella Science (2016) for a narrative of Hamilton’s life and achievements.

Even his children asked him “Well, Papa, can you multiply triplets?”, to which he answered “No, I can only add and subtract them”.

1.1.1 Definition

The set of quaternions is denoted by \mathbb{H} in honor of Hamilton. Quaternions form a four-dimensional noncommutative division ring over the real numbers. Any quaternion $q \in \mathbb{H}$ reads in its Cartesian form

$$q = a + bi + cj + dk \quad (1.1)$$

where $a, b, c, d \in \mathbb{R}$ are its *components*. Imaginary units $\mathbf{i}, \mathbf{j}, \mathbf{k}$ satisfy the fundamental formula for quaternion multiplication

$$\mathbf{i}^2 = \mathbf{j}^2 = \mathbf{k}^2 = \mathbf{ijk} = -1 \quad (1.2)$$

from which one deduces

$$\begin{aligned} \mathbf{ij} &= -\mathbf{ji} = \mathbf{k} \\ \mathbf{jk} &= -\mathbf{kj} = \mathbf{i} \\ \mathbf{ki} &= -\mathbf{ik} = \mathbf{j}. \end{aligned} \quad (1.3)$$

These cyclic relations (1.3) highlight the noncommutative nature of quaternion multiplication, *i.e.* for $q, q' \in \mathbb{H}$ in general $qq' \neq q'q$. However usual operations such as addition, scalar multiplication and equality behave similarly to the complex case. Let $q = a + b\mathbf{i} + c\mathbf{j} + d\mathbf{k}$ and $q' = a' + b'\mathbf{i} + c'\mathbf{j} + d'\mathbf{k}$ denote two quaternions, one has

$$\begin{aligned} \text{(addition)} \quad q + q' &= q' + q = (a + a') + (b + b')\mathbf{i} + (c + c')\mathbf{j} + (d + d')\mathbf{k} \\ \text{(scalar multiplication)} \quad \forall \lambda \in \mathbb{R}, \lambda q &= q\lambda = \lambda a + \lambda b\mathbf{i} + \lambda c\mathbf{j} + \lambda d\mathbf{k} \\ \text{(equality)} \quad q = q' &\Leftrightarrow a = a', b = b', c = c', d = d'. \end{aligned}$$

Any quaternion $q \in \mathbb{H}$ can be decomposed into its *scalar part* $\mathcal{S}(q)$ and its *vector part* $\mathcal{V}(q)$ such that

$$q = \mathcal{S}(q) + \mathcal{V}(q), \quad (1.4)$$

where

$$\mathcal{S}(q) = a \quad \mathcal{V}(q) = b\mathbf{i} + c\mathbf{j} + d\mathbf{k}, \quad (1.5)$$

The scalar part is real-valued $\mathcal{S}(q) \in \mathbb{R}$, whereas the vector part $\mathcal{V}(q) \in \text{span}\{\mathbf{i}, \mathbf{j}, \mathbf{k}\}$ is *purely imaginary*. This vector part $\mathcal{V}(q)$ can be uniquely identified to a vector of \mathbb{R}^3 .

$\mathcal{S}(q)$ and $\mathcal{V}(q)$ are also called the *real* and *imaginary* parts of q . When $\mathcal{S}(q) = 0$, q is called a *pure* quaternion.

The product of two quaternions $q, q' \in \mathbb{H}$ reads using the scalar-vector decomposition

$$qq' = \mathcal{S}(q)\mathcal{S}(q') - \langle \mathcal{V}(q), \mathcal{V}(q') \rangle + \mathcal{S}(q)\mathcal{V}(q') + \mathcal{S}(q')\mathcal{V}(q) + \mathcal{V}(q) \times \mathcal{V}(q') \quad (1.6)$$

where $\langle \cdot, \cdot \rangle$ and $\cdot \times \cdot$ denote the usual inner product and cross product of \mathbb{R}^3 . Eq. (1.6) emphasizes the noncommutative nature of the quaternion product, since the cross-product $\mathcal{V}(q) \times \mathcal{V}(q')$ is noncommutative.

1.1.2 Quaternion operations

The quaternion conjugate of q is denoted by \bar{q} and is obtained by reversing the sign of its vector part

$$\bar{q} = \mathcal{S}(q) - \mathcal{V}(q) = a - b\mathbf{i} - c\mathbf{j} - d\mathbf{k}. \quad (1.7)$$

Importantly the order of the quaternion product is flipped by conjugation, *i.e.* for $q, q' \in \mathbb{H}$ one has

$$\overline{qq'} = \bar{q}'\bar{q}. \quad (1.8)$$

The modulus of a quaternion $q \in \mathbb{H}$ is

$$|q| = \sqrt{q\bar{q}} = \sqrt{\bar{q}q} = \sqrt{a^2 + b^2 + c^2 + d^2}. \quad (1.9)$$

When $|q| = 1$, q is called a *unit quaternion*.

The modulus of a product qq' is simply the product of the moduli:

$$|qq'| = |q'q| = |q||q'|. \quad (1.10)$$

Since \mathbb{H} is a division algebra, any nonzero quaternion has an inverse q^{-1} such that

$$q^{-1} = \frac{\bar{q}}{|q|^2}. \quad (1.11)$$

The involution with respect to an arbitrary pure unit quaternion μ is defined by

$$\bar{q}^\mu \triangleq -\mu q \mu \quad (1.12)$$

The set of three canonical involutions $\bar{q}^i, \bar{q}^j, \bar{q}^k$ together with the associated quaternion q allow to recover the real and the three imaginary parts of any quaternion. Unlike quaternion conjugation, involutions preserve ordering when applied to a product

$$\overline{qq'}^\mu = \bar{q}^\mu \bar{q}'^\mu \quad (1.13)$$

The combination of conjugation with an arbitrary involution is denoted by

$$q^{*\mu} \triangleq \bar{q}^\mu = \overline{q^\mu} = -\mu \bar{q} \mu. \quad (1.14)$$

This operation can be interpreted as a conjugation along a particular pure unit quaternion μ .

A pure unit quaternion μ is such that $\mu^2 = -1$

For instance $\bar{q}^i = a + bi - cj - dk$

For instance $q^{*i} = a - bi + cj + dk$

1.1.3 Complex subfields

Quaternions encompass complex numbers. Given any pure unit quaternion μ such that $\mu^2 = -1$ the set

$$\mathbb{C}_\mu = \{\alpha + \beta\mu \mid \alpha, \beta \in \mathbb{R}\} \quad (1.15)$$

is a *complex subfield* of \mathbb{H} isomorphic to \mathbb{C} . There exists an infinite number of such subfields since there is an infinite number of roots of -1 in the quaternion algebra.

As a result given a complex subfield \mathbb{C}_μ and a pure unit quaternion μ_\perp such that $\mathcal{S}(\mu\mu_\perp) = 0$, any quaternion can be decomposed into a pair of complex numbers. For instance, the following decompositions

$$q = q_1 + q_2\mathbf{j}, \quad q_1, q_2 \in \mathbb{C}_i \quad \text{or} \quad q = q'_1 + \mathbf{i}q'_2, \quad q'_1, q'_2 \in \mathbb{C}_j \quad (1.16)$$

will be used extensively in this manuscript.

This infinite number of roots of -1 contrasts with the usual complex algebra. In \mathbb{C} only $-\mathbf{i}$ and \mathbf{i} are roots of -1 , with \mathbf{i} the standard complex imaginary unit.

$\mathcal{S}(\mu_1\mu_2) = 0 \Leftrightarrow \mu_1$ is orthogonal to μ_2

1.1.4 Polar forms

Alike complex numbers, any quaternion $q \in \mathbb{H}$ can be written in polar form. Its standard polar form reads

$$q = |q|e^{\mu\theta} = |q|(\cos\theta + \mu\sin\theta) \quad (1.17)$$

where μ is a pure unit quaternion and $\theta \in [0, 2\pi)$. Unit quaternions, *i.e.* $q \in \mathbb{H}$ such that $|q| = 1$ correspond to quaternion exponentials $q = \exp(\mu\theta)$. For the particular case of pure unit quaternions one gets $\mu = \exp(\mu\pi/2)$, as with usual complex imaginary units.

Due to the multiplicity of roots of -1 in \mathbb{H} , polar forms involving specific axes can also be defined. The Euler polar form of q reads

$$q = |q|e^{i\theta}e^{-k\chi}e^{j\varphi} \quad (1.18)$$

where $\theta \in [-\pi/2, \pi/2)$, $\chi \in [-\pi/4, \pi/4]$ and $\varphi \in [-\pi, \pi)$. See Appendix 1.A for an efficient computation of this Euler polar form. The polar form (1.18) will later appear as a cornerstone of our framework as it provides a direct and simple way to identify meaningful physical parameters of bivariate signals.

This particular polar form was first introduced by Bülow and Sommer (2001) to analyze the local phase in images. It corresponds to a xzy -Euler angle parameterization of the unitary part of q – a common description of 3D rotations as three successive rotations around canonical axes (Altmann, 2005).

More precisely, the set of unit quaternions form the group $SU(2)$ which is a two-fold covering of the rotation group $SO(3)$ (Altmann, 2005).

For instance the involution

$$\bar{q}^i = a + bi - cj - dk$$

is the rotation of q by angle π around axis i .

Correspondence between right-sided and left-sided definitions of the QFT can be found in Ell, Le Bihan, and Sangwine (2014).

Although he uses a left-sided convention, his results are easily transposed to the right-sided definition.

1.1.5 Quaternions and 3D rotations

The ability to handle 3D rotations easily is one of the most famous features of quaternions. 3D rotations are encoded using unit quaternions. Let $q \in \mathbb{H}$ and v a unit quaternion, the rotation of q by v is given by

$$\mathcal{R}_v q = vq\bar{v}. \quad (1.19)$$

Since v is a unit quaternion it reads in exponential form $v = \exp(\boldsymbol{\mu}\beta/2)$ and the rotation $\mathcal{R}_v q$ reads

$$\mathcal{R}_v q = e^{\boldsymbol{\mu}\frac{\beta}{2}} q e^{-\boldsymbol{\mu}\frac{\beta}{2}} = \mathcal{S}(q) + e^{\boldsymbol{\mu}\frac{\beta}{2}} \mathcal{V}(q) e^{-\boldsymbol{\mu}\frac{\beta}{2}}. \quad (1.20)$$

The pure unit quaternion $\boldsymbol{\mu}$ is identified with a vector of \mathbb{R}^3 and denotes the *axis* of the rotation, and β gives its angle. Eq. (1.20) shows that the transform (1.19) only affects the vector part of q : it is indeed a 3D rotation. A special case of 3D rotations are involutions. Comparing (1.12) with (1.19) for $v = \boldsymbol{\mu}$, involutions correspond to rotations of angle π around axis $\boldsymbol{\mu}$. More on the connection between quaternions and rotations can be found in Altmann (2005).

1.2 QUATERNION FOURIER TRANSFORM

1.2.1 Definition, existence, inversion

The Quaternion Fourier Transform (QFT) of *axis* $\boldsymbol{\mu}$ of a signal $x : \mathbb{R} \rightarrow \mathbb{H}$ is defined by

$$X(\mathbf{v}) \triangleq \int_{-\infty}^{+\infty} x(t) e^{-\boldsymbol{\mu}2\pi\mathbf{v}t} dt \quad (1.21)$$

This definition matches closely the usual Fourier transform. However it differs in two fundamental aspects. First, the position of the Fourier atom $e^{-\boldsymbol{\mu}2\pi\mathbf{v}t}$ with respect to the quaternion-valued signal $x(t)$ is crucial due to the non-commutative nature of the product in \mathbb{H} . By convention and to agree with usual Fourier transform notation we choose to place this Fourier atom on the *right side* of the signal. Second, the *axis* $\boldsymbol{\mu}$ of the QFT is a free parameter. It is only restricted to be a pure unit quaternion, or stated differently, a quaternion imaginary unit $\boldsymbol{\mu}^2 = -1$. Details on the choice of this axis $\boldsymbol{\mu}$ to process bivariate signals are given in Section 1.3.

The QFT (1.21) was first studied by Jamison (1970) in his PhD dissertation

“Extension of some theorems of complex functional analysis to linear spaces over the quaternions and Cayley numbers.”

The existence and invertibility of the QFT for functions in $L^1(\mathbb{R}; \mathbb{H})$ and $L^2(\mathbb{R}; \mathbb{H})$ was proven by Jamison (1970). The inverse Quaternion Fourier transform reads

$$x(t) = \int_{-\infty}^{+\infty} X(\nu) e^{\mu 2\pi \nu t} d\nu \quad (1.22)$$

Jamison did not extend the QFT to generalized functions, *i.e.* distributions. It can however be worked out easily by transposing proofs from the usual FT to the case of the QFT, see for instance Appel and Kowalski (2007) or Simon (2015).

Existence and inversion properties of the quaternion Fourier transform (1.21) are essentially the same as the standard (complex) Fourier transform. Indeed a direct inspection of (1.21) shows that the restriction of the QFT to signals $x : \mathbb{R} \rightarrow \mathbb{C}_\mu$ is simply the usual complex Fourier transform. Let us decompose an arbitrary quaternion-valued signal $x(t)$ into a pair of \mathbb{C}_μ -valued signals $x_1(t)$ and $x_2(t)$ such that

$$x(t) = x_1(t) + \mu_\perp x_2(t), \quad (1.23)$$

where μ_\perp is a pure unit quaternion orthogonal to μ . By (left-)linearity of the QFT (1.21) one gets

$$X(\nu) = X_1(\nu) + \mu_\perp X_2(\nu) \quad (1.24)$$

where X_1 and X_2 are the standard \mathbb{C}_μ -valued FTs of x_1 and x_2 . In other terms, the QFT of x is obtained by combining two standard FTs according to (1.24). This ensures the valid manipulation of usual signals such as sine, Dirac delta functions, etc. in the context of the quaternion Fourier transform.

1.2.2 Properties of the Quaternion Fourier transform

We study the basic properties of the quaternion Fourier transform of arbitrary axis μ . Most QFT properties are similar to the usual FT. This is a comforting fact. Nonetheless special care to the ordering of terms is required due to noncommutativity of the quaternion product. Proofs corresponding to known results are omitted for brevity and can be found in Ell, Le Bihan, and Sangwine (2014). Results regarding convolution properties, Theorem 1.1 and Theorem 1.2 are new results published in Flamant, Le Bihan, and Chainais (2017e). Proofs can be found in Appendix 1.D.

Linearity The quaternion Fourier transform is left \mathbb{H} -linear, *i.e.*

$$\alpha x(t) + \beta y(t) \xleftrightarrow{\text{QFT}} \alpha X(\nu) + \beta Y(\nu) \quad (1.25)$$

for every $\alpha, \beta \in \mathbb{H}$. It is also right \mathbb{C}_μ -linear, *i.e.*

$$x(t)y + y(t)\delta \xleftrightarrow{\text{QFT}} X(\nu)y + Y(\nu)\delta \quad (1.26)$$

for every $\gamma, \delta \in \mathbb{C}_\mu$.

Shifts The quaternion Fourier transform pair corresponding to a shift in time by τ is

$$x(t - \tau) \xleftrightarrow{\text{QFT}} X(\nu) e^{-\mu 2\pi \nu \tau} \quad (1.27)$$

and to a shift in frequency by ν_0

$$x(t) e^{\mu 2\pi \nu_0 t} \xleftrightarrow{\text{QFT}} X(\nu - \nu_0). \quad (1.28)$$

The space $L^p(\mathbb{R}; \mathbb{H})$ denotes the set of quaternion-valued functions $x : \mathbb{R} \rightarrow \mathbb{H}$ with finite p -norm, *i.e.* such that

$$\|x\|_p = \left(\int_{-\infty}^{+\infty} |x(t)|^p dt \right)^{\frac{1}{p}} < \infty,$$

and where functions which agree almost everywhere are identified.

Importantly this second type of linearity depends on the choice of the axis μ in the exponential kernel of the QFT.

Scaling The quaternion Fourier transform pair corresponding to a scaling $\alpha \in \mathbb{R}^+$ is

$$x(t/\alpha) \stackrel{\text{QFT}}{\longleftrightarrow} |\alpha|X(\alpha v). \quad (1.29)$$

Time reversal The quaternion Fourier transform pair corresponding to time reversal is

$$x(-t) \stackrel{\text{QFT}}{\longleftrightarrow} X(-v). \quad (1.30)$$

Differentiation The quaternion Fourier transform pair corresponding to differentiation with respect to time is

$$\frac{d^n x(t)}{dt^n} \stackrel{\text{QFT}}{\longleftrightarrow} X(v)(\mu 2\pi v)^n \quad (1.31)$$

and to differentiation with respect to frequency

$$x(t)(-\mu 2\pi t)^n \stackrel{\text{QFT}}{\longleftrightarrow} \frac{d^n X(v)}{dv^n}. \quad (1.32)$$

Convolution Convolution is perhaps one of the most fundamental operation in signal processing. The convolution product in time between two quaternion-valued signals $x(t)$ and $y(t)$ is defined by

$$x * y(t) = \int_{-\infty}^{+\infty} x(u)y(t-u)du. \quad (1.33)$$

Considering quaternion-valued signals however implies some constraints on this standard operation. It is no longer commutative, *i.e.* $x * y \neq y * x$ in general. Moreover it is not possible to write the QFT of (1.33) as a mere product of respective QFTs without some assumptions on the nature of y .

Let $y : \mathbb{R} \rightarrow \mathbb{C}_\mu$, that is $y(t)$ and its QFT $Y(v)$ take their values into the same complex subfield of \mathbb{H} as the Fourier atom $e^{-\mu 2\pi vt}$. Then the quaternion Fourier transform pair corresponding to the convolution product in time is

$$\begin{cases} x : \mathbb{R} \rightarrow \mathbb{H} \\ y : \mathbb{R} \rightarrow \mathbb{C}_\mu \end{cases} \quad x * y(t) \stackrel{\text{QFT}}{\longleftrightarrow} X(v)Y(v). \quad (1.34)$$

Proof. See Appendix 1.D.1. \square

The same restriction holds for its dual property, the convolution product in frequency of two signals. The quaternion Fourier transform pair corresponding to the convolution product in frequency is

$$\begin{cases} x : \mathbb{R} \rightarrow \mathbb{H} \\ y : \mathbb{R} \rightarrow \mathbb{C}_\mu \end{cases} \quad x(t)y(t) \stackrel{\text{QFT}}{\longleftrightarrow} X * Y(v). \quad (1.35)$$

The condition $y : \mathbb{R} \rightarrow \mathbb{C}_\mu$ should not seem too restrictive. In fact Eqs. (1.34) – (1.35) encompass usual smoothing operations in the time or frequency domain. Filtering relations involving *geometric operations* can not be written simply in terms of convolutions. This will be discussed in Chapter 3.

Parseval-Plancherel identities The usual Fourier transform can be seen as a linear operator on the Hilbert space of complex-valued square integrable functions $L^2(\mathbb{R}; \mathbb{C})$. This perspective proves to be particularly fruitful in signal processing, leading to geometric and intuitive reasoning.

However the definition of Hilbert spaces involving non-commutative scalars such as quaternions requires special care (Jamison, 1970). Fortunately, it can be shown that $L^2(\mathbb{R}; \mathbb{H})$ is a *left* Hilbert space over \mathbb{H} ; see Appendix 1.B for details. The inner product between two signals $x, y \in L^2(\mathbb{R}; \mathbb{H})$ is

$$\langle x, y \rangle_{L^2} = \int_{-\infty}^{+\infty} x(t) \overline{y(t)} dt, \quad (1.36)$$

which induces the L^2 -norm

$$\|x\|_{L^2}^2 = \langle x, x \rangle_{L^2} = \int_{-\infty}^{+\infty} |x(t)|^2 dt. \quad (1.37)$$

The following theorem extends fundamental results concerning invariants of the quaternion Fourier transform. It also introduces a second invariant of geometric nature.

Theorem 1.1 (Parseval-Plancherel theorem for the QFT). *Let $x, y \in L^2(\mathbb{R}; \mathbb{H})$. Then the following holds*

$$\int_{-\infty}^{+\infty} x(t) \overline{y(t)} dt = \int_{-\infty}^{+\infty} X(v) \overline{Y(v)} dv \quad (1.38)$$

$$\int_{-\infty}^{+\infty} x(t) \boldsymbol{\mu} \overline{y(t)} dt = \int_{-\infty}^{+\infty} X(v) \boldsymbol{\mu} \overline{Y(v)} dv \quad (1.39)$$

In particular for $x = y$:

$$\int_{-\infty}^{+\infty} |x(t)|^2 dt = \int_{-\infty}^{+\infty} |X(v)|^2 dv \quad (1.40)$$

$$\int_{-\infty}^{+\infty} x(t) \boldsymbol{\mu} \overline{x(t)} dt = \int_{-\infty}^{+\infty} X(v) \boldsymbol{\mu} \overline{X(v)} dv \quad (1.41)$$

This theorem shows that the QFT defines an isometry of $L^2(\mathbb{R}; \mathbb{H})$. Indeed Eqs. (1.38) and (1.40) are extensions of usual Parseval and Plancherel formulas. This theorem also shows that another quantity, of geometrical nature, is preserved by the QFT. Let $f(\cdot) = x(t)$ or $X(v)$. Focusing on (1.41), the terms $f(\cdot) \boldsymbol{\mu} \overline{f(\cdot)}$ denote 3D rotations, up to a scaling factor. To see this, write f in quaternion polar form $f(\cdot) = |f(\cdot)| e^{\boldsymbol{\mu}_f(\cdot) \theta_f(\cdot)}$. Then

$$f(\cdot) \boldsymbol{\mu} \overline{f(\cdot)} = |f(\cdot)|^2 e^{\boldsymbol{\mu}_f(\cdot) \theta_f(\cdot)} \boldsymbol{\mu} e^{-\boldsymbol{\mu}_f(\cdot) \theta_f(\cdot)} \quad (1.42)$$

corresponds to the combination of a scaling by $|f(\cdot)|^2$ and a 3D rotation of axis $\boldsymbol{\mu}_f(\cdot)$ and angle $2\theta_f(\cdot)$ of the QFT axis $\boldsymbol{\mu}$.

The preservation of geometric quantities of the form (1.42) by the QFT is a new result which is central in the proposed framework for bivariate signals. Theorem 1.1 is essential to build meaningful spectral densities (Chapter 2) or time-frequency densities (Chapter 4).

Uncertainty principle Also known as the Gabor-Heisenberg uncertainty principle, this fundamental property extends to the quaternion Fourier transform setting. Consider a finite energy signal $x \in L^2(\mathbb{R}; \mathbb{H})$. Its temporal mean $\langle t \rangle$ is defined by

$$\langle t \rangle = \frac{1}{\|x\|^2} \int_{-\infty}^{+\infty} t |x(t)|^2 dt, \quad (1.43)$$

and the mean frequency $\langle v \rangle$ as

$$\langle v \rangle = \frac{1}{\|x\|^2} \int_{-\infty}^{+\infty} v |X(v)|^2 dv. \quad (1.44)$$

Proof. See Appendix 1.D.2. \square

Similarly, it can be shown that (1.39) corresponds to a 4D rotation up to a scaling factor. See Conway and Smith (2003) for more on 4D rotations.

Spreads around these mean values are defined like

$$\sigma_t^2 = \frac{1}{\|x\|^2} \int_{-\infty}^{+\infty} (t - \langle t \rangle)^2 |x(t)|^2 dt, \quad (1.45)$$

$$\sigma_v^2 = \frac{1}{\|x\|^2} \int_{-\infty}^{+\infty} (v - \langle v \rangle)^2 |X(v)|^2 dv. \quad (1.46)$$

Theorem 1.2 (Gabor-Heisenberg uncertainty principle). *Given a signal $x \in L^2(\mathbb{R}; \mathbb{H})$ with QFT X and time (resp. frequency) spread σ_t^2 (resp. σ_v^2). The following holds:*

$$\sigma_t \sigma_v \geq \frac{1}{4\pi}. \quad (1.47)$$

Functions that exhibit minimal uncertainty $\sigma_t \sigma_v = 1/(4\pi)$ are of the form

$$x(t) = \alpha e^{-k(t-t_0)^2} e^{\mu 2\pi v_0 t}, \quad k > 0, \quad t_0, v_0 \in \mathbb{R}, \quad \alpha \in \mathbb{H}, \quad (1.48)$$

where $t_0 = \langle t \rangle$ and $v_0 = \langle v \rangle$.

Proof. See Appendix 1.D.3. □

We proved this theorem in Flamant, Le Bihan, and Chainais (2017e). It shows that the QFT behaves exactly as the usual Fourier transform regarding the tradeoff between time and frequency localizations.

Discretization The aforementioned properties demonstrate that the quaternion Fourier transform provides a valid and rigorous mathematical operator for continuous-time quaternion-valued signals. Similarly, a discrete-time quaternion Fourier transform (Q-DTFT) can be defined to account for discrete-time quaternion-valued signals. Moreover, the quaternion Fourier transform would be rather unattractive if it did not admit an efficient numerical implementation. It turns out that the discrete quaternion Fourier transform (Q-DFT) can be effectively computed based on the sole use of fast Fourier transforms (FFT). The derivation of the Q-DTFT and Q-DFT follow closely the usual derivation of the DTFT and DFT from the standard FT. See Appendix 1.C for details.

1.3 PROCESSING BIVARIATE SIGNALS WITH THE QUATERNION FOURIER TRANSFORM

A systematic study of the fundamental properties of the quaternion Fourier transform (1.21) was conducted in the last section. These properties are very similar to the usual complex Fourier transform. The main difference lies in handling non-commutativity properly. Building upon these convenient mathematical properties, the purpose of this section is now to demonstrate that the QFT provides an efficient framework for bivariate signals.

The key ideas are: (i) to consider bivariate signals as complex-valued signals and (ii) to use a dedicated QFT to process bivariate signals, ensuring a meaningful embedding of these signals into \mathbb{H} . These ideas were first proposed by Le Bihan, Sangwine, and Ell (2014). We further explored this proposition in Flamant, Le Bihan, and Chainais (2017e) to build a meaningful and efficient representation of bivariate signals.

1.3.1 Bivariate signals

A bivariate signal $x(t)$ is described by two real-valued orthogonal components denoted by $u(t)$ and $v(t)$. Thus a bivariate signal can be either represented by a 2-dimensional vector-valued signal $[u(t), v(t)]^T$, or by the complex-valued signal

$$x(t) = u(t) + \mathbf{i}v(t). \quad (1.49)$$

The choice of the complex-valued representation over the vector-valued representation is often advocated for in signal processing (Schreier and Scharf, 2010). This is mainly due to the ability of the complex representation to manipulate amplitude and phase easily with polar forms.

The bivariate signal $x(t)$ in its complex representation (1.49) can be viewed as a special type of quaternion-valued signal¹. This signal takes its values in $\text{span}\{1, \mathbf{i}\} \triangleq \mathbb{C}_{\mathbf{i}} \subset \mathbb{H}$. Considering bivariate signals as complex-valued signals embedded in quaternions is a cornerstone of our analysis since it allows to process bivariate signals using the QFT studied in Section 1.2.

1. That said, we see that the choice of \mathbf{i} as the imaginary unit in (1.49) is only a matter of convention. Any pure unit quaternion μ could have been chosen, leading to a \mathbb{C}_{μ} complex-valued representation of the bivariate signal $x(t)$.

1.3.2 Choice of the axis of the QFT

The definition of the quaternion Fourier transform (1.21) introduces a free parameter, the axis μ of the transform. By choosing $\mu = \mathbf{i}$ one recovers the usual complex Fourier transform. This shows that the QFT definition (1.21) encompasses the usual complex case, but that it offers other choices as well. Thus the pure unit quaternion μ has to be chosen wisely so that the QFT yields interesting additional properties for bivariate signals of the form (1.49).

Starting with arbitrary μ , the QFT of $x(t)$ reads

$$X(\mathbf{v}) = U(\mathbf{v}) + \mathbf{i}V(\mathbf{v}) \quad (1.50)$$

where U and V are \mathbb{C}_{μ} -valued and correspond to the usual Fourier transforms of u and v . One natural requirement is that $U(\mathbf{v})$ and $\mathbf{i}V(\mathbf{v})$ should live in non-intersecting subspaces of \mathbb{H} . Then the QFT (1.50) simply becomes isomorphic to the usual FT of the 2-dimensional vectors $[u(t), v(t)]^T$. This requirement is easily fulfilled provided that μ is orthogonal to \mathbf{i} , i.e. $\mathcal{S}(\mu\mathbf{i}) = 0$. This means that any axis of the form $\mu = a\mathbf{j} + b\mathbf{k}$ with $a, b \in \mathbb{R}$ such that $a^2 + b^2 = 1$ is a valid choice. For the sake of simplicity we choose $\mu = \mathbf{j}$.

The definition of the quaternion Fourier transform we will use in this work is then

$$X(\mathbf{v}) \triangleq \int_{-\infty}^{+\infty} x(t)e^{-j2\pi\mathbf{v}t} dt. \quad (1.51)$$

With this choice, the QFT exhibits a Hermitian-like symmetry for bivariate signals:

$$x : \mathbb{R} \rightarrow \mathbb{C}_{\mathbf{i}} \xrightarrow{\text{QFT}} X(-\mathbf{v}) = -\mathbf{i}X(\mathbf{v})\mathbf{i} = \overline{X(\mathbf{v})}^{\mathbf{i}}. \quad (1.52)$$

This is the \mathbf{i} -Hermitian symmetry property of the QFT of bivariate signals. It can be seen as the generalization of the well-known fact that the Fourier transform of a real-valued signal obeys Hermitian symmetry. This is a very desirable property, as it allows to attach a physical meaning to positive frequencies only. The quaternion-valued spectrum $X(\mathbf{v})$ restricted to positive frequencies only contains the complete information about the bivariate signal $x(t)$.

Proof. Property (1.52) arises from the separation of U and V components in (1.50). Let $x(t) = u(t) + \mathbf{i}v(t)$ a bivariate signal. Then its QFT of axis \mathbf{j} is $X(\mathbf{v}) = U(\mathbf{v}) + \mathbf{i}V(\mathbf{v})$. Since u and v are real-valued functions and that U and V are their usual $\mathbb{C}_{\mathbf{j}}$ -valued FT,

$$U(-\mathbf{v}) = \overline{U(\mathbf{v})} \text{ and } V(-\mathbf{v}) = \overline{V(\mathbf{v})}$$

so that $X(-\mathbf{v}) = \overline{U(\mathbf{v})} + \mathbf{i}\overline{V(\mathbf{v})}$. Then using that for all $z \in \mathbb{C}_{\mathbf{j}}$, $\mathbf{i}z = \overline{z}\mathbf{i}$ one gets (1.52). \square

As a result any bivariate signal $x(t)$ can be reconstructed from the restriction of its QFT to positive frequencies:

$$x(t) = \text{Proj}_{\mathbb{C}_i} \left\{ 2 \int_0^{+\infty} X(\nu) e^{j2\pi\nu t} d\nu \right\}, \quad (1.53)$$

where the factor 2 arises from the i -Hermitian symmetry (1.52). In fact, the quantity appearing in the right-hand side of (1.53) is called the *quaternion embedding* $x_+(t)$ of the bivariate or complex signal $x(t)$ such that

$$x_+(t) = 2 \int_0^{+\infty} X(\nu) e^{j2\pi\nu t} d\nu. \quad (1.54)$$

It can be viewed as a bivariate counterpart of the usual analytic signal of a real signal. Chapter 4 will provide a thorough study of this first building block for the time-frequency analysis of bivariate signals.

The \mathbb{C}_i -part of a quaternion q is computed using

$$\text{Proj}_{\mathbb{C}_i} \{q\} = (q + \bar{q}^i)/2$$

1.3.3 Monochromatic bivariate signals

The quaternion Fourier transform of axis j (1.51) enjoys numerous desirable mathematical properties making it a well-behaved tool for the analysis of bivariate signals. Using quaternion algebra, we show that the connection with the physics and the geometry of bivariate signals is straightforward.

Consider a monochromatic bivariate signal $x(t)$ of frequency $\nu_0 > 0$. Then its QFT is necessarily of the form

$$X(\nu) = \lambda \delta(\nu - \nu_0) + \bar{\lambda}^i \delta(\nu + \nu_0) \quad (1.55)$$

where $\lambda \in \mathbb{H}$ and where the negative frequency term is such that (1.52) holds. Then taking the inverse QFT of (1.55) and writing λ in Euler polar form (1.18) one gets

$$x(t) = \text{Proj}_{\mathbb{C}_i} \left\{ a e^{i\theta} e^{-k\chi} e^{j(2\pi\nu_0 t + \varphi)} \right\}, \quad (1.56)$$

which explicitly reads

$$x(t) = a e^{i\theta} [\cos(\chi) \cos(2\pi\nu_0 t + \varphi) + i \sin(\chi) \sin(2\pi\nu_0 t + \varphi)] \quad (1.57)$$

Figure 1.1 depicts the trajectory drawn in the u - v plane by the signal $x(t)$ defined by (1.57). In fact, Eq. (1.57) corresponds to the parametric equation of an ellipse. The ellipse is parameterized by its *orientation* $\theta \in [0, \pi)$ and its *ellipticity angle* $\chi \in [-\pi/4, \pi/4]$. When $\chi = \pm\pi/4$ the ellipse becomes a circle and for $\chi = 0$ the ellipse reduces to a line segment. The sign of χ gives the direction of travel within the ellipse, *i.e.* clockwise for $\chi < 0$ and counter-clockwise for $\chi > 0$. The remaining parameters are classical: the amplitude a controls the size of the ellipse, while φ gives the phase delay corresponding to frequency ν_0 .

In physics, the monochromatic signal $x(t)$ depicted in Fig. 1.1 would be called a *monochromatic polarized signal*. This stems from the interpretation of $x(t)$ as a descriptor of the two components of the field of a transverse elastic or optical plane wave. This link with polarization is explored further in Chapter 2 and subsequent chapters.

Let us consider an arbitrary bivariate signal $x(t)$. Writing its QFT $X(\nu)$ in Euler polar form the inverse QFT reads

$$x(t) = \int_{-\infty}^{+\infty} a(\nu) e^{i\theta(\nu)} e^{-k\chi(\nu)} e^{j\varphi(\nu)} e^{j2\pi\nu t} d\nu. \quad (1.58)$$

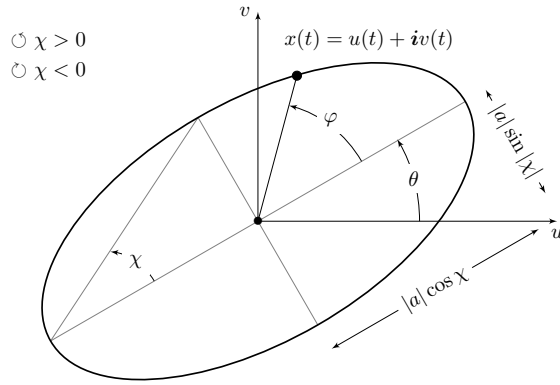


Figure 1.1: A monochromatic bivariate signal $x(t)$ draws an ellipse in the u - v plane. The ellipse is parameterized by its size a , its orientation θ and its shape given by the ellipticity angle χ . The angle φ gives the phase delay associated to the corresponding frequency.

Eq. (1.58) highlights the fact that the QFT performs a decomposition of any bivariate signal into a sum of monochromatic polarized components. As the usual Fourier transform decomposes univariate signals into a sum of (scalar) plane waves, the QFT decomposes bivariate signals into a sum of polarized plane waves. The identification of ellipse or polarization parameters for each wave is straightforward thanks to the Euler polar form (1.18).

For reference, Table 1.1 collects the properties of the QFT of axis j for generic quaternion-valued signals and for bivariate signals.

1.4 CONCLUSION

This chapter has presented the two key ingredients of the proposed framework for the analysis and filtering of bivariate signals: *quaternions* and the *quaternion Fourier transform*. The generic properties of the QFT have been studied. The QFT exhibits usual Fourier transform properties (linearity, shifts, differentiation, etc.) which sometimes require special care due to noncommutativity. We have shown that the QFT features generalized Parseval-Plancherel identities (Theorem 1.1), which state that *energy* but also an additional *geometric* quantities are preserved. We showed that the QFT obeys the usual time-frequency tradeoff of Gabor-Heisenberg inequality (Theorem 1.2). Section 1.3 has demonstrated the relevance of the QFT for the study of bivariate signals. The quaternion-valued spectrum of bivariate signals exhibits Hermitian-like symmetry, a very desirable property that allows to attach physical interpretation to positive frequencies only. As shown on the simple example of the monochromatic bivariate signal, the quaternion Euler polar form provides a straightforward *natural ellipse* parameterization. The construction of this framework has been published as part of an international journal paper (Flamant, Le Bihan, and Chainais, 2017e).

Next chapters will demonstrate the full generality of the proposed approach for the handling of bivariate signals. The subsequent Chapter 2 provides an answer to the next natural question: *How to define the notion of spectral density in this framework?*

Property	Time-domain	Frequency domain	Comments
Left linearity	$\alpha x(t) + \beta y(t)$	$\alpha X(\nu) + \beta Y(\nu)$	$\alpha, \beta \in \mathbb{H}$
Right linearity	$x(t)\gamma + y(t)\delta$	$X(\nu)\gamma + Y(\nu)\delta$	$\gamma, \delta \in \mathbb{C}_j$
Shift in time	$x(t - \tau)$	$X(\nu)e^{-\mu 2\pi\nu\tau}$	
Shift in frequency	$x(t)e^{\mu 2\pi\nu_0 t}$	$X(\nu - \nu_0)$	
Scaling	$x(t/\alpha)$	$ \alpha X(\alpha\nu)$	$\alpha \in \mathbb{R}^*$
Time reversal	$x(-t)$	$\overline{X(\nu)}$	
Differentiation in time	$\frac{d^n x(t)}{dt^n}$	$X(\nu)(\mu 2\pi\nu)^n$	
Differentiation in frequency	$x(t)(-\mu 2\pi t)^n$	$\frac{d^n X(\nu)}{d\nu^n}$	
Convolution in time	$x * y(t)$	$X(\nu)Y(\nu)$	$y: \mathbb{R} \rightarrow \mathbb{C}_j$
Convolution in frequency	$x(t)y(t)$	$X * Y(\nu)$	$y: \mathbb{R} \rightarrow \mathbb{C}_j$
Standard Plancherel equality	$\int_{-\infty}^{+\infty} x(t) ^2 dt = \int_{-\infty}^{+\infty} X(\nu) ^2 d\nu$		
Geometric Plancherel equality	$\int_{-\infty}^{+\infty} x(t)\mu\overline{x(t)}dt = \int_{-\infty}^{+\infty} X(\nu)\mu\overline{X(\nu)}d\nu$		
Gabor-Heisenberg uncertainty	$\sigma_t \sigma_\nu \geq \frac{1}{4\pi}$		
<i>i</i> -Hermitian symmetry	$x: \mathbb{R} \rightarrow \mathbb{C}_i$	$X(-\nu) = -iX(\nu)i$	

 Table 1.1: Properties of the quaternion Fourier transform of axis *j*.

APPENDICES

1.A EULER POLAR FORM COMPUTATION

We describe a numerically stable and efficient method for the computation of the Euler polar form (1.18) of any quaternion $q \in \mathbb{H}$. This method relies on the use of quaternion quadratic forms.

Let $q \in \mathbb{H}$. Recall its Euler polar form:

$$q = ae^{i\theta} e^{-k\chi} e^{j\varphi}. \quad (1.59)$$

The amplitude a is easily obtained

$$a = \sqrt{q\bar{q}} = |q|. \quad (1.60)$$

If $a = 0$ then by convention $\theta = \chi = \varphi = 0$. Assume $a \neq 0$. Angles θ and χ are obtained by computing $q\bar{j}\bar{q}$:

$$q\bar{j}\bar{q} = a^2 e^{i\theta} e^{-k\chi} e^{j\varphi} \bar{j} e^{i\theta} e^{-k\chi} e^{j\varphi} \quad (1.61)$$

$$\stackrel{(a)}{=} a^2 e^{i\theta} e^{-k\chi} e^{j\varphi} \bar{j} e^{-j\varphi} e^{k\chi} e^{-i\theta} \quad (1.62)$$

$$\stackrel{(b)}{=} a^2 e^{i\theta} e^{-2k\chi} e^{i\theta} \bar{j} \quad (1.63)$$

$$\stackrel{(b)}{=} a^2 (e^{i2\theta} \cos 2\chi - \mathbf{k} \sin 2\chi) \bar{j} \quad (1.64)$$

$$= a^2 (i \sin 2\chi + \mathbf{j} \cos 2\theta \cos 2\chi + \mathbf{k} \sin 2\theta \cos 2\chi) \quad (1.65)$$

Denoting by $\text{Im}_i, \text{Im}_j, \text{Im}_k$ the three canonical imaginary parts of a quaternion, one gets the following expressions for θ and χ :

$$\theta = \frac{1}{2} \arctan \frac{\text{Im}_k(q\bar{j}\bar{q})}{\text{Im}_j(q\bar{j}\bar{q})}, \quad (1.66)$$

$$\chi = \frac{1}{2} \arcsin \frac{\text{Im}_i(q\bar{j}\bar{q})}{a^2}. \quad (1.67)$$

The last angle φ is obtained by taking the usual complex argument of q' such that

$$\varphi = \arg q' \text{ where } q' = e^{i\theta} e^{-k\chi} q = a^2 e^{j\varphi}. \quad (1.68)$$

Using expressions (5) – (7) of Stokes parameters S_1, S_2 and S_3 given in Chapter 0, we see that (1.65) is simply the combination of these three Stokes parameters. Thus the computation of angles θ and χ directly involves Stokes parameters. This link between quaternion quadratic forms ($|q|^2$ and $q\bar{j}\bar{q}$) and Stokes parameters is discussed in detail in the next Chapter 2.

1.B HILBERT SPACES OVER QUATERNIONS

Hilbert spaces over quaternions were first studied by Teichmüller (1936) in his PhD dissertation. They were later studied by Finkelstein et al. (1962) in the development of quaternion quantum mechanics. The material presented in this section can be found in the PhD dissertation of Jamison (1970), in which a thorough treatment of Hilbert spaces over quaternions is presented.

Let us start by the definition of a vector space over quaternions. Such spaces are said either *left* or *right* vector spaces, depending from which side quaternion scalar multiplication is considered. We focus on left vector spaces, but definitions for right vector spaces can be deduced directly.

$$(a) \quad \forall x, y \in \mathbb{H}, \overline{(xy)} = \bar{y}\bar{x}$$

$$(b) \quad \forall x \in \mathbb{C}_i, xj = j\bar{x} \text{ and } \forall y \in \mathbb{C}_k, yj = j\bar{y}$$

Oswald Teichmüller called Hilbert spaces over quaternions “*Wachsschen Raum*” after their construction was suggested by Hermann Wachs, one of his fellow students. Besides being a mathematician Teichmüller was also a committed nazi (Segal, 2014, pp. 442–450). He joined the NSDAP in 1931, and he reportedly lead in 1933 the boycott of Edmund Landau’s classes in Göttingen. He died on the eastern front in 1943.

Definition 1.1 (Left vector space over \mathbb{H}). A (left) vector space \mathfrak{S} over \mathbb{H} is an additive abelian group in which the operation of scalar multiplication by elements of \mathbb{H} is defined. Scalar multiplication is assumed to obey the following laws for all $x, y \in \mathfrak{S}$ and $a, b \in \mathbb{H}$

1. $a(x + y) = ax + ay$
2. $(a + b)x = ax + bx$
3. $(ab)x = a(bx)$
4. $1 \cdot x = x$ (1 is the unit scalar quaternion)

Linear functionals over a left vector space are defined accordingly

Definition 1.2 (Linear functionals). Let \mathfrak{S} be a left vector space over \mathbb{H} . A mapping $f : \mathfrak{S} \rightarrow \mathbb{H}$ is called a linear functional if

1. $f(x + y) = f(x) + f(y), \forall x, y \in \mathfrak{S}$
2. $f(\alpha x) = \alpha f(x), \forall x \in \mathfrak{S}$ and $\forall \alpha \in \mathbb{H}$

Definition 1.3 (Inner product space). Let \mathfrak{S} be a left vector space over \mathbb{H} . \mathfrak{S} will be called an inner product space if there exists a function $\langle \cdot, \cdot \rangle : \mathfrak{S} \times \mathfrak{S} \rightarrow \mathbb{H}$ with the properties

1. $\langle x, y + z \rangle = \langle x, y \rangle + \langle x, z \rangle$
2. $\langle \alpha x, y \rangle = \alpha \langle x, y \rangle$
3. $\langle x, y \rangle = \overline{\langle y, x \rangle}$
4. $\langle x, x \rangle > 0, x \neq 0$

where this has to be true $\forall x, y, z \in \mathfrak{S}$ and $\forall \alpha \in \mathbb{H}$.

Left inner product spaces feature the usual Cauchy-Schwartz inequality.

Lemma 1.1 (Cauchy-Schwartz inequality). If x, y are two elements of \mathfrak{S} then

$$|\langle x, y \rangle| \leq \langle x, x \rangle^{1/2} \langle y, y \rangle^{1/2}$$

Proof. See Jamison (1970, p. 69)

□

Importantly, any left inner product space over \mathbb{H} is a left normed space. It suffices to define

$$\|x\| = \langle x, x \rangle^{1/2} \quad \forall x \in \mathfrak{S} \quad (1.69)$$

A left inner product space \mathfrak{S} equipped with the metric $d(x, y) = \langle x - y, x - y \rangle^{1/2}$ that is complete is a *left Hilbert space*.

The Hilbert space $L^2(\mathbb{R}; \mathbb{H})$ The set of square integrable quaternion-valued functions $x : \mathbb{R} \rightarrow \mathbb{H}$, denoted $L^2(\mathbb{R}; \mathbb{H})$, and equipped with the inner product

$$\forall x, y \in L^2(\mathbb{R}; \mathbb{H}), \quad \langle x, y \rangle_{L^2} \triangleq \int x(t) \overline{y(t)} dt \quad (1.70)$$

is a left Hilbert space. The proof is analogous to the classical case and can be found in Jamison (1970). Note that the inner product $\langle \cdot, \cdot \rangle_{L^2}$ satisfies the requirements of Definition 1.3, and is in particular left-quaternion linear.

1.C DISCRETIZATION OF THE QUATERNION FOURIER TRANSFORM

For simplicity, we only consider the quaternion Fourier transform of axis j defined by

$$X(v) = \int_{-\infty}^{+\infty} x(t) e^{-j2\pi vt} dt \quad (1.71)$$

The inverse transform is defined according to (1.22). Write the signal $x(t)$ as a pair of 2 \mathbb{C}_j -valued components $u(t)$ and $v(t)$ such that $x(t) = u(t) + \mathbf{i}v(t)$. Then the QFT of $x(t)$ reads

$$X(\mathbf{v}) = U(\mathbf{v}) + \mathbf{i}V(\mathbf{v}) \quad (1.72)$$

where $U(\mathbf{v})$ and $V(\mathbf{v})$ are standard complex \mathbb{C}_j -valued Fourier transforms of $u(t)$ and $v(t)$. It shows that the QFT is simply obtained by performing two standard Fourier transforms. Thus extending the continuous-time QFT definition to discrete-time and discrete finite sequences is straightforward. Definitions follow directly from usual Fourier transform results, see *e.g.* Percival and Walden (1993) or Vetterli, Kovačević, and Goyal (2014).

1.C.1 Discrete-time quaternion Fourier transform

Let $\{x[n]\}_{n \in \mathbb{Z}}$ be a discrete-time signal, sampled at intervals Δ_t such that sampled instants are $t_n = n\Delta_t$. Let $\nu_{\mathcal{N}} = 1/(2\Delta_t)$ denotes the Nyquist critical frequency. Then, the discrete-time quaternion Fourier transform (Q-DTFT) of x reads

$$X(\mathbf{v}) \triangleq \Delta_t \sum_{n=-\infty}^{+\infty} x[n] e^{-j2\pi \mathbf{v} n \Delta_t}. \quad (1.73)$$

The Q-DTFT is periodic with period $2\nu_{\mathcal{N}}$. Therefore the inverse Q-DTFT is

$$x[n] = \int_{-\nu_{\mathcal{N}}}^{\nu_{\mathcal{N}}} X(\mathbf{v}) e^{j2\pi \mathbf{v} n \Delta_t} d\mathbf{v} \quad (1.74)$$

Properties of the Q-DTFT follow from direct adaptation of the properties of the continuous-time QFT.

1.C.2 Discrete quaternion Fourier transform

Consider a sequence $\{x[n]\}_{n=0,1,\dots,N-1}$ of length N sampled at intervals of Δ_t . The discrete quaternion Fourier transform (Q-DFT) of x is

$$X[m] = \sum_{n=0}^{N-1} x[n] e^{-j2\pi \frac{nm}{N}}, \quad m = 0, 1, \dots, N-1 \quad (1.75)$$

where $X[m]$ is associated to the frequency $f_m = m/(N\Delta_t)$. The inverse Q-DFT is

$$x[n] = \frac{1}{N} \sum_{m=0}^{N-1} X[m] e^{j2\pi \frac{nm}{N}} \quad (1.76)$$

Again, properties of the Q-DFT follow directly from the properties of the continuous-time QFT. Importantly, remark that thanks to (1.72) the Q-DFT can be efficiently computed using two standard FFTs.

1.D PROOFS OF QUATERNION FOURIER TRANSFORM PROPERTIES

We gather in this section several proofs regarding the properties of the quaternion Fourier transform of arbitrary axis $\boldsymbol{\mu}$ introduced in Section 1.2.

1.D.1 Convolution properties (1.34) and (1.35)

Let us prove (1.34). The dual property (1.35) is proven analogously. Let $x : \mathbb{R} \rightarrow \mathbb{H}$ and $y : \mathbb{R} \rightarrow \mathbb{C}_\mu$ two signals. We suppose that they satisfy sufficient conditions so that their QFT is well-defined. By direct calculation, one gets

$$\int (x * y)(t) e^{-\mu 2\pi vt} dt = \int \left(\int x(u) y(t-u) du \right) e^{-\mu 2\pi vt} dt \quad (1.77)$$

$$= \int x(u) Y(v) e^{-\mu 2\pi vu} du \quad (1.78)$$

$$= X(v) Y(v). \quad (1.79)$$

The last expression is obtained using the fact that $Y(v)$ and $e^{-\mu 2\pi vu}$ commute since $y(t)$ and $Y(v)$ are \mathbb{C}_μ -complex valued.

In the next sections, we use the notation \int instead of $\int_{-\infty}^{+\infty}$ to ease expressions.

1.D.2 Theorem 1.1 (Parseval-Plancherel)

First, remark that Plancherel formulas (1.40) and (1.41) can be obtained directly with $x = y$ in Parseval formulas (1.38) and (1.39). Thus we only give a proof for Parseval's formula, and particularly we focus on the proof of (1.39) as it is peculiar to the QFT. The classical Parseval formula (1.38) is proven along the same lines.

Let $x, y \in L^2(\mathbb{R}; \mathbb{H})$. One has

$$\int_{-\infty}^{+\infty} x(t) \mu \overline{y(t)} dt = \int \left(\int X(v) e^{\mu 2\pi vt} dv \right) \mu \overline{y(t)} dt \quad (1.80)$$

$$\stackrel{(a)}{=} \iint X(v) \mu \overline{(y(t) e^{-\mu 2\pi vt})} dt dv \quad (1.81)$$

$$= \int X(v) \mu \overline{\left(\int y(t) e^{-\mu 2\pi vt} dt \right)} dv \quad (1.82)$$

$$= \int X(v) \mu \overline{Y(v)} dv. \quad (1.83)$$

$$(a) \quad \forall x, y \in \mathbb{H}, \overline{(xy)} = \bar{y} \bar{x}$$

1.D.3 Theorem 1.2 (Gabor-Heisenberg uncertainty principle)

We use the same notations as in Theorem 1.2. Let $x \in L^2(\mathbb{R}; \mathbb{H})$. We also suppose that its derivative $x'(t)$ is in $L^2(\mathbb{R}; \mathbb{H})$ and that $tx(t)$ is also in $L^2(\mathbb{R}; \mathbb{H})$. It is sufficient to give a proof for the case $\langle t \rangle = \langle v \rangle = 0$ since any other case can be retrieved by a change of variables. The proof is very similar to the proof of the uncertainty principle for the standard Fourier transform (Mallat, 2008). First let us note that

$$\sigma_t^2 \sigma_v^2 = \frac{1}{\|x\|^4} \int |tx(t)|^2 dt \int |vX(v)|^2 dv \quad (1.84)$$

Since $X(v) \mu 2\pi v$ is the quaternion Fourier transform of $x'(t)$, using the Plancherel identity applied to $X(v) \mu 2\pi v$ yields

$$\sigma_t^2 \sigma_v^2 = \frac{1}{4\pi^2 \|x\|^4} \int |tx(t)|^2 dt \int |x'(t)|^2 dt \quad (1.85)$$

Then using Cauchy-Schwartz inequality one gets

$$\sigma_t^2 \sigma_v^2 \geq \frac{1}{4\pi^2 \|x\|^4} \left| \int x'(t) \overline{tx(t)} dt \right|^2 \quad (1.86)$$

$$\geq \frac{1}{4\pi^2 \|x\|^4} \left[\int \mathcal{S} \left(x'(t) \overline{tx(t)} \right) dt \right]^2 \quad (1.87)$$

$$\geq \frac{1}{4\pi^2 \|x\|^4} \left[\int \frac{t}{2} \left(x'(t) \overline{x(t)} + x(t) \overline{x'(t)} \right) dt \right]^2 \quad (1.88)$$

$$\geq \frac{1}{16\pi^2 \|x\|^4} \left[\int t (|x(t)|^2)' dt \right]^2 \quad (1.89)$$

Now, using integration by parts we obtain

$$\sigma_t^2 \sigma_v^2 \geq \frac{1}{16\pi^2 \|x\|^4} \left[\int |x(t)|^2 dt \right]^2 = \frac{1}{16\pi^2}. \quad (1.90)$$

The lower bound of the inequality is attained in the equality case of the Cauchy-Schwarz inequality (1.86), that is for $x'(t) = \lambda tx(t)$, where $\lambda \in \mathbb{H}$. However, the minimal uncertainty $\sigma_t \sigma_v = 1/(4\pi)$ is only obtained for $\lambda \in \mathbb{R}$. To see this, remark that (1.86) and (1.87) are in fact equalities if and only if

$$\left[\int |x(t)|^2 |\lambda| dt \right]^2 = \left[\int \mathcal{S}(|x(t)|^2 \bar{\lambda}) dt \right]^2 \iff |\lambda|^2 = \mathcal{S}(\lambda)^2 \iff \lambda \in \mathbb{R} \quad (1.91)$$

Solving now the differential equation $x'(t) = -ktx(t)$ and restricting to $k > 0$ so that $x \in L^2(\mathbb{R}; \mathbb{H})$ one gets the usual Gaussian functions

$$x(t) = \alpha e^{-kt^2}, \quad k > 0, \alpha \in \mathbb{H}. \quad (1.92)$$

The general form of these functions including arbitrary time and frequency shifts reads

$$x(t) = \alpha e^{-k(t-t_0)^2} e^{i2\pi\nu_0 t}, \quad t_0, \nu_0 \in \mathbb{R}. \quad (1.93)$$

The fact that the lower bound $1/(4\pi)$ can only be obtained for $\lambda \in \mathbb{R}$ is similar to the usual Fourier transform. See Flandrin (1998, p. 15) for instance. Taking $\lambda \in \mathbb{H}$ yields signals with Gaussian amplitude but also with quadratic phase. Intuitively, this increases the frequency spread σ_v and thus $\sigma_t \sigma_v$ exceeds $1/(4\pi)$.

Spectral analysis of bivariate signals

2

This chapter introduces the notion of spectral density for deterministic and random bivariate signals in the quaternion Fourier transform framework. The *quaternion spectral density* of a bivariate signal is defined in terms of the two Parseval invariants of the quaternion Fourier transform. This ensures its interpretation as a density as well as a natural separation between the energetic and geometric contents. Remarkably, we show that the quaternion spectral density is directly related to meaningful parameters describing polarization known as Stokes parameters in physics. It also provides further geometric interpretations thanks to the associated Poincaré sphere representation and an explicit decomposition of the spectral density into polarized and unpolarized parts. The proposed approach offers an original and powerful characterization of the energetic or second-order properties of bivariate signals.

Section 2.1 first tackles the simpler case of deterministic signals. It introduces the notion of quaternion spectral density for finite energy and finite power signals.

Section 2.2 deals with stationary random bivariate signals and addresses the second-order characterization of their statistical properties. A fundamental spectral representation theorem for the quaternion Fourier transform is proven. It permits a rigorous definition of the quaternion power spectral density (PSD) of a stationary random bivariate signal, as well as the related notions of quaternion (cross-)covariance and quaternion cross-spectral properties.

Section 2.3 illustrates the usefulness of the formalism by providing clear, elegant and natural interpretations of the quaternion PSD in terms of frequency-dependent polarization parameters. Several examples with detailed computations demonstrate the practical use of this original framework.

Section 2.4 introduces nonparametric spectral estimates of the quaternion power spectral density. These are obtained by leveraging usual univariate periodogram or multitaper estimates. The estimation of polarization parameters requires special care and is discussed in detail. Examples and numerical illustrations support the presentation.

Section 2.5 gathers concluding remarks. Appendices provide complementary results and proofs.

The major part of the material of this chapter has been published in an international journal and presented at a national conference:

 J. Flamant, N. Le Bihan, and P. Chainais. 2017c. “Spectral analysis of stationary random bivariate signals.” *IEEE Transactions on Signal Processing* 65 (23): 6135–6145. doi:10.1109/TSP.2017.2736494

 J. Flamant, N. Le Bihan, and P. Chainais. 2017a. “Analyse spectrale des signaux aléatoires bivariés.” In *GRETSI 2017*. Juan-les-Pins, France

CHAPTER CONTENTS

2.1	Quaternion spectral density for deterministic bivariate signals Finite energy signals • Finite power signals •	50
2.2	Stationary random bivariate signals Spectral representation theorem • Quaternion power spectral density • Quaternion autocovariance • Cross-covariances and cross-spectral densities •	51
2.3	The quaternion spectral density in practice Stokes parameters • Degree of polarization. Unpolarized and polarized parts decomposition. • Poincaré sphere representation • Examples •	56
2.4	Nonparametric spectral estimation Conventional spectral estimators • Estimation of polarization parameters • Illustration •	64
2.5	Conclusion	70
APPENDICES		
2.A	Circularity of spectral increments	72
2.B	Expressions for the quaternion power spectral density and the quaternion autocovariance	72
2.C	Unpolarized signals and non-Gaussianity	73
2.D	Proofs Proof of the spectral representation Theorem 2.1 • Proof of Theorems 2.2 and 2.3 •	74

2.1 QUATERNION SPECTRAL DENSITY FOR DETERMINISTIC BIVARIATE SIGNALS

2.1.1 Finite energy signals

Consider a continuous-time bivariate signal $x : \mathbb{R} \rightarrow \mathbb{C}_i$ which reads explicitly $x(t) = u(t) + \mathbf{i}v(t)$ with u and v real-valued signals. Let us assume that x is of finite energy, that is $x \in L^2(\mathbb{R}; \mathbb{H})$. The Parseval-Plancherel theorem 1.1 states that the quaternion Fourier transform has two invariants:

$$\int_{-\infty}^{+\infty} |x(t)|^2 dt = \int_{-\infty}^{+\infty} |X(\nu)|^2 d\nu \quad (2.1)$$

$$\int_{-\infty}^{+\infty} x(t) \mathbf{j} \overline{x(t)} dt = \int_{-\infty}^{+\infty} X(\nu) \mathbf{j} \overline{X(\nu)} d\nu \quad (2.2)$$

Eq. (2.1) is classical and shows that *energy* is preserved. Eq. (2.2) is specific to the QFT. It shows that an additional quadratic or energetic quantity related to *geometric content* is preserved.

Eqs. (2.1) and (2.2) guarantee the interpretation of quantities $|X(\nu)|^2$ and $X(\nu) \mathbf{j} \overline{X(\nu)}$ as spectral domain densities. Moreover since

$$|X(\nu)|^2 \geq 0 \quad \text{and} \quad X(\nu) \mathbf{j} \overline{X(\nu)} \in \text{span}\{\mathbf{i}, \mathbf{j}, \mathbf{k}\} \quad (2.3)$$

they can be suitably combined to define the *quaternion-valued energy spectral density* of x as

$$\Gamma_{xx}^E(\nu) = \underbrace{|X(\nu)|^2}_{\text{energy}} + \underbrace{X(\nu) \mathbf{j} \overline{X(\nu)}}_{\text{geometry}}. \quad (2.4)$$

This definition of $\Gamma_{xx}^E(\nu)$ makes use of the scalar-vector part decomposition of quaternions. It provides a natural separation between *energetic* content (scalar part) and *geometric content* (vector part).

Example: windowed monochromatic signal Fig. 2.1 shows an example of a windowed monochromatic bivariate signal x . The window $g(t)$ is real-valued and square integrable $\|g\|_{L^2} < \infty$ such that $x \in L^2(\mathbb{R}; \mathbb{H})$. The signal x reads

$$\begin{aligned} x(t) &= \text{Proj}_{\mathbb{C}_i} \{g(t) e^{i\theta} e^{-k\chi} e^{j\varphi} e^{2\pi\nu_0 t}\} \\ &= g(t) e^{i\theta} [\cos \chi \cos(2\pi\nu_0 t + \varphi) + \mathbf{i} \sin \chi \sin(2\pi\nu_0 t + \varphi)]. \end{aligned} \quad (2.5)$$

The parameters θ and χ define the elliptical trajectory of $x(t)$ in the 2D-plane. The energy spectral density (2.4) associated to x is

$$\Gamma_{xx}^E(\nu) = |G(\nu - \nu_0)|^2 (1 + \boldsymbol{\mu}_x) + |G(\nu + \nu_0)|^2 (1 + \mathbf{i} \boldsymbol{\mu}_x \mathbf{i}) \quad (2.6)$$

where G is the QFT of g and $\boldsymbol{\mu}_x$ is called the *polarization axis* of x :

$$\boldsymbol{\mu}_x = \sin 2\chi \mathbf{i} + \cos 2\theta \cos 2\chi \mathbf{j} + \sin 2\theta \cos 2\chi \mathbf{k}. \quad (2.7)$$

The energy spectral density given in (2.6) is symmetric in ν , so that we can focus on positive frequencies only. As it is a pure phase delay term, φ does not appear in the energy spectral density expression (2.6). The quantity $|G(\nu - \nu_0)|^2$ provides the repartition of the energy in the spectral domain. Moreover, the polarization axis $\boldsymbol{\mu}_x$ carries the information about the geometry of $x(t)$, *i.e.* the ellipse described by $x(t)$. Further physical and geometric interpretations of the polarization axis will be given in Section 2.3 for the case of random bivariate signals.

Superscript ^E stands here for “energy”.

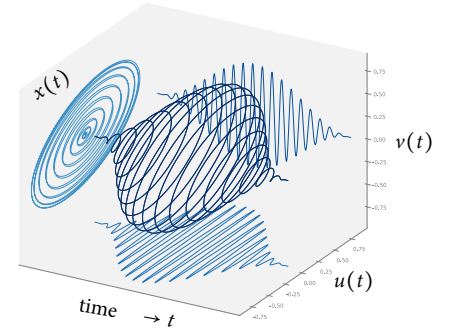


Figure 2.1: Windowed monochromatic signal example for $\theta = \pi/8$ and $\chi = -\pi/6$ and a Hanning window. The 3D trajectory (time-unwrapped) of the bivariate signal $x(t)$ is shown. Projection panels display the complex trace of $x(t)$ and its univariate components $u(t)$ and $v(t)$.

2.1.2 Finite power signals

Extending the definition of the quaternion spectral density (2.4) to bivariate signals with finite power follows the usual derivation. Namely, let x be a finite power signal, that is such that

$$\lim_{T \rightarrow \infty} \frac{1}{T} \int_{-\frac{T}{2}}^{\frac{T}{2}} |x(t)|^2 dt < \infty. \quad (2.8)$$

Define $x_T(t) = x(t)\mathbf{1}_{[-\frac{T}{2}, \frac{T}{2}]}(t)$ and denote by $X_T(\mathbf{v})$ its quaternion Fourier transform. Then the *quaternion power spectral density* of x is

$$\Gamma_{xx}(\mathbf{v}) = \lim_{T \rightarrow \infty} \frac{1}{T} \left(|X_T(\mathbf{v})|^2 + X_T(\mathbf{v}) \overline{jX_T(\mathbf{v})} \right) \quad (2.9)$$

As for the energy spectral density (2.4), the scalar part of $\Gamma_{xx}(\mathbf{v})$ is a pure power quantity. The vector part describes geometric or polarization properties in terms of power-homogeneous quantities. We will detail them later on.

$\mathbf{1}_{[-\frac{T}{2}, \frac{T}{2}]}(t)$ denotes the indicatrix function on the time interval $[-\frac{T}{2}, \frac{T}{2}]$

2.2 STATIONARY RANDOM BIVARIATE SIGNALS

Random signals appear in many signal processing applications, *e.g.* when the signal of interest is corrupted by noise or when mechanisms producing the signal carry some randomness themselves. We focus here on an important class of random bivariate signals: second-order stationary random bivariate signals. Such signals exhibit some kind of regularity, *i.e.* their first and second-order moments are invariant to time-shifts. The goal of this section is to define the notion of second-order properties, namely covariances and power spectral densities, in the quaternion Fourier transform (QFT) framework. To this aim, Section 2.2.1 introduces a spectral representation theorem for the QFT. Section 2.2.2 defines the quaternion power spectral density (PSD) of a stationary random bivariate signal. Section 2.2.3 defines its time-domain counterpart, called the quaternion autocovariance. Finally, Section 2.2.4 explores the concepts of quaternion cross-covariance and quaternion cross-PSD to characterize the joint properties of two second-order stationary random bivariate signals.

Second-order stationarity is also referred to as *wide-sense stationarity* by many authors (Schreier and Scharf, 2010).

The quaternion PSD encodes the complete second-order statistical structure of random bivariate signals. Compared to usual PSD or augmented PSD matrices (see Section 0.2.1 and Section 0.2.2), it has a straightforward geometric and physical interpretation in terms of frequency-dependent polarization parameters. However for the sake of clarity we concentrate in this section on mathematical and statistical aspects only. Detailed physical interpretations and examples are postponed to Section 2.3.

Discussions below stand for continuous-time bivariate signals. The correspondence with the discrete-time case follows directly from the discrete-time quaternion Fourier transform presented in Appendix 1.C. Second-order stationary random bivariate signals can be defined as follows (Priestley, 1981).

Definition 2.1 (Second-order stationary random bivariate signals). *Let x be a continuous-time random bivariate signal such that $x(t) = u(t) + iv(t)$, where u and v are real-valued random signals. A random bivariate signal x is second-order stationary if u and v are jointly second-order stationary:*

1. *The mean of x is constant*

$$m_x(t) = \mathbf{E}\{x(t)\} = \mathbf{E}\{u(t)\} + i\mathbf{E}\{v(t)\} = m, \quad t \in \mathbb{R} \quad (2.10)$$

$\mathbf{E}\{\cdot\}$ denotes the mathematical expectation.

2. *The variance of x is finite and constant:*

$$\sigma_x^2(t) = \mathbf{E}\{|x(t)|^2\} = \mathbf{E}\{|u(t)|^2\} + \mathbf{E}\{|v(t)|^2\} = \sigma_u^2 + \sigma_v^2 < \infty \quad (2.11)$$

3. *The auto- and crosscovariances of u and v depend only on the time lag τ :*

$$R_{uu}(t, \tau) = \mathbf{E}\{u(t)u(t-\tau)\} = R_{uu}(\tau), \quad t, \tau \in \mathbb{R} \quad (2.12)$$

$$R_{vv}(t, \tau) = \mathbf{E}\{v(t)v(t-\tau)\} = R_{vv}(\tau), \quad t, \tau \in \mathbb{R} \quad (2.13)$$

$$R_{uv}(t, \tau) = \mathbf{E}\{u(t)v(t-\tau)\} = R_{uv}(\tau), \quad t, \tau \in \mathbb{R} \quad (2.14)$$

R_{uu}, R_{vv}, R_{uv} denote usual autocovariance and crosscovariance sequences of real-valued random signals.

For convenience, second-order stationarity is simply referred to as *stationarity* unless differently stated. In the remaining of this chapter bivariate signals are stationary in the sense of Definition 2.1 with zero-mean $m = 0$.

In definition 2.1, Condition 3 is equivalent to the requirement that the covariance function and the complementary-covariance of x depend on τ only, i.e. $R_{xx}(t, \tau) = R_{xx}(\tau)$ and $\tilde{R}_{xx}(t, \tau) = \tilde{R}_{xx}(\tau)$.

2.2.1 Spectral representation theorem

To generalize the quaternion spectral density definition to random bivariate signals, one first needs to extend the concept of quaternion Fourier transform to random signals. The spectral representation Theorem 2.1 below answers this key point. It plays the same role as the Cramér-Loève spectral representation theorem for univariate signals.

Theorem 2.1 (Spectral representation of stationary bivariate signals). *Let $x(t) = u(t) + iv(t)$ be a zero-mean stationary random bivariate signal. Suppose that x is harmonizable. Then there exists a quaternion-valued process $X(\nu)$ with orthogonal increments $dX(\nu) \triangleq X(\nu + d\nu) - X(\nu)$ such that*

$$x(t) = \int_{-\infty}^{+\infty} dX(\nu) e^{j2\pi\nu t}, \quad (2.15)$$

the equality being in the mean-square sense. The process $X(\nu)$ has the following properties:

1. $\forall \nu, \mathbf{E}\{dX(\nu)\} = 0$,
2. $\forall \nu, \mathbf{E}\{|dX(\nu)|^2\} + \mathbf{E}\{dX(\nu)\overline{jdX(\nu)}\} = d\Gamma_{xx}^{(I)}(\nu)$ where $\Gamma_{xx}^{(I)}(\nu)$ is the integrated power spectrum of x ,
3. *For any $\nu \neq \nu'$, the process $X(\nu)$ has orthogonal increments:*

$$\mathbf{E}\{dX(\nu)\overline{dX(\nu')}\} = \mathbf{E}\{dX(\nu)\overline{jdX(\nu')}\} = 0.$$

The quaternion Fourier-Stieltjes integral (2.15) is called the quaternion spectral representation of the random bivariate signal $x(t)$. It shows that any random bivariate signal $x(t)$ can be interpreted as an “infinite” sum of monochromatic signals at frequency ν with associated random quaternion-valued coefficients $dX(\nu)$. These are called the *spectral increments* of the random bivariate signal $x(t)$.

We say that the bivariate signal $x(t) = u(t) + iv(t)$ is harmonizable if the real univariate signals u and v are harmonizable, i.e. if they both admit a standard spectral representation (Priestley, 1981).

Proof. See Appendix 2.D.1. \square

The existence of the spectral representation (2.15) directly follows from the existence of usual \mathbb{C}_j -complex-valued spectral increments of u and v . In short, one requires the random signals u and v to be harmonizable, see Appendix 2.D.1 for details. Spectral increments of x directly read

$$dX(v) = dU(v) + \mathbf{i}dV(v), \quad (2.16)$$

where dU and dV are the usual \mathbb{C}_j -valued spectral increments of real univariate signals u and v . It illustrates that the quaternion spectral representation (2.15) is obtained as a linear combination of usual spectral representations of real-valued signals.

Properties 1 to 3 of the spectral increments $dX(v)$ encode the self and joint properties of the spectral increments of u and v . In particular property 3 illustrates that the spectral increments $dX(v)$ are twice orthogonal: it yields interesting second-order circularity properties for the case of bivariate signals. See Appendix 2.A for details.

See Blanc-Lapierre and Fortet (1953, p. 344) or Loeve (1978, p. 140) for details on harmonizable signals.

2.2.2 Quaternion power spectral density

Property 2 of Theorem 2.1 introduces the *quaternion integrated spectrum* $\Gamma_{xx}^{(I)}$ of x such that

$$d\Gamma_{xx}^{(I)}(v) = \mathbf{E} \{ |dX(v)|^2 \} + \mathbf{E} \{ dX(v) \overline{\mathbf{j}dX(v)} \}. \quad (2.17)$$

The integrated spectrum can be decomposed¹ into two parts such that

$$\Gamma_{xx}^{(I)}(v) = \Gamma_{xx}^{(I),c}(v) + \Gamma_{xx}^{(I),d}(v) \quad (2.18)$$

where $\Gamma_{xx}^{(I),c}$ is absolutely continuous and $\Gamma_{xx}^{(I),d}$ is a step function. These two quantities identify with the *continuous* and *discrete* part of the spectrum, respectively.

When it exists, the derivative $d\Gamma_{xx}^{(I)}/dv$ defines the quaternion power spectral density (PSD) Γ_{xx} . In full generality it can be defined only when the integrated spectrum features no discrete component. However, a useful abuse is to consider the discrete part of the spectrum to be differentiable in the sense of distributions by using Dirac delta functions. The quaternion PSD corresponding to the integrated spectrum (2.18) is

$$\Gamma_{xx}(v) = \Gamma_{xx}^c(v) + \sum_{\ell} c_{\ell} \delta(v - v_{\ell}), \quad (2.19)$$

where Γ_{xx}^c is the spectral density associated to $\Gamma_{xx}^{(I),c}$ and c_{ℓ}, v_{ℓ} are respectively the quaternion-valued coefficients and frequencies associated to jumps in $\Gamma_{xx}^{(I),d}$.

In practice one prefers to work with the quaternion PSD Γ_{xx} instead of the quaternion integrated spectrum $\Gamma_{xx}^{(I)}$. Keeping in mind that $\Gamma_{xx}(v)$ is in general a mixture of continuous and discrete components, see Eq. (2.19), we consider from now on the following definition for the quaternion PSD

$$\Gamma_{xx}(v)dv = \mathbf{E} \{ |dX(v)|^2 \} + \mathbf{E} \{ dX(v) \overline{\mathbf{j}dX(v)} \}. \quad (2.20)$$

It involves two second-order moments of the spectral increments, of the same form as the two invariants of the quaternion Fourier transform. The combination of these two moments in Γ_{xx} provides a natural separation between

1. The decomposition (2.18) is in fact the Lebesgue decomposition of the integrated spectrum, see e.g. Percival and Walden (1993). In full generality this decomposition includes a third term which is continuous with derivatives vanishing almost everywhere. Following standard practice (Hannan, 1970) this pathological term is neglected in decomposition (2.18).

purely energetic and geometric information, similarly to the deterministic case discussed in Section 2.1. To see that $\Gamma_{xx}(\nu)$ is indeed a power spectral density, remark that

$$\int_{-\infty}^{+\infty} \Gamma_{xx}(\nu) d\nu = \mathbf{E} \{|x(t)|^2\} + \mathbf{E} \{x^2(t)\} \mathbf{j}. \quad (2.21)$$

The right-hand side of (2.21) contains the complete second-order properties of the random variable $x(t)$, i.e. the instantaneous second-order properties of the random signal $x(t)$.

Since $x(t)$ is a \mathbb{C}_i -valued bivariate signal, the spectral increments of x satisfy the same i -Hermitian symmetry as the QFT of \mathbb{C}_i -valued signals:

$$dX(-\nu) = -i dX(\nu) i. \quad (2.22)$$

As a result, the quaternion power spectral density (2.20) has the following symmetry

$$\Gamma_{xx}(-\nu) = -i \overline{\Gamma_{xx}(\nu)} i \quad (2.23)$$

This symmetry is essential to the physical interpretation of $\Gamma_{xx}(\nu)$. It shows that the study of bivariate signals can be carried out using only the positive frequencies of its quaternion-valued power spectral density. It contrasts with approaches relying on second-order circularity of complex-valued processes where both positive and negative frequencies carry information, see Section 0.2.2 of the introduction.

Remark that the right-hand side of (2.21) involves explicitly the covariance $\mathbf{E} \{|x(t)|^2\}$ and complementary covariance $\mathbf{E} \{x^2(t)\}$ appearing in the study of the circularity of complex random variables (Picinbono, 1994; Adahi, Schreier, and Scharf, 2011).

This symmetry means that 1, \mathbf{j} and \mathbf{k} components of $\Gamma_{xx}(\nu)$ are even whereas its i component is odd.

2.2.3 Quaternion autocovariance

The study of random univariate signals often starts with the notion of autocovariance. The spectral density is introduced next, and some authors define it as the Fourier transform of the autocovariance, thanks to the Wiener-Khintchine theorem. Thus autocovariance and spectral density functions are Fourier transform pairs – a convenient feature one would like to keep for the analysis of bivariate signals with the quaternion Fourier transform.

For random bivariate signals we have proceeded differently. The quaternion power spectral density has been defined thanks to the spectral representation Theorem 2.1. The notion of quaternion autocovariance remains to be defined.

We define the quaternion autocovariance γ_{xx} as the inverse quaternion Fourier transform of the quaternion spectral density Γ_{xx}

$$\gamma_{xx}(\tau) \triangleq \int_{-\infty}^{+\infty} \Gamma_{xx}(\nu) e^{j2\pi\nu\tau} d\nu. \quad (2.24)$$

The quaternion autocovariance and the quaternion power spectral density thus form a natural quaternion Fourier transform pair. The autocovariance $\gamma_{xx}(\tau)$ can be explicitly written in terms of usual covariance functions of components u and v :

$$\gamma_{xx}(\tau) = R_{uu}(\tau) + R_{vv}(\tau) + \mathbf{j}(R_{uu}(\tau) - R_{vv}(\tau)) + 2\mathbf{k}R_{vu}(\tau). \quad (2.25)$$

The autocovariance function (2.25) contains the complete second-order information about the bivariate signal x . It takes its values in $\text{span}\{1, \mathbf{j}, \mathbf{k}\}$. It is not symmetric with respect to τ , since the cross-covariance $R_{vu}(\tau)$ is not symmetric in general.

See Appendix 2.B for details.

In fact, Eq. (2.25) results from the left-linearity of the QFT and from the component-wise application of the usual Wiener-Khintchine theorem in (2.24).

It is legitimate to wonder whether it is possible to rewrite (2.25) as an expression involving the signal x only. Using (2.21), the value of the autocovariance at the origin reads

$$\gamma_{xx}(0) = \mathbf{E} \{ |x(t)|^2 \} + \mathbf{E} \{ x^2(t) \} \mathbf{j}. \quad (2.26)$$

This expression involves usual covariance and complementary-covariance of *complex random variables*. Unfortunately this does not extend to $\tau \neq 0$, since there is no simple expression of $\gamma_{xx}(\tau)$ in terms of covariance and complementary-covariance functions of *complex random signals*. However Theorem 2.2 below provides a direct link between $x(t)$ and its quaternion spectral density (2.4).

Theorem 2.2. *Let x be a second-order stationary random bivariate signal. Then one has*

$$\mathcal{S}(\Gamma_{xx}(\mathbf{v})) = \int_{-\infty}^{+\infty} \mathbf{E} \{ x(t) e^{-j2\pi\mathbf{v}\tau} \overline{x(t-\tau)} \} d\tau \quad (2.27)$$

$$\mathcal{V}(\Gamma_{xx}(\mathbf{v})) = \int_{-\infty}^{+\infty} \mathbf{E} \{ x(t) e^{-j2\pi\mathbf{v}\tau} \overline{jx(t-\tau)} \} d\tau \quad (2.28)$$

In particular, by a straightforward integration of (2.27) and (2.28) over frequencies one recovers (2.21), *i.e.* the interpretation of Γ_{xx} as a spectral density. This Wiener-Khinchine flavored theorem 2.2 will also inspire the formal construction of generic bilinear time-frequency-polarization representations, see Section 4.4.

For a complex random signal x one usually defines its covariance function as

$$R_{xx}(\tau) \triangleq \mathbf{E} \{ x(t) \overline{x(t-\tau)} \}$$

and its complementary-covariance function as

$$\tilde{R}_{xx}(\tau) \triangleq \mathbf{E} \{ x(t) x(t-\tau) \}.$$

See Section 0.2.2 and Schreier and Scharf (2010) for details.

Proof. See Appendix 2.D.2. □

2.2.4 Cross-covariances and cross-spectral densities

Let $x(t) = u_x(t) + \mathbf{i}v_x(t)$ and $y(t) = u_y(t) + \mathbf{i}v_y(t)$ be two continuous-time, jointly² stationary and zero-mean random bivariate signals. Two equivalent notions are introduced to characterize the *joint* second-order properties of x and y : the *quaternion cross-spectral power density* in the spectral domain and the *quaternion cross-covariance* in the time-lag domain. In particular the uncorrelatedness condition between two random bivariate signals is easily formulated in both domains.

Definitions Suppose that x and y are both harmonizable, so that their quaternion spectral representation is given by Theorem 2.1. The quaternion cross power spectral density Γ_{xy} is defined as

$$\Gamma_{xy}(\mathbf{v})d\mathbf{v} = \mathbf{E} \{ dX(\mathbf{v}) \overline{dY(\mathbf{v})} \} + \mathbf{E} \{ dX(\mathbf{v}) \mathbf{j} \overline{dY(\mathbf{v})} \} \quad (2.29)$$

where dX and dY are the spectral increments of x and y , respectively.

The quaternion-valued cross-covariance function γ_{xy} is defined by the inverse quaternion Fourier transform of Γ_{xy} given by (2.29). It explicitly reads in terms of usual covariances functions between u_x , u_y , v_x and v_y :

$$\begin{aligned} \gamma_{xy}(\tau) &= R_{u_x u_y}(\tau) + R_{v_y v_x}(\tau) + \mathbf{i} [R_{v_x u_y}(\tau) - R_{v_y u_x}(\tau)] \\ &+ \mathbf{j} [R_{u_x u_y}(\tau) - R_{v_y v_x}(\tau)] + \mathbf{k} [R_{v_x u_y}(\tau) + R_{v_y u_x}(\tau)]. \end{aligned} \quad (2.30)$$

It is clear from (2.30) that γ_{xy} encodes the complete covariance structure between real and imaginary parts of x and y . The following theorem links the spectral and time domain cross properties of x and y . It can be seen as a generalization of Theorem 2.2.

2. This means that x and y are stationary bivariate signals in the sense of Definition 2.1, and that the four cross-covariances between u_x , u_y , v_x and v_y depend only on the time-lag τ .

Theorem 2.3. *Let x and y be two continuous-time jointly stationary random bivariate signals. Suppose that x and y are harmonizable. Then*

$$\mathbf{E} \left\{ dX(\mathbf{v}) \overline{dY(\mathbf{v})} \right\} / d\mathbf{v} = \int_{-\infty}^{+\infty} \mathbf{E} \left\{ x(t) e^{-j2\pi\mathbf{v}\tau} \overline{y(t-\tau)} \right\} d\tau \quad (2.31)$$

$$\mathbf{E} \left\{ dX(\mathbf{v}) \mathbf{j} \overline{dY(\mathbf{v})} \right\} / d\mathbf{v} = \int_{-\infty}^{+\infty} \mathbf{E} \left\{ x(t) e^{-j2\pi\mathbf{v}\tau} \mathbf{j} \overline{y(t-\tau)} \right\} d\tau \quad (2.32)$$

where dX and dY are the spectral increments of x and y .

Proof. See Appendix 2.D.2. \square

Symmetries Since x and y are \mathbb{C}_i -valued, their spectral increments satisfy the i -Hermitian symmetry (2.22). Therefore the quaternion cross power spectral density exhibits the following symmetry

$$\Gamma_{xy}(-\mathbf{v}) = -\mathbf{i} \overline{\Gamma_{yx}(\mathbf{v})} \mathbf{i} \quad (2.33)$$

which reduces to (2.23) when $x = y$. Just like the quaternion autocovariance, the quaternion cross-covariance $\gamma_{xy}(\tau)$ does not exhibit any particular symmetry.

Uncorrelatedness From the explicit expression (2.30) of the quaternion cross-covariance, we see that two jointly stationary random bivariate signals are *uncorrelated* if and only if their quaternion cross-covariance vanishes, *i.e.*

$$\forall \tau, \gamma_{xy}(\tau) = 0 \iff x \text{ and } y \text{ are uncorrelated.} \quad (2.34)$$

It is sometimes more practical to express this condition in the spectral domain,

$$\forall \mathbf{v}, \Gamma_{xy}(\mathbf{v}) = 0 \iff x \text{ and } y \text{ are uncorrelated.} \quad (2.35)$$

Thanks to (2.33), we also see that if $\Gamma_{xy}(\mathbf{v}) = 0$ for all \mathbf{v} , then one has also $\Gamma_{yx}(\mathbf{v}) = 0$ for all \mathbf{v} . These spectral domain expressions will be useful later on for the computation of filters with specific output correlation properties, see Section 3.3.4.

Usual properties regarding the sum of two signals are then recovered. Given two signal x and y , the quaternion power spectral density $x + y$ is

$$\Gamma_{x+y, x+y}(\mathbf{v}) = \Gamma_{xx}(\mathbf{v}) + \Gamma_{yy}(\mathbf{v}) + \Gamma_{xy}(\mathbf{v}) + \Gamma_{yx}(\mathbf{v}). \quad (2.36)$$

When x and y are uncorrelated, the quaternion power spectral density of the sum is the sum of quaternion power spectral densities. A similar result holds for the autocovariance γ_{x+y} .

Note that $\Gamma_{x+y, x+y}(\mathbf{v}) = \Gamma_{xx}(\mathbf{v}) + \Gamma_{yy}(\mathbf{v})$ is not equivalent to x and y being uncorrelated. In fact it only implies that $\Gamma_{xy} = \Gamma_{yx}$, that is using (2.33), $\Gamma_{xy}(\mathbf{v}) = -\mathbf{i} \overline{\Gamma_{xy}(-\mathbf{v})} \mathbf{i}$.

2.3 THE QUATERNION SPECTRAL DENSITY IN PRACTICE

The last section precisely defined the notion of quaternion power spectral density as well as quaternion autocovariance for stationary random bivariate signals. So far only mathematical and statistical aspects have been discussed. Section 2.3.1 to Section 2.3.3 below explore the physical interpretation of these novel quantities. Unlike descriptors from standard approaches (matrix PSD or augmented matrix PSD) the quaternion PSD offers straightforward and efficient descriptions of bivariate random signals in terms of frequency-dependent

polarization properties. The power and interpretability of the approach is demonstrated by several examples provided in Section 2.3.4.

We focus on continuous-time, stationary random bivariate signals $x(t)$ as in Definition 2.1. The quaternion autocovariance $\gamma_{xx}(\tau)$ and the quaternion power spectral density $\Gamma_{xx}(\nu)$ form a quaternion Fourier transform pair:

$$\gamma_{xx}(\tau) \stackrel{\text{QFT}}{\longleftrightarrow} \Gamma_{xx}(\nu). \quad (2.37)$$

This correspondence between time-lag and frequency domain turns out to be very convenient for the calculation of quaternion spectral densities for (time-domain) models of random bivariate signals.

2.3.1 Stokes parameters

The quaternion spectral density Γ_{xx} defined by (2.20) is directly related to a set of four real-valued parameters called *Stokes parameters*. These parameters were introduced by Stokes (1852) to describe the *polarization state* of light. Stokes parameters are energetic quantities and thus experimentally³ measurable. The definition of Stokes parameters in terms of usual spectral densities of $u(t)$ and $v(t)$ can be found in Born and Wolf (1980) and in Schreier and Scharf (2010).

Definition 2.2 (Stokes parameters). *Stokes parameters are denoted by $S_0(\nu)$, $S_1(\nu)$, $S_2(\nu)$ and $S_3(\nu)$. They are related to spectral densities of u and v by*

$$S_0(\nu) = P_{uu}(\nu) + P_{vv}(\nu) \quad (2.38)$$

$$S_1(\nu) = P_{uu}(\nu) - P_{vv}(\nu) \quad (2.39)$$

$$S_2(\nu) = 2\text{Re}\{P_{uv}(\nu)\} \quad (2.40)$$

$$S_3(\nu) = 2\text{Im}\{P_{uv}(\nu)\} \quad (2.41)$$

Using the expression of the quaternion power spectral density in terms of $P_{uu}(\nu)$, $P_{vv}(\nu)$ and $P_{uv}(\nu)$ given by (2.96) in Appendix 2.B one obtains the following remarkable equation:

$$\Gamma_{xx}(\nu) = S_0(\nu) + \mathbf{i}S_3(\nu) + \mathbf{j}S_1(\nu) + \mathbf{k}S_2(\nu). \quad (2.42)$$

Eq. (2.42) shows that the quaternion power spectral density Γ_{xx} is isomorphic to the frequency-dependent⁴ *Stokes vector*, widely used by physicists (Gil, 2007). Thus $\Gamma_{xx}(\nu)$ gives a frequency-dependent description of the polarization properties of any stationary random bivariate signal $x(t)$.

Stokes parameters provide a natural separation between contributions from *unpolarized* and *polarized* components. The scalar part of $\Gamma_{xx}(\nu)$ is the first Stokes parameter $S_0(\nu)$. It gives the *total* power spectral density, *i.e.* the sum of the power spectral density of the unpolarized part and the polarized part. The three remaining Stokes parameters $S_1(\nu)$, $S_2(\nu)$ and $S_3(\nu)$ constitute the vector part of $\Gamma_{xx}(\nu)$, and describe the frequency evolution of the *polarization* properties of x , *i.e.* the properties of its polarized part.

Let us introduce the normalized Stokes parameters s_1, s_2, s_3 such that

$$s_1(\nu) \triangleq \frac{S_1(\nu)}{S_0(\nu)}, \quad s_2(\nu) \triangleq \frac{S_2(\nu)}{S_0(\nu)}, \quad s_3(\nu) \triangleq \frac{S_3(\nu)}{S_0(\nu)} \quad (2.43)$$

when $S_0(\nu) \neq 0$. Normalized Stokes parameters (s_1, s_2, s_3) encode the polarization state at a given frequency ν . Fig. 2.2 depicts examples of polarization

3. In optics, one can only perform intensity or energetic measurements, since it is not possible to 'sample' fast enough the electromagnetic field, which oscillates typically at $4 - 8 \times 10^{14}$ Hz for visible light.

4. In optics the frequency dependence is often dropped due to an (implicit) narrow-band signal assumption.

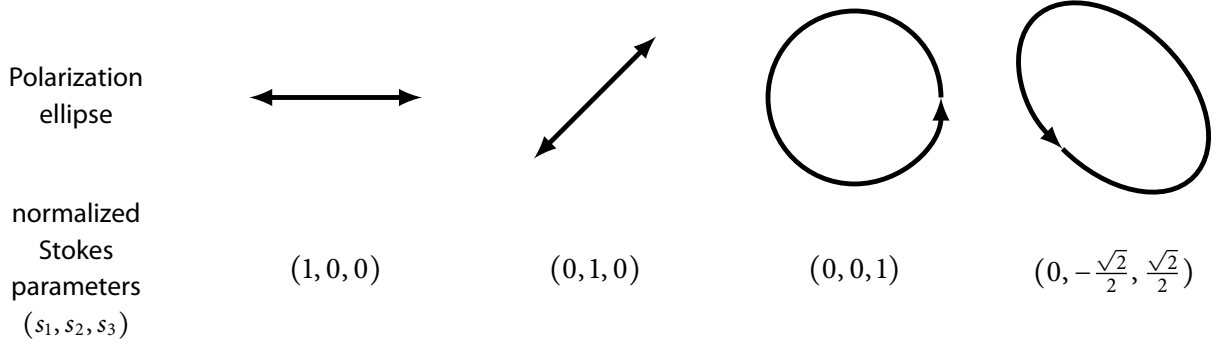


Figure 2.2: Polarization ellipses and their associated normalized Stokes parameters.

ellipses and their corresponding normalized Stokes parameters. The parameter s_3 describes the amount of circular polarization; it can be positive (counter-clockwise circular polarization) or negative (clockwise circular polarization). Parameters s_1 and s_2 control the amount of linear horizontal and linear 45° polarization, respectively. Normalized Stokes parameters can be further interpreted thanks to a geometric representation of polarization states called *Poincaré sphere*. See details in Section 2.3.3 below.

2.3.2 Degree of polarization. Unpolarized and polarized parts decomposition.

The *degree of polarization* of x is the frequency-dependent quantity $\Phi_x(\nu)$ defined as the ratio

$$\Phi_x(\nu) = \frac{|\mathcal{V}\{\Gamma_{xx}(\nu)\}|}{\mathcal{S}\{\Gamma_{xx}(\nu)\}} = \frac{\sqrt{S_1(\nu)^2 + S_2(\nu)^2 + S_3(\nu)^2}}{S_0(\nu)}. \quad (2.44)$$

Using the definition of Stokes parameters in terms of usual spectral densities, see Eqs. (2.38) – (2.41), one can show that $0 \leq \Phi_x(\nu) \leq 1$ for every ν . When $\Phi_x(\nu) = 1$, x is said to be *fully polarized* at frequency ν ; when $\Phi_x(\nu) = 0$, x is said to be *unpolarized* at frequency ν . Otherwise, $0 < \Phi_x(\nu) < 1$ and x is said to be *partially polarized* at frequency ν . Figure 2.3 summarizes these denominations. The degree of polarization is invariant with respect to the choice of basis in which the polarization parameters are measured. It is thus a robust parameter, which has raised interest in many applications, see e.g. Kikuchi (2001) and Shirvany, Chabert, and Tournet (2012).

The degree of polarization rules the power repartition between the unpolarized and polarized part of the spectral density. Remark indeed that the quaternion PSD (2.42) can be rewritten as

$$\Gamma_{xx}(\nu) = \underbrace{(1 - \Phi_x(\nu)) S_0(\nu)}_{\Gamma_{xx}^u(\nu), \text{ unpolarized part}} + \underbrace{\Phi_x(\nu) S_0(\nu) + \mathbf{i}S_3(\nu) + \mathbf{j}S_1(\nu) + \mathbf{k}S_2(\nu)}_{\Gamma_{xx}^p(\nu), \text{ fully polarized part}}. \quad (2.45)$$

Thus one has

$$\forall \nu, \quad \Gamma_{xx}(\nu) = \Gamma_{xx}^u(\nu) + \Gamma_{xx}^p(\nu) \quad (2.46)$$

where the u and p superscripts stand for unpolarized and (fully) polarized parts, respectively. This decomposition is unique and corresponds to the usual decomposition given in optics textbooks, see e.g. Brosseau (1998, p. 127) or

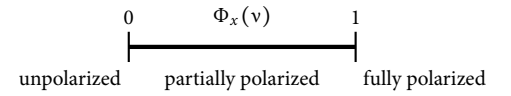


Figure 2.3: Denominations corresponding to values of the degree of polarization.

From the definition (2.44) of the degree of polarization, it is easy to see that, for every ν , $\Gamma_{xx}^u(\nu)$ has a null degree of polarization $\Phi_x^u(\nu) = 0$ and that $\Gamma_{xx}^p(\nu)$ has a unit degree of polarization $\Phi_x^p(\nu) = 1$.

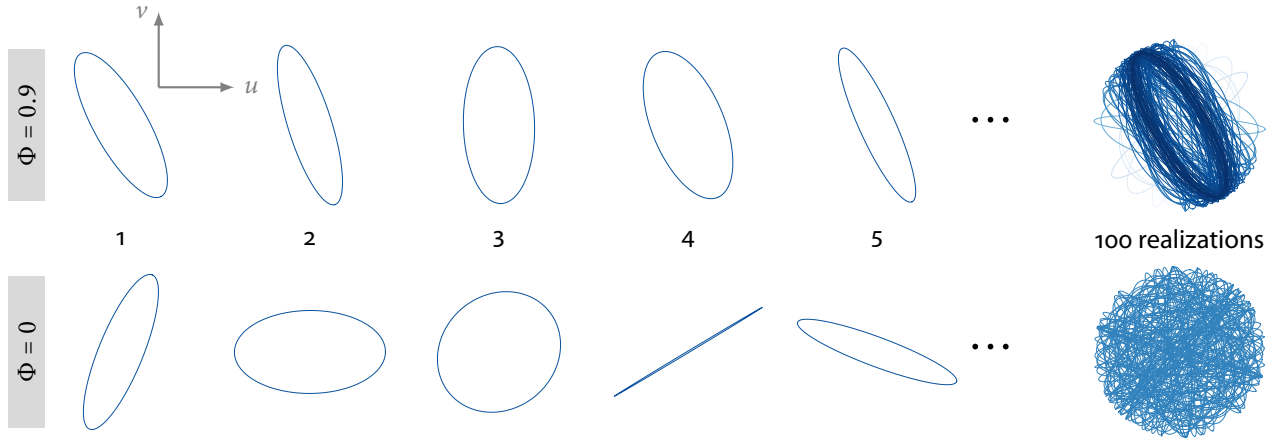


Figure 2.4: At a given frequency ν , the degree of polarization $\Phi(\nu)$ quantifies the statistical stability of the corresponding elliptical trajectory in the $u - \nu$ plane. The closer $\Phi(\nu)$ is from 1, the more stable is the elliptical trajectory. For $\Phi(\nu) = 0$, ellipses are drawn uniformly under Gaussianity.

Born and Wolf (1980, p. 551). The main difference is that Eqs. (2.45)-(2.46) use quaternions in place of usual Stokes vectors.

Figure 2.4 illustrates the interpretation of the degree of polarization as a measure of “stability” or “dispersion” of the polarization ellipse” for the case of a monochromatic bivariate signal. Polarization ellipses corresponding to an arbitrary frequency ν_0 are represented for different realizations of a Gaussian⁵ monochromatic signal in the case of a strongly partially polarized monochromatic signal $\Phi(\nu_0) = 0.9$ and unpolarized monochromatic signal $\Phi(\nu_0) = 0$. The distribution of polarization ellipses is visualized by superimposing polarization ellipses obtained for 100 realizations. Note the uniform distribution of polarization ellipses for $\Phi(\nu) = 0$.

Note that the above discussion stands for the case of a single frequency, or more generally for the case where Γ_{xx} features only discrete spectra, see Eq. (2.19). Gaussian signals $x(t)$ having discrete spectra are known to be non-ergodic (Koopmans, 1995) and thus it is not possible to conclude on the value of $\Phi_x(\nu)$ given a single realization. For signals with continuous quaternion PSD Γ_{xx} , an ergodic interpretation of the degree of polarization is however possible. Consider for instance a narrow-band partially polarized signal with constant polarization properties. Replacing in Figure 2.4 the realization indices 1, 2, ... by time instants, one observes the slow evolution of the *instantaneous* polarization ellipse compared to the average frequency. The closer Φ_x to 1, the more stable the ellipse with time.

Traditionally in optics the degree of polarization is defined in the time-domain, see e.g. Born and Wolf (1980). In contrast, the degree of polarization (2.44) is defined here in the spectral domain. For brevity, we do not investigate further this subject here. In fact, no simple relationship exists between the temporal and spectral definition of the degree of polarization; see for instance the discussion in Setälä, Nunziata, and Friberg (2010) and Réfrégier, Setälä, and Friberg (2011).

5. The fact that the signal has Gaussian statistics is key in the interpretation of these figures. Gaussian statistics implies that the distribution of polarization states of unpolarized monochromatic components is uniform on the Poincaré sphere (Ellis and Dogariu, 2004). This topic is further discussed in Appendix 2.C.

2.3.3 Poincaré sphere representation

A powerful geometric representation of polarization states has been introduced in 1892 by Poincaré in his treatise *Théorie mathématique de la lumière* (Poincaré,

1892). It provides a geometric interpretation for normalized Stokes parameters, which corresponds to Cartesian coordinates of a point lying inside the 2D sphere of unit radius.

The so-called Poincaré sphere representation of polarization states motivates an alternative parameterization of the quaternion power spectral density. Observe that (2.42) can be rewritten like

$$\Gamma_{xx}(\nu) = S_0(\nu) + S_0(\nu)\Phi_x(\nu)\boldsymbol{\mu}_x(\nu), \quad (2.47)$$

where $\Phi_x(\nu)\boldsymbol{\mu}_x(\nu)$ is a pure quaternion which reads in terms of normalized Stokes parameters:

$$\Phi_x(\nu)\boldsymbol{\mu}_x(\nu) = \mathbf{i}s_3(\nu) + \mathbf{j}s_1(\nu) + \mathbf{k}s_2(\nu). \quad (2.48)$$

Given any ν , the quantity $\Phi_x(\nu)\boldsymbol{\mu}_x(\nu)$ identifies a vector of \mathbb{R}^3 .

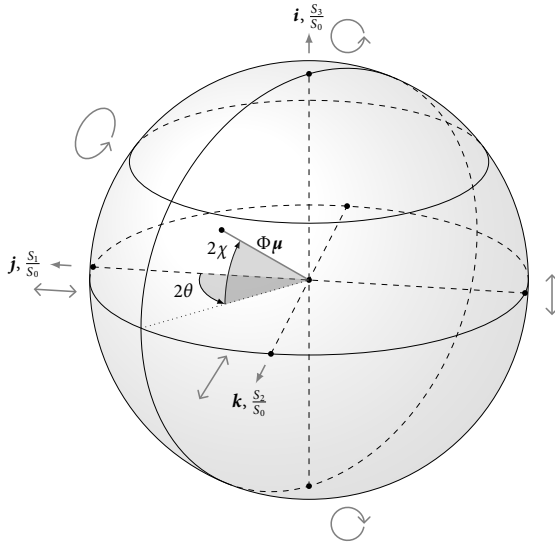


Figure 2.5: Poincaré sphere representation of polarization states. Spherical coordinates $(2\theta, 2\chi)$ gives the orientation θ and the ellipticity χ of the polarization ellipse. The degree of polarization Φ gives the radius of the polarization state encoded by the pure quaternion $\Phi\boldsymbol{\mu}$. Cartesian coordinates correspond to the normalized Stokes parameters.

Figure 2.5 displays the so-called Poincaré sphere of polarization states (Brosseau, 1998; Born and Wolf, 1980). The pure quaternion $\Phi_x(\nu)\boldsymbol{\mu}_x(\nu)$ is represented as a point inside the Poincaré sphere of unit radius. The *polarization axis* $\boldsymbol{\mu}_x(\nu)$ is a pure unit quaternion encoding the polarization ellipse. It is identified with a unit vector of \mathbb{R}^3 of spherical coordinates $(2\theta, 2\chi)$ corresponding to the orientation θ and the ellipticity χ of the polarization ellipse. For instance, $\boldsymbol{\mu}_x(\nu) = \mathbf{i}$ corresponds to counter-clockwise circular polarization, whereas $\boldsymbol{\mu}_x(\nu) = -\mathbf{j}$ denotes vertical linear polarization. In full generality, normalized Stokes parameters s_1, s_2 and s_3 are related to the degree of polarization Φ_x , the orientation θ and the ellipticity χ by means of a Cartesian-to-spherical coordinates transformation:

$$s_1 = \Phi_x \cos 2\chi \cos 2\theta, \quad (2.49)$$

$$s_2 = \Phi_x \cos 2\chi \sin 2\theta, \quad (2.50)$$

$$s_3 = \Phi_x \sin 2\chi. \quad (2.51)$$

Orthogonal polarizations are an important concept. Given two polarization ellipses denoted by (θ_1, χ_1) and (θ_2, χ_2) respectively, they correspond to orthogonal polarizations if and only if $\theta_2 = \theta_1 + \pi/2$ and $\chi_2 = -\chi_1$. Orthogonal

polarizations are thus identified with antipodal points on the Poincaré sphere of unit radius, e.g. clockwise and counter-clockwise circular polarizations are orthogonal polarizations. While it may sound disturbing at first, two polarization axes $\boldsymbol{\mu}_1$ and $\boldsymbol{\mu}_2$ correspond to two orthogonal polarizations when they are anti-aligned $\langle \boldsymbol{\mu}_1, \boldsymbol{\mu}_2 \rangle = -1$.

2.3.4 Examples

This section presents several examples of stationary random bivariate signals. We demonstrate the usefulness of the approach by providing explicit calculations of the quaternion autocovariance and quaternion PSD. We also discuss its relation to standard spectral analysis of complex-valued random signals.

Proper and improper signals Second-order circularity of complex-valued signals, also called properness has attracted a wide interest in the signal processing community over the last two decades, see Picinbono and Bondon (1997), Adali, Schreier, and Scharf (2011), and Schreier and Scharf (2010) and references therein. We recall some results from Section 0.2.2. To account for the full second-order statistical structure of a second-order stationary complex signal $x(t)$, one has to consider both the usual autocovariance $R_{xx}(\tau)$ and the complementary covariance $\tilde{R}_{xx}(\tau)$ such that:

$$R_{xx}(\tau) = \mathbf{E} \left\{ x(t) \overline{x(t-\tau)} \right\} \quad (2.52)$$

$$\tilde{R}_{xx}(\tau) = \mathbf{E} \{ x(t) x(t-\tau) \} \quad (2.53)$$

Proper signals are characterized by a zero complementary covariance, meaning that a signal $x(t)$ is uncorrelated with its complex conjugate $\overline{x(t-\tau)}$, for all τ . It follows that

$$\forall \tau, R_{uu}(\tau) = R_{vv}(\tau) \text{ and } R_{vu}[-\tau] + R_{vu}(\tau) = 0. \quad (2.54)$$

A direct consequence is that the quaternion power spectral density (2.20) of a proper signal $x(t)$ reads

$$\Gamma_{xx}(\nu) = S_0(\nu) + \mathbf{i}S_3(\nu) \quad (2.55)$$

as conditions (2.54) are equivalent to $S_1(\nu) = S_2(\nu) = 0$ for all ν . Eq. (2.55) shows that a proper signal is in general partially circularly polarized.

Fig. 2.6 presents two extreme cases, where two proper signals represent two very different physical interpretations. One is fully circularly polarized whereas the other one is unpolarized. This demonstrates that *properness* of complex random signals may not be the most relevant feature when dealing with physical properties of random bivariate signals such as polarization.

Monochromatic bivariate signals Let $x(t)$ be the continuous-time, random phase, monochromatic bivariate signal defined by

$$x(t) = ae^{i\theta} [\cos \chi \cos(2\pi\nu_0 t + \varphi) + \mathbf{i} \sin \chi \sin(2\pi\nu_0 t + \varphi)]. \quad (2.56)$$

Quantities a , θ , χ are assumed to be fixed. The phase φ is random with uniform distribution on $[0, 2\pi)$, which makes $x(t)$ a stationary random bivariate signal. The autocovariance of $x(t)$ is computed using (2.25) and reads

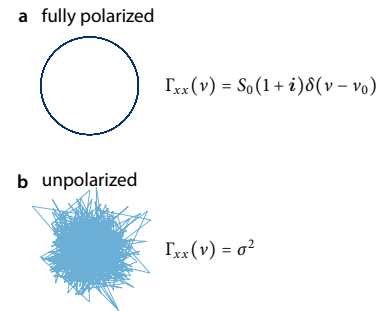


Figure 2.6: Two proper signals may capture two very different physical situations. (a) fully circularly polarized signal. (b) unpolarized signal – simply proper complex white Gaussian noise. Expressions for Γ_{xx} are restricted to positive frequencies only.

Recall ellipse parameters:
Scale $a \geq 0$
Orientation $\theta \in [-\pi/2, \pi/2]$
Ellipticity $\chi \in [-\pi/4, \pi/4]$

$$\gamma_{xx}(\tau) = \frac{a^2}{2} \{ \cos(2\pi\nu_0\tau) + \mathbf{j}s_1 \cos(2\pi\nu_0\tau) + \mathbf{k}(s_2 \cos(2\pi\nu_0\tau) + s_3 \sin(2\pi\nu_0\tau)) \} \quad (2.57)$$

where s_1, s_2, s_3 are the normalized Stokes parameters⁶ such that

$$s_1 = \cos(2\theta) \cos(2\chi), \quad s_2 = \sin(2\theta) \cos(2\chi), \quad s_3 = \sin(2\chi). \quad (2.58)$$

The autocovariance is not symmetric. The value of s_3 , *i.e.* the amount of circular polarization controls the odd contribution, whereas the remaining terms are all even. It therefore follows that the autocovariance function of a monochromatic bivariate signal is even if and only if the signal is linearly polarized, *i.e.* if $s_3 = 0$. The quaternion power spectral density $\Gamma_{xx}(\nu)$ is obtained by the QFT of $\gamma_{xx}(\tau)$ given in (2.57):

$$\Gamma_{xx}(\nu) = \frac{a^2}{4} (1 + \mathbf{i}s_3 + \mathbf{j}s_1 + \mathbf{k}s_2) \delta(\nu - \nu_0) + \frac{a^2}{4} (1 - \mathbf{i}s_3 + \mathbf{j}s_1 + \mathbf{k}s_2) \delta(\nu + \nu_0). \quad (2.59)$$

From the expression of normalized Stokes parameters above, the degree of polarization at frequency ν_0 is

$$\Phi(\nu_0) = \frac{|\mathcal{V}(\Gamma_{xx}(\nu_0))|}{\mathcal{S}(\Gamma_{xx}(\nu_0))} = \sqrt{s_1^2 + s_2^2 + s_3^2} = 1 \quad (2.60)$$

which highlights the fact that *a monochromatic bivariate signal with random phase is fully polarized*. The shape and orientation of the ellipse remain the same realization after realization. In fact, this could have already been intuited from the fact θ and χ are fixed for this example. However if at least one of these two angles is drawn at random in the model (2.56) it will in general yield a *partially polarized* monochromatic signal. See Appendix 2.C for an example of *unpolarized* monochromatic signal.

Bivariate white Gaussian noise White noise is ubiquitous in signal processing. The proposed framework enables an interesting description of bivariate white Gaussian noise (wGn) in terms of polarization properties. It also leads to new insights on the structure and simulation of bivariate wGn using the unpolarized-parts decomposition. This section uses discrete-time signals. This choice is motivated by the fact that continuous-time white Gaussian noise is much harder to define than discrete-time white Gaussian noise, which is merely a sequence of i.i.d. Gaussians random variables. See *e.g.* Holden et al. (2010, Chapter 2.1) for more on the construction of continuous-time white noise.

Let $w[n]$ denote the zero-mean discrete-time bivariate white Gaussian noise such that $w[n] = u[n] + \mathbf{i}v[n]$ where u and v are zero-mean real white Gaussian noises with covariances

$$R_{uu}[k] = \sigma_u^2 \delta_{k,0}; \quad R_{vv}[k] = \sigma_v^2 \delta_{k,0}; \quad R_{vu}[k] = \rho_{uv} \sigma_u \sigma_v \delta_{k,0}, \quad (2.61)$$

where $\rho_{uv} \in [-1, 1]$ is the correlation coefficient between u and v . The autocovariance of w is obtained using (2.25):

$$\gamma_{ww}[k] = [\sigma_u^2 + \sigma_v^2 + \mathbf{j}(\sigma_u^2 - \sigma_v^2) + 2\mathbf{k}\rho_{uv}\sigma_u\sigma_v] \delta_{k,0}. \quad (2.62)$$

The spectral density is obtained by QFT:

$$\Gamma_{ww}(\nu) = \sigma_u^2 + \sigma_v^2 + \mathbf{j}(\sigma_u^2 - \sigma_v^2) + 2\mathbf{k}\rho_{uv}\sigma_u\sigma_v. \quad (2.63)$$

6. These are the normalized Stokes parameters for fully polarized signals, see Eqs (2.49) – (2.51).

Kronecker's delta function: $\delta_{k,0}$

$$\delta_{k,0} = \begin{cases} 1 & \text{if } k = 0 \\ 0 & \text{otherwise} \end{cases}$$

This spectral density is constant. It has no i -component, so that $S_3(\mathbf{v}) = 0$ for all \mathbf{v} . As a consequence, a bivariate white Gaussian noise is either *unpolarized* or *linearly polarized* (fully or partially). The polarization properties are identical at all frequencies.

The degree of polarization defined by (2.44) is:

$$\Phi_w = \frac{\sqrt{(\sigma_u^2 - \sigma_v^2)^2 + 4\rho_{uv}^2\sigma_u^2\sigma_v^2}}{\sigma_u^2 + \sigma_v^2}, \quad (2.64)$$

where we see that $w[n]$ is unpolarized at all frequencies if and only if $\sigma_u = \sigma_v$ and $\rho_{uv} = 0$. In this case, $w[n]$ corresponds to proper or second-order circular white noise, see e.g. Picinbono and Bondon (1997) and also Section 0.2.2. When $\Phi_w \neq 0$, the angle θ_w of the linear polarization is given by $\theta_w = 0$ if $\rho_{uv} = 0$ and by

$$\theta_w = \begin{cases} \frac{1}{2} \operatorname{atan2} \left[\frac{2\rho_{uv}\sigma_u\sigma_v}{(\sigma_u^2 - \sigma_v^2)} \right] & \text{if } \sigma_u \neq \sigma_v \\ \frac{\pi}{4} & \text{if } \sigma_u = \sigma_v \end{cases} \quad (2.65)$$

when $\rho_{uv} \neq 0$ and where $\operatorname{atan2}$ denotes the four-quadrant inverse tangent.

Fig. 2.7 depicts the evolution of the degree of polarization Φ_w (2.64) and linear polarization angle θ_w (2.65) with the ratio σ_u/σ_v for several values of ρ_{uv} . The degree of polarization is minimum when $\sigma_u = \sigma_v$, and increases together with the imbalance between σ_u and σ_v . The minimum value of the degree of polarization is fixed by ρ_{uv} , and increases as $|\rho_{uv}| \rightarrow 1$. When $|\rho_{uv}| = 1$, the degree of polarization is always equal to one. The polarization angle evolves from $\theta_w = \pi/2$ for $\sigma_u/\sigma_v \rightarrow 0$ to $\theta_w = 0$ for $\sigma_u/\sigma_v \rightarrow \infty$ for strictly positive values of ρ_{uv} . For strictly negative values of ρ_{uv} the evolution is symmetric about the σ_u/σ_v -axis. The absolute value of ρ_{uv} controls the sharpness of the transition. For $\rho_{uv} = 0$, $\theta_w = 0$ everywhere.

The decomposition (2.46) of the quaternion power spectral density in unpolarized and polarized parts provides a simple procedure to simulate bivariate white Gaussian noise with desired polarization properties. Let $0 \leq \Phi_w \leq 1$ be the desired degree of polarization, $\theta_w \in [-\pi/2, \pi/2]$ the linear polarization angle and $S_0 > 0$ the total power or variance. Let $w^u[n]$ be a \mathbb{C}_i -valued unpolarized white Gaussian noise with unit variance, i.e. such that $R_{w^u w^u}[k] = \delta_{k,0}$. Let $w^p[n]$ be a real-valued white Gaussian noise with unit variance. Assume further that $w^u[n]$ and $w^p[n]$ are independent. Then the bivariate white Gaussian noise $w[n]$ constructed as

$$w[n] = \sqrt{1 - \Phi_w} \sqrt{S_0} w^u[t] + \sqrt{\Phi_w} \sqrt{S_0} e^{i\theta_w} w^p[t] \quad (2.66)$$

has spectral density

$$\Gamma_{ww}(\mathbf{v}) = S_0 [1 + \Phi_w (j \cos 2\theta_w + k \sin 2\theta_w)]. \quad (2.67)$$

Identifying (2.67) with (2.47), one recognizes a linear polarization state corresponding to spherical coordinates $(\Phi_w, 2\theta_w, 0)$ in the Poincaré sphere representation, see Fig. 2.5. Fig. 2.8 illustrates this synthesis procedure.

Fractional Gaussian noise, time-reversibility of Gaussian processes. The quaternion PSD and its straightforward interpretation in terms of meaningful physical parameters permit new insights and an original characterization of more

Alternatively, one can define the notion of bivariate white noise as a signal having a constant quaternion PSD. Symmetry condition (2.23) shows that i -component should be an odd function of \mathbf{v} . Therefore to have a constant quaternion PSD, this i -component has to be zero.

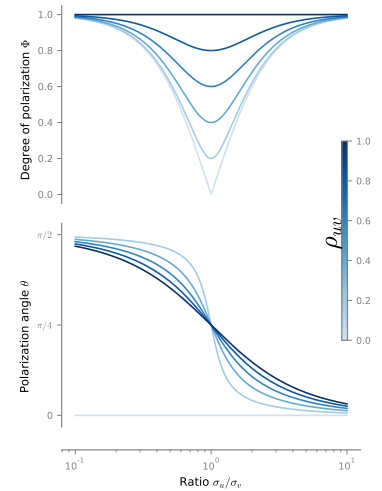


Figure 2.7: Evolution of the degree of polarization and polarization angle of bivariate white noise with ratio σ_u/σ_v for different values of $\rho_{uv} = 0, 0.2, 0.4, 0.6, 0.8, 1$. Negative values of ρ_{uv} are omitted: $\Phi_w(-\rho_{uv}) = \Phi_w(\rho_{uv})$ and $\theta_w(-\rho_{uv}) = -\theta_w(\rho_{uv})$.

The polarization state of a bivariate wGn thus always lies in the *equatorial* plane of the Poincaré sphere.

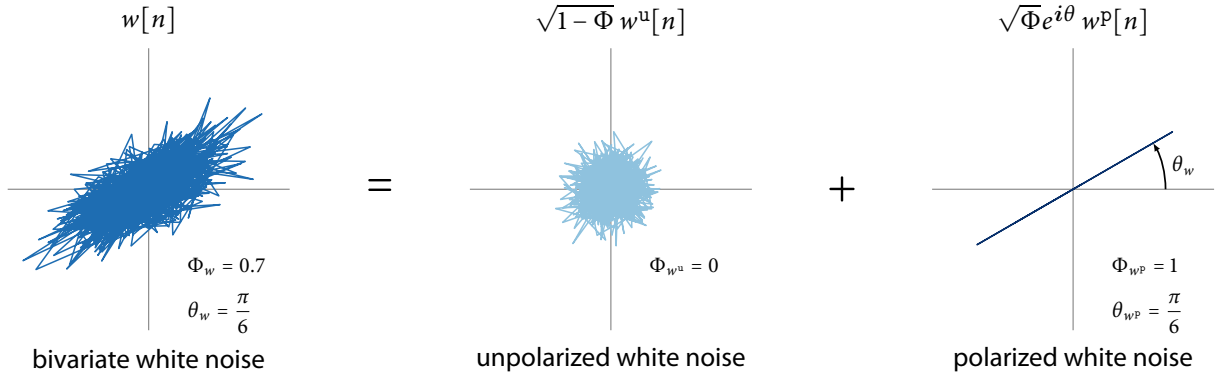


Figure 2.8: Simulation of bivariate white Gaussian noise with prescribed degree of polarization $\Phi_w = 0.7$ and linear polarization angle $\theta_w = \pi/6$. Bivariate white Gaussian noise is synthesized using the unpolarized - polarized parts decomposition (2.66).

sophisticated random bivariate signals. For instance, Lefèvre, Le Bihan, and Amblard (2018) have recently demonstrated the relevance of Stokes parameters for the geometric characterization of bivariate fractional Gaussian noise (fGn). Based on fGn covariances functions developed in Amblard et al. (2012), the explicit expression of the quaternion PSD can be derived. This provides new indications of the correlation structure in the spectral domain. In addition, Lefèvre, Le Bihan, and Amblard (2018) proposed to simulate bivariate fGn as a sum of unpolarized and polarized fGn. This shows the generality and usefulness of the unpolarized-polarized parts decomposition (2.46) for the synthesis of arbitrary random bivariate signals.

Lefèvre, Le Bihan, and Amblard (2018) show as well that Stokes parameters enable an elegant characterization of the time-reversibility of Gaussian bivariate signals. Such a signal x is time-reversible when changing the time t into $-t$ does not affect its statistical properties. This important invariance property is easily formulated in the proposed framework: a Gaussian bivariate signal is reversible iff it is linearly polarized at all frequencies, *i.e.* $S_3(\nu) = 0$ for every frequency ν . These findings highlight the potential of the proposed framework towards the generic study of random bivariate processes.

2.4 NONPARAMETRIC SPECTRAL ESTIMATION

The aim of this section is to show that the quaternion power spectral density (2.20) can be estimated using conventional nonparametric spectral estimators. The adaptation of usual tools such as the *periodogram* or the *multitaper* estimates to the quaternion Fourier transform setting presents no particular difficulty. Moreover, we put the emphasis on the statistical properties of the estimators of the degree of polarization and natural ellipse parameters. We note that the presentation of these results involves some unavoidable technicalities.

Throughout this section only discrete-time stationary random bivariate signals are considered. The time sampling size is Δ_t , so that the n^{th} sample corresponds to $t = (n - 1)\Delta_t$, and the signal is assumed to be zero-mean. We also assume that its quaternion power spectral density Γ_{xx} is a continuous function of the frequency ν . We consider a realization $x[1], x[2], \dots, x[N]$ of length N of such a signal.

2.4.1 Conventional spectral estimators

First the estimation of the quaternion spectral density Γ_{xx} given the realization $x[1], x[2], \dots, x[N]$ of a random signal x is considered.

Polarization periodogram This naive quaternion spectral density estimator is derived using the same technique as the usual periodogram (Percival and Walden, 1993). One starts by computing an estimator $\hat{\gamma}_{xx}^{(p)}[k]$ of the quaternion autocovariance sequence $\gamma_{xx}[k]$. Using (2.25), such an estimator is obtained by combining usual estimators of autocovariances and cross-covariances

$$\hat{R}_{uu}^{(p)}[k] \triangleq \begin{cases} \frac{1}{N} \sum_{n=1}^{N-|k|} u[n]u[n+|k|] & |k| < N \\ 0 & |k| \geq N \end{cases}, \quad (2.68)$$

The estimator $\hat{R}_{vv}^{(p)}[k]$ is defined similarly. The cross-covariance estimator is

$$\hat{R}_{vu}^{(p)}[k] = \frac{1}{N} \sum_{n=1}^{N-k} v[n+k]u[n], \quad 0 \leq k < N \quad (2.69)$$

where $\hat{R}_{vu}^{(p)}[k] = \hat{R}_{uv}^{(p)}[-k]$ for $k = -1, \dots, -(N-1)$ and $\hat{R}_{vu}^{(p)}[k] = 0$ for $|k| \geq N$. Then combining these estimators according to (2.25) yields the quaternion autocovariance estimate $\hat{\gamma}_{xx}^{(p)}[k]$:

$$\hat{\gamma}_{xx}^{(p)}[k] = \hat{R}_{uu}^{(p)}[k] + \hat{R}_{vv}^{(p)}[k] + \mathbf{j}(\hat{R}_{uu}^{(p)}[k] - \hat{R}_{vv}^{(p)}[k]) + 2\mathbf{k}\hat{R}_{vu}^{(p)}[k] \quad (2.70)$$

The quaternion Fourier transform of the autocovariance estimate (2.70) reads

$$\hat{\Gamma}_{xx}^{(p)}(\mathbf{v}) = \frac{\Delta_t}{N} \left| \sum_{n=1}^N x[n]e^{-j2\pi v n \Delta_t} \right|^2 + \frac{\Delta_t}{N} \left(\sum_{n=1}^N x[n]e^{-j2\pi v n \Delta_t} \right) \mathbf{j} \left(\sum_{n=1}^N x[n]e^{-j2\pi v n \Delta_t} \right) \quad (2.71)$$

We call $\hat{\Gamma}_{xx}^{(p)}(\mathbf{v})$ the *polarization periodogram* of the realization $x[1], x[2], \dots, x[N]$ by analogy with the usual periodogram. It shares many of its statistical properties.

The polarization periodogram is a biased and inconsistent estimator of the quaternion power spectral density. More precisely,

$$\mathbf{E} \left\{ \hat{\Gamma}_{xx}^{(p)}(\mathbf{v}) \right\} = \int_{-v_{\mathcal{N}}}^{+v_{\mathcal{N}}} \mathcal{F}_N(\mathbf{v} - \mathbf{v}') \Gamma_{xx}(\mathbf{v}') d\mathbf{v}' \quad (2.72)$$

where $\mathcal{F}_N(\cdot)$ is known as Fejér's kernel:

$$\mathcal{F}_N(\mathbf{v}) = \frac{\Delta_t \sin^2(\pi N \mathbf{v} \Delta_t)}{N \sin^2(\pi \mathbf{v} \Delta_t)} \quad (2.73)$$

This kernel has large sidelobes, as seen in Fig. 2.9. Fejér's kernel behaves as a Dirac delta function as $N \rightarrow \infty$ (Percival and Walden, 1993). Since $\Gamma_{xx}(\mathbf{v})$ is a continuous function of \mathbf{v} , then

$$\lim_{N \rightarrow \infty} \mathbf{E} \left\{ \hat{\Gamma}_{xx}^{(p)}(\mathbf{v}) \right\} = \Gamma_{xx}(\mathbf{v}) \quad (2.74)$$

meaning that the polarization periodogram is an asymptotically unbiased estimator of the quaternion power spectral density.

For bivariate white Gaussian noise, the quaternion power spectral density is constant. Therefore, the polarization periodogram of white Gaussian noise

Estimators $\hat{R}_{uu}^{(p)}[k], \hat{R}_{uu}^{(p)}[k], \hat{R}_{uu}^{(p)}[k]$ are usual *biased* estimators of autocovariances and crosscovariance. The choice of these *biased* estimates over *unbiased* estimates is discussed in detail by Priestley (1981, Section 5.3).

$v_{\mathcal{N}} = \frac{1}{2\Delta_t}$ is the Nyquist frequency.

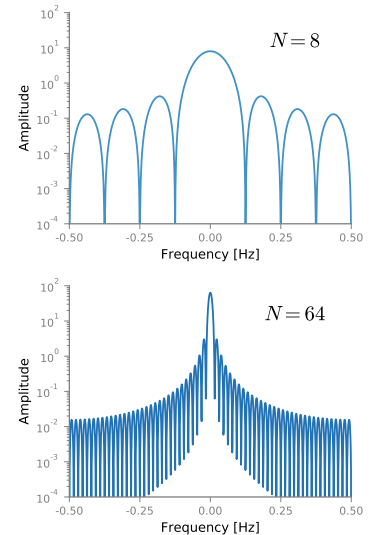


Figure 2.9: Fejér's kernel for $\Delta_t = 1$ and $N = 8$ (top) and $N = 64$ (bottom).

is unbiased for any N . This is a bivariate counterpart of a classical result, see *e.g.* Percival and Walden (1993, p. 202).

Just like in the spectral analysis of univariate signals, data tapers can be employed to produce direct spectral estimators with better bias properties than the naive polarization periodogram. In a nutshell, given a real-valued sequence $h[1], h[2], \dots, h[N]$, one can construct a *direct* spectral estimator $\hat{\Gamma}_{xx}^{(d)}$ such that

$$\hat{\Gamma}_{xx}^{(d)}(\nu) = \Delta_t \left| \sum_{n=1}^N h[n]x[n]e^{-j2\pi\nu n\Delta_t} \right|^2 + \Delta_t \left(\sum_{n=1}^N h[n]x[n]e^{-j2\pi\nu n\Delta_t} \right) \mathbf{j} \left(\overline{\sum_{n=1}^N h[n]x[n]e^{-j2\pi\nu n\Delta_t}} \right) \quad (2.75)$$

The window h is called a *data taper* and permits to reduce bias. The derivation of the statistical properties of direct spectral estimators (2.75) follows from standard spectral analysis (Percival and Walden, 1993). As a consequence, we shall not dwell much further into this topic here.

Multitaper estimates The multitaper approach was first proposed by Thomson (1982). It is a well established spectral estimation method (Percival and Walden, 1993; Walden, 2000) that allows to design spectral density estimates with controlled bias-variance tradeoff. The basic idea is to compute a series of M *direct estimators* $\hat{\Gamma}_{xx}^m(\nu)$, $m = 1, \dots, M$ that are approximately uncorrelated (Percival and Walden, 1993) and to average them out to obtain the multitaper estimate. The m^{th} spectral estimator reads

$$\hat{\Gamma}_{xx}^m(\nu) = \Delta_t \left| \sum_{n=1}^N h_m[n]x[n]e^{-j2\pi\nu n\Delta_t} \right|^2 + \Delta_t \left(\sum_{n=1}^N h_m[n]x[n]e^{-j2\pi\nu n\Delta_t} \right) \mathbf{j} \left(\overline{\sum_{n=1}^N h_m[n]x[n]e^{-j2\pi\nu n\Delta_t}} \right) \quad (2.76)$$

where the h_m 's are orthonormal real-valued sequences of length N :

$$\sum_{n=1}^N h_m[n]^2 = 1 \quad \text{and} \quad \sum_{n=1}^N h_m[n]h_{m'}[n] = \delta_{m,m'}. \quad (2.77)$$

The multitaper estimate is obtained by averaging:

$$\hat{\Gamma}_{xx}^{(\text{mt})}(\nu) = \frac{1}{M} \sum_{m=1}^M \hat{\Gamma}_{xx}^m(\nu). \quad (2.78)$$

This is the simplest form of average, although other choices are possible. See *e.g.* Thomson (1982) and Percival and Walden (1993, Section 7.4).

The expected value of the multitaper estimate $\hat{\Gamma}_{xx}^{(\text{mt})}$ is written as

$$\mathbf{E} \left\{ \hat{\Gamma}_{xx}^{(\text{mt})}(\nu) \right\} = \int_{-\nu_{\mathcal{N}}}^{+\nu_{\mathcal{N}}} \mathcal{H}^{(\text{mt})}(\nu - \nu') \Gamma_{xx}(\nu') d\nu' \quad (2.79)$$

where the *spectral window* $\mathcal{H}^{(\text{mt})}$ is

$$\mathcal{H}^{(\text{mt})}(\nu) = \frac{1}{M} \sum_{m=1}^M \mathcal{H}_m(\nu), \quad \mathcal{H}_m(\nu) = \Delta_t \left| \sum_{n=1}^N h_m[n]e^{-j2\pi\nu n\Delta_t} \right|^2. \quad (2.80)$$

By an appropriate choice of the sequences h_m one is able to control the bias properties of the multitaper estimate. For instance, to minimize *broad-band bias*, *i.e.* bias introduced by sidelobes of $\mathcal{H}^{(\text{mt})}$, then the h_m 's are chosen to be Slepian tapers (Slepian, 1978). These are also known as discrete prolate spheroidal sequences (DPSS) and concentrate their energy in a given frequency band $[-W, W]$, see Fig. 2.10 for an example. Moreover as explained in Percival and Walden (1993), if the spectral estimators $\hat{\Gamma}_{xx}^m$ have common variance and

The choice of the class of data tapers depends on the type of bias one wants to address. *E.g.* to minimize *local bias* or smoothing bias, sine tapers are to be used (Riedel and Sidorenko, 1995) instead of Slepian tapers.

are pairwise uncorrelated⁷ then the variance of $\hat{\Gamma}_{xx}^{(mt)}$ is smaller than that of $\hat{\Gamma}_{xx}^m$ by a factor $1/M$.

Let us finally detail the choice of the number of tapers M . Given a resolution bandwidth $2W$ corresponding to frequency band $[-W, W]$, the number of Slepian tapers we use is $M = 2NW\Delta_t - 1$ (Walden, 2000). In practice, the *bandwidth-duration product* $2NW\Delta_t$ is typically chosen between $2NW\Delta_t = 2$ and $2NW\Delta_t = 10$ leading to $M \leq 10$ tapers.

To summarize, usual practice and tradeoffs from univariate spectral analysis apply to the nonparametric estimation of the quaternion power spectral density. We now consider the more complicated problem of the estimation of polarization parameters from realizations of a stationary random bivariate signal.

2.4.2 Estimation of polarization parameters

One of the specificities of the bivariate case is that polarization features – which are relevant physical parameters – need to be estimated. This estimation requires some specific effort. One is interested in the decomposition (2.47) of the quaternion power spectral density into its scalar and vector parts:

$$\Gamma_{xx}(\nu) = S_0(\nu) + S_0(\nu)\Phi_x(\nu)\boldsymbol{\mu}_x(\nu). \quad (2.81)$$

This decomposition is of considerable importance, since it directly gives the description of (i) the frequency distribution $S_0(\nu)$ of the total⁸ power of the signal x and (ii) the dependence of polarization properties on frequency ν .

In the following, we investigate the problem of the estimation for a given frequency ν of the degree of polarization $\Phi_x(\nu)$ and to a lesser extent, the estimation of the polarization axis $\boldsymbol{\mu}_x(\nu)$. For simplicity, we consider a situation where nonparametric spectral estimators are unbiased. Such a situation arises when the length N of the recorded sequence tends to infinity.

Degree of polarization The estimation of the degree of polarization (2.44) has attracted interest in the signal processing community (Medkour and Walden, 2008; Santalla del Rio et al., 2006) in relation to many fields (Kikuchi, 2001; Shirvany, Chabert, and Tourneret, 2012). The degree of polarization $\Phi_x(\nu)$ is defined (2.44) as a ratio of statistical averages. Thus remark that a naive estimator based upon the polarization periodogram (2.71) or the direct spectral estimate (2.75) would be trivial since:

$$\hat{\Phi}_x^{(e)}(\nu) = \frac{|\mathcal{V}(\hat{\Gamma}_{xx}^{(e)}(\nu))|}{\mathcal{S}(\hat{\Gamma}_{xx}^{(e)}(\nu))} = 1, \quad \text{where } e = p \text{ or } d \quad (2.82)$$

which is systematically biased, except for frequencies where the signal x is fully polarized. To overcome this issue we must consider a situation where M approximately uncorrelated estimates of the spectral density are available – having multiple realizations of x or using a multitaper estimate (2.78). Then one can form a new estimate of the degree of polarization as

$$\hat{\Phi}_x^M(\nu) = \frac{|\sum_{m=1}^M \mathcal{V}(\hat{\Gamma}_{xx}^m(\nu))|}{\sum_{m=1}^M \mathcal{S}(\hat{\Gamma}_{xx}^m(\nu))}, \quad (2.83)$$

7. Approximate uncorrelatedness of the m -direct spectral estimators Γ_{xx}^m follows from the orthogonality of sequences (2.77) under some regularity conditions on $\Gamma_{xx}(\nu)$, namely $\Gamma_{xx}(\nu)$ should not vary too rapidly over the interval $[\nu - W, \nu + W]$ (Percival and Walden, 1993, Section 7.3).

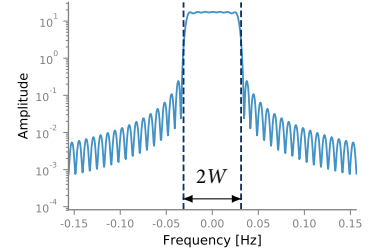


Figure 2.10: Multitaper spectral window $\mathcal{H}^{(mt)}(\nu)$ for $N = 1024$, $NW = 4$ and $\Delta_t = 1$ corresponding to $K = 7$ Slepian tapers. Note that $\mathcal{H}^{(mt)}(\nu)$ is approximately constant over the selected bandwidth interval $[-W, W]$ with $W = 1/32$.

8. *i.e.* the sum of the power of *unpolarized* and *polarized* parts.

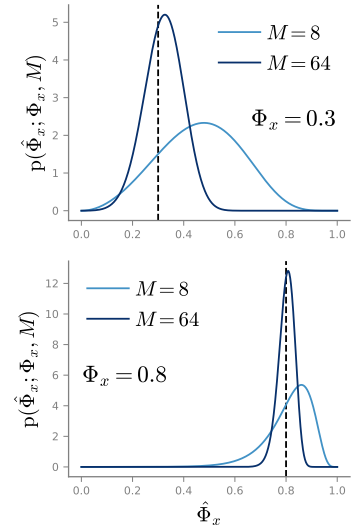


Figure 2.11: The pdf (2.84) for $M = 8$ and $M = 64$ independent realizations and for two values of the true degree of polarization $\Phi_x = 0.3$ and $\Phi_x = 0.8$ – indicated by dashed black lines (– –).

which is a better estimator of $\Phi_x(\mathbf{v})$ than (2.82). Santalla del Rio et al. (2006) and Medkour and Walden (2008) have studied theoretically this estimator for the case of Gaussian signals. We recall here some of their results.

Let us drop the frequency dependence for notational simplicity and remove the superscript M to avoid confusion with exponentiation. The probability density function (pdf) for the estimated degree of polarization $\hat{\Phi}_x$ obtained by (2.83) using M independent realizations of a Gaussian signal is (Santalla del Rio et al., 2006; Medkour and Walden, 2008)

$$p(\hat{\Phi}_x; \Phi_x, M) = \frac{4^{1-M} (1 - \Phi_x^2)^M \hat{\Phi}_x (1 - \hat{\Phi}_x^2)^{M-2}}{\mathcal{B}(M, M-1) \Phi_x} \left[(1 - \hat{\Phi}_x \Phi_x)^{1-2M} - (1 + \hat{\Phi}_x \Phi_x)^{1-2M} \right] \quad (2.84)$$

with $\mathcal{B}(a, b)$ the Beta function. Fig. 2.11 depicts this pdf for $M = 8$ and $M = 64$ independent realizations and for two values of the true degree of polarization $\Phi_x = 0.3$ and $\Phi_x = 0.8$. The variance is majored for $\Phi_x \rightarrow 0$ and decreases as M increases.

The bias $\mathbf{E}\{\hat{\Phi}_x\} - \Phi_x$ can be directly computed from the pdf (2.84). Expressions are rather involved and can be found in Medkour and Walden (2008). Fig. 2.12 shows the bias of this estimator as a function of the true degree of polarization for increasing values of $M = 1, 5, 10$ and 100 . Results are obtained by numerical integration of the pdf (2.84). Given M , the bias increases as the true degree of polarization goes to zero. The bias decreases with larger values of M . It becomes negligible for $M \rightarrow \infty$, meaning that $\hat{\Phi}_x$ is asymptotically (w.r.t. M) unbiased. Note that for typical values of M (2 to 10) used in multitaper estimation, the bias remains significant up to $\Phi_x \simeq 0.6$.

Polarization axis The estimation of the polarization axis $\boldsymbol{\mu}_x$ involves the estimation of the natural ellipse parameters θ, χ or, equivalently, the normalized Stokes parameters s_1, s_2, s_3 . These two equivalent estimation problems have been already studied in detail in the literature. We briefly survey these results and, for the sake of brevity, we omit a complete treatment of these estimation problems.

Results available in the literature focus on Gaussian signals. Regarding the estimation of natural ellipse parameters, pdfs of the orientation θ and the *aspect ratio* $\varepsilon = \tan \chi$ were derived by Walden and Medkour (2007) and Rubin-Delanchy and Walden (2008). Similar results were obtained by Barakat (1985) in the context of optics. Statistics of normalized Stokes parameters have been studied by Brosseau (1995) and detailed statistics for s_3 such as bias or confidence interval were obtained by Chandna and Walden (2011). Remark that the third normalized Stokes parameter s_3 is also known as the *rotary coefficient* to oceanographers. In a nutshell, distributions tend to spread as the degree of polarization tends to zero. This makes the estimation of the polarization axis particularly difficult for bivariate signals with low degree of polarization. One can however expect to mitigate this issue by averaging out multiple uncorrelated spectral estimates to reduce bias and variance.

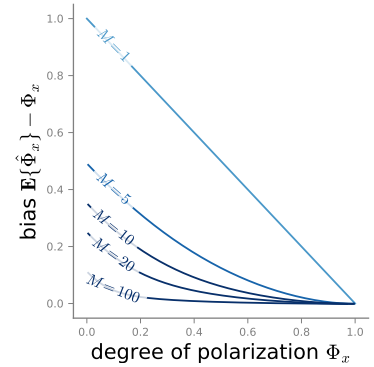


Figure 2.12: Bias in the estimation of the degree of polarization. The bias decreases as M increases and $\Phi_x \rightarrow 1$.

2.4.3 Illustration

To conclude this chapter, we consider the problem of the estimation of the quaternion power spectral density of a narrow-band signal x corrupted by

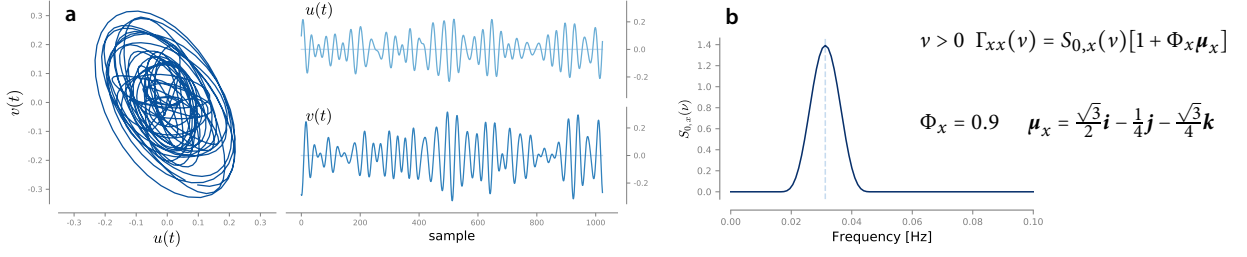


Figure 2.13: (a) Realization of a stationary narrow-band partially elliptically polarized signal x . (b) Corresponding spectral profile $S_{0,x}(v)$ and polarization parameters ($\Phi_x = 0.9$, $\theta_x = 2\pi/3$, $\chi_x = \pi/6$).

bivariate white Gaussian noise w . Observations are constructed as $y = x + w$ where x is a zero-mean stationary narrow-band bivariate signal with constant polarization features. Fig. 2.13a depicts a realization of this signal. The length of the realization is $N = 1024$, and the time-sampling step $\Delta_t = 1$. The quaternion PSD of this signal x is

$$\forall v > 0, \quad \Gamma_{xx}(v) = S_{0,x}(v) + S_{0,x}(v)\Phi_x\mu_x \quad (2.85)$$

Negative frequencies are obtained by symmetry (2.23). Fig. 2.13 shows the total power spectral density $S_{0,x}(v)$ and polarization parameters of x . This signal is chosen to have a high degree of polarization $\Phi_x = 0.9$ and with fixed elliptical polarization parameters $\theta_x = 2\pi/3$ and $\chi_x = \pi/6$. The resulting polarization axis is $\mu_x = \frac{\sqrt{3}}{2}\mathbf{i} - \frac{1}{4}\mathbf{j} - \frac{\sqrt{3}}{4}\mathbf{k}$.

The bivariate white Gaussian noise w has quaternion power spectral density

$$\Gamma_{ww}(v) = S_{0,w} + \Phi_w S_{0,w} [\cos 2\theta_w \mathbf{j} + \sin 2\theta_w \mathbf{k}]. \quad (2.86)$$

We consider a degree of polarization $\Phi_w = 0.4$ and a linear polarization angle $\theta_w = 0$ so that w exhibit partial linear horizontal polarization.

Since we assume x and w uncorrelated, plugging (2.35) into (2.36) one gets the quaternion power spectral density of the observations y

$$\forall v > 0, \quad \Gamma_{yy}(v) = \Gamma_{xx}(v) + \Gamma_{ww}(v) \quad (2.87)$$

$$= S_{0,y}(v) + S_{0,y}(v)\Phi_y\mu_y(v) \quad (2.88)$$

where

$$S_{0,y}(v) = S_{0,x}(v) + S_{0,w} \quad \text{and} \quad \Phi_y(v)\mu_y(v) = \frac{S_{0,x}(v)\Phi_x\mu_x + S_{0,w}\Phi_w\mu_w}{S_{0,x}(v) + S_{0,w}}. \quad (2.89)$$

The polarization properties of y depend on the frequency v due to the interaction between second-order properties of x and w . In particular it shows that in the frequency band related to x , the polarization axis of y is not equal to the polarization axis of x . Since the noise w is polarized, it corrupts also the observed polarization properties. This effect is majored for strongly polarized noise and small values of signal-to-noise ratio.

Fig. 2.14 investigates the spectral estimation of the quaternion power spectral density Γ_{yy} . We simulate $K = 20$ independent realizations of the process y . Then for each realization we compute its polarization periodogram and a multitaper estimate with bandwidth parameter $NW = 4$. Then to reduce bias we compute an averaged polarization periodogram and an averaged multitaper estimate. As expected the averaged multitaper estimates exhibits less variance

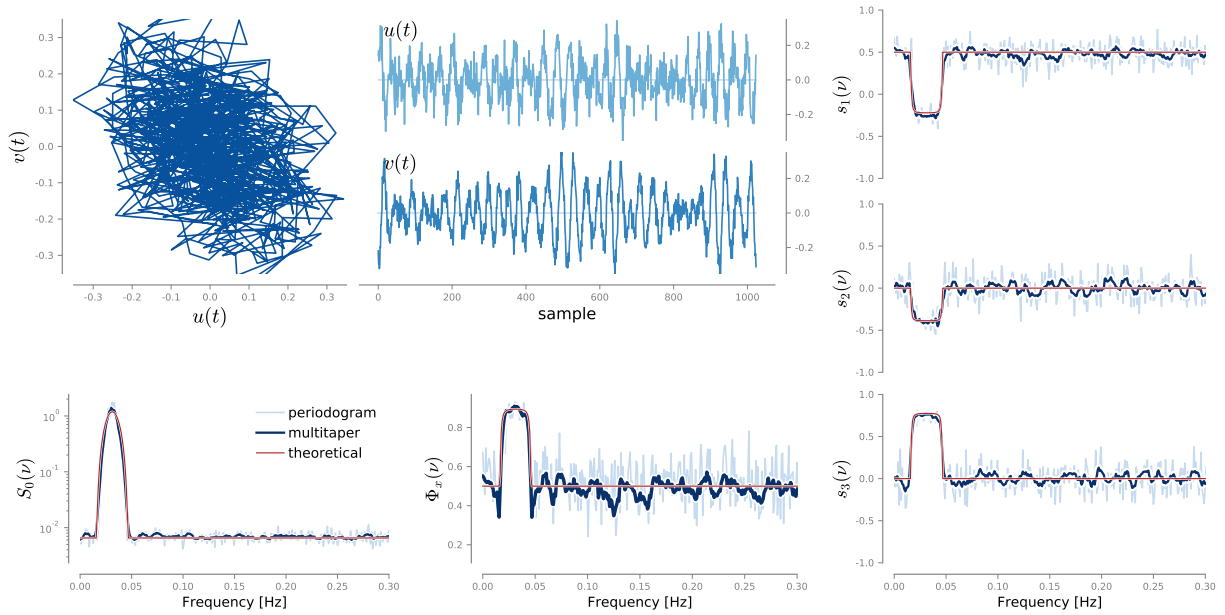


Figure 2.14: Nonparametric spectral density estimation of the signal $y = x + w$ where x is a narrow-band bivariate signal and w is a bivariate white Gaussian noise. Averaged polarization periodogram and averaged multitaper estimate (computed with $M = 9$ Slepian tapers) are shown. They are constructed by averaging single estimates obtained via $K = 20$ independent observations of the process y . Red lines indicate theoretical values.

and better bias properties than the average polarization periodogram. Results indicate a good agreement with theoretical values and show that spectral estimates have limited bias. Frequencies $0.3 < \nu \leq 0.5$ Hz have not been displayed to enhance the visualization.

2.5 CONCLUSION

This chapter has introduced a powerful and relevant framework for an interpretable and efficient spectral analysis of bivariate signals. The richness of the quaternion algebra and the QFT properties permits the construction of physically meaningful quantities that remain mathematically valid and easy to compute. The quaternion power spectral density (PSD) of a stationary random bivariate signal is the cornerstone of the proposed approach. Its definition appears naturally from the quaternion-valued spectral representation of a stationary random bivariate signal (Theorem 2.1). It has a straightforward interpretation in terms of common tools of physicists, namely Stokes parameters and Poincaré sphere representation. It enables also a natural discrimination between energetic and polarization features thanks to the degree of polarization of a stationary random bivariate signal. Quantities related to the quaternion PSD (autocovariance, cross-correlation properties) are also defined to provide a complete and practical characterization of second-order stationary bivariate signals. Simple examples demonstrate the relevance of the approach. Nonparametric spectral density estimation of the quaternion PSD has been investigated and resembles the usual univariate case. The issue of the estimation of the degree of polarization and polarization attributes has been raised. The proposed framework can be used for the spectral analysis of deterministic or random bivariate signals, even though the estimation of polarization properties calls for some special care.

These new tools are made publicly available thanks to the companion Python package BiSPy. These findings have been published in an international journal (Flamant, Le Bihan, and Chainais, 2017c) and presented at a national conference (Flamant, Le Bihan, and Chainais, 2017a).

APPENDICES

2.A CIRCULARITY OF SPECTRAL INCREMENTS

Consider a continuous-time stationary random bivariate signal $x(t)$. If x is harmonizable, it has a quaternion spectral representation given by Theorem 2.1. Corresponding spectral increments $dX(\nu)$ form a collection of quaternion-valued random variables.

Usually, the description of the second-order statistics of a quaternion random variable q is carried by four moments, e.g.

$$\mathbf{E}\{|q|^2\}, \quad \mathbf{E}\{qi\bar{q}\}, \quad \mathbf{E}\{qj\bar{q}\}, \quad \mathbf{E}\{qk\bar{q}\}, \quad (2.90)$$

although any set of linearly independent moments are equally valid. Like for complex random variables, the second-order moments in (2.90) may satisfy some *invariance* or *symmetry* properties. This leads to the notion of *second-order circularity* or *properness* of quaternion random variables. This topic has been investigated by several authors (Vakhania, 1999; Amblard and Le Bihan, 2004; Vía, Ramírez, and Santamaría, 2010) and was reviewed recently by Le Bihan (2017).

Recall that the spectral increments of x satisfy the double orthogonality property

$$\forall \nu \neq \nu', \quad \mathbf{E}\{dX(\nu)\overline{dX(\nu')}\} = \mathbf{E}\{dX(\nu)\mathbf{j}\overline{dX(\nu')}\} = 0 \quad (2.91)$$

In addition, since x is \mathbb{C}_i -valued its spectral increments satisfy the *i*-Hermitian symmetry $dX(-\nu) = -\mathbf{i} dX(\nu)\mathbf{i}$. Plugging this symmetry into (2.91) for $\nu' = -\nu$ yields

$$\forall \nu, \quad \mathbf{E}\{dX(\nu)\mathbf{i}\overline{dX(\nu)}\} = \mathbf{E}\{dX(\nu)\mathbf{k}\overline{dX(\nu)}\} = 0 \quad (2.92)$$

It shows that the spectral increments are $(1, \mathbf{j})$ -proper in the denomination of Le Bihan (2017), also denoted as \mathbb{C}_j -properness by Amblard and Le Bihan (2004). If x is Gaussian, then following Le Bihan (2017) it means that for every frequency ν

$$dX(\nu) \stackrel{d}{=} dX(\nu)\mathbf{j} \quad (2.93)$$

that is spectral increments are invariant by *right isoclinic* rotations (Altmann, 2005) of axis \mathbf{j} and angle $\pi/2$. This result can be seen as a generalization of the properness of the complex-valued spectral increments of a real-valued stationary process (Picinbono, 1994).

The only nonzero second-order moments are $\mathbf{E}\{|dX(\nu)|^2\}$ and $\mathbf{E}\{dX(\nu)\mathbf{j}\overline{dX(\nu)}\}$, precisely those that appear in the definition of the quaternion power spectral density (2.20). It shows that with this definition, the quaternion power density contains the complete second-order structure of x .

Note that for a complex valued random variable z , the second-order statistics are given by

$$\mathbf{E}\{|z|^2\} \text{ and } \mathbf{E}\{z^2\}$$

See e.g. Picinbono and Bondon (1997).

The notation $\stackrel{d}{=}$ stands for equality in distribution

2.B EXPRESSIONS FOR THE QUATERNION POWER SPECTRAL DENSITY AND THE QUATERNION AUTOCOVARANCE

Let $x(t) = u(t) + \mathbf{i}v(t)$ be an harmonizable stationary random bivariate signal. Its spectral increments are $dX(\nu) = dU(\nu) + \mathbf{i}V(\nu)$. The quaternion power spectral density is defined by (2.20). It involves the following two moments which explicitly read

$$\mathbf{E} \{ |dX(v)|^2 \} = \mathbf{E} \{ |dU(v)|^2 \} + \mathbf{E} \{ |dV(v)|^2 \}, \quad (2.94)$$

$$\mathbf{E} \{ dX(v) \mathbf{j} \overline{dX(v)} \} = [\mathbf{E} \{ |dU(v)|^2 \} - \mathbf{E} \{ |dV(v)|^2 \}] \mathbf{j} + 2\mathbf{k} \mathbf{E} \{ dV(v) \overline{dU(v)} \}. \quad (2.95)$$

Now using P_{uu}, P_{vv} to denote the usual power spectral density of u and v respectively, and P_{vu} to denote the cross-power spectral density between v and u , one gets

$$\Gamma_{xx}(v) = P_{uu}(v) + P_{vv}(v) + \mathbf{j} [P_{uu}(v) - P_{vv}(v)] + 2\mathbf{k} P_{vu}(v). \quad (2.96)$$

The quaternion autocovariance is obtained by inverse quaternion Fourier transform of (2.96):

$$\gamma_{xx}(\tau) = R_{uu}(\tau) + R_{vv}(\tau) + \mathbf{j} [R_{uu}(\tau) - R_{vv}(\tau)] + 2\mathbf{k} R_{vu}(\tau). \quad (2.97)$$

Recall that

$$P_{uu}(v) dv = \mathbf{E} \{ |dU(v)|^2 \}$$

$$P_{vv}(v) dv = \mathbf{E} \{ |dV(v)|^2 \}$$

$$P_{vu}(v) dv = \mathbf{E} \{ dV(v) \overline{dU(v)} \}$$

Remark also that $\mathbf{k} P_{vu}(v) = \overline{P_{vu}(v)} \mathbf{k} = P_{uv}(v) \mathbf{k}$ since P_{vu} is \mathbb{C}_j -valued.

2.C UNPOLARIZED SIGNALS AND NON-GAUSSIANITY

Consider for simplicity a stationary unpolarized monochromatic signal $x(t)$. Consider a realization $x_k(t)$ of $x(t)$. The corresponding polarization ellipse can be characterized by a polarization axis, say $\boldsymbol{\mu}_k$, which can be represented as a point on the Poincaré sphere of unit radius \mathbb{S}^2 . For many realizations of $x(t)$ one thus obtains a *distribution* of polarization states on \mathbb{S}^2 . Since $x(t)$ is unpolarized – and if $x(t)$ has Gaussian statistics – this distribution is the uniform distribution on \mathbb{S}^2 , as illustrated in Fig. 2.4.

However with no assumption on the statistics of unpolarized monochromatic $x(t)$ the corresponding distribution of polarization states is not necessarily uniform on the Poincaré sphere of unit radius. In fact, Ellis and Dogariu (2004) give a sufficient condition which is that the corresponding pdf $p(\cdot)$ on \mathbb{S}^2 should have an equal probability of antipodal points, *i.e.* $p(-\boldsymbol{\mu}) = p(\boldsymbol{\mu})$. For instance, a monochromatic signal $x(t)$ with polarization axis $\boldsymbol{\mu}_x$ drawn either as $\boldsymbol{\mu}_0$ or $-\boldsymbol{\mu}_0$ with equal probability will be unpolarized.

This subtlety in the interpretation of *unpolarization* can be explained by noticing that the degree of polarization Φ_x only involves second-order moments of the spectral increments. Thus, for non-Gaussian signals $\Phi_x = 0$ does not entirely specifies the underlying pdf on \mathbb{S}^2 .

Example Let us consider a monochromatic bivariate signal $x(t)$ such that

$$x(t) = e^{i\theta} \cos(2\pi\nu_0 t + \varphi) \quad (2.98)$$

where $\varphi \sim \mathcal{U}([0, 2\pi])$ and θ are independent random variables. The probability density function for θ is denoted by $\pi(\cdot)$ and is left unspecified for now. For a given realization, this signal appears to be linearly polarized with linear polarization angle or orientation θ . However upon specific choices for $\pi(\cdot)$, this signal can be unpolarized.

The signal $x(t) = u(t) + i v(t)$ is second-order stationary due to the random phase φ . Covariances involving $u(t)$ and $v(t)$ are given by

$$R_{uu}(\tau) = \frac{1}{2} \mathbf{E}_\pi \{ \cos^2 \theta \} \cos 2\pi\nu_0 \tau \quad (2.99)$$

$$R_{vv}(\tau) = \frac{1}{2} \mathbf{E}_\pi \{ \sin^2 \theta \} \cos 2\pi\nu_0 \tau \quad (2.100)$$

$$R_{vu}(\tau) = \frac{1}{4} \mathbf{E}_\pi \{ \sin 2\theta \} \cos 2\pi\nu_0 \tau \quad (2.101)$$

The autocovariance function (2.25) reads:

$$\gamma_{xx}(\tau) = \frac{1}{2} [1 + \mathbf{j}\mathbf{E}_\pi \{\cos 2\theta\} + \mathbf{k}\mathbf{E}_\pi \{\sin 2\theta\}] \cos 2\pi\nu_0\tau \quad (2.102)$$

The quaternion power spectral density is obtained by quaternion Fourier transform

$$\Gamma_{xx}(\nu) = \frac{1}{4} [1 + \mathbf{j}\mathbf{E}_\pi \{\cos 2\theta\} + \mathbf{k}\mathbf{E}_\pi \{\sin 2\theta\}] [\delta(\nu - \nu_0) + \delta(\nu + \nu_0)] \quad (2.103)$$

The degree of polarization at frequencies $\pm\nu_0$ is thus

$$\Phi_x(\pm\nu_0) = \sqrt{(\mathbf{E}_\pi \{\cos 2\theta\})^2 + (\mathbf{E}_\pi \{\sin 2\theta\})^2} \quad (2.104)$$

Thus the signal $x(t)$ is unpolarized if and only if the two expectations appearing above are zero. This is the case *e.g.* when $\pi(\cdot) = \mathcal{U}([-\pi/2, \pi/2])$. The signal $x(t)$ is unpolarized, but is not Gaussian since it has a fixed amplitude $a = 1$ in (2.98). The distribution of polarizations states of each realization is the uniform distribution on the equator of the Poincaré sphere of unit radius.

Such distribution is referred to as *Type-II unpolarized light* in Ellis and Dogariu (2004).

2.D PROOFS

2.D.1 Proof of the spectral representation Theorem 2.1

Let $x(t) = u(t) + \mathbf{i}v(t)$ a continuous-time random stationary bivariate signal in the sense of Definition 2.1. We assume that x has zero-mean. The proof is divided in two parts. We first state under which conditions the random bivariate signal x admits the spectral representation (2.15). Then we study the properties of its spectral increments.

Existence of the spectral representation Let $x(t) = u(t) + \mathbf{i}v(t)$ a continuous-time random stationary bivariate signal. Suppose that $u(t)$ and $v(t)$ are harmonizable (Loeve, 1978; Blanc-Lapierre and Fortet, 1953). These real processes admit a spectral representation, such that

$$\begin{aligned} u(t) &\stackrel{\text{m.s.}}{=} \int_{-\infty}^{+\infty} dU(\nu) \exp(\mathbf{j}2\pi\nu t), \\ v(t) &\stackrel{\text{m.s.}}{=} \int_{-\infty}^{+\infty} dV(\nu) \exp(\mathbf{j}2\pi\nu t), \end{aligned} \quad (2.105)$$

where dU, dV are the \mathbb{C}_j -valued spectral increments of u and v respectively.

Lemma 2.1 (Existence of the spectral representation). *Let u and v be harmonizable with spectral increments dU and dV . Define the quaternion-valued spectral increment process $dX(\nu) = dU(\nu) + \mathbf{i}dV(\nu)$. Then for all t ,*

$$x(t) \stackrel{\text{m.s.}}{=} \int_{-\infty}^{+\infty} dX(\nu) e^{j2\pi\nu t} \quad (2.106)$$

and we say that x is harmonizable.

Proof. If u and v are harmonizable, then for all t

$$\mathbf{E} \left\{ \left| u(t) - \int_{-\infty}^{+\infty} dU(\nu) e^{j2\pi\nu t} \right|^2 \right\} = 0, \quad (2.107)$$

$$\mathbf{E} \left\{ \left| v(t) - \int_{-\infty}^{+\infty} dV(\nu) e^{j2\pi\nu t} \right|^2 \right\} = 0. \quad (2.108)$$

Mean square (m.s.) equality

$$x \stackrel{\text{m.s.}}{=} y \Leftrightarrow \mathbf{E} \{|x - y|^2\} = 0$$

Now one has directly for all t

$$\mathbf{E} \left\{ \left| x(t) - \int_{-\infty}^{+\infty} dX(\nu) e^{j2\pi\nu t} \right|^2 \right\} \quad (2.109)$$

$$= \mathbf{E} \left\{ \left| u(t) - \int_{-\infty}^{+\infty} dU(\nu) e^{j2\pi\nu t} \right|^2 \right\} \quad (2.110)$$

$$+ \mathbf{E} \left\{ \left| v(t) - \int_{-\infty}^{+\infty} dV(\nu) e^{j2\pi\nu t} \right|^2 \right\} \quad (2.111)$$

$$= 0. \quad (2.112)$$

□

Properties of the spectral increments The approach below follows from Priestley (1981). The properties of the spectral increments $dX(\nu)$ are a direct consequence of the properties of the spectral increments of u and v , respectively. Since x is assumed zero-mean and stationary,

$$\forall t, \mathbf{E} \{x(t)\} = \int_{-\infty}^{+\infty} \mathbf{E} \{dX(\nu)\} e^{j2\pi\nu t} = 0 \quad (2.113)$$

which immediately yields

$$\forall \nu, \mathbf{E} \{dX(\nu)\} = \mathbf{E} \{x(t)\} = 0. \quad (2.114)$$

Turning to the second-order properties of the spectral increments, let us consider the spectral representation of u and v . Second-order stationarity implies that

$$\forall \nu \neq \nu', \begin{cases} \mathbf{E} \{dU(\nu) \overline{dU(\nu')}\} = 0 \\ \mathbf{E} \{dV(\nu) \overline{dV(\nu')}\} = 0 \end{cases} \quad (2.115)$$

and autocovariance functions of u and v read

$$\mathbf{E} \{u(t)u(t-\tau)\} = \int_{-\infty}^{+\infty} \mathbf{E} \{|dU(\nu)|^2\} e^{j2\pi\nu\tau}, \quad (2.116)$$

$$\mathbf{E} \{v(t)v(t-\tau)\} = \int_{-\infty}^{+\infty} \mathbf{E} \{|dV(\nu)|^2\} e^{j2\pi\nu\tau}. \quad (2.117)$$

To fully characterize the spectral increments of x , we also need the covariance between the spectral increments of u and v . Since u and v are jointly second-order stationary,

$$\forall \nu \neq \nu', \mathbf{E} \{dV(\nu) \overline{dU(\nu')}\} = 0, \quad (2.118)$$

and the cross-covariance function reads

$$\mathbf{E} \{v(t)u(t-\tau)\} = \int_{-\infty}^{+\infty} \mathbf{E} \{dV(\nu) \overline{dU(\nu)}\} e^{j2\pi\nu\tau}. \quad (2.119)$$

Using expressions from Appendix 2.B Eqs. (2.115) and (2.118) can be written directly in terms of spectral increments of x :

$$\forall \nu \neq \nu', \mathbf{E} \{dX(\nu) \overline{dX(\nu')}\} = 0, \quad (2.120)$$

$$\forall \nu \neq \nu', \mathbf{E} \{dX(\nu) j \overline{dX(\nu')}\} = 0. \quad (2.121)$$

When $\nu' = \nu$, the second-order properties are summarized by introducing the quaternion integrated spectrum $\Gamma_{xx}^{(I)}(\nu)$:

$$\mathbf{E} \{|dX(\nu)|^2\} + \mathbf{E} \{dX(\nu) j \overline{dX(\nu)}\} = d\Gamma_{xx}^{(I)}(\nu) \quad (2.122)$$

which separates in quaternion algebra the information contained in the two moments of the spectral increments. This theorem holds also for quaternion-valued stationary signals by simply adapting the proof.

2.D.2 Proof of Theorems 2.2 and 2.3

We give only a proof for Theorem 2.3. By taking $x = y$ one obtains the proof for 2.2. Let $x(t) = u_x(t) + \mathbf{i}v_x(t)$ and $y(t) = u_y(t) + \mathbf{i}v_y(t)$ be two continuous-time jointly stationary random bivariate signals. In order to prove (2.31) and (2.32), we compute each side of the equation separately and show that there are equal.

Start with the left-hand side of (2.31). We drop explicit frequency dependence for notational convenience. One has

$$\mathbf{E} \{dX d\bar{Y}\} = \mathbf{E} \{[dU_x + dV_x] [d\bar{U}_y - \mathbf{i}d\bar{V}_y]\} \quad (2.123)$$

$$= \mathbf{E} \{dU_x d\bar{U}_y\} + \mathbf{E} \{dV_y d\bar{V}_x\} \\ + \mathbf{i} [\mathbf{E} \{dV_x d\bar{U}_y\} - \mathbf{E} \{dV_y d\bar{U}_x\}] \quad (2.124)$$

$$= (P_{u_x u_y} + P_{v_y v_x} + \mathbf{i} [P_{v_x u_y} - P_{v_y u_x}]) d\mathbf{v} \quad (2.125)$$

For the right-hand side of (2.31) one gets

$$\int_{-\infty}^{+\infty} \mathbf{E} \{x(t) e^{-j2\pi\nu\tau} \overline{y(t-\tau)}\} d\tau \quad (2.126)$$

$$= \int_{-\infty}^{+\infty} \mathbf{E} \{(u_x(t) + \mathbf{i}v_x(t)) e^{-j2\pi\nu\tau} (u_y(t-\tau) - \mathbf{i}v_y(t-\tau))\} d\tau \quad (2.127)$$

$$= \int_{-\infty}^{+\infty} R_{u_x u_y}(\tau) e^{-j2\pi\nu\tau} d\tau + \int_{-\infty}^{+\infty} R_{v_x v_y}(\tau) e^{j2\pi\nu\tau} d\tau \\ + \mathbf{i} \int_{-\infty}^{+\infty} R_{v_x u_y}(\tau) e^{-j2\pi\nu\tau} d\tau - \mathbf{i} \int_{-\infty}^{+\infty} R_{u_x v_y}(\tau) e^{j2\pi\nu\tau} d\tau \quad (2.128)$$

$$= P_{u_x u_y}(\nu) + P_{v_x v_y}(-\nu) + \mathbf{i} [P_{v_x u_y}(\nu) - P_{u_x v_y}(-\nu)] \quad (2.129)$$

$$= P_{u_x u_y}(\nu) + P_{v_y v_x}(\nu) + \mathbf{i} [P_{v_x u_y}(\nu) - P_{v_y u_x}(\nu)] \quad (2.130)$$

which proves (2.31). The same approach is used for the proof of (2.32) and will not be reproduced here.

Linear-time invariant filters

3

This chapter studies one of the most fundamental signal processing operations, *i.e.* linear time-invariant (LTI) filtering, in the quaternion Fourier transform (QFT) framework. Usually, the LTI filtering theory of bivariate signals is formulated using either linear algebra – leading to the *Jones* calculus in optics (Gil, 2007) – or *widely linear filters*, depending on the choice of the representation, vector or complex. However, as explained in Chapter 0, these current approaches do not allow for straightforward physical or geometric interpretations of filtering operations. In contrast, the QFT framework provides, at no extra cost, an elegant, compact and insightful calculus which highlights the geometric treatment of polarization states. Filtering relations are explicitly given in terms of eigenproperties, making it easy to interpret or prescribe any desired physical behavior. Thanks to the notion of quaternion power spectral density developed in Chapter 2, the proposed formalism offers a new generic and meaningful approach to the filtering of bivariate signals.

Section 3.1 describes the derivation of quaternion filters for bivariate signals. Starting from the usual matrix representation of LTI filters we obtain their corresponding quaternion representation. We take advantage of the polar decomposition of matrices and identify two important classes of filters, unitary and Hermitian ones, respectively.


Section 3.2 then provides a thorough study of LTI filters in the quaternion representation. Sections 3.2.1 and 3.2.2 deal with unitary filters and Hermitian filters, respectively. In particular, they feature parameters related to two fundamental properties of optical media: unitary filters model *birefringence*, which corresponds to phase delays that depend on the input polarization state; Hermitian filters encode *diattenuation*, which describes how the gain of a filter depends on the input polarization state. Section 3.2.3 then discusses the general form of LTI filtering as a combination of unitary and Hermitian filters.


Section 3.3 intends to demonstrate the generality and relevance of the proposed approach for standard signal processing operations as well as for original treatments specific to bivariate signals. A fast but approximate spectral synthesis method is presented in 3.3.1. Section 3.3.2 presents the unpolarizing-whitening filter. Wiener denoising is addressed by Section 3.3.3: the proposed formalism sheds some new light on this well-known filter in terms of polarization attributes. Section 3.3.4 shows that the QFT framework makes natural various original descriptions of bivariate signals in two components with specific geometric or statistical properties. Finally Section 3.3.5 illustrates how *unitary filters* can model *polarization mode dispersion*, a phenomenon which appears in many applications such as optical fiber transmission or seismology. Numerical experiments are given throughout to support our discussion.

CHAPTER CONTENTS

3.1 From matrix to quaternion representation of LTI filters	78
LTI filtering of bivariate signals using linear algebra • From matrices to quaternions • Quaternions and physics •	
3.2 Quaternion filters for bivariate signals	80
Unitary filters • Hermitian filters • General form of LTI filters •	
3.3 Some applications of quaternion filters	86
Spectral synthesis by Hermitian filtering • Whitening and unpolarizing filter • Wiener filtering • Some decompositions of bivariate signals • Modeling Polarization Mode Dispersion •	
3.4 Conclusion	97
APPENDICES	
3.A Output-input cross-spectral properties	98
3.B Filter identification using unpolarized white Gaussian noise	98
3.C Linear algebra and quaternion equivalence	99
Matrix-vector and quaternion operations • Unitary transforms • Hermitian transforms •	
3.D Wiener filter derivation	101

Results presented in this chapter have been presented at an international conference and published in an international journal:

 J. Flamant, P. Chainais, and N. Le Bihan. 2018a. “A complete framework for linear filtering of bivariate signals.” *IEEE Transactions on Signal Processing* 66, no. 17 (September): 4541–4552. doi:10.1109/TSP.2018.2855659

 J. Flamant, P. Chainais, and N. Le Bihan. 2018b. “Linear filtering of bivariate signals using quaternions.” In *IEEE Statistical Signal Processing Workshop (SSP), 2018, Freiburg*, 1–5. Best Student Paper Award

3.1 FROM MATRIX TO QUATERNION REPRESENTATION OF LTI FILTERS

In order to formulate a generic linear time-invariant (LTI) filtering theory for bivariate signals in the proposed framework, we start with a natural approach which uses standard multivariate filtering theory. The corresponding quaternion expressions can be derived afterwards. This back-and-forth procedure is made possible by the formal identification between quaternions and 2-dimensional \mathbb{C}_j -complex vectors:

$$\mathbf{x} = [x_1, x_2]^T \in \mathbb{C}_j^2 \longleftrightarrow x = x_1 + \mathbf{i}x_2 \in \mathbb{H}, \quad x_1, x_2 \in \mathbb{C}_j. \quad (3.1)$$

We call \mathbf{x} the 2-d vector representation of the quaternion x . The approach can be summarized as follows. We recall first the general matrix form of LTI filters for bivariate vector-valued signals. Then we identify two special types of LTI filters, respectively *unitary* and *Hermitian* ones. Finally we give the quaternion representation of these filters in the frequency domain, leaving the thorough study of their respective properties for Section 3.2.

Notations The derivation below involves several notations to disambiguate between matrix, vector and quaternion-valued quantities. First, time-domain quantities are given in lowercase letters and frequency domain quantities in uppercase letters. Scalar quantities are denoted by standard case letters *e.g.* x or X . They are either quaternion-valued or \mathbb{C}_j -valued. Vectors are denoted by bold straight letters, *e.g.* \mathbf{x} or \mathbf{X} and matrices are written as bold straight underlined letters, *e.g.* $\underline{\mathbf{m}}$ or $\underline{\mathbf{M}}$. Vectors and matrices are always complex \mathbb{C}_j -valued.

3.1.1 LTI filtering of bivariate signals using linear algebra

LTI filters for bivariate signals are described by 2-by-2 complex matrix-valued functions, see *e.g.* Priestley (1981, Chapter 9). In the time-domain a LTI filter is described by its matrix impulse function $m : \mathbb{R} \rightarrow \mathbb{C}_j^{2 \times 2}$ such that for a vector input $\mathbf{x}(t)$ the vector output $\mathbf{y}(t)$ reads

$$\mathbf{y}(t) = \underline{\mathbf{m}} * \mathbf{x}(t). \quad (3.2)$$

The notation $*$ denotes entry-wise convolution. Equivalently, this filtering relation can be given in the frequency domain. It reads

$$\mathbf{Y}(\mathbf{v}) = \underline{\mathbf{M}}(\mathbf{v})\mathbf{X}(\mathbf{v}), \quad (3.3)$$

Explicitly, if

$$\underline{\mathbf{m}}(t) = \begin{bmatrix} m_{11}(t) & m_{12}(t) \\ m_{21}(t) & m_{22}(t) \end{bmatrix} \quad \text{and} \quad \mathbf{x}(t) = \begin{bmatrix} x_1(t) \\ x_2(t) \end{bmatrix}$$

then $\mathbf{y}(t)$ reads

$$\mathbf{y}(t) = \begin{bmatrix} m_{11} * x_1(t) + m_{12} * x_2(t) \\ m_{21} * x_1(t) + m_{22} * x_2(t) \end{bmatrix}$$

where \mathbf{Y} and \mathbf{X} are respectively the Fourier transforms of \mathbf{y} and \mathbf{x} , and where $\underline{\mathbf{M}}$ is the entry-wise Fourier transform of $\underline{\mathbf{m}}$. Eq. (3.3) shows that a LTI filter introduces for every frequency ν a linear relationship between the Fourier transforms of the input and the output.

Polar decomposition For frequency ν , the matrix $\underline{\mathbf{M}}(\nu)$ embodies the linear relation between Fourier vectors $\mathbf{Y}(\nu)$ and $\mathbf{X}(\nu)$. Let us fix ν and drop now this dependence for ease of notation. The generic linear relation $\mathbf{Y} = \underline{\mathbf{M}}\mathbf{X}$ can be further characterized using the *polar decomposition* (Lancaster and Tismenetsky, 1985) of $\underline{\mathbf{M}}$. It reads

$$\underline{\mathbf{M}} = \underline{\mathbf{U}}\underline{\mathbf{H}}, \quad (3.4)$$

where $\underline{\mathbf{U}}$ is unitary and $\underline{\mathbf{H}}$ is Hermitian positive semi-definite, *i.e.* $\underline{\mathbf{H}}^\dagger = \underline{\mathbf{H}}$ and its eigenvalues are nonnegative. Geometrically (3.4) decomposes $\underline{\mathbf{M}}$ as a stretch (Hermitian matrix $\underline{\mathbf{H}}$) followed by an isometry (unitary matrix $\underline{\mathbf{U}}$).

The polar decomposition (3.4) suggests to study separately two fundamental transforms, respectively *unitary* and *Hermitian* ones. Remarkably, it will appear that the quaternion representation of these two transforms seizes directly their respective eigenproperties.

$\underline{\mathbf{H}}^\dagger$ denotes the conjugate-transpose of $\underline{\mathbf{H}}$.

3.1.2 From matrices to quaternions

Unitary transform Let $U(2)$ denote the set of 2-by-2 \mathbb{C}_j -complex unitary matrices, *i.e.* for $\underline{\mathbf{U}} \in U(2)$ one has $\underline{\mathbf{U}}\underline{\mathbf{U}}^\dagger = \underline{\mathbf{U}}^\dagger\underline{\mathbf{U}} = \underline{\mathbf{I}}_2$. Lemma 3.1 gives the quaternion representation of the unitary transform $\mathbf{Y} = \underline{\mathbf{U}}\mathbf{X}$, where $\mathbf{Y}, \mathbf{X} \in \mathbb{C}_j^2$.

$\underline{\mathbf{I}}_2$ denotes the 2-by-2 identity matrix.

Lemma 3.1 (Unitary transform). *Let $\underline{\mathbf{U}} \in U(2)$. Then*

$$\mathbf{Y} = \underline{\mathbf{U}}\mathbf{X} \iff Y = e^{\mu_b \frac{\beta}{2}} X e^{j\varphi} \quad (3.5)$$

where $\mu_b \in \text{span}\{\mathbf{i}, \mathbf{j}, \mathbf{k}\}$ with $\mu_b^2 = -1$, and $\beta, \varphi \in [0, 2\pi)$.

A unitary transform is described by three parameters: a pure unit quaternion¹ μ_b and two angles β and φ . The parameter φ is the argument of $\det \underline{\mathbf{U}}$. The parameter μ_b is related to the eigenvectors of $\underline{\mathbf{U}}$, while β encodes its eigenvalues, see Appendix 3.C.2. Section 3.2.1 will provide detailed evidence of this connection with eigenproperties. Note that for $\varphi = 0$, the matrix $\underline{\mathbf{U}}$ becomes unitary with unit determinant, *i.e.* $\underline{\mathbf{U}} \in \text{SU}(2)$. In this case (3.5) becomes the familiar unit quaternion representation of special unitary matrices (Altmann, 2005).

Proof. See Appendix 3.C.2. \square

1. The subscript $_b$ stands for the physical interpretation of unitary filters as *birefringent* filters, see Section 3.2.1 below.

Hermitian transform Consider a positive semi-definite Hermitian matrix $\underline{\mathbf{H}}$. Lemma 3.2 gives the quaternion representation of the Hermitian transform $\mathbf{Y} = \underline{\mathbf{H}}\mathbf{X}$.

Lemma 3.2 (Hermitian transform). *Let $\underline{\mathbf{H}} \in \mathbb{C}_j^{2 \times 2}$ be Hermitian positive semi-definite. Then*

$$\mathbf{Y} = \underline{\mathbf{H}}\mathbf{X} \iff Y = K[X - \eta\mu_d X j] \quad (3.6)$$

where $\mu_d \in \text{span}\{\mathbf{i}, \mathbf{j}, \mathbf{k}\}$ with $\mu_d^2 = -1$, $K \in \mathbb{R}^+$ and $\eta \in [0, 1]$.

A Hermitian transform is thus described by three parameters: a pure unit quaternion² μ_d and two scalars K and η . As shown in Appendix 3.C.3, the parameters K and η depend directly on the eigenvalues of $\underline{\mathbf{H}}$. The parameter μ_d encodes the eigenvectors of $\underline{\mathbf{H}}$. Section 3.2.2 will provide detailed evidence of this connection with eigenproperties.

Unitary and Hermitian transforms are described in the quaternion domain each by a dedicated set of three parameters. Each set conveys explicitly the eigenstructure of each transform and thus enables an efficient design of unitary and Hermitian filters. Before studying in detail each filter in Section 3.2, we briefly give some associated physical interpretations.

Proof. See Appendix 3.C.3. □

2. The subscript _d stands for the physical interpretation of Hermitian filters as *diattenuation* filters, see Section 3.2.2 below.

3.1.3 Quaternions and physics

The polar decomposition (3.4) shows that a generic LTI filter can be expressed as a combination of two filters: one is unitary and the other is Hermitian. The field of polarization optics (Brosseau, 1998; Gil and Ossikovski, 2016) has for long time taken advantage of this decomposition to provide meaningful interpretations to these two classes of filters.

Fig. 3.1 summarizes the decomposition of a generic LTI filter into successive Hermitian and unitary filtering operations. Hermitian filters model *diattenuation*: there exist at each frequency two orthogonal eigenpolarizations corresponding to maximum and minimum values of the gain. The gain of this filter depends in general on the alignment between the input polarization axis and the filter axis μ . As a limiting case, when the output polarization axis does not depend on the input polarization axis, this filter is called a *polarizer*. Unitary filters model *birefringence*: there exist at each frequency two *fast* and *slow* orthogonal eigenpolarizations which are delayed differently by the filter. Such a filter preserves the power and degree of polarization of the input. For an arbitrary polarized input, it performs a 3D rotation of the polarization axis. For presentation purposes, Fig. 3.1 depicts the special case where Hermitian and unitary axes coincide ($\mu_d = \mu_b = \mu$). In full generality, a generic LTI filter may exhibit different axes $\mu_d \neq \mu_b$: see Section 3.2.3 for further discussion. Fig. 3.1 displays for completeness the filtering relations associated to unitary and Hermitian filters. The next section aims at establishing these expressions and deciphering their physical implications.

3.2 QUATERNION FILTERS FOR BIVARIATE SIGNALS

The definition of unitary and Hermitian filters relies on the quaternion representation of unitary and Hermitian transforms, as given by Lemmas 3.1 and 3.2, respectively. Section 3.2.1 and Section 3.2.2 explore in detail each type of filter, unitary and Hermitian ones, respectively. We give input-output filtering relations in the spectral domain as well as relations between respective quaternion power spectral densities. These relations permit meaningful interpretations for the case of stationary random bivariate signals. Section 3.2.3 then discusses the generic LTI filtering case by combination of a unitary and a Hermitian filter.

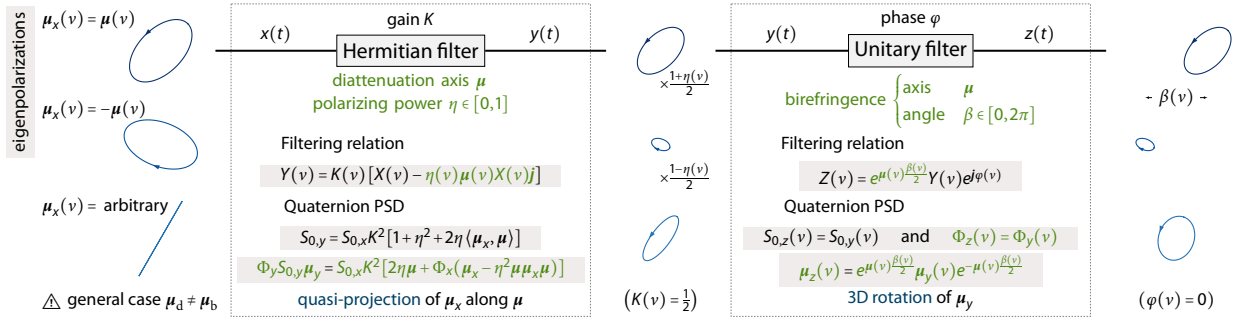


Figure 3.1: A generic LTI filter for a bivariate signal x results from the combination of a unitary filter and a Hermitian filter. For every frequency each filter has two orthogonal eigenpolarizations encoded by the axis μ . Unitary filters model birefringence, *i.e.* eigenpolarizations are delayed differently. Hermitian filters model diattenuation, *i.e.* eigenpolarizations are attenuated or amplified asymmetrically. To emphasize the geometric operations performed by the unitary and the Hermitian filter, values of the usual gain K and phase φ are chosen to limit their incidence. Note that in full generality, unitary and Hermitian filters may exhibit different axes $\mu_d \neq \mu_b$.

In the following the explicit form of the quaternion PSD of a stationary random bivariate signal x in terms of polarization parameters will be intensively used:

$$\Gamma_{xx}(\nu) = S_{0,x}(\nu) + S_{0,x}(\nu)\mu_x(\nu)\Phi_x(\nu). \quad (3.7)$$

Moreover strictly speaking, spectral-domain filtering relations between stationary random signals $x(t)$ and $y(t)$ should involve their respective spectral increments $dX(\nu)$ and $dY(\nu)$, see Theorem 2.1. However to keep expressions digestible and with little abuse, we write filtering relations as if the QFT $X(\nu)$, $Y(\nu)$ of these random signals existed. This does not change any of the fundamental results presented in this chapter.

3.2.1 Unitary filters

A unitary filter performs a unitary transform at each frequency. Such filter makes the *polarization axis* of the input rotate and leaves the total power spectral density $S_{0,x}(\nu)$ and degree of polarization $\Phi_x(\nu)$ invariant. This is known as *birefringence*, see *e.g.* (Gil, 2007; Gil and Ossikovski, 2016).

Three frequency-dependent quantities define unitary filters. Two model birefringence: the *birefringence axis* $\mu_b(\nu)$ and the *birefringence angle* $\beta(\nu)$. The third parameter is the *phase* $\varphi(\nu)$. It is classical and quantifies the *time delay* associated to each frequency.

Proposition 3.1 below gives the unitary filtering relation for bivariate signals and the corresponding relation between input and output quaternion power spectral densities.

Proposition 3.1 (Unitary filter). *Let $x : \mathbb{R} \rightarrow \mathbb{C}_i$ be the input and y be the output of the unitary filter, with respective QFTs X and Y . The filtering relation is*

$$Y(\nu) = e^{\mu_b(\nu)\frac{\beta(\nu)}{2}} X(\nu) e^{j\varphi(\nu)}, \quad (3.8)$$

with $\mu_b(-\nu) = -i\mu_b(\nu)i$, $\beta(-\nu) = \beta(\nu)$ and $\varphi(-\nu) = -\varphi(\nu)$ for all $\nu \in \mathbb{R}$. The quaternion power spectral density of y is

$$\Gamma_{yy}(\nu) = e^{\mu_b(\nu)\frac{\beta(\nu)}{2}} \Gamma_{xx}(\nu) e^{-\mu_b(\nu)\frac{\beta(\nu)}{2}} \quad (3.9)$$

Inserting the explicit expression of the quaternion PSD (3.7) in terms of polarization features into (3.9) yields

$$\begin{aligned} \Gamma_{yy}(\nu) &= e^{\mu_b(\nu)\frac{\beta(\nu)}{2}} S_{0,x}(\nu) [1 + \Phi_x(\nu)\mu_x(\nu)] e^{-\mu_b(\nu)\frac{\beta(\nu)}{2}} \\ &= S_{0,x}(\nu) + \Phi_x(\nu) e^{\mu_b(\nu)\frac{\beta(\nu)}{2}} \mu_x(\nu) e^{-\mu_b(\nu)\frac{\beta(\nu)}{2}}. \end{aligned} \quad (3.10)$$

Symmetry conditions on μ_b , β and φ ensure that the output y remains \mathbb{C}_i -valued for a \mathbb{C}_i -valued input x . This ensures in particular that the *i*-Hermitian symmetry (1.52) is satisfied for $Y(\nu)$.

Sketch of proof. Eq. (3.8) is obtained directly from Lemma 3.1. To obtain (3.9) replace QFTs by spectral increments in (3.8). Then thanks to the quaternion PSD definition (2.20) one gets (3.9). \square

Eqs. (3.9)–(3.10) illustrate the *geometric operation* performed by the unitary filter: a 3D rotation of the input quaternion PSD $\Gamma_{xx}(\nu)$. It affects only the imaginary components of the quaternion PSD, see Section 1.1.5 for details. This operation is physically interpreted as *birefringence*. It can be visualized on the Poincaré sphere in Fig. 2.5: the output polarization axis $\boldsymbol{\mu}_y(\nu)$ is given by the rotation of the input polarization axis $\boldsymbol{\mu}_x(\nu)$. This rotation is defined by the birefringence axis $\boldsymbol{\mu}_b(\nu)$ and the birefringence angle $\beta(\nu)$. Eq. (3.10) also highlights that both the total PSD and the degree of polarization are rotation invariant: $S_{0,y}(\nu) = S_{0,x}(\nu)$ and $\Phi_y(\nu) = \Phi_x(\nu)$. This emphasizes the *unitary* nature of the filter.

Eigenpolarizations At a given ν , unitary filters have two orthogonal eigenpolarizations. When the polarization of the input is an eigenpolarization, input and output polarization axes coincide: inputs are simply delayed by the filter. Let us write the birefringence axis $\boldsymbol{\mu}_b(\nu)$ in terms of its spherical coordinates $(\theta(\nu), \chi(\nu))$ on the Poincaré sphere:

$$\boldsymbol{\mu}_b(\nu) = \mathbf{i} \sin 2\chi(\nu) + \mathbf{j} \cos 2\theta(\nu) \cos 2\chi(\nu) + \mathbf{k} \sin 2\theta(\nu) \cos 2\chi(\nu). \quad (3.11)$$

Consider $Z_+(\nu)$ and $Z_-(\nu)$ two spectral components at frequency ν associated with orthogonal polarization axes $\boldsymbol{\mu}_{Z_\pm}(\nu) = \pm \boldsymbol{\mu}_b(\nu)$:

$$Z_+(\nu) = e^{i\theta(\nu)} e^{-k\chi(\nu)} \quad \text{and} \quad Z_-(\nu) = e^{i(\theta(\nu)+\frac{\pi}{2})} e^{k\chi(\nu)} \quad (3.12)$$

These fully polarized spectral components define eigenpolarizations since

$$e^{\boldsymbol{\mu}_b(\nu) \frac{\beta(\nu)}{2}} Z_+(\nu) e^{j\varphi(\nu)} = Z_+(\nu) e^{j(\varphi(\nu)+\beta(\nu)/2)}, \quad (3.13)$$

$$e^{\boldsymbol{\mu}_b(\nu) \frac{\beta(\nu)}{2}} Z_-(\nu) e^{j\varphi(\nu)} = Z_-(\nu) e^{j(\varphi(\nu)-\beta(\nu)/2)}. \quad (3.14)$$

Clearly, the birefringence axis $\boldsymbol{\mu}_b(\theta, \chi)$ encodes the eigenvectors of the filter. The associated eigenvalues are unit \mathbb{C}_j -complex numbers $\exp[j(\varphi(\nu) \pm \beta(\nu)/2)]$. Eqs. (3.13)–(3.14) provide an additional characterization of birefringence. Unitary filters introduce a phase difference $\beta(\nu)$ between the *fast* eigenpolarization $Z_+(\nu)$ and the *slow* eigenpolarization $Z_-(\nu)$.

Identification Eigenpolarizations properties (3.13)–(3.14) yield a simple identification method of unitary filters. The approach generalizes a well known procedure of experimental optics (Gil and Ossikovski, 2016) to frequency dependent parameters. Working with monochromatic signals of increasing frequency, one can adjust the input polarization axis until it coincides with the output polarization axis. It gives immediately the birefringence axis $\boldsymbol{\mu}_b(\nu)$. Measuring phase delays with respect to fast and slow eigenpolarizations then permits using (3.13)–(3.14) to identify the birefringence angle $\beta(\nu)$ and the phase $\varphi(\nu)$. Section 3.B discusses an additional identification method using unpolarized white Gaussian noise.

3.2.2 Hermitian filters

A Hermitian filter performs a Hermitian transform at each frequency. This second type of filter modifies both power and polarization properties of the input signal. The gain of the filter is a function of the input polarization

We use that

$$\begin{aligned} \boldsymbol{\mu}_b(\nu) &\leftrightarrow (\theta(\nu), \chi(\nu)) \\ -\boldsymbol{\mu}_b(\nu) &\leftrightarrow (\theta(\nu) + \pi/2, -\chi(\nu)) \end{aligned}$$

To prove (3.13)–(3.14) use the fact that

$$\boldsymbol{\mu}_b = e^{i\theta} e^{-k\chi} \mathbf{j} e^{k\chi} e^{-i\theta}$$

axis: eigenpolarizations correspond to maximum and minimum values of this gain. This filter represents *diattenuation* effects, see e.g. Gil (2007) or Gil and Ossikovski (2016) and references therein.

Three frequency-dependent quantities parameterize a Hermitian filter. Two are related to *diattenuation*: the *polarizing power* $\eta(\nu)$ and the *diattenuation axis* $\boldsymbol{\mu}_d(\nu)$. The third quantity is the *homogeneous gain* $K(\nu) \geq 0$. When $\eta(\nu) = 0$, diattenuation effects are removed and $K(\nu)$ is interpreted as an usual filter gain.

Proposition 3.2 below gives the Hermitian filtering relation for bivariate signals. It also presents the expression of the output quaternion PSD Γ_{yy} . The use of the explicit expression (3.7) of Γ_{xx} provides a direct interpretation of the spectral properties of y .

Proposition 3.2 (Hermitian filter). *Let $x : \mathbb{R} \rightarrow \mathbb{C}_i$ denote the input and y denote the output of the Hermitian filter with respective QFTs X and Y . The filtering relation is*

$$Y(\nu) = K(\nu)[X(\nu) - \eta(\nu)\boldsymbol{\mu}_d(\nu)X(\nu)\mathbf{j}] \quad (3.15)$$

with $K(-\nu) = K(\nu)$, $\eta(-\nu) = \eta(\nu)$ and $\boldsymbol{\mu}_d(-\nu) = -\overline{\mathbf{i}\boldsymbol{\mu}_d(\nu)\mathbf{i}}$ for all $\nu \in \mathbb{R}$. Using (3.7), the quaternion PSD of y is then given by (dropping ν dependence for convenience)

$$\mathcal{S}(\Gamma_{yy}) = S_{0,x}K^2[1 + \eta^2 + 2\eta\Phi_x\langle\boldsymbol{\mu}_d, \boldsymbol{\mu}_x\rangle] \quad (3.16)$$

$$\mathcal{V}(\Gamma_{yy}) = S_{0,x}K^2[2\eta\boldsymbol{\mu}_d + \Phi_x[\boldsymbol{\mu}_x - \eta^2\boldsymbol{\mu}_d\boldsymbol{\mu}_x\boldsymbol{\mu}_d]] \quad (3.17)$$

where $\langle\boldsymbol{\mu}_1, \boldsymbol{\mu}_2\rangle = \mathcal{S}(\boldsymbol{\mu}_1\overline{\boldsymbol{\mu}_2})$ is the usual inner product of \mathbb{R}^3 .

To avoid notational clutter the explicit dependence in frequency ν is now dropped in most expressions. Unless otherwise stated, discussions below are for a single frequency. This means that statements such as “ x is partially polarized” are to be interpreted as “ x is partially polarized at frequency ν ”.

Gain The *power gain* G of the filter is defined by the ratio

$$G = \frac{\mathcal{S}(\Gamma_{yy})}{\mathcal{S}(\Gamma_{xx})} = \frac{S_{0,y}}{S_{0,x}} \geq 0. \quad (3.18)$$

Using (3.16) this gain becomes

$$G = K^2[1 + \eta^2 + 2\eta\Phi_x\langle\boldsymbol{\mu}_d, \boldsymbol{\mu}_x\rangle]. \quad (3.19)$$

When $\eta = 0$ the power gain reduces to its usual expression $G = K^2$. When $\eta \neq 0$, the gain depends on K and η but most importantly, on the alignment $\langle\boldsymbol{\mu}_d, \boldsymbol{\mu}_x\rangle$ between diattenuation and input polarization axes.

Eigenpolarizations Hermitian filters have two orthogonal eigenpolarizations. When the polarization of the input is an eigenpolarization, input and output polarization axes coincide: inputs are simply attenuated or amplified by the filter.

Using the same ingredients as for the unitary filter case, write the diattenuation axis $\boldsymbol{\mu}_d = \boldsymbol{\mu}_d(\theta, \chi)$ in spherical coordinates as in (3.11). Next consider two spectral components Z_+ and Z_- with orthogonal polarization axes

These symmetry requirements ensure that $y(t)$ remains \mathbb{C}_i -valued for $x : \mathbb{R} \rightarrow \mathbb{C}_i$. They are obtained by enforcing the \mathbf{i} -Hermitian symmetry (1.52) on $Y(\nu)$.

Sketch of proof. Eq. (3.15) is obtained directly from Lemma 3.2. To obtain (3.16)-(3.17) replace QFTs by corresponding spectral increments in (3.15). Plugging (3.15) into the quaternion PSD definition (2.20) with the use of (3.7) yields (3.16)-(3.17). \square

$\boldsymbol{\mu}_{Z_{\pm}} = \pm \boldsymbol{\mu}_d(\nu)$. These fully polarized spectral components define eigenpolarizations:

$$K[Z_+ - \eta \boldsymbol{\mu}_d Z_+ \cdot \mathbf{j}] = K[1 + \eta]Z_+ \quad (3.20)$$

$$K[Z_- - \eta \boldsymbol{\mu}_d Z_- \cdot \mathbf{j}] = K[1 - \eta]Z_- \quad (3.21)$$

The *diattenuation axis* $\boldsymbol{\mu}_d(\theta, \chi)$ directly encodes the eigenvectors of the Hermitian filter. The remaining parameters define the eigenvalues $K[1 \pm \eta]$. Eqs. (3.20)–(3.21) show that eigenpolarizations have different gain values depending on the polarizing power η when $\eta \neq 0$. This characterizes *diattenuation* (Gil, 2007; Gil and Ossikovski, 2016).

Identification using eigenproperties Just like for the unitary filter, the parameters of an Hermitian filter are easily identified thanks to eigenpolarization properties (3.20)–(3.21). The identification method follows directly from experimental optics. Eigenpolarizations Z_+ and Z_- are obtained as maximum and minimum values of the gain G , see (3.19) for $\boldsymbol{\mu}_x = \pm \boldsymbol{\mu}_d$. Once these eigenpolarizations have been identified the remaining parameters K and η are given by

$$\frac{2\eta}{1 + \eta^2} = \frac{G_{\max} - G_{\min}}{G_{\max} + G_{\min}} \quad \text{and} \quad K^2 = \frac{G_{\max} - G_{\min}}{4\eta}, \quad (3.22)$$

where $G_{\max} = G(\boldsymbol{\mu}_x = \boldsymbol{\mu}_d)$ and $G_{\min} = G(\boldsymbol{\mu}_x = -\boldsymbol{\mu}_d)$ denote the maximum and minimum gain values. Repeating the operation for a wide range of frequencies completes the characterization procedure.

Role of the polarizing power η The parameter η rules the strength of interaction between the input polarization properties and the filter parameters. The two extreme cases $\eta = 0$ and $\eta = 1$ illustrate the ability of Hermitian filters to produce rich and interpretable behaviors.

- *Null polarizing power $\eta = 0$.* The filtering relation (3.15) becomes $Y = KX$ and thus $\Gamma_{yy} = K^2\Gamma_{xx}$. The input is simply amplified or attenuated and polarization properties are not modified.
- *Maximal polarizing power $\eta = 1$.* Borrowing the term from optics, the Hermitian filter becomes a *polarizer*. The output is always fully polarized $\Phi_y = 1$ and its polarization axis is directly the diattenuation axis $\boldsymbol{\mu}_y = \boldsymbol{\mu}_d$. The gain G (3.19) quantifies the ‘‘closeness’’ between $\boldsymbol{\mu}_x$ and $\boldsymbol{\mu}_d$:

$$G = 2S_{0,x}K^2[1 + \Phi_x \langle \boldsymbol{\mu}_x, \boldsymbol{\mu}_d \rangle]. \quad (3.23)$$

In particular, for the eigenpolarizations Z_{\pm} of the filter:

$$Y_+ = 2KZ_+ \quad \text{and} \quad Y_- = 0 \quad (3.24)$$

meaning that the output cancels out for a fully polarized signal with input polarization axis $\boldsymbol{\mu}_x = -\boldsymbol{\mu}_d$ (orthogonal polarization). This effect is purely geometric since the homogenous gain K does not need to be zero.

These two simple cases illustrate that as soon as $\eta > 0$ the output polarization properties of a Hermitian filter result from the intertwining between input polarization properties and diattenuation parameters.

Identically to the unitary filter:

$$Z_+ = e^{i\theta} e^{-k\chi}$$

$$Z_- = e^{i(\theta + \frac{\pi}{2})} e^{k\chi}$$

Identification procedures using unpolarized wGn are described in Section 3.B.

To see this rewrite the term $\boldsymbol{\mu}_x - \boldsymbol{\mu}_d \boldsymbol{\mu}_x \boldsymbol{\mu}_d$ in (3.17) as

$$\boldsymbol{\mu}_x - \boldsymbol{\mu}_d \boldsymbol{\mu}_x \boldsymbol{\mu}_d = 2 \langle \boldsymbol{\mu}_x, \boldsymbol{\mu}_d \rangle \boldsymbol{\mu}_d.$$

Polarizers perform a projection of $\boldsymbol{\mu}_x$ onto the diattenuation axis $\boldsymbol{\mu}_d$. Properties $\Phi_y = 1$ and $\boldsymbol{\mu}_y = \boldsymbol{\mu}_d$ follow directly from (3.16)–(3.17).

Output degree of polarization The generic expression for Φ_y reads

$$\Phi_y = \left[1 - \frac{(1 - \Phi_x^2)(\eta^2 - 1)^2}{(1 + \eta^2)^2 + 4\eta^2\Phi_x^2 \langle \boldsymbol{\mu}_d, \boldsymbol{\mu}_x \rangle^2 + 4\eta(1 + \eta^2)\Phi_x \langle \boldsymbol{\mu}_d, \boldsymbol{\mu}_x \rangle} \right]^{\frac{1}{2}}. \quad (3.25)$$

A straightforward check shows that $\Phi_y(\eta = 0) = \Phi_x$ and $\Phi_y(\eta = 1) = 1$ as already discussed above. Eq. (3.25) also shows that $\Phi_y = 1$ for a fully polarized input $\Phi_x = 1$. It relates to the fact that *Jones matrices* are *nondepolarizing*, i.e. a fully polarized input always remains fully polarized. Note that *nondepolarizing* does not mean at all that the degree of polarization Φ_y cannot be less than Φ_x for partially polarized inputs: this can be readily checked from (3.25). See also Simon (1990) for a discussion of this in the context of optics. For an unpolarized input $\Phi_x = 0$ the output degree of polarization reads

$$\Phi_y(\Phi_x = 0) = \frac{2\eta}{1 + \eta^2}, \quad (3.26)$$

i.e. Φ_y depends directly from η . This expression is particularly useful for the spectral synthesis of bivariate signals from unpolarized wGn, see Section 3.3.1.

3.2.3 General form of LTI filters

A generic LTI filter results from a combination of a unitary and an Hermitian filter. Let $\boldsymbol{\mu}_b, \alpha, \varphi$ denote the parameters of the unitary filter and let $K, \boldsymbol{\mu}_d, \eta$ denote the parameters of the Hermitian filter. Following the polar decomposition (3.4) the generic LTI filtering relation is

$$Y(\mathbf{v}) = e^{\boldsymbol{\mu}_b(\mathbf{v})\frac{\beta(\mathbf{v})}{2}} K(\mathbf{v}) [X(\mathbf{v}) - \eta(\mathbf{v})\boldsymbol{\mu}_d(\mathbf{v})X(\mathbf{v})\mathbf{j}] e^{j\varphi(\mathbf{v})}. \quad (3.27)$$

The output quaternion PSD is given by (dropping again \mathbf{v} for simplicity)

$$\mathcal{S}(\Gamma_{yy}) = S_{0,x}K^2 [1 + \eta^2 + 2\eta\Phi_x \langle \boldsymbol{\mu}_d, \boldsymbol{\mu}_x \rangle] \quad (3.28)$$

$$\mathcal{V}(\Gamma_{yy}) = S_{0,x}K^2 e^{\boldsymbol{\mu}_b\frac{\beta}{2}} [2\eta\boldsymbol{\mu}_d + \Phi_x[\boldsymbol{\mu}_x - \eta^2\boldsymbol{\mu}_d\boldsymbol{\mu}_x\boldsymbol{\mu}_d]] e^{-\boldsymbol{\mu}_b\frac{\beta}{2}} \quad (3.29)$$

The scalar part of Γ_{yy} gives the total PSD. It only depends on the features of the Hermitian filter. The vector part of Γ_{yy} carries the geometric and polarization attributes of the output. They result from the application of the Hermitian filter on x followed by the unitary filter. In particular, the generic LTI filtering relation (3.27) would describe a linear media that simultaneously exhibits two very different physical effects: *birefringence* (unitary filter) and *diattenuation* (Hermitian filter). Fig. 3.1 summarizes this generic LTI filtering relation for the case $\boldsymbol{\mu}_b = \boldsymbol{\mu}_d = \boldsymbol{\mu}$.

Linear and time-invariance properties Eq. (3.27) describes the generic LTI filtering relation for bivariate signals. However, the term ‘linear’ should be specified since quaternion multiplication is noncommutative. Let x_1 and x_2 denote two bivariate signals. Denote by y_1 and y_2 the corresponding outputs resulting from the filtering relation (3.27). Then clearly, if $x = x_1 + x_2$ then one has $y = y_1 + y_2$. It is straightforward to check that for any $\lambda \in \mathbb{C}_j$ the input $x\lambda$ yields output $y\lambda$. Hence ‘linear’ should be understood as ‘right- \mathbb{C}_j -linear’.

This expression is obtained using that $(\Phi_y\boldsymbol{\mu}_y)^2 = -\Phi_y^2$ and with

$$\Phi_y\boldsymbol{\mu}_y = \frac{2\eta\boldsymbol{\mu}_d + \Phi_x[\boldsymbol{\mu}_x - \eta^2\boldsymbol{\mu}_d\boldsymbol{\mu}_x\boldsymbol{\mu}_d]}{1 + \eta^2 + 2\eta\Phi_x \langle \boldsymbol{\mu}_x, \boldsymbol{\mu}_d \rangle},$$

see Eqs. (3.16)–(3.17).

Depolarizing linear media requires to introduce Mueller calculus, see e.g. Gil and Ossikovski (2016). In short, Mueller calculus models the linear relationship between input and output Stokes parameters using $\mathbb{R}^{4 \times 4}$ matrices. It gives filtering relations between power spectral densities, but not directly between signals $x(t)$ and $y(t)$.

Subscripts ‘b’ and ‘d’ refer to ‘birefringence’ and ‘diattenuation’, respectively.

This directly shows that (3.27) is *time-invariant*. Indeed if y is the filter response to x , then for any $\tau \in \mathbb{R}$

$$x(t - \tau) \xrightarrow{(3.27)} y(t - \tau) \quad \text{since } x(t - \tau) \xleftrightarrow{\text{QFT}} X(\nu) e^{-j2\pi\nu\tau}. \quad (3.30)$$

The fact that (3.27) is not ‘quaternion-linear’ emphasizes that it induces geometric operations on the input signal. The only ‘quaternion-linear’ filtering relations correspond to usual (gain-phase) univariate filters:

$$Y(\nu) = X(\nu)K(\nu)e^{j\varphi(\nu)}, \quad (3.31)$$

i.e. when no geometric operation is performed ($\beta = \eta = 0$ in (3.27)). Note finally that (3.31) is the only case where the filtering relation admits a simple form as a convolution in time-domain. Namely, let g be the inverse QFT of $G(\nu) = K(\nu)e^{j\varphi(\nu)}$. Then the time-domain equivalent of (3.31) reads

$$y(t) = x * g(t), \quad (3.32)$$

which is the usual convolution operation associated with univariate LTI filters. This relation does not hold in general for (3.27).

Unitary-Hermitian or Hermitian-Unitary? Eq. (3.27) is obtained following the polar decomposition of matrices (3.4). However a matrix $\underline{\mathbf{M}} \in \mathbb{C}_j^{2 \times 2}$ can be equivalently decomposed (Lancaster and Tismenetsky, 1985) as $\underline{\mathbf{M}} = \underline{\mathbf{U}}\underline{\mathbf{H}} = \underline{\mathbf{L}}\underline{\mathbf{U}}$, where $\underline{\mathbf{L}}$ is Hermitian positive semidefinite. This means that the Hermitian filtering followed by unitary filtering in (3.27) is somewhat arbitrary. Eq. (3.27) could be rewritten in the reverse order. Diattenuation parameters require however to be adapted so that the reverse decomposition corresponds to the same filter defined by (3.27).

Eigenvectors In general the filter (3.27) does not admit *orthogonal eigenpolarizations*. It only arises when Hermitian and unitary filters share the same eigenvectors, *i.e.* when $\boldsymbol{\mu}_b = \boldsymbol{\mu}_d$. Then Hermitian and unitary filtering operations commute. In optics such filters are called *homogeneous* (Lu and Chipman, 1994) or *normal* (Gil and Ossikovski, 2016) since diattenuation and birefringence axes coincide. They usually represent the optical properties of *bulk* media: a media that would mix birefringence and diattenuation at the infinitesimal scale with $\boldsymbol{\mu}_b \neq \boldsymbol{\mu}_d$ has *a priori* no physical meaning (Pellat-finet, 1984).

The study of the eigenproperties of the case $\boldsymbol{\mu}_b \neq \boldsymbol{\mu}_d$ is out of the scope of the present manuscript. This topic has been widely studied in optics: it corresponds to *inhomogeneous* or *non-normal* Jones matrices, see *e.g.* Lu and Chipman (1994), Sudha and Rao (2001) or Gil and Ossikovski (2016) and references therein. As an example, a composite media with one diattenuation (Hermitian) layer followed by a birefringent (unitary) layer would be described by a filter with $\boldsymbol{\mu}_b \neq \boldsymbol{\mu}_d$.

In particular $\boldsymbol{\mu}_b \neq \boldsymbol{\mu}_d$ can yield *degenerate* filters, with only one linearly independent eigenpolarization (Gil and Ossikovski, 2016).

3.3 SOME APPLICATIONS OF QUATERNION FILTERS

3.3.1 Spectral synthesis by Hermitian filtering

We propose a new simulation method for Gaussian stationary random bivariate signals by filtering of bivariate white Gaussian noise. This method

is fast and approximate and extends a well-known simulation algorithm for univariate signals (Thompson, 1973; Percival, 1992) to the case of bivariate random signals. It can also be seen as a special case of the algorithm proposed by Chambers (1995) for multivariate Gaussian signals. However the present algorithm provides an explicit control of the power and polarization features of the simulated signal by exploiting the quaternion representation of LTI filters.

Consider an unpolarized white Gaussian noise $w(t)$. Its quaternion PSD is then $\Gamma_{ww}(\nu) = \sigma^2$, where $\sigma^2 > 0$ is the noise variance. Let x denote the signal obtained by the Hermitian filtering (3.15) of w . Then by Eqs-(3.16)–(3.17) the quaternion PSD of x is

$$\Gamma_{xx}(\nu) = \sigma_0^2 K^2(\nu) [1 + \eta^2(\nu)] \left[1 + \frac{2\eta(\nu)}{1 + \eta^2(\nu)} \boldsymbol{\mu}_d(\nu) \right]. \quad (3.33)$$

Eq. (3.33) shows that any stationary Gaussian bivariate signal x with arbitrary spectral density Γ_{xx} can be obtained by Hermitian filtering of unpolarized white Gaussian noise. More precisely set $\Gamma_0(\nu) = S_0(\nu) [1 + \Phi_0(\nu) \boldsymbol{\mu}_0(\nu)]$ as the *target* quaternion PSD. The following choice of parameters for the Hermitian filter ensure that $\Gamma_{xx}(\nu) = \Gamma_0(\nu)$ for any ν

$$\begin{cases} \boldsymbol{\mu}_d(\nu) &= \boldsymbol{\mu}_0(\nu) \\ \eta(\nu) &= \frac{1 - \sqrt{1 - \Phi_y^2(\nu)}}{\Phi_y(\nu)} \quad (\Phi_y(\nu) \neq 0) \\ K(\nu) &= \left(\frac{S_{0,y}(\nu)}{\sigma_0^2 (1 + \eta^2(\nu))} \right)^{\frac{1}{2}} \end{cases} \quad (3.34)$$

and $\eta(\nu) = 0$ when $\Phi_0(\nu) = 0$.

These results give a straightforward procedure to simulate realizations of the signal $x(t)$. The implementation of the discrete Hermitian filtering relation corresponding to (3.33)–(3.34) is numerically efficient as it relies on FFTs only. However just like the standard univariate method (Thompson, 1973; Percival, 1992) this method is only approximate. This means that the spectral properties of the simulated sequence $x[1], x[2], \dots, x[N]$ of length N will only approximately match those of Γ_0 . Another downside of the approach is that $x[1]$ and $x[N]$ will be close in value due to the periodic nature of the DFT. Following usual practice (Percival, 1992; Chambers, 1995), these effects can be mitigated by simulating a sequence of size $M > N$ and keeping only a subsample of size N .

Example Figure 3.2a depicts a realization of a narrow-band stationary random bivariate signal with constant polarization properties. The simulation is of length $N = 1024$ and was obtained using a $M = 10N$ length unpolarized white noise sequence. The signal is partially polarized $\Phi_x = 0.7$ and exhibits elliptical polarization axis. The power is distributed in a Gaussian-shaped fashion around normalized frequency $\nu_0 = 0.02$, see Figure 3.2b for details. Note that the instantaneous polarization state evolves with time. This is a feature of partial polarization for quasi-monochromatic signals with constant polarization axis.

With slight abuse we consider w to be continuous-time (CT), although CT white Gaussian noise does not formally exist.

Spectral synthesis of random bivariate signals

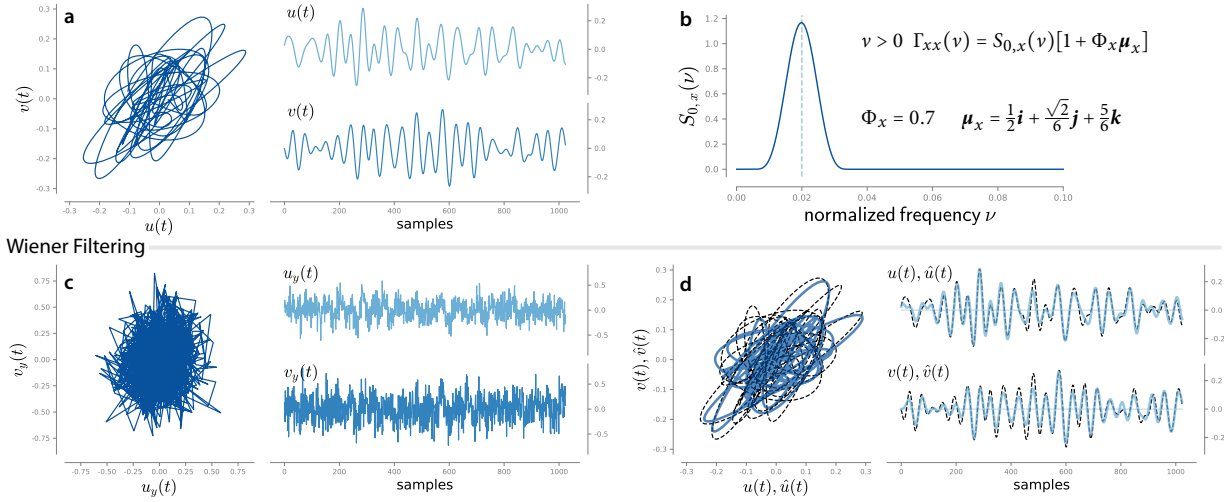


Figure 3.2: (a) Partially elliptically polarized narrow-band signal simulated using the spectral synthesis method described in Section 3.3.1. This signal is a reference for subsequent illustrations. (b) Power spectral distribution and polarization parameters used in (a). (c) Reference signal in partially ($\Phi_w = 0.4$) vertically polarized white noise with SNR = -5 dB. (d) Output of the Wiener denoising filter described in Section 3.3.3. Dashed lines indicate the original signal of (a).

3.3.2 Whitening and unpolarizing filter

Given a bivariate signal $x(t)$ with quaternion PSD $\Gamma_{xx}(\nu)$ is it possible to design a filter so that the output $y(t)$ has the same second-order properties as unpolarized white noise? Such filter, when it exists, is called the *unpolarizing whitening filter* of x .

The output $y(t)$ has required spectral density $\Gamma_{yy}(\nu) = \sigma^2$ where σ^2 is the noise variance. Since unitary filters do not affect the degree of polarization, y is necessarily obtained by Hermitian filtering of x . Suppose that x is not fully polarized nor unpolarized $0 < \Phi_x(\nu) < 1$ for all frequencies. Then imposing $\Phi_y(\nu) = 0$ in (3.25) is equivalent to

$$\mu_d(\nu) = -\mu_x(\nu) \quad \text{and} \quad \eta(\nu) = \frac{1 - \sqrt{1 - \Phi_x^2(\nu)}}{\Phi_x(\nu)} \quad (3.35)$$

This arises from the fact that Φ_y is minimum for $\langle \mu_x, \mu_d \rangle = -1$, see (3.25). To impose that $\Gamma_{yy}(\nu) = \sigma^2$, the homogeneous gain K is set by plugging (3.35) into (3.16). One finds that

$$K(\nu) = \frac{\sigma}{(2S_{0,x}(\nu))^{\frac{1}{2}}} \frac{\Phi_x(\nu)}{[1 - \Phi_x^2(\nu)]^{\frac{1}{2}} [1 - \sqrt{1 - \Phi_x^2(\nu)}]^{\frac{1}{2}}} \quad (3.36)$$

where we shall further require that $S_{0,x}(\nu) > 0$ for all ν , which means that x contains power for all frequencies. Remark that K is obtained by the product of 2 terms in (3.36): a power term and a pure geometric term depending only on the degree of polarization of x .

The unpolarizing whitening filter only exists if two conditions are met: (i) x has no fully polarized spectral component, *i.e.* $\Phi_x(\nu) < 1$ for all ν and (ii) x exhibits power at all frequencies, *i.e.* $S_{0,x}(\nu) > 0$ for all ν . The filter parameters $K(\nu)$, $\eta(\nu)$ and $\mu_d(\nu)$ are given by (3.35)–(3.36) when $0 < \Phi_x(\nu) < 1$. For frequencies such that $\Phi_x(\nu) = 0$, simply set $\eta(\nu) = 0$ and $K(\nu) = \sigma S_{0,x}^{-1/2}$. Fig. 3.3 illustrates the unpolarizing whitening filter of a Gaussian signal x with constant polarization properties and first-order spectral profile. The output is unpolarized white Gaussian noise with power adjusted to $\sigma^2 = 1$.

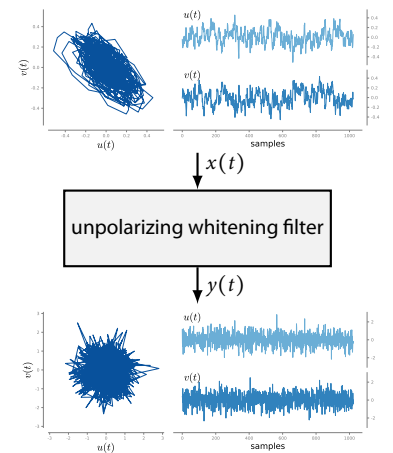


Figure 3.3: Unpolarizing-whitening filter of a stationary Gaussian signal x with constant polarization properties ($\Phi_x(\nu) = 0.9$, $\mu_x(\nu) = -2^{-1/2}(\mathbf{i} + \mathbf{k})$) and first-order spectral profile $S_{0,x}(\nu) \propto (1 + \nu/\nu_0)^2$. Here $\nu_0 = 0.02$ and $K(\nu)$ is set thanks to (3.36) such that $\sigma^2 = 1$.

3.3.3 Wiener filtering

The Wiener filter produces a linear estimate $\hat{x}(t)$ from a signal of interest $x(t)$ given *measurements* $y(t)$. Its quaternion representation yields insightful interpretations and a straightforward design in terms of polarization parameters. We restrict our attention to the denoising case, *i.e.* where $y(t)$ is of the form

$$y(t) = x(t) + w(t) \quad (3.37)$$

where $w(t)$ is bivariate noise supposed independent from $x(t)$. All signals are assumed to be zero-mean, second-order stationary with known spectral densities. The Wiener filter output $\hat{x}(t)$ is optimal in the sense that it solves the minimum-mean-square-error (MMSE) problem

$$\min \mathbf{E} \{ |\hat{x}(t) - x(t)|^2 \}. \quad (3.38)$$

Intuitively the Wiener filter should behave like a *polarizer* when the signal of interest $x(t)$ is deterministic (hence fully polarized) and the noise $w(t)$ is unpolarized. The output \hat{x} is constructed by the projection of every spectral component of the measurements y along the polarization axis $\boldsymbol{\mu}_x(\mathbf{v})$ of the signal of interest. Fortunately, this intuition is proven right by the generic expression of the Wiener filter.

Frequency-domain expression We omit frequency dependence for notational convenience. See Appendix 3.D for the complete derivation of the Wiener filter. The Wiener denoising filter is a Hermitian filter :

$$\hat{X} = \frac{S_{0,x} (1 - \Phi_x \Phi_y \langle \boldsymbol{\mu}_x, \boldsymbol{\mu}_y \rangle)}{S_{0,y} [1 - \Phi_y^2]} \left[Y - \frac{\Phi_x \boldsymbol{\mu}_x - \Phi_y \boldsymbol{\mu}_y}{1 - \Phi_x \Phi_y \langle \boldsymbol{\mu}_x, \boldsymbol{\mu}_y \rangle} Y \mathbf{j} \right]. \quad (3.39)$$

The homogeneous gain $K(\mathbf{v})$, the polarizing power $\eta(\mathbf{v})$ and the diattenuation axis $\boldsymbol{\mu}_d(\mathbf{v})$ of this Hermitian filter can be readily identified from (3.39).

Unpolarized noise case The expression of the Wiener Filter (3.39) simplifies greatly when $w(t)$ can be assumed unpolarized for every frequency. Then $\Gamma_{ww}(\mathbf{v}) = \sigma^2(\mathbf{v}) \in \mathbb{R}^+$ and the quaternion PSD of y is

$$\Gamma_{yy}(\mathbf{v}) = \underbrace{S_{0,x}(\mathbf{v}) + \sigma^2(\mathbf{v})}_{S_{0,y}(\mathbf{v})} + \underbrace{S_{0,x}(\mathbf{v}) \Phi_x(\mathbf{v}) \boldsymbol{\mu}_x(\mathbf{v})}_{S_{0,y}(\mathbf{v}) \Phi_y(\mathbf{v}) \boldsymbol{\mu}_y(\mathbf{v})} \quad (3.40)$$

The polarization axis is not affected by the noise: $\boldsymbol{\mu}_y(\mathbf{v}) = \boldsymbol{\mu}_x(\mathbf{v})$ for all \mathbf{v} . Introduce the frequency-domain signal-to-noise ratio (SNR) $\alpha = S_{0,x}/\sigma^2$. The degree of polarization of the measurement y is then

$$\Phi_y(\mathbf{v}) = \frac{\alpha(\mathbf{v})}{1 + \alpha(\mathbf{v})} \Phi_x(\mathbf{v}). \quad (3.41)$$

The Wiener filter (3.39) then simplifies to

$$\hat{X} = \frac{\alpha + \alpha^2 [1 - \Phi_x^2]}{1 + 2\alpha + \alpha^2 [1 - \Phi_x^2]} \left[Y - \frac{\Phi_x}{1 + \alpha [1 - \Phi_x^2]} \boldsymbol{\mu}_x Y \mathbf{j} \right]. \quad (3.42)$$

The diattenuation axis of the filter is the polarization axis $\boldsymbol{\mu}_x$ of the signal of interest. Homogeneous gain and polarizing power depend on its degree of

This direct link with polarization parameters is one the advantages of the quaternion representation over the usual matrix representation.

On account of second-order stationarity the MSE error is independent from t .

We use the explicit form (3.7) of $\Gamma_{yy}(\mathbf{v}) = \Gamma_{xx}(\mathbf{v}) + \Gamma_{ww}(\mathbf{v})$ to simplify notations:

$$\Gamma_{yy}(\mathbf{v}) = S_{0,y}(\mathbf{v}) [1 + \Phi_y(\mathbf{v}) \boldsymbol{\mu}_y(\mathbf{v})]$$

See Proposition 3.2 for the Hermitian filtering relation.

Remark that for large SNR ($\alpha \gg 1$),

$$\hat{X}(\mathbf{v}) \sim Y(\mathbf{v}) \sim X(\mathbf{v})$$

i.e. the Wiener filter recovers directly the signal of interest x .

polarization Φ_x and on frequency-domain SNR α . In particular, when x is deterministic (hence totally polarized at all frequencies) then the Wiener filter reduces to

$$\hat{X}(v) = \frac{S_{0,x}(v)}{2S_{0,x}(v) + \sigma^2(v)} [Y(v) - \mu_x(v)Y(v)\mathbf{j}]. \quad (3.43)$$

Eq. (3.43) defines a polarizer and validates our initial intuition. Each spectral component of y is projected along the polarization axis $\mu_x(v)$.

Expression of the MMSE The optimal MSE is $\varepsilon_{\text{opt}} = \mathbf{E} \{ |\hat{x}(t) - x(t)|^2 \}$ with $\hat{x}(t)$ given by (3.39). As explained in Appendix 3.D the MMSE can be rewritten as a frequency domain integral

$$\varepsilon_{\text{opt}} = \int_{-\infty}^{+\infty} \varepsilon_{\text{opt}}(v) dv \quad (3.44)$$

where $\varepsilon_{\text{opt}}(v)$ is the MMSE per frequency:

$$\varepsilon_{\text{opt}}(v) = S_{0,x} \left(1 - \frac{S_{0,x}}{S_{0,y}} \frac{1 + \Phi_x^2 - 2\Phi_x \Phi_y \langle \mu_x, \mu_y \rangle}{1 - \Phi_y^2} \right) \quad (3.45)$$

$$= S_{0,x} \frac{1 - \Phi_w^2 + \alpha[1 - \Phi_x^2]}{1 - \Phi_w^2 + \alpha^2[1 - \Phi_x^2] + 2\alpha[1 - \Phi_x \Phi_w \langle \mu_x, \mu_w \rangle]}. \quad (3.46)$$

Eqs (3.45)-(3.46) illustrate the dependence of the optimal error in terms of polarization properties of the signal x , observation y or noise w . Fixing all parameters excepted $\langle \mu_x, \mu_w \rangle$ in (3.46), the optimal error is minimum when signal and noise exhibit orthogonal polarizations, *i.e.* when their polarization axes are anti-aligned $\langle \mu_x, \mu_w \rangle = -1$. The error is maximum when signal and noise have same polarization $\langle \mu_x, \mu_w \rangle = 1$. Given α , asymmetry between minimum and maximum values is accentuated for strongly polarized signal and noise ($\Phi_x, \Phi_w \simeq 1$). For $\alpha \gg 1$ (3.46) becomes $\varepsilon_{\text{opt}}(v) \approx S_{0,x}(v)/\alpha(v)$, while for $\alpha \ll 1$ one gets $\varepsilon_{\text{opt}}(v) \approx S_{0,x}(v)$, as expected. Fig. 3.4 displays this behavior of the optimal MSE in two different configurations. In particular, the optimal MSE ε_{opt} is maximum for $\Phi_w = \Phi_x$ and $\langle \mu_x, \mu_w \rangle = 1$, *i.e.* when the polarization properties of noise and signal coincide.

Example Figs. 3.2c and 3.2d provide an example of Wiener filter denoising. The signal of interest $x(t)$ is taken as the synthesized signal of Fig. 3.2a. It is a partially elliptically polarized narrow-band signal whose spectral density parameters are given in Fig. 3.2b. Measurements $y(t)$ are constructed using (3.37) with $w(t)$ a partially vertically ($\Phi_w = 0.4, \mu_w = -\mathbf{j}$) polarized white Gaussian noise. Noise variance is adjusted so that $\text{SNR} = -5$ dB. Fig. 3.2c represents the measurements $y(t)$. Noise level is larger on the vertical axis because of the partial vertical polarization of $w(t)$. Figure 3.2d shows the output of the Wiener filter. The reconstruction SNR is $10 \log_{10} (\|x(t)\|_2^2 / \|\hat{x}(t) - x(t)\|_2^2) = 9.92$ dB, where $\|\cdot\|_2$ is the standard 2-norm. It illustrates the good performances in recovering the original signal $x(t)$.

3.3.4 Some decompositions of bivariate signals

Given a bivariate signal $x(t)$ we search for its decompositions into 2 parts $x_a(t)$ and $x_b(t)$ such that

$$x(t) = x_a(t) + x_b(t). \quad (3.47)$$

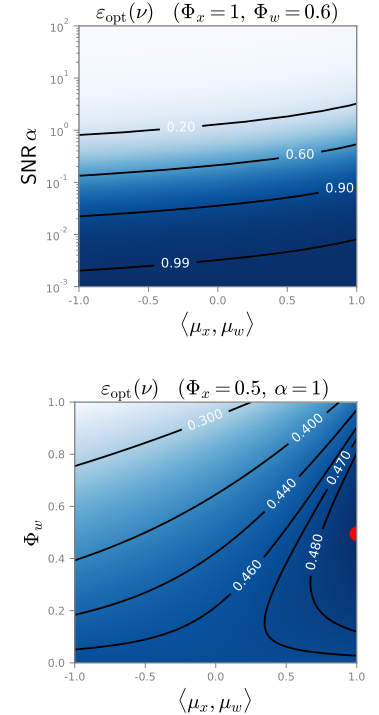


Figure 3.4: Illustrations of the behavior of the optimal MSE per frequency given by (3.45)-(3.46) for $S_{0,x} = 1$. (top) evolution w.r.t. alignment $\langle \mu_x, \mu_w \rangle$ and SNR α in the case ($\Phi_x = 1, \Phi_w = 0.6$) (bottom) evolution w.r.t. alignment $\langle \mu_x, \mu_w \rangle$ and noise degree of polarization Φ_w in the case ($\Phi_x = .5, \alpha = 1$). The red dot indicate the maximum value of the optimal MSE.

The 2 parts $x_a(t)$ and $x_b(t)$ are bivariate signals with distinct spectral properties. They are obtained by linear time-invariant filtering of $x(t)$. The search for such decompositions is motivated by the possible physical interpretations of decomposition (3.47): e.g. *unpolarized - polarized* parts, *orthogonally polarized* parts or *uncorrelated* parts.

Unitary filters do not modify the degree of polarization nor are able to uncorrelate two signals: it is necessary to use a Hermitian filter. The filtering relations read

$$X_a(\mathbf{v}) = K(\mathbf{v}) [X(\mathbf{v}) - \eta(\mathbf{v})\boldsymbol{\mu}_d(\mathbf{v})X(\mathbf{v})\mathbf{j}], \quad (3.48)$$

$$\begin{aligned} X_b(\mathbf{v}) &= X(\mathbf{v}) - X_a(\mathbf{v}) \\ &= [1 - K(\mathbf{v})]X(\mathbf{v}) + \eta(\mathbf{v})K(\mathbf{v})\boldsymbol{\mu}_d(\mathbf{v})X(\mathbf{v})\mathbf{j}. \end{aligned} \quad (3.49)$$

The second part $x_b(t)$ is simply such that (3.47) holds. The choice of the gain $K(\mathbf{v})$, polarizing power $\eta(\mathbf{v})$ and diattenuation axis $\boldsymbol{\mu}_d(\mathbf{v})$ rules the nature of the decomposition (3.47).

Various flavors of unpolarized-polarized decompositions Widely mentioned in optics (Brosseau, 1998; Born and Wolf, 1980), the decomposition of the spectral density of a bivariate signal $x(t)$ as the sum of unpolarized and fully polarized spectral densities is

$$\begin{aligned} \Gamma_{xx}(\mathbf{v}) &= [1 - \Phi_x(\mathbf{v})]S_{0,x}(\mathbf{v}) + \Phi_x(\mathbf{v})S_{0,x}(\mathbf{v})[1 + \boldsymbol{\mu}_x(\mathbf{v})] \\ &= \Gamma_{xx}^u(\mathbf{v}) + \Gamma_{xx}^p(\mathbf{v}), \end{aligned} \quad (3.50)$$

where superscripts u and p stand respectively for *unpolarized* and *polarized* parts. The decomposition (3.50) is unique. It motivates the study of decompositions of the form (3.47) where $x_a(t)$ is fully polarized along $\boldsymbol{\mu}_x(\mathbf{v})$. In addition we shall require that (i) $x_a(t)$ has spectral density $\Gamma_{xx}^p(\mathbf{v})$ and (ii) $x_b(t)$ is unpolarized for every frequency with spectral density $\Gamma_{xx}^u(\mathbf{v})$; Unfortunately no such LTI filter performing exactly this decomposition exists. Each requirement corresponds to a distinct filter: only one requirement at a time can be met.

The requirement for $x_a(t)$ to be fully polarized along $\boldsymbol{\mu}_x(\mathbf{v})$ imposes that $\eta(\mathbf{v}) = 1$ and $\boldsymbol{\mu}_d(\mathbf{v}) = \boldsymbol{\mu}_x(\mathbf{v})$ for every \mathbf{v} . Then the choice of the gain $K(\mathbf{v})$ permits to satisfy either condition (i) or (ii).

Table 3.1 summarizes expressions of the gain and spectral densities of $x_a(t)$ and $x_b(t)$ for requirements (i) and (ii). We also give their cross-correlation properties. To meet (i) the gain $K(\mathbf{v})$ is adjusted thanks to (3.16) such that $\Gamma_{x_a, x_a}(\mathbf{v}) = \Gamma_{xx}^p(\mathbf{v})$. However $x_b(t)$ is partially polarized and components are correlated. For (ii) starting from (3.49) and using (3.17) with $\boldsymbol{\mu}_d(\mathbf{v}) = -\boldsymbol{\mu}_x(\mathbf{v})$ one computes the vector part of $\Gamma_{x_b, x_b}(\mathbf{v})$. Then the gain $K(\mathbf{v})$ is obtained by imposing $\Phi_b(\mathbf{v}) = 0$ for every \mathbf{v} . Fortunately the corresponding expression for $K(\mathbf{v})$ yields $\Gamma_{x_b, x_b}(\mathbf{v}) = \Gamma_{xx}^u(\mathbf{v})$. The first component $x_a(t)$ is fully polarized like $x(t)$, but has weaker intensity than that of $\Gamma_{xx}^p(\mathbf{v})$. Components are also correlated.

This discussion answers an important and natural question: starting from (3.50), is it possible to decompose by linear filtering any bivariate signal into uncorrelated unpolarized and polarized components? Unfortunately the answer is negative. The uncorrelatedness requirement leads to a very different

This decomposition was already introduced in Section 2.3.2.

	$K(\nu)$	$\Gamma_{x_a, x_a}(\nu)$	$\Gamma_{x_b, x_b}(\nu)$	correlation
(i)	$\sqrt{\frac{\Phi_x(\nu)}{2(1+\Phi_x(\nu))}}$	$S_{0,x}(\nu)\Phi_x(\nu)[1+\boldsymbol{\mu}_x(\nu)]$	$\kappa(\nu)S_{0,x}(\nu)[1-\Phi(\nu)\boldsymbol{\mu}_x(\nu)]$	correlated
			with $\kappa(\nu) = \frac{(1+\Phi_x(\nu) - 2(\Phi_x(\nu)+1)K(\nu))}{1+\Phi_x(\nu) - 2[\Phi_x(\nu)+1]K(\nu)}$ $\Phi(\nu) = \frac{1-2\Phi_x(\nu) + 2[\Phi_x(\nu)+1]K(\nu)}{1+\Phi_x(\nu) - 2[\Phi_x(\nu)+1]K(\nu)}$	
(ii)	$1 - \frac{\Phi_x(\nu)}{\Phi_x(\nu) + 1 - \sqrt{1-\Phi_x^2(\nu)}}$	$2S_{0,x}(\nu)K^2(\nu)[1+\Phi_x(\nu)][1+\boldsymbol{\mu}_x(\nu)]$	$S_{0,x}(\nu)[1-\Phi_x(\nu)]$	correlated

answer, as explained below. Nevertheless this hypothetical decomposition can still be used as a synthesis tool, see *e.g.* the synthesis method of bivariate wGn described in Section 2.3.4.

Orthogonal polarizations decomposition In many situations it is useful to resolve bivariate signals into a pair of orthogonal fully polarized components, *e.g.* linear horizontal and vertical polarization. This decomposition can be generalized to any arbitrary polarization axis $\boldsymbol{\mu}(\nu)$, possibly frequency-dependent. Note that for $\boldsymbol{\mu}(\nu) = \pm \mathbf{i}$ one obtains the decomposition of $x(t)$ into counter-clockwise and clockwise circular polarization. This is precisely the *rotary components* widely used in both signal processing and oceanographic communities, see *e.g.* Gonella (1972) or Walden (2013).

The two parts $x_a(t)$ and $x_b(t)$ are obtained by Hermitian filters with respective axis $\boldsymbol{\mu}(\nu)$ and $-\boldsymbol{\mu}(\nu)$. Since $x_a(t)$ and $x_b(t)$ are required to be fully polarized this imposes that (3.48) and (3.49) defines *polarizers*. Then one has directly $\eta(\nu) = 1$ from (3.48). Eq. (3.48) constrains the value of the gain to $K(\nu) = \frac{1}{2}$. The quaternion PSD of the two parts are then

$$\Gamma_{x_a x_a}(\nu) = \frac{S_{0,x}(\nu)}{2} [1 + \Phi_x(\nu) \langle \boldsymbol{\mu}_x(\nu), \boldsymbol{\mu}(\nu) \rangle] [1 + \boldsymbol{\mu}(\nu)], \quad (3.51)$$

$$\Gamma_{x_b x_b}(\nu) = \frac{S_{0,x}(\nu)}{2} [1 - \Phi_x(\nu) \langle \boldsymbol{\mu}_x(\nu), \boldsymbol{\mu}(\nu) \rangle] [1 - \boldsymbol{\mu}(\nu)]. \quad (3.52)$$

Parts $x_a(t)$ and $x_b(t)$ are in general correlated with quaternion cross-spectral power density given by

$$\Gamma_{x_a x_b}(\nu) = \frac{\Phi_x(\nu)}{4} [\boldsymbol{\mu}_x(\nu) \boldsymbol{\mu}(\nu) - \boldsymbol{\mu}(\nu) \boldsymbol{\mu}_x(\nu)] [1 - \boldsymbol{\mu}(\nu)]. \quad (3.53)$$

Uncorrelated parts Another possibility is to impose $x_a(t)$ and $x_b(t)$ to be uncorrelated. This is expressed in the spectral domain by

$$\forall \nu, \quad \Gamma_{x_a, x_b}(\nu) = \Gamma_{x_b, x_a}(\nu) = 0. \quad (3.54)$$

Suppose that $\eta(\nu) > 0$ for all ν . Using the filters expressions (3.48)–(3.49) a direct calculation shows that (3.54) implies that

$$\forall \nu, \quad K(\nu) = \frac{1}{2} \quad \text{and} \quad \eta(\nu) = 1. \quad (3.55)$$

These are the same parameters as for the orthogonal polarization decomposition: $\Gamma_{x_a, x_b}(\nu)$ is given by (3.53). If $x(t)$ is unpolarized at each frequency, then any choice of diattenuation axis $\boldsymbol{\mu}$ will provide $x_a(t)$ and $x_b(t)$ uncorrelated. Otherwise, it is easy to check that (3.53) is identically zero if and only

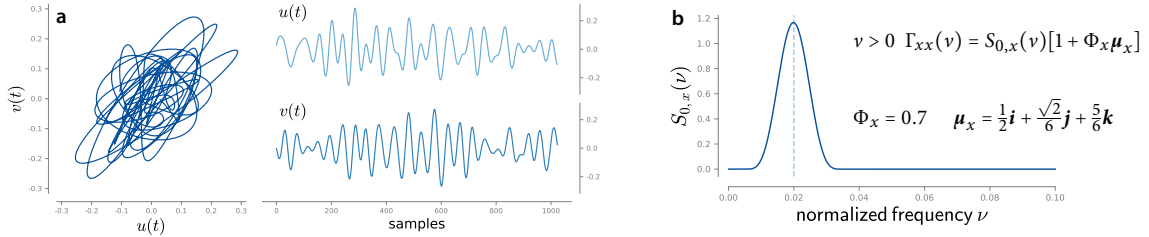
Table 3.1: Various flavors of unpolarized-polarized parts decompositions. The choice of the gain $K(\nu)$ rules the nature of the decomposition of a bivariate signal x into two parts x_a and x_b such that $x(t) = x_a(t) + x_b(t)$. (Here $\boldsymbol{\mu}_d(\nu) = \boldsymbol{\mu}_x(\nu)$ and $\eta(\nu) = 1$.)

When $\eta(\nu) = 0$ for all ν there is no geometric interaction. Uncorrelatedness is then expressed as in the usual univariate case:

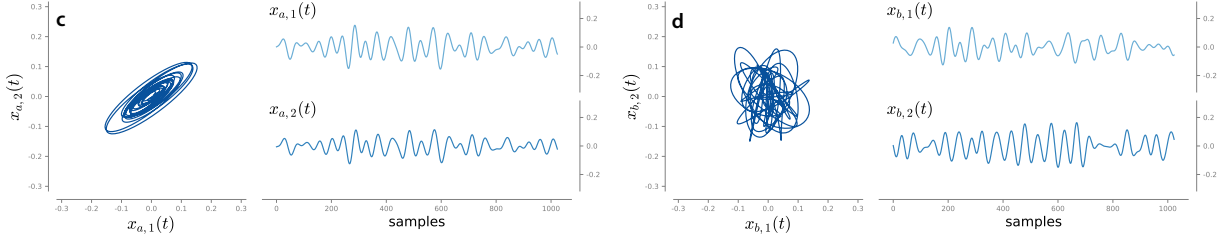
$$\forall \nu, \quad \Gamma_{x_a, x_b}(\nu) = [1 - K(\nu)] K(\nu) \Gamma_{xx}(\nu) = 0$$

which is immediately satisfied if the gain $K(\nu)$ is either 1 or 0 for all frequencies.

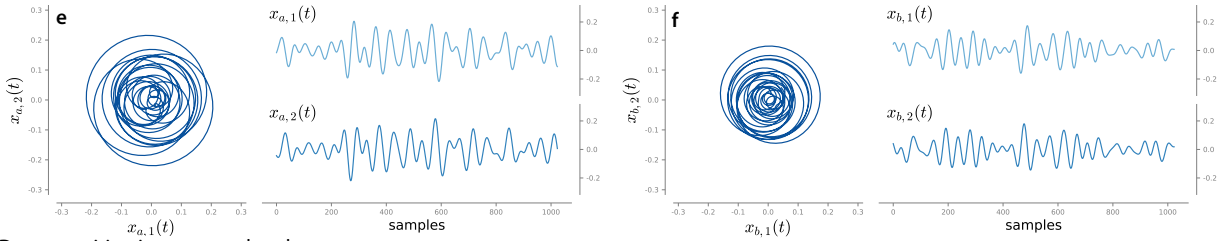
Original signal



Decomposition into unpolarized and polarized parts



Decomposition into orthogonal circularly polarized components



Decomposition into uncorrelated components

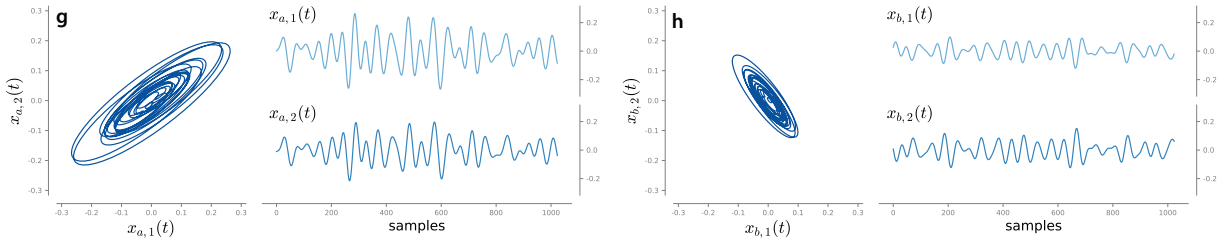


Figure 3.5: Three different decompositions of the bivariate signal represented in **a**. See text for details.

if $\boldsymbol{\mu}_d(\nu) = \pm \boldsymbol{\mu}_x(\nu)$ for all ν . This means that $x_a(t)$ and $x_b(t)$ are the *eigenpolarizations* of $x(t)$: fully polarized signals with orthogonal polarization axes $\pm \boldsymbol{\mu}_x(\nu)$. Their respective spectral densities³ are for $\boldsymbol{\mu}_d(\nu) = \boldsymbol{\mu}_x(\nu)$

$$\Gamma_{x_a x_a}(\nu) = \frac{S_{0,x}(\nu)}{2} [1 + \Phi_x(\nu)] [1 + \boldsymbol{\mu}_x(\nu)] \quad (3.56)$$

$$\Gamma_{x_b x_b}(\nu) = \frac{S_{0,x}(\nu)}{2} [1 - \Phi_x(\nu)] [1 - \boldsymbol{\mu}_x(\nu)] \quad (3.57)$$

The power of each part is balanced by the degree of polarization $\Phi_x(\nu)$.

Illustrations Fig. 3.5 illustrates the three kind of decompositions presented in this section. Fig. 3.5a depicts the signal to be decomposed – which has been previously studied in Fig. 3.2. Its spectral properties are given in Fig. 3.2b. Fig. 3.5c and 3.5d represent the *unpolarized-polarized* parts decomposition of $x(t)$. It corresponds to case (ii) in Table 3.1. Note that the two parts are correlated. Fig. 3.5e and 3.5f illustrate the decomposition of $x(t)$ into orthogonal circularly polarized components. This is precisely the celebrated *rotary component* decomposition. These two components are also correlated. Fig. 3.5g and 3.5h

3. The choice of $\boldsymbol{\mu}_d(\nu) = -\boldsymbol{\mu}_x(\nu)$ simply swaps the role of x_a and x_b .

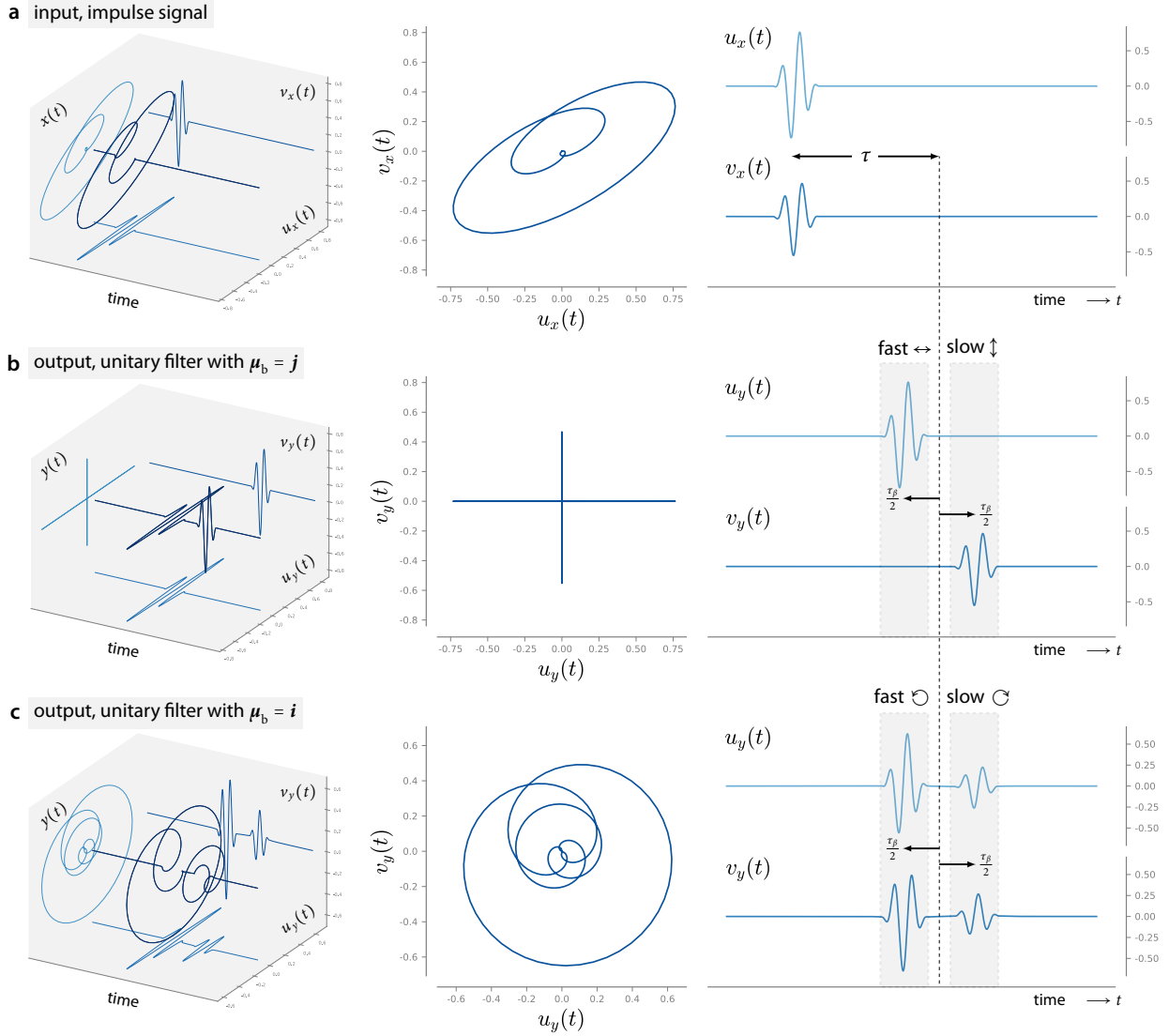


Figure 3.6: Illustration of shear wave splitting. (a) the elliptically polarized impulse input. (b) corresponding unitary filter output for $\mu_b = j$. (c) corresponding unitary filter output for $\mu_b = i$. The two filters have common birefringence angle $\beta(v) = 2\pi v\tau_\beta$. The interaction between a polarized impulse signal and a birefringent media exhibiting first-order PMD causes the output signal to separate into the fast and slow eigenpolarizations of the filter.

finally give the *uncorrelated* parts decomposition of $x(t)$. The two parts are orthogonally polarized, along μ_x and $-\mu_x$, respectively.

3.3.5 Modeling Polarization Mode Dispersion

So far only applications involving Hermitian filters have been presented. As a prospect, we explore now the potential of unitary filters to model *polarization mode dispersion* (PMD). This linear phenomenon is of fundamental importance in many fields of application such as geophysical monitoring or fiber telecommunications. PMD appears when birefringence is a function of the frequency: variations of birefringence angle $\beta(v)$ and birefringence axis $\mu(v)$ introduce specific and intriguing effects. We review two popular phenomenons. The first is *shear wave splitting* – one manifestation of PMD in geophysical sciences, see e.g. Silver and Chan (1991), Silver and Savage (1994), and Wolfe and Silver (1998). The second is *pulse distortion*, which arises in optical telecommunications when the optical fiber is subject to PMD, see e.g.

Poole and Wagner (1986), Karlsson (1998), Gordon and Kogelnik (2000), and Damask (2004).

These two examples illustrate the potential of the approach to model and understand distinctive physical effects relevant to bivariate signals. More importantly, together with adequate identification methods, the proposed framework would allow to extract meaningful information about a material structure, using *e.g.* measurements exhibit shear-wave splitting. It would also provide a complete toolbox for the design of compensators of PMD-induced distortion in optical fibers. One can expect to reduce *e.g.* the impact of PMD on the transmission rate.

Shear wave splitting We consider the propagation of a narrow-band polarized pulse $x(t)$ through birefringent media. The effects of birefringent media onto the signal can be modeled by a unitary filter. Let $x(t)$ be defined by

$$x(t) = \text{Proj}_{\mathbb{C}_i} \left\{ a(t) e^{i\theta} e^{-k\chi} e^{j2\pi\nu_0 t} \right\} \quad (3.58)$$

where $a(t)$ is the pulse envelope, θ and χ define the signal polarization state and ν_0 is the mean frequency of the pulse. Consider a unitary filter with parameters $\beta(\nu)$, $\mu_b(\nu)$ and $\varphi(\nu)$. The phase delay is related to the mean time τ of propagation in the media such that $\varphi(\nu) = -2\pi\nu\tau$. The simplest form of PMD is first order PMD:

$$\beta(\nu) = 2\pi\nu\tau_\beta, \quad \forall \nu > 0 \quad (3.59)$$

and with constant birefringence axis $\mu_b(\nu) = \mu_b$ for positive frequencies. To give an explicit expression for the output $y(t)$ of the filter, we first decompose $x(t)$ into orthogonal polarizations defined by the eigenpolarizations of the filter μ_b and $-\mu_b$:

$$x(t) = x_{\mu_b}(t) + x_{-\mu_b}(t). \quad (3.60)$$

Then, by the eigenpolarization properties (3.13)–(3.14) of the unitary filter

$$Y(\nu) = X_{\mu_b}(\nu) e^{-j2\pi\nu(\tau - \frac{\tau_\beta}{2})} + X_{-\mu_b}(\nu) e^{-j2\pi\nu(\tau + \frac{\tau_\beta}{2})}, \quad (3.61)$$

so that the output $y(t)$ reads explicitly

$$y(t) = x_{\mu_b} \left(t - \tau + \frac{\tau_\beta}{2} \right) + x_{-\mu_b} \left(t - \tau - \frac{\tau_\beta}{2} \right). \quad (3.62)$$

Eq. (3.62) shows that the output y is the superposition of the two orthogonally polarized parts of x with different delays. If τ_β is sufficiently large compared to the support of the signal (controlled by the envelope $a(t)$) one will observe *polarization splitting* or *shear-wave splitting*: orthogonally polarized components corresponding to eigenpolarizations of the filter will be “separated” by the unitary filter.

Fig. 3.6 illustrates this phenomenon for two different choices of the birefringence axis μ_b . Fig. 3.6a shows the elliptically polarized input signal. Fig. 3.6b displays the corresponding output for $\mu_b = \mathbf{j}$, *i.e.* the fast and slow eigenpolarizations are linear horizontal polarization and linear vertical polarization. Fig. 3.6c depicts the corresponding output for $\mu_b = \mathbf{i}$, *i.e.* the fast and slow eigenpolarizations are counter-clockwise circular polarization and clockwise circular polarization. In both cases one observes a mean delay τ and more

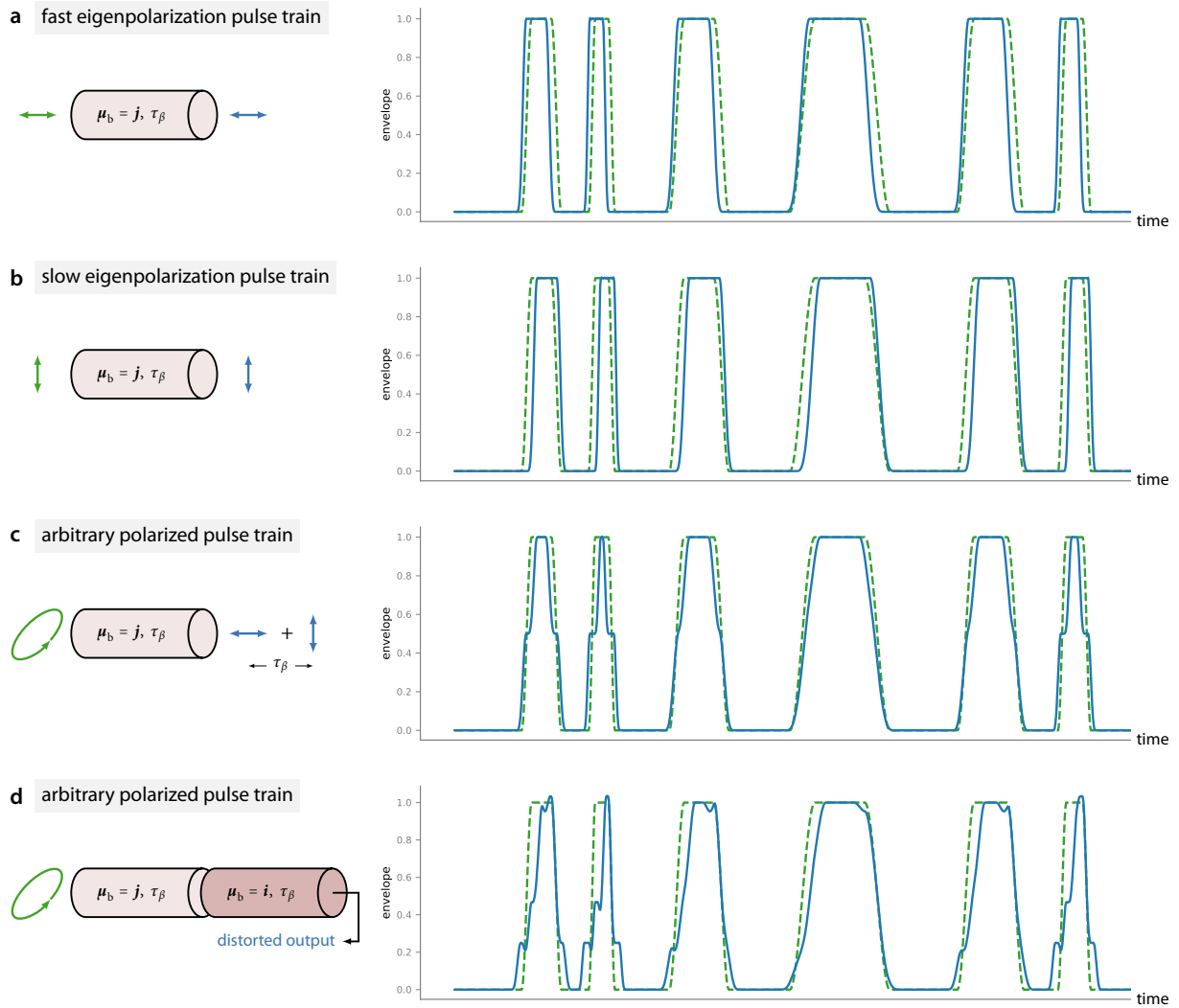


Figure 3.7: Illustration of pulse distortion induced by PMD in single-mode optical fibers. See text for details.

importantly, a splitting of the input signal into the two eigenpolarizations of the filter. The separation between these two orthogonally polarized components is controlled by τ_β : the larger τ_β is, the larger the separation. These two cases confirm the expression (3.62) of the output $y(t)$ for first-order PMD.

Pulse distortion in single-mode optical fibers As another illustration of the critical importance of PMD, we consider optical pulse transmission in single-mode optical fibers. PMD in optical fibers can arise as a result of stress-induced birefringence (Poole and Wagner, 1986; Damask, 2004). It causes pulse distortion leading to many impairments, such as transmission rate reduction (Francia et al., 1998; Gordon and Kogelnik, 2000).

Fig. 3.7a and 3.7b represent transmitted pulse trains (blue lines) along fast and slow eigenpolarizations, respectively. Green dashed lines indicate the initial pulse train. Only envelopes are represented for simplicity. The filter exhibits first-order PMD with birefringence axis $\mu = j$. Note that value of τ_α in optical fibers is typically much smaller than in shear wave splitting. Fig. 3.7c depicts the distorted pulse train obtained when the input polarization is

elliptic, *i.e.* is not aligned with one of the eigenpolarizations of the filter. We observe that, due to PMD, the output pulses tends to broaden and are distorted. This effect is accentuated for short pulses.

Fig. 3.7d illustrates the effects of the concatenation of two optical fiber segments that exhibits first order PMD – but with nonaligned eigenpolarizations. This is a typical case in optical telecommunications. It is known (Damask, 2004) that such concatenation can lead to higher-order PMD effects, increasing distortion (Damask, 2004). The pulse train has the same elliptical polarization as in Fig. 3.7c. It passes through a concatenation of two unitary filters with respective axis $\boldsymbol{\mu} = \mathbf{j}$ (fast axis: linear horizontal polarization) and $\boldsymbol{\mu} = \mathbf{i}$ (fast axis: counter- clockwise circular polarization). Both filters have the same value for τ_α . Remarkably this simple concatenation already yields dramatic distortion of the input pulse train.

3.4 CONCLUSION

This chapter introduced a complete and powerful description of the linear time-invariant filtering of bivariate signals in the quaternion Fourier transform framework. Unlike standard approaches based on linear algebra, it features a direct description of filtering in terms of physical quantities borrowed from polarization optics. Building on an usual decomposition from polarization optics, a generic LTI filter is described as a combination of two distinct filters: a unitary and a Hermitian one. The detailed study of these two classes of filters enables strong physical interpretations in terms of birefringence and diattenuation effects, as well as a powerful geometric handling of linear filtering. The proposed formalism reveals the specificity of bivariate signals and is crucial to the physical understanding of even basic operations such as linear filtering. The natural and elegant expression of each filter directly in terms of its eigenproperties and relevant physical parameters simplifies modeling, design, calculations and interpretations. It makes straightforward many standard operations that would be otherwise complicated to obtain using conventional approaches presented in Section 0.2.3 and Sections 0.2.4, *e.g.* widely linear filtering. The efficient numerical implementation of the QFT (based on 2 FFTs) guarantees practical and computationally fast filtering relations.

Several fundamental applications of signal processing demonstrate the generality and usefulness of the approach. A spectral synthesis method to simulate any Gaussian stationary random bivariate signal with desired spectral and polarization properties has been presented. It has been shown that the Wiener denoising problem can be efficiently designed in the quaternion domain, leading to new interpretations for the bivariate case. Original decompositions of bivariate signals into two parts with specific properties (orthogonal polarizations, unpolarized and polarized, uncorrelated) have been studied. The potential of unitary filters to model physical effects relevant to *optical fiber telecommunications*, *e.g. polarization mode dispersion* has been illustrated.

This complete description of linear filtering theory paves the way to further developments in estimation, detection simulation and modeling of bivariate signals. It has been accepted for publication in an international journal (Flamant, Chainais, and Le Bihan, 2018a) and has been presented at an international conference (Flamant, Chainais, and Le Bihan, 2018b).

APPENDICES

3.A OUTPUT-INPUT CROSS-SPECTRAL PROPERTIES

Let $x(t)$ and $y(t)$ denote the input and output of a LTI filter, respectively. Suppose that both x and y are second-order stationary and harmonizable, so that their quaternion-valued spectral representation is given by Theorem 2.1. The cross-spectral properties between y and x are encoded by the quaternion cross-spectral power density Γ_{yx} defined Section 2.2.4. We give an explicit expression for Γ_{yx} for unitary and Hermitian filters. These results are of practical interest for the identification of filter parameters as discussed in Section 3.B.

Unitary filters The unitary filtering relation (3.8) becomes for harmonizable signals

$$dY(\mathbf{v}) = e^{\mu_b(\mathbf{v})\frac{\beta(\mathbf{v})}{2}} dX(\mathbf{v}) e^{j\varphi(\mathbf{v})} \quad (3.63)$$

Then by definition of Γ_{yx} , see Eq. (2.29) one gets

$$\Gamma_{yx} = \mathbf{E} \{ dY d\bar{X} \} + \mathbf{E} \{ dY j d\bar{X} \} \quad (3.64)$$

$$\stackrel{(3.63)}{=} e^{\mu_b\frac{\beta}{2}} \mathbf{E} \{ dX e^{j\varphi} d\bar{X} \} + e^{\mu_b\frac{\beta}{2}} \mathbf{E} \{ dX e^{j\varphi} j d\bar{X} \} \quad (3.65)$$

$$= e^{\mu_b\frac{\beta}{2}} \left[\cos \varphi \left(\mathbf{E} \{ |dX|^2 \} + \mathbf{E} \{ |dX j d\bar{X}| \} \right) - \sin \varphi \left(\mathbf{E} \{ |dX|^2 \} - \mathbf{E} \{ |dX j d\bar{X}| \} \right) \right] \quad (3.66)$$

which yields the final result in compact form:

$$\Gamma_{yx} = e^{\mu_b\frac{\beta}{2}} \left(\cos \varphi \Gamma_{xx} - \sin \varphi \overline{\Gamma_{xx}} \right). \quad (3.67)$$

Hermitian filters We proceed as above. The Hermitian filtering relation (3.15) becomes for harmonizable signals

$$dY(\mathbf{v}) = K(\mathbf{v}) [dX(\mathbf{v}) - \eta(\mathbf{v}) \boldsymbol{\mu}_d(\mathbf{v}) dX(\mathbf{v}) \mathbf{j}] \quad (3.68)$$

Dropping again frequency dependence for convenience, the quaternion cross-spectral power density Γ_{yx} reads

$$\Gamma_{yx} = \mathbf{E} \{ dY d\bar{X} \} + \mathbf{E} \{ dY j d\bar{X} \} \quad (3.69)$$

$$\stackrel{(3.68)}{=} K \left[\mathbf{E} \{ |dX|^2 \} - \eta \boldsymbol{\mu}_d \mathbf{E} \{ dX j d\bar{X} \} + \mathbf{E} \{ dX j d\bar{X} \} + \eta \boldsymbol{\mu}_d \mathbf{E} \{ |dX|^2 \} \right] \quad (3.70)$$

which gives the final result

$$\Gamma_{yx} = K \left[\Gamma_{xx} + \eta \boldsymbol{\mu}_d \overline{\Gamma_{xx}} \right]. \quad (3.71)$$

We drop frequency dependence for notational convenience.

3.B FILTER IDENTIFICATION USING UNPOLARIZED WHITE GAUSSIAN NOISE

We now discuss a practical identification method which uses the cross-spectral properties between the *output* y and *input* x when the input is unpolarized white Gaussian noise. The method uses the quaternion cross-spectral power density expressions for unitary and Hermitian filters given in Appendix 3.A. Let x be an unpolarized bivariate white Gaussian noise. Its quaternion PSD is

$\Gamma_{xx}(\mathbf{v}) = \sigma^2$ where σ^2 is the noise variance. Plugging Γ_{xx} into (3.67) one finds for the unitary filter

$$\Gamma_{yx}(\mathbf{v}) = \sigma^2 \sqrt{2} \sin \left[\frac{\pi}{4} - \varphi(\mathbf{v}) \right] e^{\mu_b(\mathbf{v}) \frac{\beta(\mathbf{v})}{2}}. \quad (3.72)$$

The quaternion polar form of (3.72) gives directly access to the parameters of the filter: μ_b, β are given by the axis and angle of Γ_{yx} and φ is related to the modulus of Γ_{yx} like

$$|\Gamma_{yx}(\mathbf{v})| = \sigma^2 \sqrt{2} \left| \sin \left[\frac{\pi}{4} - \varphi(\mathbf{v}) \right] \right|. \quad (3.73)$$

The phase $\varphi(\mathbf{v})$ is not uniquely defined. This minor technical issue can be solved by imposing continuity constraints on filter parameters using that (i) e.g. sign changes of $\varphi(\mathbf{v})$ can be compensated by phase unwrapping of $\beta(\mathbf{v})$ into $\varphi(\mathbf{v})$ and (ii) using the fact that $\varphi(0) = 0$ on account of the symmetry $\varphi(-\mathbf{v}) = -\varphi(\mathbf{v})$, see Proposition 3.1.

For Hermitian filters, the identification is straightforward. Inserting $\Gamma_{xx}(\mathbf{v}) = \sigma^2$ in (3.71) one finds that

$$\Gamma_{yx}(\mathbf{v}) = \sigma^2 K(\mathbf{v}) [1 + \eta(\mathbf{v}) \mu_d(\mathbf{v})]. \quad (3.74)$$

Filters parameters are then obtained in cascade by relations

$$K(\mathbf{v}) = \frac{1}{\sigma^2} \mathcal{S}(\Gamma_{yx}(\mathbf{v})) \quad (3.75)$$

$$\eta(\mathbf{v}) = \frac{1}{\sigma^2 K(\mathbf{v})} |\mathcal{V}(\Gamma_{yx}(\mathbf{v}))| \quad (3.76)$$

$$\mu_d(\mathbf{v}) = \frac{1}{\sigma^2 K(\mathbf{v}) \eta(\mathbf{v})} \mathcal{V}(\Gamma_{yx}(\mathbf{v})) \quad (3.77)$$

Note that $\mu_d(\mathbf{v})$ is not defined when $\eta(\mathbf{v}) = 0$ or $K(\mathbf{v}) = 0$. Similarly, $\eta(\mathbf{v})$ is undefined for $K(\mathbf{v}) = 0$.

3.C LINEAR ALGEBRA AND QUATERNION EQUIVALENCE

3.C.1 Matrix-vector and quaternion operations

Eq. (3.1) shows that quaternions can be represented as complex \mathbb{C}_j -vectors. Let $\mathbf{X} = [X_1, X_2]^T$ and $\mathbf{Y} = [Y_1, Y_2]^T$ be complex \mathbb{C}_j -vectors corresponding to quaternions $X = X_1 + \mathbf{i}X_2$ and $Y = Y_1 + \mathbf{i}Y_2$. The most generic linear transform of \mathbb{C}_j^2 is given by the matrix-vector relation $\mathbf{Y} = \mathbf{M}\mathbf{X}$, where $\mathbf{M} \in \mathbb{C}_j^{2 \times 2}$ is an arbitrary 2-by-2 complex matrix.

The corresponding relation between quaternions Y and X is obtained by writing explicitly the matrix-vector relation

$$\begin{pmatrix} Y_1 \\ Y_2 \end{pmatrix} = \begin{pmatrix} a & b \\ c & d \end{pmatrix} \begin{pmatrix} X_1 \\ X_2 \end{pmatrix} = \begin{pmatrix} aX_1 + bX_2 \\ cX_1 + dX_2 \end{pmatrix} \quad (3.78)$$

where $a, b, c, d \in \mathbb{C}_j$. Using (3.1) and that for any $q = q_1 + \mathbf{i}q_2 \in \mathbb{H}$, $q_1, q_2 \in \mathbb{C}_j$ one has $q_1 = (q + \bar{q}^j)/2$ and $\mathbf{i}q_2 = (q - \bar{q}^j)/2$:

$$\begin{aligned} Y &= Y_1 + \mathbf{i}Y_2 = aX_1 + bX_2 + \mathbf{i}(cX_1 + dX_2) \\ &= \frac{1}{2} (a - b\mathbf{i} + \mathbf{i}c - \mathbf{i}d\mathbf{i}) X \\ &\quad - \frac{1}{2} (a + b\mathbf{i} + \mathbf{i}c + \mathbf{i}d\mathbf{i}) \mathbf{j}X\mathbf{j}. \end{aligned} \quad (3.79)$$

Eq. (3.79) is the quaternion domain representation of a generic linear transform of vectors of \mathbb{C}_j^2 .

3.C.2 Unitary transforms

Let $\underline{\mathbf{U}} \in \mathbf{U}(2) \subset \mathbb{C}_j^{2 \times 2}$, i.e. such that $\underline{\mathbf{U}}\underline{\mathbf{U}}^* = \underline{\mathbf{U}}^*\underline{\mathbf{U}} = \underline{\mathbf{I}}_2$. Remark that $\underline{\mathbf{U}} = \underline{\tilde{\mathbf{U}}}\det(\underline{\mathbf{U}})$ where $\underline{\tilde{\mathbf{U}}} \in \mathbf{SU}(2)$ and $\det \underline{\mathbf{U}} = \exp(j\varphi) \in \mathbb{C}_j$.

Using notations from (3.78), the matrix $\underline{\tilde{\mathbf{U}}}$ is characterized by $d = \bar{a}$, $c = -\bar{b}$ and $|a|^2 + |b|^2 = 1$. Thus (3.79) simplifies for $\underline{\tilde{\mathbf{U}}}$ to

$$Y = (a - b\mathbf{i})X = \exp(\mu_b\beta/2)X. \quad (3.80)$$

Since $|a|^2 + |b|^2 = 1$, $a - b\mathbf{i}$ is a unit quaternion which can be reparameterized in polar form by its axis μ_b and angle β such that

$$\mu_b = \frac{-i\operatorname{Re} b + j\operatorname{Im}_j a + k\operatorname{Im}_j b}{|-i\operatorname{Re} b + j\operatorname{Im}_j a + k\operatorname{Im}_j b|}, \quad (3.81)$$

$$\beta = 2 \arccos \operatorname{Re} a \quad (3.82)$$

Back to $\underline{\mathbf{U}} \in \mathbf{U}(2)$, remark that

$$\mathbf{Y} = \underline{\mathbf{U}}\mathbf{X} = \underline{\tilde{\mathbf{U}}}\begin{bmatrix} X_1 e^{j\varphi} \\ X_2 e^{j\varphi} \end{bmatrix}, \quad (3.83)$$

so that replacing X by the quaternion $Xe^{j\varphi}$ in (3.80) yields,

$$\text{For } \underline{\mathbf{U}} \in \mathbf{U}(2), \mathbf{Y} = \underline{\mathbf{U}}\mathbf{X} \iff Y = e^{\mu_b \frac{\beta}{2}} X e^{j\varphi}. \quad (3.84)$$

3.C.3 Hermitian transforms

Let $\underline{\mathbf{H}}$ be Hermitian, i.e. such that $\underline{\mathbf{H}}^\dagger = \underline{\mathbf{H}}$. Using notations from (3.78) one has $a, d \in \mathbb{R}$ and $c = -\bar{b} \in \mathbb{C}_j$. Positive semidefiniteness is given by Sylvester Criterion: $a \geq 0$ $ad - |b|^2 \geq 0$, which also implies that $d \geq 0$. Eq. (3.79) becomes

$$Y = \frac{1}{2}(a + d)X - \frac{1}{2}(2b\mathbf{k} + (a - d)\mathbf{j})X\mathbf{j} \quad (3.85)$$

which can be reparameterized such as

$$K = \frac{a + d}{2} \in \mathbb{R}^+ \quad (3.86)$$

$$\mu_d = \frac{(a - d)\mathbf{j} + 2b\mathbf{k}}{[(a - d)^2 + 4|b|^2]^{1/2}}, \quad \mu_d^2 = -1 \quad (3.87)$$

$$\eta = \frac{[(a - d)^2 + 4|b|^2]^{1/2}}{a + d} \in [0, 1] \quad (3.88)$$

Respective domains of K, μ_d, η ensure that the change of variable defines a valid one-to-one mapping. Finally, the input-output relation reads

$$Y = K(X - \eta\mu_d X\mathbf{j}). \quad (3.89)$$

Parameters K and η can be expressed in terms of eigenvalues λ_1, λ_2 ($\lambda_1 \geq \lambda_2 \geq 0$) of the matrix $\underline{\mathbf{M}}$:

$$K = \frac{\lambda_1 + \lambda_2}{2} \quad \eta = \frac{\lambda_1 - \lambda_2}{\lambda_1 + \lambda_2}. \quad (3.90)$$

3.D WIENER FILTER DERIVATION

We keep notations from Section 3.3.3. Let $\mathbf{y}(t)$, $\hat{\mathbf{x}}(t)$, $\mathbf{x}(t)$ denote \mathbb{C}_j^2 -vector representations of quaternion-valued signals $y(t)$, $\hat{x}(t)$ and $x(t)$. Remark that (3.38) is equivalent to its vector form:

$$\min \mathbf{E} \{ \|\hat{\mathbf{x}}(t) - \mathbf{x}(t)\|^2 \}, \quad (3.91)$$

where $\|\cdot\|$ is the Euclidean norm of \mathbb{C}_j^2 . The solution to (3.91) in the Fourier domain is well known, see e.g. Schreier and Scharf (2010):

$$\hat{\mathbf{X}}(\mathbf{v}) = \underline{\mathbf{P}}_{\mathbf{xy}}(\mathbf{v}) \underline{\mathbf{P}}_{\mathbf{yy}}^{-1}(\mathbf{v}) \mathbf{Y}(\mathbf{v}) \quad (3.92)$$

where $\underline{\mathbf{P}}_{\mathbf{xy}}(\mathbf{v})$, $\underline{\mathbf{P}}_{\mathbf{yy}}(\mathbf{v})$ are the usual (cross-) spectral density matrices of $\mathbf{x}(t)$, $\mathbf{y}(t)$, respectively. The Wiener filter for the denoising problem (3.37) is

$$\hat{\mathbf{X}}(\mathbf{v}) = \underline{\mathbf{P}}_{\mathbf{xx}}(\mathbf{v}) \underline{\mathbf{P}}_{\mathbf{yy}}^{-1}(\mathbf{v}) \mathbf{Y}(\mathbf{v}) \quad (3.93)$$

Eq. (3.93) shows that $\hat{\mathbf{X}}(\mathbf{v})$ is obtained from $\mathbf{Y}(\mathbf{v})$ by 2 successive Hermitian filters, since spectral density matrices are Hermitian – and so are their sum and inverse. Introducing an intermediate variable \mathbf{Z} one gets

$$\mathbf{Z}(\mathbf{v}) = \underline{\mathbf{P}}_{\mathbf{yy}}^{-1}(\mathbf{v}) \mathbf{Y}(\mathbf{v}) \quad (3.94)$$

$$\hat{\mathbf{X}}(\mathbf{v}) = \underline{\mathbf{P}}_{\mathbf{xx}}(\mathbf{v}) \mathbf{Z}(\mathbf{v}) \quad (3.95)$$

Quaternions equivalents are readily obtained using (3.79) and definitions of matrix spectral densities in terms of Stokes parameters S_i , $i = 0, 1, 2, 3$ (see Eqs. (2.38)–(2.41))

$$\begin{aligned} Z(\mathbf{v}) &= 2 \left[(1 - \Phi_y^2(\mathbf{v})) S_{0,y}(\mathbf{v}) \right]^{-1} \\ &\quad \times \left(Y(\mathbf{v}) + \Phi_y(\mathbf{v}) \boldsymbol{\mu}_y(\mathbf{v}) Y(\mathbf{v}) \mathbf{j} \right) \end{aligned} \quad (3.96)$$

$$\hat{\mathbf{X}}(\mathbf{v}) = 2^{-1} S_{0,x}(\mathbf{v}) \left(Z(\mathbf{v}) - \boldsymbol{\mu}_x(\mathbf{v}) \Phi_x(\mathbf{v}) Z(\mathbf{v}) \mathbf{j} \right) \quad (3.97)$$

since Stokes parameters and polarization axis are related like $S_0 \Phi \boldsymbol{\mu} = \mathbf{i} S_3 + \mathbf{j} S_1 + \mathbf{k} S_2$, see Section 2.3.1. Plugging (3.96) into (3.97) and reorganizing terms yields to the general Wiener filter expression (3.39). To obtain the error expression remark that by Theorem 2.2

$$\varepsilon = \int_{-\infty}^{\infty} \mathcal{S}(\Gamma_{ee}(\mathbf{v})) d\mathbf{v} \quad (3.98)$$

where $e(t) = \hat{x}(t) - x(t)$. Using the quaternion power spectral density definition (2.20) together with the Wiener filter expression (3.39) one gets the optimal error expression (3.45) by developing (3.98). To obtain (3.46) start by writing explicitly $\Gamma_{yy}(\mathbf{v}) = \Gamma_{xx}(\mathbf{v}) + \Gamma_{ww}(\mathbf{v})$ such that (\mathbf{v} -dependence omitted):

$$\Gamma_{yy} = S_{0,x} + S_{0,w} + S_{0,x} \Phi_x \boldsymbol{\mu}_x + S_{0,w} \Phi_w \boldsymbol{\mu}_w \quad (3.99)$$

$$= S_{0,y} [1 + \Phi_y \boldsymbol{\mu}_y], \quad (3.100)$$

where, using $\alpha = S_{0,x}/S_{0,w}$ the frequency domain SNR:

$$S_{0,y} = S_{0,x} + S_{0,w} \quad (3.101)$$

$$\Phi_y \boldsymbol{\mu}_y = \frac{\alpha}{1 + \alpha} \Phi_x \boldsymbol{\mu}_x + \frac{1}{\alpha + 1} \Phi_w \boldsymbol{\mu}_w. \quad (3.102)$$

Plugging (3.101) and (3.102) into (3.45) yields (3.46).

Time-frequency representations

4

This chapter introduces a generic approach towards time-frequency analysis of bivariate signals. It extends usual time-frequency notions – such as the analytic signal, spectrograms or scalograms – to the case of bivariate signals. These novel tools are tailored to the analysis of the *instantaneous features* of bivariate signals and provide clear and meaningful interpretations. Usual practice from time-frequency analysis directly applies and the implementation is numerically efficient.

We focus on *deterministic* signals. Recall that from Chapter 2, deterministic signals are interpreted as *fully polarized* bivariate signals. The extension of time-frequency analysis to the case of *random* and thus *partially polarized* signals is left for future work.

Section 4.1 develops a bivariate analogue of the analytic signal called the *quaternion embedding* of a bivariate signal. This quaternion-valued signal has a one-to-one correspondence with the original bivariate signal. Its spectrum is supported on positive-frequencies only. Its definition relies on the *i*-Hermitian symmetry (1.52) of the QFT of \mathbb{C}_i -valued signals. It provides a unique way to define *instantaneous features* for bivariate signals: besides usual instantaneous amplitude and phase parameters, the instantaneous orientation and ellipticity parameters are also introduced. These two extra parameters are specific to the setting of bivariate signals: they describe the instantaneous polarization state of the signal. Our analysis yields a natural bivariate or polarized amplitude modulated - frequency modulated (AM-FM) model, which can serve as an elementary block for the description of non-stationary bivariate signals.

Section 4.2 overcomes the limitations of the quaternion embedding approach by introducing two time-frequency-polarization representations. These representations are based on a quaternion short-term Fourier transform (Q-STFT) and a quaternion continuous wavelet transform (Q-CWT) respectively. We define the *energy spectrogram* (resp. *scalogram*) which is interpreted as an usual time-frequency energy density. We also define the *polarization spectrogram* (resp. *scalogram*), a novel quantity that reveals the time-frequency-polarization features of bivariate signals. Two fundamental theorems for the Q-STFT and Q-CWT guarantee the invertibility and interpretation as densities of such quantities.

Section 4.3 explores further the notion of *ridges* of the Q-STFT and the Q-CWT using an asymptotic analysis. Loosely speaking we show that the local maxima of the energy spectrogram and energy scalogram concentrate around lines of instantaneous frequency.

Section 4.4 provides a starting point towards the generic time-frequency-polarization representation of bivariate signals. We first introduce the quaternion Wigner-Ville distribution, a bilinear time-frequency-polarization representation which perfectly localizes polarized linear chirps. Its properties are studied. Then a general class of bilinear time-frequency-polarization representations is introduced. We adopt a parameterization close to the usual Cohen

CHAPTER CONTENTS

4.1 Quaternion embedding of bivariate signals	104
Definition • Instantaneous parameters • Examples •	
4.2 Spectrograms and scalograms for bivariate signals	109
Quaternion short-term Fourier transform • Quaternion continuous wavelet transform •	
4.3 Asymptotic analysis and ridges	115
Ridges of the quaternion short-term Fourier transform • Ridges of the quaternion continuous wavelet transform • Ridge extraction •	
4.4 Generic time-frequency-polarization representations	117
Quaternion Wigner-Ville distribution • Cohen class for bivariate signals •	
4.5 An application to seismic data	124
4.6 Conclusion	125
APPENDICES	
4.A Canonical quadruplet of bivariate signals	127
4.B Stationary phase approximation	128
4.C Proofs	129
Proof of Theorem 4.1 • Proof of Theorem 4.2 •	

class of bilinear time-frequency representations. This broad class of solutions allows to design new and flexible time-frequency-polarization representations.

Section 4.5 finally performs a time-frequency-polarization analysis on a real-data example from geophysics.

The material in Section 4.1 and Section 4.2 has been published in an international journal (Flamant, Le Bihan, and Chainais, 2017e). Some parts were presented at an international conference (Flamant, Le Bihan, and Chainais, 2017b) and at national conference (Flamant, Le Bihan, and Chainais, 2017d). The application to seismic data was also developed in Flamant, Le Bihan, and Chainais (2017e):

-  J. Flamant, N. Le Bihan, and P. Chainais. 2017e. “Time-frequency analysis of bivariate signals.” In Press, *Applied and Computational Harmonic Analysis*. doi:10.1016/j.acha.2017.05.007
-  J. Flamant, N. Le Bihan, and P. Chainais. 2017b. “Polarization spectrogram of bivariate signals.” In *IEEE International Conference on Acoustics, Speech, and Signal Processing (ICASSP), 2017, New Orleans, USA*
-  J. Flamant, N. Le Bihan, and P. Chainais. 2017d. “Spectrogramme de polarisation pour l’analyse des signaux bivariés.” In *GRETSI 2017*. Juan-les-Pins, France

The definition of the quaternion Wigner-Ville transform (Section 4.4.1) and the original construction of the class of bilinear time-frequency-polarization representations (Section 4.4.2) constitute prospects and have not yet been published.

4.1 QUATERNION EMBEDDING OF BIVARIATE SIGNALS

For simple real-valued signals, a natural and interpretable model is $x(t) = a(t) \cos \varphi(t)$ where $a(t) \geq 0$ is the *instantaneous amplitude* and $\varphi(t)$ is the *instantaneous phase* (Cohen, 1995; Flandrin, 1998). This amplitude-modulation and frequency-modulation (AM-FM) model is the very first building block of time-frequency analysis. Superposition of AM-FM components are widely used, e.g. to model audio or speech signals (Dimitriadis, Maragos, and Potamianos, 2005).

Given a real-valued signal $x(t)$, a unique pair of instantaneous amplitude $a(t)$ and instantaneous phase $\varphi(t)$ is obtained by considering the analytic signal of $x(t)$ (Gabor, 1946; Ville, 1948). The complex-valued analytic signal enables a one-to-one correspondence between $x(t)$ and the *canonical pair* $[a(t), \varphi(t)]$. It is obtained by suppressing negative frequencies from the spectrum (Boashash, 1992; Picinbono, 1997). This operation is motivated by the Hermitian symmetry of the Fourier transform of real signals: the negative frequencies spectrum carries no additional information with respect to positive ones.

Just like univariate or real-valued signals are associated with their complex-valued analytic signal representation, bivariate or \mathbb{C}_i -valued signals can be associated with their *quaternion embedding* representation, namely

$$\begin{array}{ccc} \text{bivariate signal } x(t) & \longleftrightarrow & \text{quaternion embedding } x_+(t) \\ x : \mathbb{R} \rightarrow \mathbb{C}_i & & x_+ : \mathbb{R} \rightarrow \mathbb{H} \end{array} \quad (4.1)$$

This one-to-one mapping relies on the desirable properties of the quaternion Fourier transform of bivariate signals. The quaternion nature of $x_+(t)$ provides a straightforward identification of meaningful instantaneous parameters. It also generalizes the AM-FM model to the bivariate case.

The idea of associating a quaternion-valued signal to a complex or bivariate signal roots in the work of Le Bihan, Sangwine, and Ell (2014). They introduce the formal construction of the quaternion embedding by suppressing the negative frequencies from the spectrum.. They obtain instantaneous attributes using the polar Cayley-Dickson form of quaternions (Sangwine and Le Bihan, 2010). It yields a canonical pair $[a(t), \varphi(t)]$, with $a(t)$ and $\varphi(t)$ complex-valued functions. While it is possible to interpret $a(t)$ as the instantaneous complex amplitude, the meaning of the complex instantaneous phase $\varphi(t)$ is not clear. Le Bihan, Sangwine, and Ell (2014) restrict $\varphi(t)$ to be real, which prevents from considering generic bivariate signals.

We first review the construction of the quaternion embedding of a bivariate signal. Using the Euler polar form (1.18), we obtain meaningful instantaneous parameters for bivariate signals. The proposed approach solves previous issues of interpretability.

The quaternion embedding is called the *hypercomplex representation* of a complex signal in Le Bihan, Sangwine, and Ell (2014)

4.1.1 Definition

Let $x : \mathbb{R} \rightarrow \mathbb{C}_i$ an arbitrary bivariate signal. Its quaternion Fourier transform satisfies the *i*-Hermitian symmetry

$$X(-\nu) = -iX(\nu)i. \tag{4.2}$$

It shows that the negative frequencies of the quaternion-valued spectrum of $x(t)$ do not carry supplementary information to positive ones. This motivates the first definition 4.1 of the quaternion embedding $x_+(t)$ of $x(t)$ below.

Definition 4.1 (Quaternion embedding of bivariate signals). *Let $x : \mathbb{R} \rightarrow \mathbb{C}_i$ a bivariate signal. Its quaternion embedding $x_+(t)$ is defined as*

$$x_+(t) \triangleq 2 \int_0^{+\infty} X(\nu)e^{j2\pi\nu t} d\nu \tag{4.3}$$

where $X : \mathbb{R} \rightarrow \mathbb{H}$ is the quaternion Fourier transform of x .

The quaternion embedding of a bivariate signal has a one-sided spectrum and for positive frequencies $\nu \geq 0$, $x_+(t)$ and $x(t)$ share the same frequency content. Define the Hardy space on the real line $H^2(\mathbb{R}; \mathbb{H})$

$$H^2(\mathbb{R}; \mathbb{H}) \triangleq \{x \in L^2(\mathbb{R}; \mathbb{H}) \mid X(\nu) = 0 \text{ for all } \nu < 0\}. \tag{4.4}$$

By construction for a bivariate signal $x \in L^2(\mathbb{R}; \mathbb{C}_i)$, its quaternion embedding $x_+(t)$ belongs to $H^2(\mathbb{R}; \mathbb{H})$. The quaternion embedding representation establishes a one-to-one mapping between $L^2(\mathbb{R}; \mathbb{C}_i)$ and $H^2(\mathbb{R}; \mathbb{H})$.

Alternatively, the quaternion embedding $x_+(t)$ can be defined in the time domain thanks to Proposition 4.1.

We choose to call $x_+(t)$ the quaternion embedding of $x(t)$. We avoid terms such as *quaternion analytic* or *hyperanalytic* as the construction of $x_+(t)$ does not involve any result on analytic functions of quaternion variables.

Proposition 4.1 (Time-domain expression). *Let $x : \mathbb{R} \rightarrow \mathbb{C}_i$ a bivariate signal. Its quaternion embedding $x_+(t)$ defined by (4.3) reads*

$$x_+(t) = x(t) + \mathcal{H}\{x\}(t)\mathbf{j} \quad (4.5)$$

where $\mathcal{H}\{\cdot\}$ denotes the Hilbert transform

$$\mathcal{H}\{x\}(t) \triangleq \frac{1}{\pi} \text{p.v.} \int_{-\infty}^{+\infty} \frac{x(\tau)}{t - \tau} d\tau. \quad (4.6)$$

Proof. We show that (4.5) and (4.3) are identical definitions. Let $x(t) = u(t) + \mathbf{i}v(t)$ be a bivariate signal, with u and v real signals. Denote symbolically by \mathcal{F} the quaternion Fourier transform. Then one has

$$\mathcal{F}\{\mathcal{H}\{u\}\}(v) = -\text{sign}(v)U(v)\mathbf{j} \quad (4.7)$$

$$\mathcal{F}\{\mathcal{H}\{v\}\}(v) = -\text{sign}(v)V(v)\mathbf{j} \quad (4.8)$$

By linearity of the Hilbert transform, $\mathcal{H}\{x\}(t) = \mathcal{H}\{u\}(t) + \mathbf{i}\mathcal{H}\{v\}(t)$ so that

$$\mathcal{F}\{\mathcal{H}\{x\}\}(v) = -\text{sign}(v)(U(v) + \mathbf{i}V(v))\mathbf{j} = -\text{sign}(v)X(v)\mathbf{j} \quad (4.9)$$

and finally the quaternion Fourier transform of (4.5) reads

$$X_+(v) = (1 + \text{sign}(v))X(v) = 2\mathfrak{U}(v)X(v). \quad (4.10)$$

Taking the inverse quaternion Fourier transform of (4.10) yields (4.3) and concludes the proof. \square

Eq. (4.5) shows that the quaternion embedding $x_+(t)$ is obtained by adding two components in quadrature to $x(t)$, along the remaining imaginary axes \mathbf{j} and \mathbf{k} . One also recovers the original signal $x(t)$ by projection of its quaternion embedding $x_+(t)$ onto \mathbb{C}_i

$$x(t) = \text{Proj}_{\mathbb{C}_i}\{x_+(t)\}. \quad (4.11)$$

This shows that the quaternion embedding $x_+(t)$ for bivariate signals plays the same role as the usual analytic signal for univariate or real signals.

Sign function

$$\text{sign}(v) = \begin{cases} 1 & v > 0 \\ 0 & v = 0 \\ -1 & v < 0 \end{cases}$$

Heaviside unit step function

$$\mathfrak{U}(v) = \begin{cases} 1 & v > 0 \\ 1/2 & v = 0 \\ 0 & v < 0 \end{cases}$$

4.1.2 Instantaneous parameters

Canonical quadruplet One can associate a unique canonical pair $[a(t), \varphi(t)]$ to any real signal using the polar form of its analytic signal. Similarly one can associate to any bivariate signal $x(t)$ a unique *canonical quadruplet* $[a(t), \theta(t), \chi(t), \varphi(t)]$ thanks to the Euler polar form (1.18) of its quaternion embedding $x_+(t)$:

$$x_+(t) = a(t)e^{i\theta(t)}e^{-\mathbf{k}\chi(t)}e^{\mathbf{j}\varphi(t)}. \quad (4.12)$$

Using (4.11) one obtains the bivariate AM-FM model of $x(t)$

$$x(t) = a(t)e^{i\theta(t)}[\cos \chi(t) \cos \varphi(t) + \mathbf{i} \sin \chi(t) \sin \varphi(t)] \quad (4.13)$$

The canonical quadruplet of $x(t)$ consists of four real-valued functions. These instantaneous parameters can be meaningfully interpreted when $x(t)$ is a

narrow-band bivariate signal. Broadly speaking, this means that $\varphi(t)$ varies much more rapidly than the other canonical quadruplet components, that is

$$|\varphi'(t)| \gg |\chi'(t)|, |\theta'(t)|, |a'(t)/a(t)|. \quad (4.14)$$

Under this assumption (4.13) describes a bivariate signal which exhibits locally an elliptical trajectory in the $u-v$ plane. It extends the monochromatic bivariate signal model (1.57) to time-dependent ellipse parameters. The quantity $a(t)$ defines the *instantaneous amplitude* of $x(t)$. The *instantaneous orientation* is given by $\theta(t)$ and the *instantaneous ellipticity* is given by $\chi(t)$. The quantity $\varphi(t)$ is called the *instantaneous phase* of $x(t)$, and its time-derivative $\varphi'(t)$ gives the *instantaneous frequency*.

Given a quadruplet $[a(t), \theta(t), \chi(t), \varphi(t)]$, it is natural to ask under which conditions it corresponds to a canonical quadruplet. That is, under which conditions the quaternion signal constructed from this quadruplet forms a quaternion embedding? Appendix 4.A discusses this important point. In particular it specifies requirement (4.14) by proving a Bedrosian-like theorem for the quaternion embedding.

Instantaneous Stokes parameters The instantaneous ellipse parameters $a(t)$, $\theta(t)$ and $\chi(t)$ describe the instantaneous *polarization* state of the bivariate signal $x(t)$. In physics polarization states are usually given by Stokes parameters, as explained in previous chapters. Instantaneous Stokes parameters of $x(t)$ are directly obtained from its quaternion embedding $x_+(t)$ like

$$|x_+(t)|^2 = S_0(t), \quad x_+(t)\overline{jx_+(t)} = \mathbf{i}S_3(t) + \mathbf{j}S_1(t) + \mathbf{k}S_2(t). \quad (4.15)$$

Remark that $S_1^2(t) + S_2^2(t) + S_3^2(t) = S_0^2(t)$ meaning that $x(t)$ is fully polarized. It is a consequence of the deterministic nature of $x(t)$. Note that instantaneous Stokes parameters are instantaneous energetic quantities, and thus their expression does not involve the instantaneous phase $\varphi(t)$. They can be combined to form the quaternion instantaneous energy $E(t)$

$$\begin{aligned} E(t) &= |x_+(t)|^2 + x_+(t)\overline{jx_+(t)} \\ &= S_0(t) + \mathbf{i}S_3(t) + \mathbf{j}S_1(t) + \mathbf{k}S_2(t) \end{aligned} \quad (4.16)$$

This quantity forms an instantaneous energy density, since by the Parseval-Plancherel theorem 1.1 one has for finite energy signals

$$\int_{-\infty}^{+\infty} E(t)dt = 2 \int_0^{\infty} \left[|X(\nu)|^2 + X(\nu)\overline{jX(\nu)} \right] d\nu = E_0 \in \mathbb{H}. \quad (4.17)$$

4.1.3 Examples

Eq. (4.13) provides a natural and explicit AM-FM model for bivariate signals. In particular, we note that it is a reparameterization in terms of natural ellipse parameters θ , χ of the Modulated Elliptical Signal (MES) model (33) proposed by Lilly and Gascard (2006) and Lilly and Olhede (2010a). In some sense, the quaternion embedding method provides an *a posteriori* justification to their model. The possibilities offered by the bivariate AM-FM model (4.13) are illustrated below. In particular, it provides a precise control of the instantaneous geometry of bivariate signals.

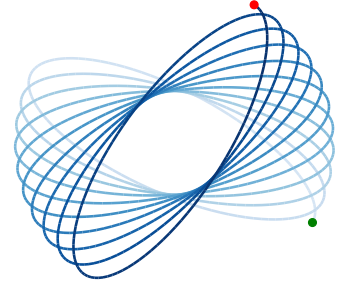


Figure 4.1: Trace of a bivariate signal with slowly evolving orientation and constant ellipticity.

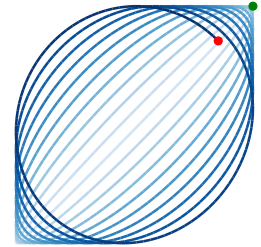


Figure 4.2: Trace of a bivariate signal with slowly evolving ellipticity and constant orientation.

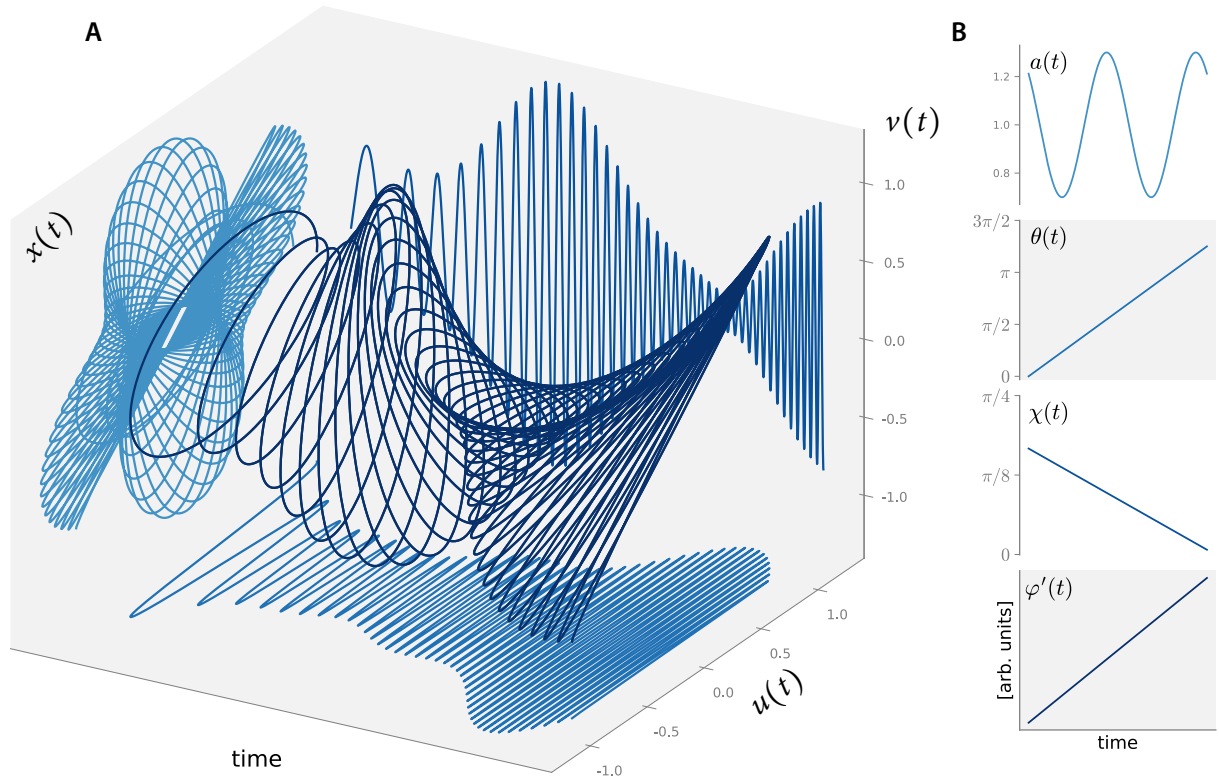


Figure 4.3: (a) Example of a bivariate AM-FM signal generated using (4.13). (b) Instantaneous amplitude, orientation, ellipticity and frequency associated with this signal.

Consider the model (4.13) with a constant amplitude $a = a_0$ and a constant frequency ν_0 such that $\varphi(t) = 2\pi\nu_0 t$. Suppose that the instantaneous orientation $\theta(t)$ and instantaneous ellipticity evolve slowly with respect to $\varphi(t)$.

Fig. 4.1 displays the trajectory of such a bivariate signal with a constant ellipticity $\chi(t) = \pi/10$ and an orientation evolving from $\theta = -\pi/6$ to $\theta = \pi/3$. Fig. 4.2 depicts the trajectory obtained for a constant orientation $\chi(t) = \pi/4$ and ellipticity evolving from $\chi = 0$ (linear polarization) to $\chi = -\pi/4$ (clockwise circular polarization). Recall that the sign of χ encodes the circulation direction in the ellipse, counter-clockwise for $\chi > 0$ and clockwise for $\chi < 0$.

More generally, the bivariate AM-FM model (4.13) provides a broad and flexible design of bivariate signals with specific instantaneous features. Fig. 4.3 shows a bivariate signal which exhibits simultaneously: (i) an instantaneous frequency increasing linearly (linear chirp) (ii) a slowly rotating instantaneous orientation $\theta(t)$ and (iii) a slowly decreasing ellipticity, from $\chi > 0$ to $\chi \approx 0$ and (iv) a slight modulation of its amplitude $a(t)$. The quaternion embedding method provides a simple and efficient way to determine these instantaneous canonical parameters without any ambiguity. It appears as a generalization of the analytic signal to the case of bivariate signals.

4.2 SPECTROGRAMS AND SCALOGRAMS FOR BIVARIATE SIGNALS

Limitations of the quaternion embedding The analytic signal does not provide useful information when considering multicomponent real signals. As expected, the quaternion embedding suffers from the same pitfalls. Consider a two component bivariate signal $x(t) = \cos 2\pi\nu_1 t + \cos 2\pi\nu_2 t$ with $\nu_2 > \nu_1 > 0$. It is a sum of two horizontally linearly polarized bivariate signals at frequencies ν_1 and ν_2 . Its quaternion embedding reads

$$x_+(t) = e^{j2\pi\nu_1 t} + e^{j2\pi\nu_2 t} = 2 \cos\left(2\pi \frac{\nu_1 - \nu_2}{2} t\right) e^{j2\pi \frac{\nu_1 + \nu_2}{2} t}, \quad (4.18)$$

which gives immediately the Euler polar form, with the canonical parameters given by $\chi(t) = \theta(t) = 0$, $a(t) = 2|\cos(2\pi \frac{\nu_1 - \nu_2}{2} t)|$ and $\varphi(t) = 2\pi \frac{\nu_1 + \nu_2}{2} t + \pi \text{sign}[a(t)]$. Although the values of $\theta(t)$ and $\chi(t)$ show that the polarization state is correctly obtained, the values of $a(t)$ and $\varphi(t)$ do not correspond to the instantaneous features of each component of $x(t)$. Note that when polarization states of each component differ, a polarization beating effect will also occur. Since the quaternion embedding performs a global operation on frequencies – and not a local one –, it is unable to identify the instantaneous parameters of each component separately.

Multicomponent bivariate signals A generic bivariate signal $x(t)$ with k components can be written as a sum of elementary bivariate AM-FM signals (4.13) such that

$$x(t) = \sum_{k=1}^K a_k(t) e^{i\theta_k(t)} [\cos \chi_k(t) \cos \varphi_k(t) + \mathbf{i} \sin \chi_k(t) \sin \varphi_k(t)], \quad (4.19)$$

and where $[a_k(t), \theta_k(t), \chi_k(t), \varphi_k(t)]$ is the *canonical quadruplet* associated to the k^{th} component. We assume that each component satisfies the narrow-band condition (4.14).

The goal of time-frequency analysis of bivariate signals is to extract and estimate the canonical parameters of these k components. To this aim we introduce two novel time-frequency-polarization representations based respectively on a quaternion short-term Fourier transform and on a quaternion continuous wavelet transform. The mathematical validity of these novel representations is guaranteed by two fundamental theorems.

4.2.1 Quaternion short-term Fourier transform

The very first tool for the time-frequency analysis is the *quaternion short-time Fourier transform*.

Definition Let $g \in L^2(\mathbb{R}; \mathbb{R})$ a real and symmetric $g(t) = g(-t)$ window. We assume that g is normalized such that $\|g\|_{L^2} = 1$. For $\tau, \nu \in \mathbb{R}$ the translated and modulated version of this window g is

$$g_{\tau, \nu}(t) = g(t - \tau) e^{j2\pi\nu t}. \quad (4.20)$$

The functions $g_{\tau, \nu} : \mathbb{R} \rightarrow \mathbb{C}_j$ define *time-frequency-polarization atoms*. Although this definition is classical, the term *polarization* emphasizes that these functions take their values in \mathbb{C}_j .

The quaternion short-term Fourier transform (Q-STFT) of a signal $x \in L^2(\mathbb{R}; \mathbb{H})$ is given by

$$F_x^g(\tau, \nu) = \langle x, g_{\tau, \nu} \rangle = \int_{-\infty}^{+\infty} x(t)g(t - \tau)e^{-j2\pi\nu t} dt. \quad (4.21)$$

Properties

Theorem 4.1 (Inversion formula and energy conservation). *Let $x \in L^2(\mathbb{R}; \mathbb{H})$ and consider a window $g \in L^2(\mathbb{R}; \mathbb{R})$, real and symmetric $g(-t) = g(t)$ such that $\|g\|_{L^2} = 1$. Then the inversion formula reads*

$$x(t) = \int_{-\infty}^{+\infty} \int_{-\infty}^{+\infty} F_x^g(\tau, \nu)g(t - \tau)e^{j2\pi\nu t} d\tau d\nu, \quad (4.22)$$

and the energy of x is conserved,

$$\int_{-\infty}^{+\infty} |x(t)|^2 dt = \int_{-\infty}^{+\infty} \int_{-\infty}^{+\infty} |F_x^g(\tau, \nu)|^2 d\tau d\nu, \quad (4.23)$$

as well as the polarization properties of x :

$$\int_{-\infty}^{+\infty} x(t)\overline{jx(t)} dt = \int_{-\infty}^{+\infty} \int_{-\infty}^{+\infty} F_x^g(\tau, \nu)\overline{jF_x^g(\tau, \nu)} d\tau d\nu. \quad (4.24)$$

This fundamental theorem ensures that the Q-STFT defines a valid and meaningful time-frequency-polarization representation of bivariate signals.

Proof. See Appendix 4.C.1. \square

The quantity $|F_x^g(\tau, \nu)|^2$ is called the *energy spectrogram* of x . Thanks to (4.23) it defines a valid time-frequency energy density. The quantity $F_x^g(\tau, \nu)\overline{jF_x^g(\tau, \nu)}$ is called the *polarization spectrogram* of x . Its interpretation as a time-frequency density is guaranteed by (4.24).

The energy spectrogram and the polarization spectrogram correspond to *time-frequency Stokes parameters* of the signal x :

$$|F_x^g(\tau, \nu)|^2 = S_0(\tau, \nu) \quad \text{and} \quad F_x^g(\tau, \nu)\overline{jF_x^g(\tau, \nu)} = iS_3(\tau, \nu) + jS_1(\tau, \nu) + kS_2(\tau, \nu) \quad (4.25)$$

This provides a direct and natural interpretation of the energy spectrogram and polarization spectrogram.

Note that the modulus of the polarization spectrogram is simply the energy spectrogram, since x is fully polarized (being deterministic).

The Q-STFT has a reproducing kernel Hilbert space (RKHS) structure. Plugging the inversion formula (4.22) in the expression of the Q-STFT (4.21) at time-frequency point $(\tau_0, \nu_0) \in \mathbb{R}^2$ it shows that the image of $L^2(\mathbb{R}; \mathbb{H})$ by the Q-STFT is a RKHS with reproducing kernel

$$K(\tau, \nu, \tau_0, \nu_0) = \langle g_{\tau, \nu}, g_{\tau_0, \nu_0} \rangle. \quad (4.26)$$

The Q-STFT of a signal x is redundant representation, just like the usual STFT:

$$F_x^g(\tau_0, \nu_0) = \int_{-\infty}^{+\infty} \int_{-\infty}^{+\infty} F_x^g(\tau, \nu)K(\tau, \nu, \tau_0, \nu_0) d\tau d\nu. \quad (4.27)$$

When $x(t) \in \mathbb{C}_i$ -valued, the Q-STFT exhibits *i*-Hermitian symmetry in the frequency variable, *i.e.*

$$F_x^g(\tau, -\nu) = -iF_x^g(\tau, \nu)i. \quad (4.28)$$

This allows to consider positive frequencies only when representing energy and polarization spectrograms.

This kernel is identical to the kernel of the STFT, excepted that it takes its values in \mathbb{C}_j and not in \mathbb{C}_i .

Note that the window g is assumed to be a real-valued function.

Examples An analytical example and a synthetic numerical example are presented below. They correspond to usual examples of signals found in time-frequency textbooks (Flandrin, 1998; Mallat, 2008) adapted to the case of bivariate signals and the Q-STFT: monochromatic bivariate signals and two polarized linear chirps. This approach is very generic and usual practice from time-frequency analysis of univariate signals is easily transposed in the Q-STFT setting.

Monochromatic bivariate signal Consider first a monochromatic bivariate signal at frequency ν_0 defined by its quaternion embedding $x_+(t)$ such that

$$x_+(t) = a_0 e^{i\theta_0} e^{-k\chi_0} e^{j2\pi\nu_0 t} \quad (4.29)$$

Its Q-STFT reads

$$F_{x_+}^g(\tau, \nu) = a_0 e^{i\theta_0} e^{-k\chi_0} G(\nu - \nu_0) e^{-j2\pi(\nu - \nu_0)\tau} \quad (4.30)$$

where G is the Fourier transform of the window g . The Q-STFT is localized around frequency $\nu = \nu_0$ in the time-frequency plane, as expected. The energy spectrogram of x is

$$|F_{x_+}^g(\tau, \nu)|^2 = a_0^2 |G(\nu - \nu_0)|^2 \quad (4.31)$$

and gives $S_0(\tau, \nu)$, the first time-frequency Stokes parameter. The polarization spectrogram of x is

$$F_x^g(\tau, \nu) \overline{jF_{x_+}^g(\tau, \nu)} = a_0^2 |G(\nu - \nu_0)|^2 [\mathbf{i} \sin 2\chi_0 + \mathbf{j} \cos 2\theta_0 \cos 2\chi_0 + \mathbf{k} \sin 2\theta_0 \cos 2\chi_0], \quad (4.32)$$

which gives the three time-frequency Stokes parameters S_1, S_2 and S_3 that describe the polarization properties of x .

Two polarized linear chirps Fig. 4.4a shows a composite signal $x(t) = x_1(t) + x_2(t)$ constructed as a superposition of two polarized linear chirps. Each chirp has its own polarization properties given by (4.33) and (4.34) below

$$\theta_1(t) = \frac{\pi}{4}, \quad \chi_1(t) = \frac{\pi}{6} - t, \quad \varphi_1(t) = 50\pi t + 250\pi t^2 \quad (4.33)$$

$$\theta_2(t) = \frac{\pi}{4} 10t, \quad \chi_2(t) = -\frac{\pi}{8}, \quad \varphi_2(t) = 150\pi t + 250\pi t^2 \quad (4.34)$$

This signal can be seen as a polarized version of the classical parallel linear chirps signal (Mallat, 2008). It is defined on the time interval $[0, 1]$ by $N = 1024$ equispaced samples. Its Q-STFT is computed with a Hanning window of size 101 samples, providing good time-frequency clarity.

Fig. 4.4b shows the energy spectrogram (S_0) and the normalized polarization spectrogram (s_1, s_2, s_3). The energy spectrogram corresponds to an usual time-frequency density. It permits the identification of the two linear chirps. The polarization spectrogram has to be normalized by the energy spectrogram to be meaningfully interpreted. The three normalized Stokes parameters provide a reading of time-frequency-polarization properties of the two chirps. Note that since s_3 is directly an image of the χ one directly recovers the ellipticity modulation law from the s_3 time-frequency map. The orientation modulation law is recovered by simultaneously inspecting the three time-frequency normalized Stokes parameters. Fig. 4.4c shows the instantaneous orientation and ellipticity extracted from the *ridge* of each chirp. The polarization properties of each chirp are correctly recovered.

Recall that a_0 is the amplitude, θ_0 is the orientation and χ_0 is the ellipticity.

Our choice of normalization is

$$is_3 + js_1 + ks_2 = \frac{F_x^g(t, \nu) \overline{jF_{x_+}^g(t, \nu)}}{|F_x^g(t, \nu)|^2 + \alpha}$$

with $\alpha = 0.01 \max_{t, \nu} |F_x^g(t, \nu)|^2$.

See Section 4.3 for a detailed discussion on ridges.

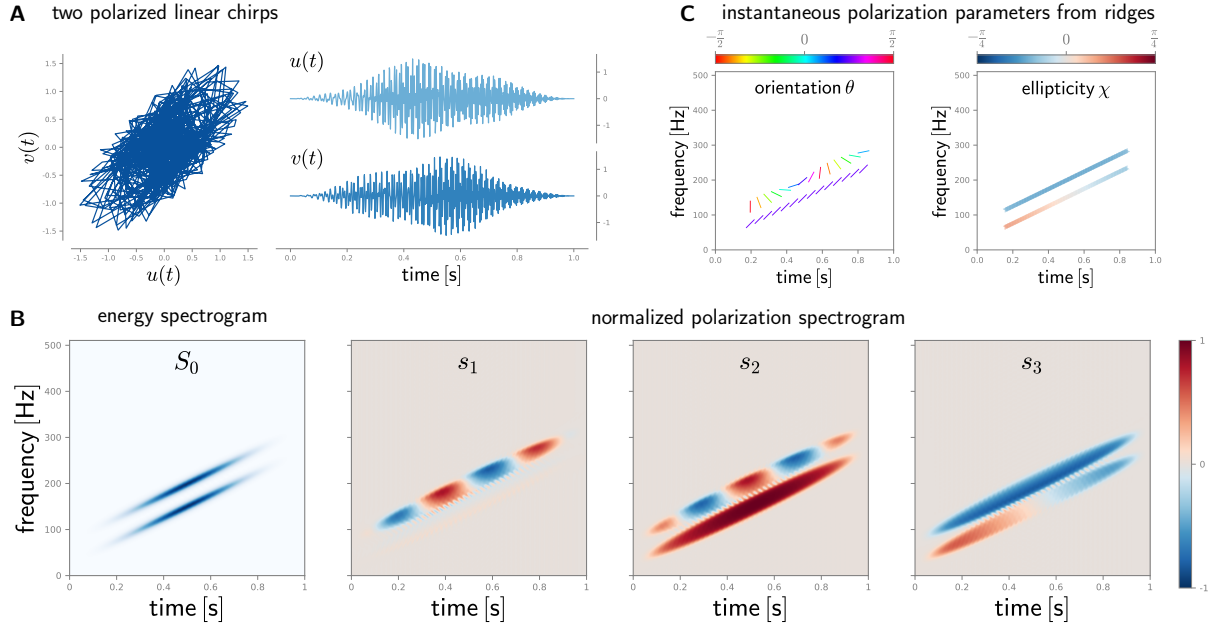


Figure 4.4: Sum of two polarized linear chirps example. (a) the bivariate signal (b) energy spectrogram and polarization spectrogram of this signal (c) instantaneous orientation and ellipticity extracted from the ridge of each component. Top chirp is elliptically polarized with a varying orientation, whereas the bottom chirp shows a slowly varying ellipticity with constant orientation.

4.2.2 Quaternion continuous wavelet transform

The time-frequency atoms underpinning the Quaternion short-term Fourier transform atoms have a constant time-frequency localization. This prevents from using the Q-STFT to analyze a large range of frequencies over short time scales. To address this limitation, it is natural to introduce the quaternion continuous wavelet transform (Q-CWT). Its derivation closely follows the usual CWT theory (Daubechies, 1992; Mallat, 2008) excepted that wavelets are \mathbb{C}_j -valued to analyze the time-frequency-polarization content of signals.

Definition The analysis of the time-frequency (or time-scale) content of signals requires the use of *complex analytic wavelets* (Mallat, 2008). For bivariate signals, let $\psi \in H^2(\mathbb{R}; \mathbb{C}_j)$ be such a wavelet, which is additionally normalized $\|\psi\|_{L^2} = 1$. Assume that the wavelet $\psi(t)$ is admissible, *i.e.*

$$C_\psi \triangleq \int_0^{+\infty} v^{-1} |\Psi(v)|^2 dv < \infty. \quad (4.35)$$

The admissibility condition implies in particular that $\psi(t)$ has zero mean, hence it is an oscillating function of t .

Generalized Morse wavelets (Daubechies and Paul, 1988; Olhede and Walden, 2002) form a wide class of analytic and admissible wavelets. Their expression in the frequency domain is

$$\Psi_{\beta,\gamma}(v) \triangleq \mathfrak{U}(v) \alpha_{\beta,\gamma} v^{-\beta} e^{-v^\gamma}, \quad (4.36)$$

where $\mathfrak{U}(\cdot)$ is Heaviside's unit step function. Parameters $\beta, \gamma > 0$ control the wavelet properties (Lilly and Olhede, 2009; Lilly and Olhede, 2012) and $\alpha_{\beta,\gamma}$ is a normalizing constant.

For $\tau \in \mathbb{R}$ and $s > 0$ the translated - dilated version of the wavelet ψ is

$$\psi_{\tau,s}(t) \triangleq \frac{1}{\sqrt{s}} \psi\left(\frac{t-\tau}{s}\right). \quad (4.37)$$

This definition ensures that the time-scale atoms $\psi_{\tau,s}$ remain normalized $\|\psi_{\tau,s}\|_{L^2} = 1$. The dilation permits to visit all frequencies. The quaternion continuous wavelet transform (Q-CWT) of a signal $x \in L^2(\mathbb{R}; \mathbb{H})$ is

$$W_x(\tau, s) \triangleq \langle x, \psi_{\tau,s} \rangle = \int_{-\infty}^{+\infty} x(t) \frac{1}{\sqrt{s}} \overline{\psi\left(\frac{t-\tau}{s}\right)} dt. \quad (4.38)$$

Properties

Theorem 4.2 (Inversion formula and energy conservation). *Let $x_+ \in H^2(\mathbb{R}; \mathbb{H})$ and an analytic wavelet $\psi \in H^2(\mathbb{R}; \mathbb{C}_j)$. Suppose that ψ is admissible such that (4.35) holds. Then the following inverse reconstruction formula is valid:*

$$x_+(t) = C_\psi^{-1} \int_0^{+\infty} \int_{-\infty}^{+\infty} W_{x_+}(\tau, s) \psi_{\tau,s}(t) d\tau \frac{ds}{s^2}, \quad (4.39)$$

and the energy of x_+ is conserved,

$$C_\psi^{-1} \int_0^{+\infty} \int_{-\infty}^{+\infty} |W_{x_+}(\tau, s)|^2 d\tau \frac{ds}{s^2} = \|x_+\|_{L^2}^2, \quad (4.40)$$

as well as the polarization properties of x_+ :

$$\int_{-\infty}^{+\infty} x_+(t) \overline{jx_+(t)} dt = C_\psi^{-1} \int_0^{+\infty} \int_{-\infty}^{+\infty} W_{x_+}(\tau, s) \overline{jW_{x_+}(\tau, s)} d\tau \frac{ds}{s^2} \quad (4.41)$$

The restriction to quaternion embedding signals $x_+ \in H^2(\mathbb{R}; \mathbb{H})$ is purely for notational convenience. Since there is a one-to-one correspondence between a bivariate signal $x \in L^2(\mathbb{R}; \mathbb{C}_i)$ and its quaternion embedding $x_+ \in H^2(\mathbb{R}; \mathbb{H})$ one has

$$W_x(\tau, s) = \frac{1}{2} W_{x_+}(\tau, s). \quad (4.42)$$

In particular, the reconstruction formula (4.39) becomes for $x \in L^2(\mathbb{R}; \mathbb{C}_i)$

$$x(t) = \text{Proj}_{\mathbb{C}_i} \left\{ 2C_\psi^{-1} \int_{-\infty}^{+\infty} \int_0^{+\infty} W_x(\tau, s) \psi_{\tau,s}(t) d\tau \frac{ds}{s^2} \right\}. \quad (4.43)$$

The quantity $|W_x(\tau, s)|^2$ is called the *energy scalogram* of x . Eq. (4.40) shows that it defines a time-scale energy density. The quantity $W_{x_+}(\tau, s) \overline{jW_{x_+}(\tau, s)}$ is the *polarization scalogram* of x and defines a time-scale density thanks to (4.41). These two quantities are related to the time-scale Stokes parameters of x the following way:

$$|W_x(\tau, s)|^2 = S_0(\tau, s) \quad \text{and} \quad W_x(\tau, s) \overline{jW_x(\tau, s)} = \mathbf{i}S_3(\tau, s) + \mathbf{j}S_1(\tau, s) + \mathbf{k}S_2(\tau, s). \quad (4.44)$$

The Q-CWT exhibits a RKHS structure. Consider $x_+ \in H^2(\mathbb{R}; \mathbb{H})$. Plugging the inversion formula (4.39) into the Q-CWT definition (4.38) shows that the image of $H^2(\mathbb{R}; \mathbb{H})$ by the Q-CWT is a RKHS with reproducing kernel

$$K(\tau, s, \tau_0, s_0) = \langle \psi_{\tau,s}, \psi_{\tau_0,s_0} \rangle. \quad (4.45)$$

Similarly to the usual CWT, the Q-CWT is a redundant representation such that for $(\tau_0, s_0) \in \mathbb{R} \times \mathbb{R}_+^*$

$$W_{x_+}(\tau_0, s_0) = C_\psi^{-1} \int_0^{+\infty} \int_{-\infty}^{+\infty} W_{x_+}(\tau, s) K(\tau, s, \tau_0, s_0) d\tau \frac{ds}{s^2}. \quad (4.46)$$

Proof. See Appendix 4.C.2. \square

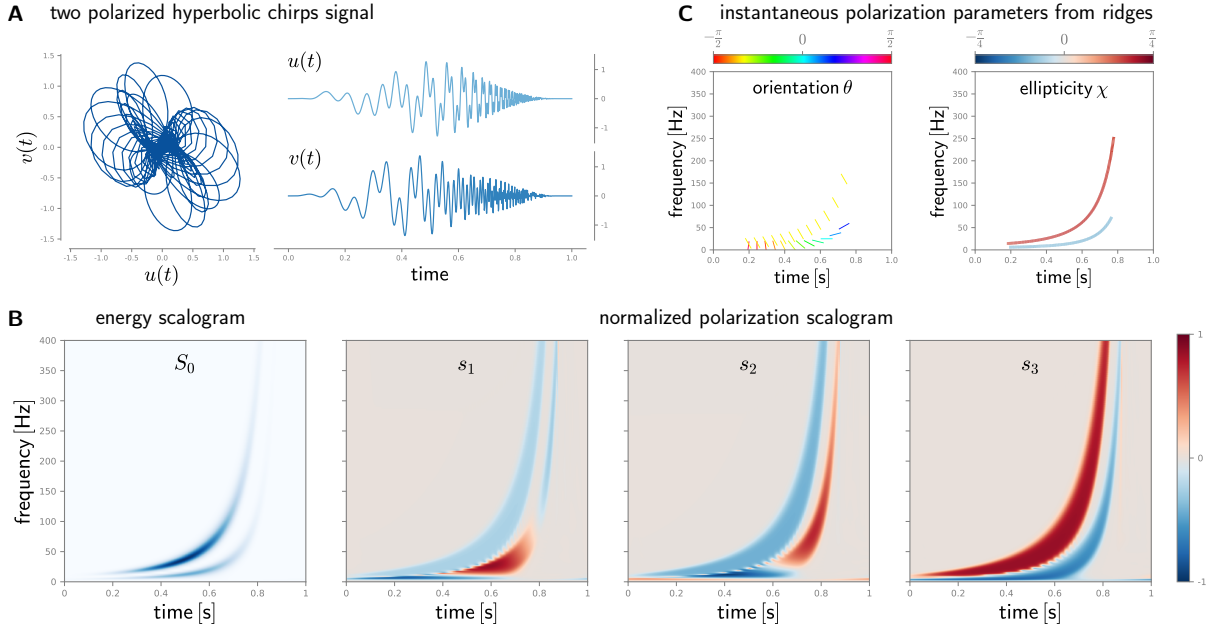


Figure 4.5: Sum of two polarized hyperbolic chirps example. (a) the bivariate signal (b) energy scalogram and polarization scalogram of this signal (c) instantaneous orientation and ellipticity extracted from the ridge of each component. Top chirp shows positive ellipticity, whereas the bottom chirp shows a negative one.

Examples An analytical example and a synthetic numerical example are presented below. These are bivariate versions of examples of signals frequently encountered in the literature (Mallat, 2008) to illustrate the straightforward connection between usual practice and the behavior of the Q-CWT.

Monochromatic bivariate signal Let $x(t)$ be a bivariate monochromatic signal defined by its quaternion embedding $x_+(t)$ as given by (4.29). The Q-CWT of $x_+(t)$ reads

$$W_{x_+}(\tau, s) = a_0 e^{i\theta_0} e^{-k\chi_0} s^{\frac{1}{2}} \overline{\Psi(sv_0)} e^{j2\pi\nu_0\tau}. \quad (4.47)$$

If $|\Psi(\cdot)|$ attains its maximum value at frequency ν_p , then the Q-CWT is localized in the time-scale plane around $s = \nu_p/\nu_0$. The energy scalogram of x_+ is

$$|W_{x_+}(\tau, s)|^2 = sa_0^2 |\Psi(sv_0)|^2 \quad (4.48)$$

and its polarization scalogram is

$$W_{x_+}(\tau, s) \overline{jW_{x_+}(\tau, s)} = sa_0^2 |\Psi(sv_0)|^2 [i \sin 2\chi_0 + j \cos 2\theta_0 \cos 2\chi_0 + k \sin 2\theta_0 \cos 2\chi_0]. \quad (4.49)$$

From these two equations one immediately obtains the four time-scale Stokes parameters that describe the energetic and polarization properties of x .

Two polarized hyperbolic chirps Fig. 4.5a depicts the signal $x(t) = x_1(t) + x_2(t)$ made of two hyperbolic chirps with their own polarization properties:

$$\theta_1(t) = -\frac{\pi}{3}, \quad \chi_1(t) = \frac{\pi}{6}, \quad \varphi_1(t) = \frac{15\pi}{0.8-t} \quad (4.50)$$

$$\theta_2(t) = 5t, \quad \chi_2(t) = -\frac{\pi}{10}, \quad \varphi_2(t) = \frac{5\pi}{0.8-t}. \quad (4.51)$$

It is defined on the time interval $[0, 1]$, with $N = 1024$ samples. The Q-CWT was computed using a Morse wavelet (4.36) with $\beta = 12$ and $\gamma = 3$.

As given by Lilly and Olhede (2009) for generalized Morse wavelets $\Psi_{\beta,\gamma}$ (4.36),

$$\nu_p = \left(\frac{\beta}{\gamma}\right)^{\frac{1}{\gamma}}.$$

Fig. 4.5b shows the energy scalogram (S_0) and the normalized polarization scalogram (s_1, s_2, s_3). The energy scalogram is an usual time-scale energy density and yields a direct identification of the two hyperbolic chirps. Again, the polarization scalogram needs to be normalized by the energy scalogram to be meaningfully interpreted. The three normalized Stokes parameters provide the time-scale-polarization properties of the two chirps. Fig. 4.5c show that the instantaneous orientation and instantaneous ellipticity are correctly recovered from the ridge of each chirp.

Normalization is performed similarly to the Q-STFT

$$is_3 + js_1 + ks_2 = \frac{W_x(t, s) \overline{jW_x(t, s)}}{|W_x(t, s)|^2 + \alpha}$$

with $\alpha = 0.01 \max_{t,v} |W_x(t, s)|^2$.

4.3 ASYMPTOTIC ANALYSIS AND RIDGES

Spectrograms and scalograms tend to concentrate around lines of maxima called *ridges* that carry most of the significant information. Ridges form a set of points in the time-frequency (resp. time-scale) plane from which the instantaneous properties of the signal can be recovered. For univariate signals such results have first been developed by Delprat et al. (1992). Several theoretical results were developed in a more general setting by Mallat (2008) and in the context of the analytic wavelet transform by Lilly and Olhede (2010b). This section provides similar results on the *ridges* of the Q-STFT and the Q-CWT.

We extend the approach proposed by Delprat et al. (1992) which was also discussed by Torr sani (1995) to the case of bivariate signals. It essentially relies on *asymptotic* arguments. For the sake of simplicity we only consider monocomponent bivariate signals $x(t)$. We require that (4.14) holds: x is said to be *asymptotic*, or in other terms the instantaneous phase vary much faster than the other instantaneous quantities. Under such conditions, we will show that the Q-STFT and the Q-CWT concentrate on ridges defined in terms of the instantaneous frequency of the signal. Expressions of these transforms on ridges involve explicitly the quaternion embedding of the signal, providing a simple way to extract instantaneous parameters. Finally, we will discuss how well known algorithms in ridge analysis can be applied to the bivariate setting.

4.3.1 Ridges of the quaternion short-term Fourier transform

In order to simplify the discussion we restrict our analysis to points $(\tau, \nu) \in \Omega \subset \mathbb{R} \times \mathbb{R}_+^*$ such that the time-frequency-polarization atoms $g_{\tau, \nu}$ belong to the Hardy space $H^2(\mathbb{R}; \mathbb{C}_j)$. This restriction ensures that $g_{\tau, \nu}$ is analytic in the sense that it is supported on positive frequencies only. As a result for every $(\tau, \nu) \in \Omega$ one has

$$F_x^g(\tau, \nu) = \frac{1}{2} F_{x_+}^g(\tau, \nu). \quad (4.52)$$

The Q-STFT of x is obtained using the polar form of the quaternion embedding x_+

$$F_x^g(\tau, \nu) = \frac{1}{2} \int_{-\infty}^{+\infty} a(t) e^{i\theta(t)} e^{-k\chi(t)} g(t - \tau) e^{j(\varphi(t) - 2\pi\nu(t - \tau))} dt. \quad (4.53)$$

Eq. (4.53) is an oscillatory integral which can be approximated using the method of stationary phase described in Appendix 4.B. Define $\Phi_{\tau, \nu}(t) = \varphi(t) - 2\pi\nu(t - \tau)$, and denote by $\tau_s = \tau_s(\tau, \nu)$ a stationary phase point such that $\Phi'_{\tau, \nu}(\tau_s) = 0$. We assume that $\tau_s(\nu)$ is unique¹ for each ν and that $\Phi''_{\tau, \nu}(\tau_s) \neq 0$

See Eq. (4.4) for the definition of $H^2(\mathbb{R}; \mathbb{C}_j)$.

For practical reasons this section use the following definition for $g_{\tau, \nu}(t)$

$$g_{\tau, \nu}(t) = g(t - \tau) e^{j2\pi\nu(t - \tau)}$$

which add a phase term $e^{-j2\pi\nu\tau}$ to definition (4.20).

1. If there are multiple stationary points, one must sum their contributions. Also, if $\Phi''_{\tau, \nu}(\tau_s) = 0$, then we search the smallest $k \geq 2$ such that $\Phi_{\tau, \nu}^{(k)}(\tau_s) \neq 0$. Formula follow by straightforward adjustment.

for simplicity. The stationary phase approximation of (4.53) is

$$F_x^g(\tau, \nu) \approx x_+(\tau_s) \sqrt{\frac{\pi}{2}} \frac{g(\tau_s - \tau)}{\sqrt{|\varphi''(\tau_s)|}} e^{j\frac{\pi}{4} \text{sign } \varphi''(\tau_s)} e^{-j2\pi\nu(\tau_s - \tau)}. \quad (4.54)$$

Ridge of the Q-STFT The set of points $(\tau, \nu) \in \Omega$ such that $\tau_s(\tau, \nu) = \tau$ defines the *ridge* \mathcal{R} of the Q-STFT. On the ridge, one has

$$\nu_{\mathcal{R}}(\tau) = \frac{1}{2\pi} \varphi'(\tau), \quad (4.55)$$

which is precisely the instantaneous frequency of the bivariate signal $x(t)$. The restriction of the Q-STFT to the ridge is

$$F_x^g(\tau, \nu_{\mathcal{R}}(\tau)) \approx x_+(\tau) \underbrace{\sqrt{\frac{\pi}{2}} \frac{g(0)}{\sqrt{|\varphi''(\tau)|}} e^{j\frac{\pi}{4} \text{sign } \varphi''(\tau)}}_{\mathbb{C}_j\text{-valued corrective factor}}. \quad (4.56)$$

This shows that the Q-STFT on the ridge is simply the quaternion embedding of x up to some corrective factor *on the right* taking values in \mathbb{C}_j ; it means that the instantaneous amplitude, orientation and ellipticity can be readily obtained from the Euler polar form of the ridge of the Q-STFT.

4.3.2 Ridges of the quaternion continuous wavelet transform

Let us write the wavelet $\psi \in H^2(\mathbb{R}; \mathbb{C}_j)$ in polar form $\psi(t) = a_\psi(t) \exp[j\varphi_\psi(t)]$. Using (4.42), the Q-CWT of x reads

$$W_x(\tau, s) = \frac{1}{2\sqrt{s}} \int_{-\infty}^{+\infty} a_\psi\left(\frac{t-\tau}{s}\right) a(t) e^{i\theta(t)} e^{-\mathbf{k}\chi(t)} e^{j(\varphi(t) - \varphi_\psi[(t-\tau)/s])} dt, \quad (4.57)$$

where we have used the Euler polar form of its quaternion embedding $x_+(t)$. As above, this oscillatory integral can be evaluated using a stationary phase approximation, see Appendix 4.B. For $(\tau, s) \in \mathbb{R} \times \mathbb{R}_+^*$ we assume that $\tau_s = \tau_s(\tau, s)$ is the unique stationary point of $\Phi_{\tau,s}(t) = \varphi(t) - \varphi_\psi[(t-\tau)/s]$ such that $\Phi'_{\tau,s}(\tau_s) = 0$ and $\Phi''_{\tau,s}(\tau_s) \neq 0$. Then

$$W_x(\tau, s) \approx x_+(\tau_s) \frac{\sqrt{\pi}}{\sqrt{2s|\Phi''_{\tau,s}(\tau_s)|}} \overline{\psi\left(\frac{\tau_s - \tau}{s}\right)} e^{j\frac{\pi}{4} \text{sign } \Phi''_{\tau,s}(\tau_s)}. \quad (4.58)$$

Ridge of the Q-CWT The set of points $(\tau, s) \in \mathbb{R} \times \mathbb{R}_+^*$ such that $\tau_s(\tau, s) = \tau$ defines the ridge \mathcal{R} . By definition of τ_s it follows that

$$s_{\mathcal{R}}(\tau) = \frac{\varphi'_\psi(0)}{\varphi'(\tau)}, \quad (4.59)$$

which corresponds to the instantaneous frequency of the analyzing wavelet at the origin divided by the instantaneous frequency of x . On the ridge, the Q-CWT can be approximated by

$$W_x(\tau, s_{\mathcal{R}}(\tau)) \approx x_+(\tau) \underbrace{\frac{\sqrt{\pi}}{\sqrt{2s_{\mathcal{R}}|\Phi''_{\tau,s_{\mathcal{R}}}(\tau)|}} \overline{\psi(0)}}_{\mathbb{C}_j\text{-valued corrective factor}} e^{j\frac{\pi}{4} \text{sign } \Phi''_{\tau,s_{\mathcal{R}}}(\tau)}. \quad (4.60)$$

Similarly to the Q-STFT, on the ridge the Q-CWT corresponds to the quaternion embedding of x up to some corrective factor *on the right* taking values in \mathbb{C}_j . Therefore instantaneous amplitude, orientation and ellipticity are directly given from the Euler polar form of the Q-CWT coefficients on the ridge.

Remark that

$$\Phi'_{\tau,s}(t) = \varphi'(t) - \frac{1}{s} \varphi'_\psi\left(\frac{t-\tau}{s}\right)$$

4.3.3 Ridge extraction

The most natural approach towards ridge extraction is to in detect local maxima of the energy spectrogram $|\mathbb{F}_x^g(\tau, \nu)|^2$ or the energy scalogram $|W_x(\tau, s)|^2$. However this approach can suffer from biased estimates due to strong frequency modulation. For instance for Q-STFT, Eq. (4.54) shows² that $|\mathbb{F}_x^g(\tau, \nu)|^2$ is not necessarily maximum on the ridge $\tau_s = \tau$ due to the term $\varphi''(\tau_s)$ in the denominator of the corrective factor. A similar phenomenon is observed for the Q-CWT.

2. We assume that the window $g(t)$ is maximum at $t = 0$.

Similarly to the STFT and CWT case (Delprat et al., 1992; Torr sani, 1995), the j -phase of the Q-STFT and Q-CWT coefficients allows to locate the ridge more precisely. However in the univariate case this approach is known to have shortcomings when the signal-to-noise ratio is low, and other approaches have to be used instead (Carmona, Hwang, and Torr sani, 1997; Carmona, Hwang, and Torr sani, 1999; Lilly and Olhede, 2010b). Those approaches can be thoroughly adapted to the bivariate setting.

For instance, it was proposed by Carmona, Hwang, and Torr sani (1997) to estimate the ridge using a variational approach based on minimizing an energy functional, which we can formulate for the Q-STFT as follows. The goal is to obtain a function ζ minimizing the energy functional

$$\mathcal{E}_x(\zeta) = - \int_{-\infty}^{+\infty} |\mathbb{F}_x^g(\tau, \zeta(\tau))|^2 d\tau + \int_{-\infty}^{+\infty} [\alpha \zeta'(\tau)^2 + \beta \zeta''(\tau)^2] d\tau \quad (4.61)$$

where α and β are real-valued parameters enforcing the smoothness of the function ζ by a penalization on its variations. Eq. (4.61) defines a nonconvex optimization problem which can be solved using *e.g.* a simulated annealing scheme as in Carmona, Hwang, and Torr sani (1997).

Since existing ridge extractions methods can be directly used with the Q-STFT and the Q-CWT, we shall not dwell further into this topic. In our simulations we have used a heuristic method which identifies at each instant τ local maxima of the energy density, and which computes ridges by chaining those points according to a prescribed maximal distance between consecutive points. This method – which is certainly not optimal – provides reasonably good results for our purpose.

4.4 GENERIC TIME-FREQUENCY-POLARIZATION REPRESENTATIONS

As an original contribution of this manuscript, this section answers an important question: what is the most generic class of bilinear time-frequency-polarization representations for bivariate signals? Once answered, it also asks for a careful study of the properties of each member of this class. This offers the liberty to pick a specific representation whose properties are tailored to the features of the signal considered.

Section 4.4.1 introduces as a starting point the *quaternion Wigner-Ville distribution*. Unlike spectrograms or scalograms based respectively on the Q-STFT and Q-CWT, this new time-frequency-polarization representation perfectly concentrates on polarized linear chirps. In addition it extends many properties of the usual Wigner-Ville transform to bivariate signals, *e.g.* its time and frequency marginals are the quaternion spectral density and quaternion energy, another property missed by spectrograms and scalograms.

Section 4.4.2 then introduces a generic class of bilinear time-frequency-polarization representations. We call it the *Cohen class* for bivariate signals. Any representation in this class can be expressed as a smoothing of the quaternion Wigner-Ville distribution: the quaternion spectrogram introduced in Section 4.2.1 makes no exception. The parameterization is straightforward and follows the univariate Cohen class derivation.

4.4.1 Quaternion Wigner-Ville distribution

Guided by our previous results, see e.g. Theorem 1.1 and Theorem 2.2, we propose a definition for the quaternion Wigner-Ville distribution. Its properties are studied and are similar to the usual Wigner-Ville distribution. In particular, the quaternion Wigner-Ville distribution of polarized linear chirps is perfectly localized.

Definition Let $x \in L^2(\mathbb{R}; \mathbb{H})$. We define the quaternion Wigner-Ville distribution of x as

$$\text{WV}_x(t, \nu) \triangleq \underbrace{\int_{-\infty}^{+\infty} x\left(t + \frac{\tau}{2}\right) e^{-j2\pi\nu\tau} \overline{x\left(t - \frac{\tau}{2}\right)} d\tau}_{\text{energy Wigner-Ville, } \text{EWV}_x(t, \nu) \in \mathbb{R}} + \underbrace{\int_{-\infty}^{+\infty} x\left(t + \frac{\tau}{2}\right) e^{-j2\pi\nu\tau} \overline{jx\left(t - \frac{\tau}{2}\right)} d\tau}_{\text{polarization Wigner-Ville, } \text{PWV}_x(t, \nu) \in \text{span}\{i, j, k\}}. \quad (4.62)$$

The definition of the quaternion Wigner-Ville distribution differs from the univariate Wigner-Ville definition in two points. First this expression contains two separate terms to describe simultaneously the energy and polarization features of the signal x . Second, note the position of the complex- j exponential, which is “sandwiched” by x in the two terms. This position is crucial due to noncommutative multiplication in \mathbb{H} and permits to recover many properties of the univariate Wigner-Ville distribution.

The first term called *energy Wigner-Ville* is real-valued and gives the energy time-frequency representation of the signal. It corresponds to the real part of $\text{WV}_x(t, \nu)$ and is denoted by $\text{EWV}_x(t, \nu)$. The second term is called *polarization Wigner-Ville* and denoted by $\text{PWV}_x(t, \nu)$. It corresponds to the vector part of $\text{WV}_x(t, \nu)$ and takes its values in $\text{span}\{i, j, k\}$. It encodes the polarization features of x .

The quaternion Wigner-Ville distribution of x can be rewritten

$$\text{WV}_x(t, \nu) = \text{EWV}_x(t, \nu) + \text{PWV}_x(t, \nu), \quad (4.63)$$

which is simply the scalar-vector part decomposition of the quaternion-valued function $\text{WV}_x(t, \nu)$. By decomposing $x = u(t) + iv(t)$, with $u, v: \mathbb{R} \rightarrow \mathbb{C}_j$ signals, the quaternion Wigner-Ville distribution relates to univariate Wigner-Ville distributions of u and v as follows

$$\text{EWV}_x(t, \nu) = \overline{\text{WV}}_u(t, \nu) + \overline{\text{WV}}_v(t, \nu), \quad (4.64)$$

$$\text{PWV}_x(t, \nu) = j \left[\overline{\text{WV}}_u(t, \nu) - \overline{\text{WV}}_v(t, \nu) \right] + 2k \overline{\text{WV}}_{vu}(t, \nu). \quad (4.65)$$

This direct link with usual Wigner-Ville distributions of components of x yields many properties of the quaternion Wigner-Ville distribution as detailed below. In particular since $\overline{\text{WV}}_u$ and $\overline{\text{WV}}_v$ are real-valued (Flandrin, 1998) and $\overline{\text{WV}}_{vu}$ is \mathbb{C}_j -valued, one can verify from (4.64) and (4.65) that EWV_x is real-valued and that PWV_x is purely imaginary.

For $u, v: \mathbb{R} \rightarrow \mathbb{C}_j$:

$$\overline{\text{WV}}_u(t, \nu) = \int u\left(t + \frac{\tau}{2}\right) e^{-j2\pi\nu\tau} \overline{u\left(t - \frac{\tau}{2}\right)} d\tau$$

is the univariate Wigner-Ville distribution of u and

$$\overline{\text{WV}}_{vu}(t, \nu) = \int v\left(t + \frac{\tau}{2}\right) e^{-j2\pi\nu\tau} \overline{u\left(t - \frac{\tau}{2}\right)} d\tau$$

is the univariate cross-Wigner-Ville distribution between v and u .

The *energy Wigner-Ville* and *polarization Wigner-Ville* distributions form respectively the scalar part and vector part of the quaternion Wigner-Ville distribution *i.e.* $\text{EWV}_x = \mathcal{S}\text{WV}_x$ and $\text{PWV}_x = \mathcal{V}\text{WV}_x$. Thus they live in different subspaces of \mathbb{H} . For simplicity any equation below involving these two distinct quantities stands for “scalar-scalar equality” and “vector-vector equality” otherwise specified.

Frequency domain definition The quaternion Wigner-Ville distribution can be defined in the frequency domain by replacing x by its quaternion Fourier transform:

$$\text{WV}_x(t, \nu) \triangleq \int_{-\infty}^{+\infty} X\left(\nu + \frac{\xi}{2}\right) e^{j2\pi\xi t} \overline{X\left(\nu - \frac{\xi}{2}\right)} d\xi + \int_{-\infty}^{+\infty} X\left(\nu + \frac{\xi}{2}\right) e^{j2\pi\xi t} \mathbf{j} \overline{X\left(\nu - \frac{\xi}{2}\right)} d\xi. \quad (4.66)$$

Symmetries For bivariate signals $x : \mathbb{R} \rightarrow \mathbb{C}_i$, the quaternion Wigner-Ville distribution exhibits the same symmetry (2.23) as the quaternion spectral density

$$\text{WV}_x(t, -\nu) = -\mathbf{i} \overline{\text{WV}_x(t, \nu)} \mathbf{i}. \quad (4.67)$$

In particular this means only positive frequencies of the quaternion Wigner-Ville distribution can be considered as they carry the complete information about the bivariate signal $x(t)$.

Marginals The quaternion Wigner-Ville distribution satisfies the marginal requirement, unlike the (quaternion) spectrogram and (quaternion) scalogram. A simple calculation shows that

$$\int_{-\infty}^{+\infty} \text{WV}_x(t, \nu) dt = |X(\nu)|^2 + X(\nu) \mathbf{j} \overline{X(\nu)}, \quad (4.68)$$

$$\int_{-\infty}^{+\infty} \text{WV}_x(t, \nu) d\nu = |x(t)|^2 + x(t) \mathbf{j} \overline{x(t)}. \quad (4.69)$$

The time marginal is simply the quaternion energy density (2.4). The frequency marginal is the quaternion instantaneous energy, already encountered in (4.16) in the case of quaternion embedding signals. As a consequence the quaternion Wigner-Ville distribution preserves also the quaternion energy of the signal

$$\int_{-\infty}^{+\infty} \int_{-\infty}^{+\infty} \text{WV}_x(t, \nu) d\nu dt = E \in \mathbb{H} \quad (4.70)$$

where E is defined thanks to the generalized Parseval-Plancherel theorem 1.1 for the QFT:

$$E \triangleq \int_{-\infty}^{+\infty} |x(t)|^2 dt + \int_{-\infty}^{+\infty} x(t) \mathbf{j} \overline{x(t)} dt. \quad (4.71)$$

Interferences The quaternion Wigner-Ville distribution is a quadratic functional of the signal x . For multicomponent signals it causes interferences that deteriorate the time-frequency clarity. Given a signal $x + y$, its quaternion Wigner-Ville distribution is

$$\text{WV}_{x+y}(t, \nu) = \text{WV}_x(t, \nu) + \text{WV}_y(t, \nu) + \text{WV}_{xy}(t, \nu) + \text{WV}_{yx}(t, \nu) \quad (4.72)$$

where $\text{WV}_{xy}(t, \nu)$ and $\text{WV}_{yx}(t, \nu)$ are quaternion cross-Wigner-Ville distributions defined by

$$\text{WV}_{xy}(t, \nu) \triangleq \underbrace{\int_{-\infty}^{+\infty} x\left(t + \frac{\tau}{2}\right) e^{-j2\pi\nu\tau} \overline{y\left(t - \frac{\tau}{2}\right)} d\tau}_{\text{cross-energy Wigner-Ville } \text{EWV}_{xy}(t, \nu) \in \mathbb{H}} + \underbrace{\int_{-\infty}^{+\infty} x\left(t + \frac{\tau}{2}\right) e^{-j2\pi\nu\tau} \overline{jy\left(t - \frac{\tau}{2}\right)} d\tau}_{\text{cross-polarization Wigner-Ville } \text{PWV}_{xy}(t, \nu) \in \mathbb{H}}. \quad (4.73)$$

The cross-energy and cross-polarization Wigner-ville terms are quaternion-valued and cannot be identified directly from $\text{WV}_{xy}(t, \nu)$ alone; computing $\text{WV}_{yx}(t, \nu)$ permits the identification³. Interference terms affect simultaneously the energy Wigner-Ville and polarization Wigner-Ville:

$$\text{SWV}_{x+y}(t, \nu) = \text{SWV}_x(t, \nu) + \text{SWV}_y(t, \nu) + 2\text{SEWV}_{xy}(t, \nu) \quad (4.74)$$

$$\mathcal{V}\text{WV}_{x+y}(t, \nu) = \mathcal{V}\text{WV}_x(t, \nu) + \mathcal{V}\text{WV}_y(t, \nu) + 2\mathcal{V}\text{PWV}_{xy}(t, \nu) \quad (4.75)$$

The scalar part of the cross-energy Wigner-Ville appears in the energy Wigner-Ville of $x + y$. The vector part of the cross-polarization Wigner-Ville appears in the polarization Wigner-Ville of $x + y$.

Note that bivariate signals $x : \mathbb{R} \rightarrow \mathbb{C}_i$ are a special type of multicomponents signals since $x(t) = (x_+(t) - \mathbf{i}x_+(t)\mathbf{i})/2$ where x_+ is the quaternion embedding of x . Thus looking at x one will observe interferences at null frequency due to the bivariate nature of x . Those can be removed by considering its quaternion embedding $x_+(t)$ instead. This is a bivariate analogue of an usual procedure which consists in replacing an univariate signal by its analytic version to reduce interferences, see *e.g.* Flandrin (1998, p.252).

Time and frequency support The quaternion Wigner-Ville distribution also preserves time and frequency supports of signals:

$$\forall \nu, \quad \supp_t \text{WV}_x(t, \nu) \subset \supp x(t) \quad (4.76)$$

$$\forall t, \quad \supp_\nu \text{WV}_x(t, \nu) \subset \supp X(\nu) \quad (4.77)$$

This result follows directly from time and frequency support of univariate Wigner-Ville distributions, see Claasen and Mecklenbraüker (1980).

Positivity The scalar part of the quaternion Wigner-Ville distribution, the energy Wigner-Ville distribution, is not necessarily positive. It limits the interpretation of the energy Wigner-Ville as a time-frequency energy density. This can be seen from (4.64) since univariate Wigner-Ville distributions of u and ν are known to be not necessarily positive (Flandrin, 1998). Let us note that for bivariate signals the lack of positivity has another consequence: since one needs to normalize the polarization Wigner-Ville by the energy Wigner-Ville, some sign issues could arise when the energy Wigner-Ville is locally negative.

Polarized linear chirps: perfect time-frequency localization Consider the polarized linear chirp signal $x(t)$ defined by its quaternion embedding $x_+(t) = ae^{i\theta} e^{-k\chi} e^{j2\pi(\alpha+\beta/2t)t}$, with $\alpha, \beta \in \mathbb{R}_+$. A quick computation of its quaternion Wigner-Ville transform yields

$$\text{WV}_{x_+}(t, \nu) = a^2 \delta(\alpha + \beta t - \nu) + a^2 e^{i\theta} e^{-k\chi} \mathbf{j} e^{k\chi} e^{-i\theta} \delta(\alpha + \beta t - \nu). \quad (4.78)$$

The quaternion Wigner-Ville distribution perfectly concentrates onto the instantaneous frequency line $\nu(t) = \alpha + \beta t$. In addition one recovers from (4.78) both energetic properties (first term) and polarization properties (second term) of the polarized linear chirp.

3. To see this, remark that

$$\text{EWV}_{xy} = \overline{\text{EWV}_{yx}} \text{ (Hermitian)}$$

$$\text{PWV}_{xy} = -\overline{\text{PWV}_{yx}} \text{ (anti-Hermitian)}$$

so that

$$\text{WV}_{xy} + \text{WV}_{yx} = 2\text{SEWV}_{xy} + 2\mathcal{V}\text{PWV}_{xy},$$

$$\text{WV}_{xy} - \text{WV}_{yx} = 2\text{SPWV}_{xy} + 2\mathcal{V}\text{EWV}_{xy}.$$

A theorem from Wigner (1971) shows actually that there is no positive quadratic energy distribution that satisfies the marginal requirements.

4.4.2 Cohen class for bivariate signals

This section aims to provide a general class of bilinear time-frequency-polarization representations for bivariate signals. This general family of representations obeys a covariance principle, meaning that the representation is invariant to any time-frequency shifts. Our approach closely follows the construction of the Cohen class for univariate signals as presented by Flandrin (1998). However the geometric nature of bivariate signals adds an extra layer of complexity in the definition of such representations. Those definitions also require special care to properly handle the noncommutativity of quaternions.

We search for a general family of quaternion-valued, time-frequency-polarization representations $\rho_x(t, \nu)$ such that

$$\int_{-\infty}^{+\infty} \int_{-\infty}^{+\infty} \rho_x(t, \nu) dt d\nu = E \in \mathbb{H} \quad (4.79)$$

where E is the *quaternion energy* of the signal $x \in L^2(\mathbb{R}; \mathbb{H})$ defined by

$$E = \int_{-\infty}^{+\infty} |x(t)|^2 dt + \int_{-\infty}^{+\infty} x(t) \mathbf{j} \overline{x(t)} dt. \quad (4.80)$$

Since the quaternion energy E provides a natural separation between energetic and polarization quantities, we decompose ρ_x into an *energetic* part ρ_x^E and a *polarization* part ρ_x^P such that

$$\rho_x(t, \nu) = \rho_x^E(t, \nu) + \rho_x^P(t, \nu) \quad (4.81)$$

and where we require that

$$\int_{-\infty}^{+\infty} \int_{-\infty}^{+\infty} \rho_x^E(t, \nu) dt d\nu = \int_{-\infty}^{+\infty} |x(t)|^2 dt \in \mathbb{R}^+, \quad (4.82)$$

$$\int_{-\infty}^{+\infty} \int_{-\infty}^{+\infty} \rho_x^P(t, \nu) dt d\nu = \int_{-\infty}^{+\infty} x(t) \mathbf{j} \overline{x(t)} dt \in \text{span}\{\mathbf{i}, \mathbf{j}, \mathbf{k}\}. \quad (4.83)$$

The search for quadratic time-frequency representations suggests the generic bilinear⁴ form for ρ_x^E and ρ_x^P :

$$\rho_x^E(t, \nu) = \iint x(s) K(t, \nu, s, s') \overline{x(s')} ds ds' \quad (4.84)$$

$$\rho_x^P(t, \nu) = \iint x(s) K(t, \nu, s, s') \mathbf{j} \overline{x(s')} ds ds' \quad (4.85)$$

where $K : \mathbb{R}^4 \rightarrow \mathbb{H}$ is an arbitrary kernel function. Note that we use the same kernel K for both the energetic part ρ_x^E and polarization part ρ_x^P . In full generality it could be possible to consider separate kernels, although it remains unclear which advantages it would provide.

To satisfy constraints (4.82) and (4.83) one should choose K such that

$$\iint K(t, \nu, s, s') dt d\nu = \delta(s - s'). \quad (4.86)$$

More stringent conditions on K can be derived using a covariance principle (Flandrin, 1998) adapted to the bivariate case.

Covariance principle Let $x \in L^2(\mathbb{R}; \mathbb{H})$ be an arbitrary signal. Consider its time-translated and frequency modulated version $x_{t', \nu'}$ such that

$$x_{t', \nu'}(t) = x(t - t') e^{j2\pi\nu' t}. \quad (4.87)$$

Note that we do not require $\rho_x^E(t, \nu)$ to be real-valued nor $\rho_x^P(t, \nu)$ to be purely imaginary. This topic is discussed later on and correspond to *separability*.

4. More precisely, bilinear with respect to real multiplication.

The *covariance principle* essentially means that

$$\rho_{x_{t',v'}}(t, \nu) = \rho_x(t - t', \nu - \nu'), \quad (4.88)$$

that is the quaternion density of $x_{t',v'}$ is simply the quaternion density of x translated in time from t' and in frequency by ν' . By writing $\rho_{x_{t',v'}}$ explicitly one gets

$$\begin{aligned} \rho_{x_{t',v'}}(t, \nu) &= \iint x(s) e^{j2\pi\nu'(s+t')} K(t, \nu, s + t', s' + t') e^{-j2\pi\nu'(s'+t')} \overline{x(s')} ds ds' \\ &\quad + \iint x(s) e^{j2\pi\nu'(s+t')} K(t, \nu, s + t', s' + t') e^{-j2\pi\nu'(s'+t')} \mathbf{j} \overline{x(s')} ds ds' \end{aligned} \quad (4.89)$$

One can hardly go further without an additional hypothesis on the kernel K . We now require K to be \mathbb{C}_j -valued so that \mathbb{C}_j -complex exponentials and K commute. This requirement on K seems rather reasonable if one considers K as a *smoothing* kernel. Moreover one gets

$$\begin{aligned} \rho_{x_{t',v'}}(t, \nu) &= \iint x(s) K(t, \nu, s + t', s' + t') e^{j2\pi\nu'(s-s')} \overline{x(s')} ds ds' \\ &\quad + \iint x(s) K(t, \nu, s + t', s' + t') e^{j2\pi\nu'(s-s')} \mathbf{j} \overline{x(s')} ds ds' \end{aligned} \quad (4.90)$$

By the covariance principle this latter quantity should be equal to

$$\begin{aligned} \rho_x(t - t', \nu - \nu') &= \iint x(s) K(t - t', \nu - \nu', s, s') \overline{x(s')} ds ds' \\ &\quad + \iint x(s) K(t - t', \nu - \nu', s, s') \mathbf{j} \overline{x(s')} ds ds' \end{aligned} \quad (4.91)$$

In particular for $t = t'$ and $\nu = \nu'$ one gets

$$K(t, \nu, s + t, s' + t) e^{j2\pi\nu(s-s')} = K(0, 0, s, s'), \quad (4.92)$$

or equivalently with $K_0(s, s') = K(0, 0, s, s')$:

$$K(t, \nu, s, s') = K_0(s - t, s' - t) e^{-j2\pi\nu(s-s')}. \quad (4.93)$$

We obtain a general relation for $\rho_x(t, \nu)$ by the following change of variables $s \leftarrow s + \frac{\tau}{2}$ and $s' \leftarrow s' - \frac{\tau}{2}$:

$$\begin{aligned} \rho_x(t, \nu) &= \iint x\left(s + \frac{\tau}{2}\right) K_0\left(s - t + \frac{\tau}{2}, s - t - \frac{\tau}{2}\right) e^{-j2\pi\nu\tau} \overline{x\left(s - \frac{\tau}{2}\right)} ds d\tau \\ &\quad + \iint x\left(s + \frac{\tau}{2}\right) K_0\left(s - t + \frac{\tau}{2}, s - t - \frac{\tau}{2}\right) e^{-j2\pi\nu\tau} \mathbf{j} \overline{x\left(s - \frac{\tau}{2}\right)} ds d\tau \end{aligned} \quad (4.94)$$

General parameterization To closely match the notation from Flandrin (1998), we replace the kernel K_0 by its quaternion Fourier transform in the s variable such that

$$K_0\left(s - t + \frac{\tau}{2}, s - t - \frac{\tau}{2}\right) = \int_{-\infty}^{+\infty} f(\tau, \xi) e^{j2\pi\xi(s-t)} d\xi. \quad (4.95)$$

The general parameterization for the Cohen class of quadratic time-frequency-polarization representations is then

$$\begin{aligned} \rho_x(t, \nu) &= \underbrace{\iiint x\left(s + \frac{\tau}{2}\right) f(\tau, \xi) e^{j2\pi\xi(s-t)} e^{-j2\pi\nu\tau} \overline{x\left(s - \frac{\tau}{2}\right)} d\xi ds d\tau}_{\text{energetic part } \rho_x^E(t, \nu)} \\ &\quad + \underbrace{\iiint x\left(s + \frac{\tau}{2}\right) f(\tau, \xi) e^{j2\pi\xi(s-t)} e^{-j2\pi\nu\tau} \mathbf{j} \overline{x\left(s - \frac{\tau}{2}\right)} d\xi ds d\tau}_{\text{polarization part } \rho_x^P(t, \nu)} \end{aligned} \quad (4.96)$$

The parameter function $f(\tau, \xi)$ is \mathbb{C}_j -valued and is identical to the parameter function of the Cohen class for univariate signals (Flandrin, 1998). Thus, by an appropriate choice of $f(\tau, \xi)$ one recovers *bivariate* analogue of well-known time–frequency representations, as illustrated below. This tight link with the univariate Cohen class shows that tuning the properties of parameter function in terms of usual conditions (causality, marginals, etc.) is straightforward. We will not address this ‘‘Troika of Parameterizations-Definitions-Properties’’⁵ here, focusing instead our analysis on some examples of distributions and on an important property of separability.

5. This expression is due to Flandrin (1998).

Separability between energetic and polarization parts The general definition of the Cohen class consists in two terms, namely

$$\rho_x^E(t, \nu) = \iiint x\left(s + \frac{\tau}{2}\right) f(\tau, \xi) e^{j2\pi\xi(s-t)} e^{-j2\pi\nu\tau} \overline{x\left(s - \frac{\tau}{2}\right)} d\xi ds d\tau \quad (4.97)$$

$$\rho_x^P(t, \nu) = \iiint x\left(s + \frac{\tau}{2}\right) f(\tau, \xi) e^{j2\pi\xi(s-t)} e^{-j2\pi\nu\tau} \mathbf{j}x\left(s - \frac{\tau}{2}\right) d\xi ds d\tau \quad (4.98)$$

which define the energetic part $\rho_x^E(t, \nu)$ and the polarization part $\rho_x^P(t, \nu)$ of the quaternion time-frequency-polarization distribution $\rho_x(t, \nu)$. In full generality, $\rho_x^E(t, \nu)$ and $\rho_x^P(t, \nu)$ are quaternion-valued functions.

It may be desirable to have a nice interpretation of the scalar part of ρ_x as a measure of energy and of its vector part as measure of the polarization features. This is the case when one has for every $(t, \nu) \in \mathbb{R}^2$

$$\begin{cases} \mathcal{S}\rho_x(t, \nu) &= \rho_x^E(t, \nu) \in \mathbb{R}, \\ \mathcal{V}\rho_x(t, \nu) &= \rho_x^P(t, \nu) \in \text{span}\{\mathbf{i}, \mathbf{j}, \mathbf{k}\}. \end{cases} \quad (4.99)$$

Thus this *separability* condition ensures that ρ_x^E is real and that ρ_x^P is purely imaginary. Conditions (4.99) are equivalent to $\rho_x^E(t, \nu) = \overline{\rho_x^E(t, \nu)}$ and $\rho_x^P(t, \nu) = -\overline{\rho_x^P(t, \nu)}$. Each of these conditions is sufficient to imply that

$$f(\tau, \xi) = \overline{f(-\tau, -\xi)}, \quad (4.100)$$

that is the parameter function $f(\tau, \xi)$ is Hermitian.

Now we give some examples of distributions belonging to the Cohen class. Three of them are *separable*: the quaternion Wigner-Ville distribution, the quaternion spectrogram and the quaternion Choi-Williams. The last example, the quaternion Rihaczek distribution is not separable.

Quaternion Wigner-Ville Letting $f(\tau, \xi) = 1$ one recovers the quaternion Wigner-Ville distribution introduced in the last section:

$$\rho_x^{\text{WV}}(t, \nu) = \text{WV}_x(t, \nu). \quad (4.101)$$

In particular, Eq. (4.96) shows that any Cohen class member can be seen as *smoothed* version of the quaternion Wigner-Ville distribution. Unlike for the univariate case (Flandrin, 1998) this smoothing cannot be expressed in terms of convolution operation due to noncommutativity of the quaternion product.

This condition on f corresponds to the reality requirement for the univariate Cohen Class, see Flandrin (1998, p. 117).

Quaternion spectrogram This time-frequency-polarization representation was the first introduced in Section 4.2.1 of this chapter. The quaternion spectrogram $\rho_x^S(t, \nu)$ relies on the Q-STFT F_x^g with window g such that

$$\rho_x^S(t, \nu) = |F_x^g(t, \nu)|^2 + F_x^g(t, \nu) \overline{jF_x^g(t, \nu)} \quad (4.102)$$

This representation also belongs to the Cohen class defined by (4.96). It is obtained just like in the univariate case, by taking $f(\tau, \xi)$ to be the ambiguity function of the real window g

$$f(\tau, \xi) = A_g(\tau, \xi) \triangleq \int_{-\infty}^{+\infty} g\left(r + \frac{\tau}{2}\right) g\left(r - \frac{\tau}{2}\right) e^{-j2\pi\xi r} dr \quad (4.103)$$

Plugging (4.103) into (4.96) yields (4.102) after some usual calculations.

Quaternion Choi-Williams distribution The quaternion Choi-Williams distribution is defined by the choice of the parameter function $f(\tau, \xi) = \exp(-(\pi\sigma\xi\tau)^2)$ where $\sigma > 0$ is a smoothing parameter. Since f is Hermitian, this distribution is separable. When $\sigma \rightarrow 0$, $f(\tau, \xi) \rightarrow 1$ so that for small values of σ , the quaternion Choi-Williams distribution is close to the quaternion Wigner-Ville distribution. Larger values of σ increase the smoothing of the quaternion Wigner-Ville distribution thus reducing interferences at the price of a degraded resolution.

Quaternion Rihaczek distribution This last distribution is obtained for $f(\tau, \xi) = \exp(j\pi\xi\tau)$. Since f is not Hermitian, it is not a separable time-frequency-polarization distribution. The quaternion Rihaczek distribution of x is

$$\rho_x^R(t, \nu) \triangleq x(t) e^{-j2\pi\nu t} \overline{X(\nu)} + x(t) e^{-j2\pi\nu t} j \overline{X(\nu)} \quad (4.104)$$

The two terms correspond respectively to the energetic part and to the polarization part of the Rihaczek distribution. These are both quaternion-valued functions, which limits a direct interpretation of ρ^R . The usefulness of such non-separable representations will be addressed in future work.

4.5 AN APPLICATION TO SEISMIC DATA

To conclude this chapter we perform a time-frequency-polarization analysis on a seismic trace from the 1991 Solomon Islands Earthquake. The original recording is a 3D seismic measurement leading to three channels u, v, w . We choose to analyze the bivariate signal $x(t) = u(t) + \mathbf{i}v(t)$, where u is the vertical component and v is the radial component in the frame of the received wave. This bivariate signal has been already studied by several authors in the literature (Lilly and Park, 1995; Olhede and Walden, 2003; Sykulski, Olhede, and Lilly, 2016).

Fig. 4.6a displays this signal. The part of the signal which is represented contains $N = 9000$ samples, equispaced by 0.25 s. The trace of $x(t)$ in the $u-v$ plane suggests that $x(t)$ is on average elliptically polarized. The time-evolution of each component also suggests that the instantaneous frequency of $x(t)$ is increasing with time.

We compute both the quaternion spectrogram and quaternion scalogram for this signal. The Q-STFT of the signal has been computed using a Hanning

Data is available as part of JLab (Lilly, 2016).

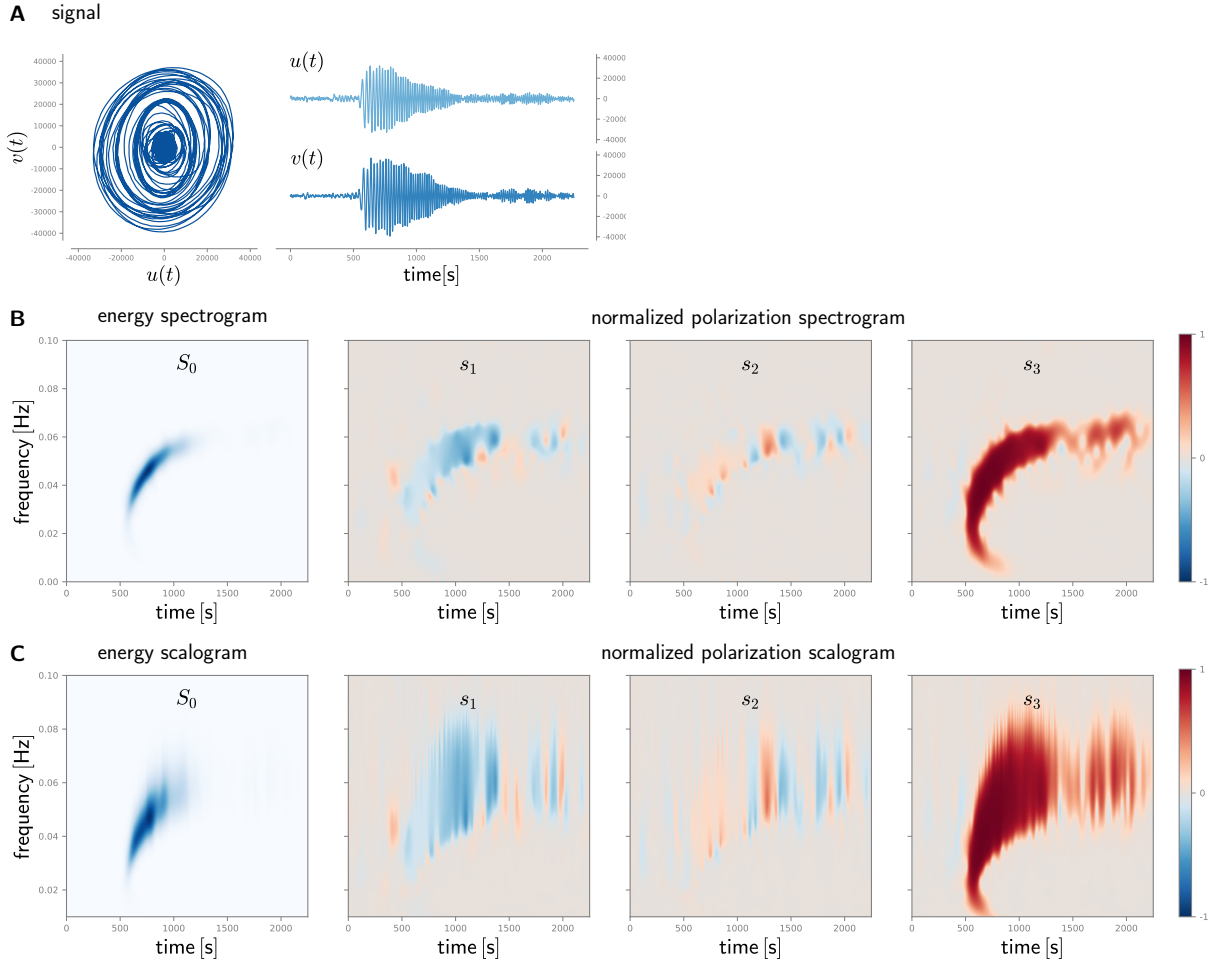


Figure 4.6: Seismic trace example from the 1991 Solomon Islands Earthquake. (a) bivariate signal corresponding to vertical (u) and radial (v) components of the original 3D signal. (b) energy and polarization spectrogram (c) energy and polarization scalogram.

window of size 801 samples, with window spacing equal to 10 samples. The Q-CWT of the signal has been computed on 400 scales using a Morse wavelet (4.36) with $\beta = 16$ and $\gamma = 2$.

Fig. 4.6b shows the energy and polarization spectrogram of x . Fig. 4.6c displays its energy and polarization scalogram. Time-frequency energy maps describe this signal as a slow linear chirp in frequency. The polarization spectrogram and polarization scalogram show that polarization properties are almost constant in the most energetic part, *i.e.* for $600s < t < 1200s$. In particular s_3 gives the instantaneous ellipticity χ which remains constant ($\chi \approx \pi/5$) in this region. It confirms the elliptical polarization obtained by visual inspection of Fig. 4.6a. The orientation is much harder to identify since the signal is strongly elliptically polarized (hence s_1 and s_2 are close to zero). A ridge extraction reveals that $\theta \approx \pi/2$ in the region $600s < t < 1200s$.

4.6 CONCLUSION

This chapter has presented a new and generic approach towards the time-frequency analysis of bivariate signals. It extends naturally usual univariate time-frequency analysis and obeys the same issues of localization, as supported by the Gabor-Heisenberg uncertainty principle for the QFT (Theorem 1.2).

Since the quaternion-valued spectrum of a bivariate signal is symmetric, considering positive frequencies only permits to define a bivariate analogue of the analytic signal of real or univariate signals. This quaternion embedding of a bivariate signal yields an instantaneous polarization ellipse description of the signal thanks to the Euler polar form. Turning to time-frequency representations to process multicomponent bivariate signals, we have defined a quaternion short-term Fourier transform (Q-STFT) and a quaternion continuous wavelet transform (Q-CWT) by using the QFT in place of the usual Fourier transform. Two fundamental theorems guarantee the conservation of energy and polarization quantities as well as reconstruction formulas. They permit to define the *energy spectrograms* and *energy scalograms*, which are interpreted as classical time-frequency energy maps. More importantly these theorems provide a natural definition of *polarization spectrograms* and *polarization scalograms* which characterize the evolution of the polarization state in the time-frequency plane. The ridges of these spectrograms and scalograms have been studied, and similar to the univariate case these ridges are shown to carry most of the significant information about the signal. We also addressed the construction of a generic class of bilinear time-frequency-polarization representation. These theoretical developments offer the possibility to tailor the representation to the features of the signal. Synthetic as well as real-world data examples have demonstrated the efficiency of the proposed approach. The resulting graphical representations make the time-frequency-polarization content of bivariate signals very readable and intelligible. On a practical ground, the numerical implementation remains simple and cheap since it relies on the use of a few fast Fourier transforms.

The findings of Section 4.1 to Section 4.3 have been published in an international journal (Flamant, Le Bihan, and Chainais, 2017e). They have been also presented at an international conference (Flamant, Le Bihan, and Chainais, 2017b) and at a national conference (Flamant, Le Bihan, and Chainais, 2017d). The definition of the quaternion Wigner-Ville transform (Section 4.4.1) and the original construction of the class of bilinear time-frequency-polarization representations (Section 4.4.2) constitute ongoing work which has not yet been published.

APPENDICES

4.A CANONICAL QUADRUPLLET OF BIVARIATE SIGNALS

Consider the bivariate AM-FM model given by (4.13)

$$x(t) = a(t)e^{i\theta(t)} [\cos \chi(t) \cos \varphi(t) + \mathbf{i} \sin \chi(t) \sin \varphi(t)], \quad (4.105)$$

where $[a(t), \theta(t), \chi(t), \varphi(t)]$ is a quadruplet characterizing $x(t)$. One of the outstanding questions arising from (4.105) is: when does the quadruplet $[a(t), \theta(t), \chi(t), \varphi(t)]$ form a *canonical quadruplet*? That is, under which conditions $x(t)$ defined by (4.105) has a quaternion embedding $x_+(t)$ which reads

$$x_+(t) = a(t)e^{i\theta(t)} e^{-k\chi(t)} e^{j\varphi(t)}. \quad (4.106)$$

A first (partial) answer to this question is found thanks to a Bedrosian theorem for the QFT.

Bedrosian theorem for the QFT Theorem 4.3 below extends the well-known Bedrosian theorem (Bedrosian, 1963) to the case of the quaternion Fourier transform.

Theorem 4.3 (Bedrosian). *Let $x : \mathbb{R} \rightarrow \mathbb{H}$ and $y : \mathbb{R} \rightarrow \mathbb{C}_j$. Suppose that X and Y have disjoint frequency support, i.e. $\text{supp}X(\nu) \subset [-B, B]$ and $\text{supp}Y(\nu) \subset (-\infty, -B'] \cup [B', +\infty)$. Assume that $B' > B > 0$ so that x is slowly varying compared to y . Then the Hilbert transform of the product $x(t)y(t)$ reads*

$$\mathcal{H}\{xy\}(t) = x(t)\mathcal{H}\{y\}(t) \quad (4.107)$$

Proof. The proof is similar to the usual Bedrosian theorem. Denote by \mathcal{F} the QFT. Then,

$$\mathcal{F}\mathcal{H}\{xy\}(\nu) = -\text{sign}(\nu)\mathcal{F}\{xy\}(\nu)\mathbf{j} \quad (4.108)$$

$$= -\text{sign}(\nu)(X * Y)(\nu)\mathbf{j} \quad (4.109)$$

$$= -\int_{-\infty}^{+\infty} X(\xi)Y(\nu - \xi)\text{sign}(\nu)\mathbf{j}d\xi \quad (4.110)$$

$$= -\int_{-\infty}^{+\infty} X(\xi)Y(\nu - \xi)\text{sign}(\nu - \xi)\mathbf{j}d\xi \quad (4.111)$$

$$= (X * \mathcal{F}\mathcal{H}\{y\})(\nu) \quad (4.112)$$

By the product property of the QFT

We use that $\text{sign}(\nu) = \text{sign}(\nu - \xi)$ for values of ξ such that $X(\xi)Y(\nu - \xi)$ is nonzero.

and by inverse QFT one finds the desired result

$$\mathcal{H}\{xy\}(t) = x(t)\mathcal{H}\{y\}(t). \quad (4.113)$$

□

Back to bivariate signals Recall the definition in the time domain of the quaternion embedding $x_+(t)$

$$x_+(t) = x(t) + \mathcal{H}\{x\}(t)\mathbf{j} \quad (4.114)$$

Let us assume that $\lambda_1(t) = a(t)e^{i\theta(t)} \cos \chi(t)$ is slowly varying and with disjoint frequency support with $\cos \varphi(t)$. Similarly assume that $\lambda_2(t) = \mathbf{i}a(t)e^{i\theta(t)} \sin \chi(t)$ is slowly varying and with disjoint frequency support with $\sin \varphi(t)$. Then, by Theorem 4.3 one has

$$x_+(t) = \lambda_1(t) \cos \varphi(t) + \lambda_2(t) \sin \varphi(t) + \mathcal{H}\{\lambda_1(t) \cos \varphi(t) + \lambda_2(t) \sin \varphi(t)\}(t) \mathbf{j} \quad (4.115)$$

$$= \lambda_1(t) [\cos \varphi(t) + \mathcal{H}\{\cos \varphi(t)\} \mathbf{j}] + \lambda_2(t) [\sin \varphi(t) + \mathcal{H}\{\sin \varphi(t)\} \mathbf{j}]. \quad (4.116)$$

As pointed out by Picinbono (1997), Bedrosian's theorem does not imply at all that $\mathcal{H}\{\cos \varphi(t)\} = \sin \varphi(t)$ or equivalently that $\mathcal{H}\{\sin \varphi(t)\} = -\cos \varphi(t)$. These relations are satisfied provided that the phase signal $z(t) = \exp(\mathbf{j}\varphi(t))$ is analytic. This is case when $z(t)$ is of the form (Picinbono, 1997)

$$z(t) = e^{j(2\pi\nu_0 t + \varphi_0)} \prod_n \frac{t - t_n}{t - \bar{t}_n} \quad (4.117)$$

where the t_n 's belong to the upper-half complex plane.

Assuming that $\varphi(t)$ is such that (4.117) holds then one obtains

$$x_+(t) = \lambda_1(t) e^{j\varphi(t)} - \lambda_2(t) e^{j\varphi(t)} \mathbf{j} \quad (4.118)$$

$$= a(t) e^{i\theta(t)} [\cos \chi(t) - \mathbf{k} \sin \chi(t)] e^{j\varphi(t)} \quad (4.119)$$

$$= a(t) e^{i\theta(t)} e^{-k\chi(t)} e^{j\varphi(t)}. \quad (4.120)$$

Together with Bedrosian's theorem assumptions on $a(t)$, $\theta(t)$ and $\chi(t)$ the technical condition (4.117) on the phase $\varphi(t)$ ensure that $[a(t), \theta(t), \chi(t), \varphi(t)]$ is a canonical quadruplet.

4.B STATIONARY PHASE APPROXIMATION

The asymptotic analysis carried out in Section 4.3 relies on a *stationary phase approximation* to study the localization of ridges in quaternion spectrograms and quaternion scalograms. This approach has first been used by Delprat et al. (1992) in the context of time-frequency analysis of univariate signals. The same arguments are used in our study, with straightforward adjustments to the quaternion context.

The stationary phase approximation (Dingle, 1973) provides an approximation to the integral

$$I = \int_{-\infty}^{+\infty} A(t) e^{j\varphi(t)} dt, \quad (4.121)$$

where $A \in C_0^\infty(\mathbb{R}; \mathbb{H})$, which ensures that $|A(t)| \rightarrow 0$ as $t \rightarrow \pm\infty$, and $\varphi \in C^\infty(\mathbb{R}; \mathbb{R})$. We assume moreover that the function φ is varying much faster than variations of A .

Let τ_s be a stationary point of φ such that is $\varphi'(\tau_s) = 0$. Assume that τ_s is unique, otherwise the contributions of all stationary points must be summed up. Rewrite the integral I as

$$I = \left(\int_{-\infty}^{+\infty} A(t) e^{j(\varphi(t) - \varphi(\tau_s))} dt \right) e^{j\varphi(\tau_s)}, \quad (4.122)$$

where we have factorized on the right of the exponential due to the noncommutativity of the product in \mathbb{H} . Let us introduce a new variable u , and suppose that $\varphi''(\tau_s) > 0$. This way, $\varphi(t) - \varphi(\tau_s)$ behaves as $(t - \tau_s)^2$ as $t \rightarrow \tau_s$ and write

$$-u^2 = (\varphi(t) - \varphi(\tau_s)) \text{ and } u^2 \underset{\tau_s}{\sim} -(t - \tau_s)^2 \varphi''(\tau_s). \quad (4.123)$$

The integral I then reads

$$I = \left[\int_{-\infty}^{+\infty} A(t(u)) \left(\frac{du}{dt} \right)^{-1} e^{-ju^2} du \right] e^{j\varphi(\tau_s)}. \quad (4.124)$$

Let us denote $\tilde{A}(u) = A(t(u)) (du/dt)^{-1}$. A Taylor series expansion of $\tilde{A}(u)$ leads to

$$I = \sum_{k=0}^{\infty} \frac{\tilde{A}^{(k)}(0)}{k!} \left[\int_{-\infty}^{+\infty} u^k e^{-ju^2} du \right] e^{j\varphi(\tau_s)}. \quad (4.125)$$

The integral is classical, related to Fresnel oscillatory integrals. It is zero for odd values of k , and for even values of k one has

$$\int_{-\infty}^{+\infty} u^{2k} e^{-ju^2} du = \Gamma(k + 1/2) e^{j\frac{\pi}{4}} e^{j\frac{\pi}{2}k}, \quad (4.126)$$

so that

$$I = \sum_{k=0}^{\infty} \frac{\tilde{A}^{(2k)}(0)}{(2k)!} \Gamma(k + 1/2) e^{j\frac{\pi}{4}} e^{j\frac{\pi}{2}k} e^{j\varphi(\tau_s)}. \quad (4.127)$$

For $k = 0$, the first term of the expansion is found to be $\tilde{A}(0) = 2^{1/2} |\varphi''(\tau_s)|^{-1/2} A(\tau_s)$ so that finally,

$$I \approx \sqrt{2\pi} \frac{A(\tau_s)}{\sqrt{|\varphi''(\tau_s)|}} e^{\text{sign}(\varphi''(\tau_s)) j\frac{\pi}{4}} e^{j\varphi(\tau_s)}. \quad (4.128)$$

4.C PROOFS

The proofs of Theorem 4.1 and Theorem 4.2 are very similar to the proofs of the usual univariate case. We thus follow the presentation given in Mallat (2008), with the additional requirement of handling properly quaternions valued expressions due to noncommutativity.

4.C.1 Proof of Theorem 4.1

Inversion formula The time-frequency-polarization atoms are of the form $g_{\tau, \nu}(t) = g(t - \tau) \exp(j2\pi\nu t)$, where g is a real and symmetric window. Let us rewrite the Q-STFT coefficients $F_x^g(\tau, \nu)$ like

$$\begin{aligned} F_x^g(\tau, \nu) &= \int_{-\infty}^{+\infty} x(t) g(t - \tau) e^{-j2\pi\nu t} dt \\ &= \left(\int_{-\infty}^{+\infty} x(t) g(t - \tau) e^{j2\pi\nu(\tau - t)} dt \right) e^{-j2\pi\nu\tau} \\ &= (x * g_{0, \nu})(\tau) e^{-j2\pi\nu\tau} \end{aligned} \quad (4.129)$$

We use that g is symmetric $g(-t) = g(t)$.

where $g_{0, \nu}(t) = g(t) \exp(j2\pi\nu t)$. The QFT of this expression yields

$$\begin{aligned} \int_{-\infty}^{+\infty} F_x^g(\tau, \nu) e^{-j2\pi\xi\tau} d\tau &= \int_{-\infty}^{+\infty} (x * g_{0, \nu})(\tau) e^{-j2\pi(\xi + \nu)\tau} d\tau \\ &= X(\xi + \nu) G_{0, \nu}(\xi + \nu) \\ &= X(\xi + \nu) G(\xi) \end{aligned} \quad (4.130)$$

thanks to the convolution property of the QFT, see Table 1.1. Using Parseval's formula with respect to τ yields

$$\int_{-\infty}^{+\infty} F_x^g(\tau, \nu) g(t - \tau) d\tau = \frac{1}{2\pi} \int_{-\infty}^{+\infty} [X(\xi + \nu) G(\xi)] e^{j2\pi\xi t} \overline{G(\xi)} d\xi \quad (4.131)$$

Since g is real, its QFT is \mathbb{C}_j -valued and commutes with the complex exponential, i.e. $e^{j2\pi\xi t} \overline{G(\xi)} = \overline{G(\xi)} e^{j2\pi\xi t}$. Using that g is a normalized window $\|g\| = 1$ one gets

$$\begin{aligned} \int_{-\infty}^{+\infty} \int_{-\infty}^{+\infty} F_x^g(\tau, \nu) g(t - \tau) e^{j2\pi\nu t} d\tau d\nu &= \int_{-\infty}^{+\infty} \int_{-\infty}^{+\infty} [X(\xi + \nu) G(\xi)] \overline{G(\xi)} e^{j2\pi(\xi + \nu)t} d\xi d\nu \\ &= \int_{-\infty}^{+\infty} \int_{-\infty}^{+\infty} X(\xi + \nu) |G(\xi)|^2 e^{j2\pi(\xi + \nu)t} d\xi d\nu \\ &= \int_{-\infty}^{+\infty} x(t) |G(\xi)|^2 d\xi \\ &= x(t), \end{aligned} \quad (4.132)$$

which concludes the proof of the inversion formula (4.22).

Energy and polarization conservation From (4.130) the QFT with respect to τ of $F_x^g(\tau, \nu)$ is $X(\xi + \nu)G(\xi)$. Then using the usual Plancherel's formula in τ yields

$$\begin{aligned} \iint |F_x^g(\tau, \nu)|^2 d\tau d\nu &= \iint |X(\xi + \nu)G(\xi)|^2 d\xi d\nu \\ &= \int |X(\xi)|^2 d\xi \\ &= \|x\|^2. \end{aligned} \quad (4.133)$$

which concludes the proof of the energy conservation property (4.23). The polarization conservation property (4.24) is proven along the same lines using the conservation of polarization properties, see Eq. (1.41). \square

4.C.2 Proof of Theorem 4.2.

Let $\psi \in H^2(\mathbb{R}; \mathbb{C}_j)$, i.e. ψ is \mathbb{C}_j -valued and analytic. Suppose also that ψ is admissible,

$$\int_0^{+\infty} \frac{|\Psi(\nu)|^2}{\nu} d\nu < +\infty. \quad (4.134)$$

We use the notation $\psi_s(t) = s^{-1/2}\psi(t/s)$. We first prove a preliminary result.

Compute the QFT with respect to τ of the Q-CWT coefficients $W_x(\tau, s)$:

$$\begin{aligned} \int_{-\infty}^{+\infty} W_x(\tau, s) e^{-j2\pi\xi\tau} d\tau &= \int_{-\infty}^{+\infty} \int_{-\infty}^{+\infty} x(t) \overline{\psi_s(t - \tau)} e^{-j2\pi\xi\tau} d\tau dt \\ &= \int_{-\infty}^{+\infty} x(t) \left(\int_{-\infty}^{+\infty} \overline{\psi_s(t - \tau)} e^{-j2\pi\xi\tau} d\tau \right) dt \\ &= \left(\int_{-\infty}^{+\infty} x(t) e^{-j2\pi\xi t} dt \right) \overline{\Psi_s(\xi)} \\ &= \underbrace{X(\xi)}_{\in \mathbb{H}} \underbrace{\overline{\Psi_s(\xi)}}_{\in \mathbb{C}_j} \end{aligned} \quad (4.135)$$

Now, since $\Psi(\xi) = 0$ for $\xi < 0$ and that $X_+(\xi) = 2X(\xi)$ for $\xi \geq 0$, we get from (4.135) that for all ξ

$$X(\xi) \overline{\Psi_s(\xi)} = \frac{1}{2} X_+(\xi) \overline{\Psi_s(\xi)}, \quad (4.136)$$

and therefore by inverse QFT of (4.136)

$$W_x(\tau, s) = \frac{1}{2} W_{x_+}(\tau, s). \quad (4.137)$$

Inversion formula For simplicity, we prove the inversion formula for the case of a quaternion embedding signal x_+ . Introduce an intermediate quantity $c(t)$

$$c(t) = \int_{-\infty}^{+\infty} \int_0^{+\infty} W_{x_+}(\tau, s) \psi_s(t - \tau) d\tau \frac{ds}{s^2} \quad (4.138)$$

Taking the QFT of $c(t)$ yields

$$\begin{aligned} C(\xi) &= \int_{-\infty}^{+\infty} \left(\int_{-\infty}^{+\infty} \int_0^{+\infty} W_{x_+}(\tau, s) \psi_s(t - \tau) d\tau \frac{ds}{s^2} \right) e^{-j2\pi\xi t} dt \\ &= \int_{-\infty}^{+\infty} \int_0^{+\infty} W_{x_+}(\tau, s) \left(\int_{-\infty}^{+\infty} \psi_s(t - \tau) e^{-j2\pi\xi t} dt \right) d\tau \frac{ds}{s^2} \\ &= \int_{-\infty}^{+\infty} \int_0^{+\infty} W_{x_+}(\tau, s) \Psi_s(\xi) e^{-j2\pi\xi\tau} d\tau \frac{ds}{s^2} \\ &= \int_{-\infty}^{+\infty} \int_0^{+\infty} W_{x_+}(\tau, s) e^{-j2\pi\xi\tau} \Psi_s(\xi) d\tau \frac{ds}{s^2} \\ &= \int_0^{+\infty} X_+(\xi) \overline{\Psi_s(\xi)} \Psi_s(\xi) \frac{ds}{s^2} \end{aligned} \quad (4.139)$$

One gets

$$C(\xi) = X_+(\xi) \int_0^{+\infty} \frac{|\Psi_s(\xi)|^2}{s} ds = X_+(\xi) C_\psi. \quad (4.140)$$

Since the wavelet is admissible $x_+(t)$ and $C_\psi^{-1}c(t)$ have the same quaternion Fourier transforms. This proves the inversion formula (4.39):

$$x_+(t) = \frac{1}{C_\psi} \int_{-\infty}^{+\infty} \int_0^{+\infty} W_{x_+}(\tau, s) \psi_s(t - \tau) d\tau \frac{ds}{s^2}. \quad (4.141)$$

Conservation of energy and polarization According to Plancherel's formula (1.40) for the energy

$$\frac{1}{C_\psi} \int_{-\infty}^{+\infty} \int_0^{+\infty} |W_{x_+}(\tau, s)|^2 d\tau \frac{ds}{s^2} = \frac{1}{C_\psi} \int_{-\infty}^{+\infty} \int_0^{+\infty} |X_+(\xi) \overline{\Psi_s(\xi)}|^2 d\xi \frac{ds}{s^2} \quad (4.142)$$

Since the wavelet is normalized $\|\psi\|_{L^2} = 1$ this expression can be simplified as

$$\frac{1}{C_\psi} \int_{-\infty}^{+\infty} \int_0^{+\infty} |W_{x_+}(\tau, s)|^2 d\tau \frac{ds}{s^2} = \int_{-\infty}^{+\infty} |X_+(\xi)|^2 d\xi = \|x_+\|^2 \quad (4.143)$$


which proves (4.40). The conservation of polarization properties (4.41) is obtained following the same lines. \square

Nonparametric characterization of gravitational waves polarizations

5

This chapter presents the potential of the presented framework for the characterization of gravitational waves polarizations emitted by precessing compact binaries. We demonstrate that the Stokes parameters computed from the quaternion embedding of the (complex) gravitational waveform provide new and relevant *nonparametric* observables for the diagnostic of precession. They allow to finely decipher the geometric configuration of the source, which would be very difficult to obtain otherwise.

The material presented in this chapter is the first outcome from a collaboration with Eric Chassande-Mottin and Fangchen Feng, both with the Astroparticule and Cosmologie laboratory in Paris. It has been presented at the international conference EUSIPCO 2018 (Flamant et al., 2018)

 J. Flamant, P. Chainais, E. Chassande-Mottin, F. Feng, and N. Le Bihan. 2018. “Non-parametric characterization of gravitational-wave polarizations.” In *26th European Signal Processing Conference (EUSIPCO), 2018*, 1–5. September

This chapter has been essentially adapted from (Flamant et al., 2018). Section 5.1 introduces gravitational waves and precessing binaries. Section 5.2 describes the modeling of the gravitational wave emitted by precessing binaries. Section 5.3 shows on a special case how Stokes parameters encode dynamical precession effects. We also discuss the generic case. Section 5.4 finally illustrate the approach on simulated gravitational waveforms in the noiseless and realistic noise settings. Appendices gather technical details and computations.

CHAPTER CONTENTS

5.1	Gravitational waves and precessing binaries	133
5.2	Modeling the emitted gravitational waveform	134
5.3	Stokes parameters characterization of precession	136
5.4	Application to precession diagnosis	137
5.5	Conclusion	138
APPENDICES		
5.A	Harmonic analysis in spherical coordinates	140
Spin weighted spherical harmonics • Wigner-D functions •		
5.B	Gravitational waveform in the inertial frame	140
Calculation of the emission modes in the inertial frame • Waveform expression •		
5.C	Instantaneous Stokes parameters	142
Quaternion embedding of the emitted waveform • Stokes parameters expressions •		

5.1 GRAVITATIONAL WAVES AND PRECESSING BINARIES

A new kind of astronomy is born with the first advanced LIGO and advanced Virgo discoveries (Abbott et al., 2017a, 2017b, 2017c, 2016a, 2016b). Those gravitational wave detectors allow the observation of astrophysical systems, such as binary black-holes, that have so far escaped conventional astronomy based on electromagnetic radiation.

Fig. 5.1 displays the estimated gravitational wave strain recorded at the Hanford detector during the first detection event GW150914. Insets on top of Fig. 5.1 show the binary black-hole coalescence. Gravitational waves carry information about the bulk motion of the emitting system relative to the observer: e.g. the wave frequency is related to the orbital or spinning period of the source mass distribution. The resulting “power-law chirp”-like waveform is characteristic of gravitational waves emitted by coalescing compact binaries (Thorne, 1987).

Gravitational waves are polarized and admit two orthogonal polarizations, denoted by h_+ and h_\times . They form a basis similar to the linear horizontal and vertical polarizations of electromagnetic waves. Gravitation-wave detectors

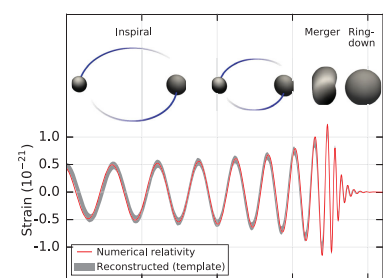


Figure 5.1: Estimated gravitational wave strain recorded at the Hanford detector during the first detection event GW150914. Insets show the binary black-hole coalescence. Reproduced from (Abbott et al., 2016b) under the Creative Commons licence.

do not measure the two gravitational-wave polarizations independently but rather a linear mixture of them. However observations from two or more non-coaligned detectors allow to reconstruct the two gravitational-wave polarizations. We assume here that h_+ and h_\times from a binary merger are reconstructed from LIGO and Virgo observations, as explained *e.g.* in Feng et al. (2018).

The amplitude and phase relationship between the two polarizations components h_+ and h_\times predicted by general relativity is related to the source orientation with respect to the observer. The evolution of the polarization pattern thus provides evidence for changes in the orientation due to precession or nutation of the system. Precession of the binary orbital plane is an important information as it indicates that at least one binary component has a large spin, misaligned with the orbital angular momentum. In turn, this provides decisive hints on how the binary has formed.

The gravitational wave strain h is usually written as the complex signal $h(t) = h_+(t) - ih_\times(t)$, which makes it interpretable as a bivariate signal. Using the time-frequency analysis tools developed in Chapter 4 we will be able to characterize the instantaneous polarization state of $h(t)$. The associated instantaneous Stokes parameters provide a set of new and nonparametric observables that characterize precession. This contrasts with conventional approaches, where the presence of precession in the detected signal is classically tested by fitting the data with waveforms obtained from precessing binary physical models. This procedure does not test precession effects alone, but rather a full description of the binary orbital dynamics, which thus includes many other dynamical effects. The approach described in the following is not bound to any dynamical model and hence is very generic.

5.2 MODELING THE EMITTED GRAVITATIONAL WAVEFORM

Following (Babak, Taracchini, and Buonanno, 2017), we assume quasi-circular orbits and introduce a set of two frames to model the sensing of gravitational waves. The modeling of the GW signal from the precessing binaries is usually done in two steps. First, the computation of the GW modes is done in the frame P instantaneously co-precessing with the binary orbital plane. Those modes are the result of the decomposition of the signal in the spin -2 weighted spherical harmonics. In the second step, the modes are rotated to the inertial frame I associated with the binary configuration at some fiducial time (which is usually associated with the time when the signal enters the observational band of the detector). This inertial frame is then associated with the position and orientation of the GW detectors (LIGO, Virgo).

In the precessing frame attached to the binary, the complex gravitational wave strain $h^P = h_+^P - ih_\times^P$ can be decomposed into spherical harmonics $h_{\ell m}^P(t)$ such that

$$h^P(t; \Omega) = \sum_{\ell=2}^{\infty} \sum_{m=-\ell}^{\ell} h_{\ell, m}^P(t) {}_{-2}Y_{\ell, m}(\Omega) \quad (5.1)$$

where Ω is the (time-varying) angle of the observer in the precessing frame and ${}_{-2}Y_{\ell, m}$ are the -2 -spin weighted spherical harmonics.

The key idea of Babak, Taracchini, and Buonanno (2017) is that the gravitational wave modes in the precessing frame resemble that of a non-precessing binary. The dominant modes correspond to $(\ell = 2, m = \pm 2)$ and they can be

See Appendix 5.A.1 for explicit expressions of -2 -spin weighted spherical harmonics.

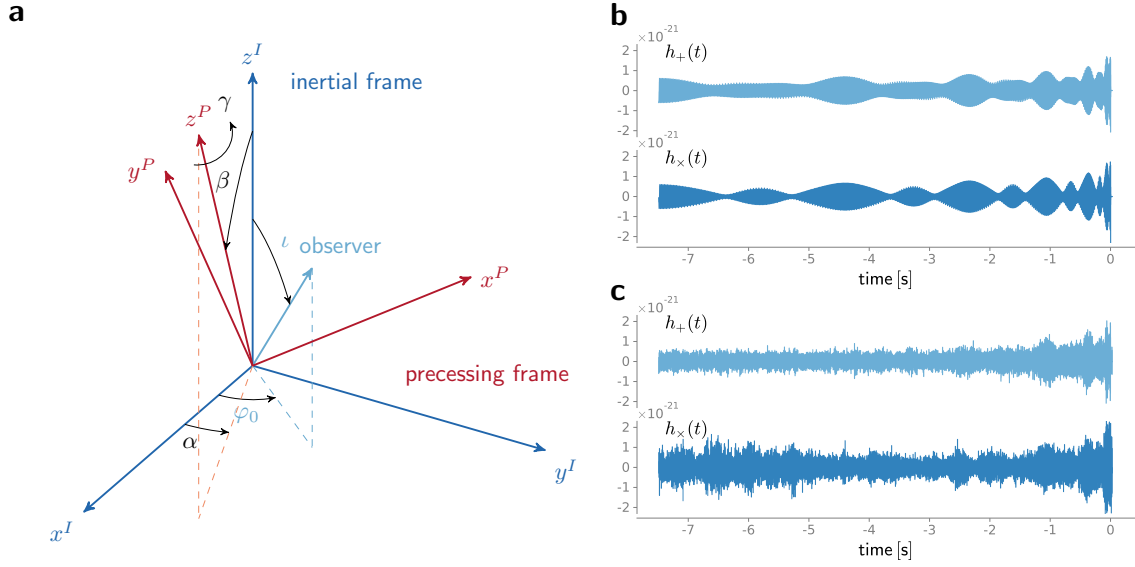


Figure 5.2: (a) The relation between precessing and inertial frames is parameterized by Euler angles α, β, γ in the zyz -convention. Spherical coordinates (l, φ_0) denote the position of the observer in the inertial frame. (b) Waveforms of the two polarizations h_+ and h_\times for a strongly precessing binary system formed by a neutron-star and a 10-solar mass black-hole with misaligned spin $\mathbf{s}_1 = (0.7, 0.7, 0)$. The binary is face-on and located at a distance of 10 Mpc. (c) Reconstructed polarizations from simulated LIGO and Virgo observations of the same binary system, see Feng et al. (2018).

approximated as

$$h_{2,\pm 2}^P(t) = a_0(t) e^{\mp i \Phi_0(t)}. \quad (5.2)$$

While Babak, Taracchini, and Buonanno (2017) derives explicit expressions for the instantaneous amplitude $a_0(t)$ and phase $\Phi_0(t)$ by resolving the binary orbital motion, we do not assume here any specific evolution for $a_0(t)$ and $\Phi_0(t)$. We only note that the instantaneous $a_0(t)$ typically varies much slowly than the instantaneous phase $\Phi_0(t)$ – this arises from the dynamics of the binary orbital motion.

The modes are rotated from the precessing frame P to the inertial frame labelled with I using the (time-dependent) Euler angles α, β and γ , see Fig. 5.2a. This change of frame involves the following correspondence between spherical harmonics coefficients of the gravitational waves expressed in each frame:

$$h_{\ell,m}^I = \sum_{m'=-\ell}^{\ell} h_{\ell,m'}^P D_{m'm}^{\ell,*}(-\gamma, -\beta, -\alpha) \quad (5.3)$$

where $D_{m'm}^{\ell}$ are the Wigner-D functions (Rose, 1957). The superscript $*$ here denotes complex conjugation. When the binary does not precess, the frames P and I coincide and $\alpha = \beta = \gamma = 0$. Since there are only $\ell = 2$ modes in the frame P , only $\ell = 2$ modes will contribute in the frame I . However, all m modes contribute to the observed signal, which therefore reads

$$h^I(t; l, \varphi_0) = \sum_{m=-2}^2 h_{2,m}^I(t) {}_{-2}Y_{2,m}(l, \varphi_0) \quad (5.4)$$

where (l, φ_0) are the spherical coordinates of the observer.

By combining Eqs (5.1–5.4), we can express the two polarizations h_+ and h_\times of the incident gravitational wave in the observation frame as a generic function of the binary orbital dynamics and the orientation of the binary. For a strongly precessing binary system composed of a neutron star and a 10 solar-mass black-hole with misaligned spin $\mathbf{s}_1 = (0.7, 0.7, 0)$, this results in the waveforms shown in Fig. 5.2b. Precession causes changes in the orientation of the binary's

See Appendix 5.A.2 for explicit expressions of Wigner-D functions.

In the geocentric frame, l therefore corresponds to the inclination of the binary orbital plane with the line of sight.

orbital plane with respect to the line of sight, that leads to the characteristic amplitude modulations clearly seen on the waveform envelop. It also leads to less obvious interrelationships between the “+” and “×” phases that we intend to discriminate with the time-frequency analysis tools introduced in Chapter 4.

5.3 STOKES PARAMETERS CHARACTERIZATION OF PRECESSION

The gravitational wave strain in the inertial frame $h^I(t; \iota, \varphi_0)$ forms a non-stationary bivariate signal. Its instantaneous polarization attributes can be obtained from its quaternion embedding, as described in Section 4.1. This set of descriptors provides a straightforward characterization of polarization evolution for precessing binaries. We consider first the special case of face-on $(\iota, \varphi_0) = (0, 0)$ binaries. The generic case $(\iota, \varphi_0) \neq (0, 0)$ is discussed afterwards.

The special case of face-on binaries Consider the observed signal (5.4) obtained for face-on $(\iota, \varphi_0) = (0, 0)$ binaries, that is when the observer is in direction z^I . From calculations detailed in Appendix 5.B, the waveform (5.4) is explicitly given by (5.18), which further simplifies in the face-on case as

$$h^I(t) = ka_0(t)e^{-2i\alpha(t)} \left[(1 + \cos^2 \beta(t)) \cos \Phi_\gamma(t) - 2i \cos \beta(t) \sin \Phi_\gamma(t) \right] \quad (5.5)$$

where $k > 0$ is a constant and $\Phi_\gamma(t) = \Phi_0(t) + 2\gamma(t)$. For most cases of astrophysical relevance the orbital dynamics can be described by osculating orbits where the precession timescale is much longer than the orbital timescales. This means that Euler angles $[\alpha(t), \beta(t), \gamma(t)]$ vary much slowly than the phase $\Phi_\gamma(t)$. It thus allows a direct¹ identification of instantaneous polarization parameters by comparing (5.5) with the bivariate AM-FM model (4.13):

$$a(t) = ka_0(t) \left[(1 + \cos^2 \beta(t))^2 + 4 \cos^2 \beta(t) \right]^{1/2} \quad (5.6)$$

$$\theta(t) = -2\alpha(t) \quad (5.7)$$

$$\chi(t) = -\arctan \frac{2 \cos \beta(t)}{1 + \cos^2 \beta(t)} \quad (5.8)$$

$$\varphi(t) = \Phi_0(t) + 2\gamma(t) \quad (5.9)$$

Eqs. (5.6)–(5.9) highlights the direct relation between standard descriptors of bivariate signals and GW parameters. In particular, Eqs. (5.7) and (5.8) explicitly show how precessing binaries generate polarization modulation effects on the observed signal $h^I(t)$. Remarkably, the face-on case features a nice decoupling between orientation $\theta(t)$ – depending only on $\alpha(t)$ and ellipticity $\chi(t)$ – depending only on $\beta(t)$. Note that $\gamma(t)$ only affects the phase $\varphi(t)$ and does not produce polarization modulation effects.

General case: arbitrary observer position In the general case $(\iota, \varphi_0) \neq (0, 0)$, the direct identification of instantaneous parameters $[a(t), \theta(t), \chi(t), \varphi(t)]$ from the expression of $h^I(t)$ is no longer straightforward. This is due to the complexity of the expression of $h^I(t)$, see for instance Eq. (5.18). Rather, precession and polarization modulation effects in $h^I(t)$ can be easily characterized using instantaneous Stokes parameters. In particular, normalized

1. More technically, we assume that the conditions of the Bedrosian theorem for bivariate signals (see Appendix 4.A) are fulfilled, and that the instantaneous phase $\Phi_\gamma(t)$ can be factorized as (4.117). In practice, the dynamics of the physical model ensure that these conditions are fulfilled, at least in the inspiral (prior to merger) part. These conditions allow a direct identification of instantaneous parameters from (5.5).

Stokes parameters $S_1/S_0, S_2/S_0, S_3/S_0$ provide a convenient description of the instantaneous polarization state of $h^I(t)$. Their explicit expressions can be obtained from the quaternion embedding of the generic model (5.4). The quaternion embedding $h_{\mathbb{H}}^I$ is computed like

$$h_{\mathbb{H}}^I(t) = h^I(t) + \mathcal{H}\{h^I(t)\} \mathbf{j}. \quad (5.10)$$

Then as explained in Section 4.1, the first instantaneous Stokes parameter is given by $S_0(t) = |h_{\mathbb{H}}^I(t)|^2$. It encodes the instantaneous energy of the signal. The three remaining Stokes parameters describe the instantaneous polarization state and are given by $h_{\mathbb{H}}(t) \mathbf{j} \overline{h_{\mathbb{H}}(t)} = \mathbf{i}S_3(t) + \mathbf{j}S_1(t) + \mathbf{k}S_2(t)$. Expressions are given in Appendix 5.C.2. These are highly voluminous, but nonetheless highlight a direct connection between precession parameters, Euler angles α, β , and the instantaneous polarization state of $h^I(t)$. Note that γ only affects the instantaneous phase of $h^I(t)$, as for the special case of face-on binaries.

To disambiguate with the gravitational wave “+” polarization we use the notation $h_{\mathbb{H}}$ instead of h_+ (as used in Chapter 4) to denote the quaternion embedding of a complex signal h .

5.4 APPLICATION TO PRECESSION DIAGNOSIS

We illustrate our findings on simulated gravitational waveforms from precessing binaries. Simulations are carried out using the generic SEOBNRv3 model of a (strongly) precessing black-hole/neutron star binary (Pan et al., 2014). This precessing case is somehow extreme and is not favored by current binary formation models. However it is not excluded and remains physically possible. Above all, waveforms presented in Fig. 5.2b serve our illustrative purposes. Fig. 5.2b depicts the two polarizations $h_+(t)$ and $h_{\times}(t)$ of a gravitational wave emitted by this binary system.

Stokes parameters provide a straightforward diagnosis of precession. The theoretical relation between normalized Stokes parameters and Euler angles can be explicitly derived, see *e.g.* expressions (5.26)–(5.29). Eqs (5.7)–(5.8) give the corresponding geometric parameters for the case of face-on binaries. For non-precessing binaries, Euler angles $\alpha(t), \beta(t), \gamma(t)$ are identically zero. In this case, the instantaneous polarization state of $h^I(t)$ is constant since Stokes parameters remain constant: this can be directly checked from (5.26)–(5.29) Since they are readily computed from the quaternion embedding of the observed signal $h^I(t)$, they provide a useful and sensitive tool for the analysis of precession effects.

Fig. 5.3a shows the instantaneous normalized Stokes parameters obtained from the quaternion embedding $h_{\mathbb{H}}(t)$ of the bivariate signal $h^I(t) = h_+(t) - \mathbf{i}h_{\times}(t)$ with waveforms presented in Fig. 5.2b. These gravitational waveforms correspond to a strong precessing binary observed face-on $(\iota, \varphi_0) = (0, 0)$. The non-parametric estimates of Stokes parameters (thin white lines) from simulated $h^I(t)$ close to perfectly match the values expected from the explicit physical model involving Euler angles (thick blue lines): the 2 curves are superposed. The presence of oscillations indicates that the instantaneous polarization state of $h^I(t)$ is modulated. This polarization modulation is directly explained by the precession dynamics. In particular for face-on binaries $S_3(t)/S_0(t)$ is a function of the precession angle $\beta(t)$ only, see (5.33).

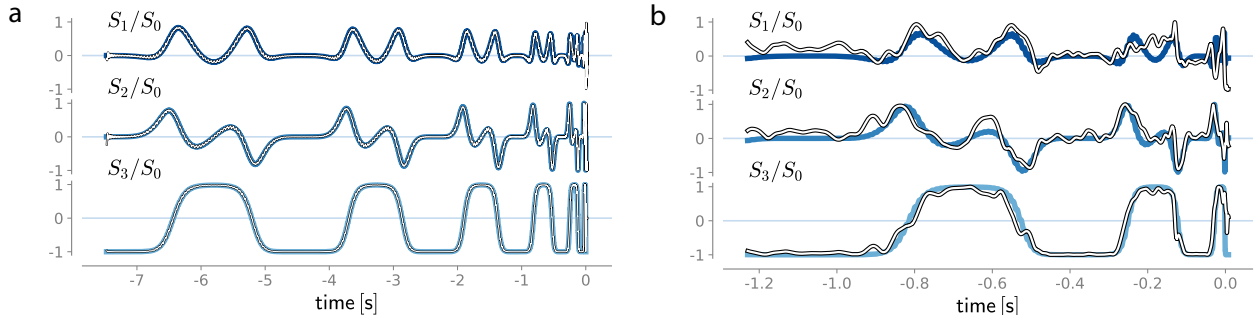


Figure 5.3: (a) Non-parametric estimates of normalized instantaneous Stokes parameters S_1/S_0 , S_2/S_0 and S_3/S_0 (thin white lines) computed from computed $h^I(t)$ depicted in Fig. 5.2b. They close to perfectly match the values expected from the explicit physical model involving Euler angles (thick blue lines). Oscillations characterize the dynamics of precessing binary. (b) Non-parametric estimates of normalized instantaneous Stokes parameters S_1/S_0 , S_2/S_0 and S_3/S_0 (thin white lines) obtained from the reconstructed polarizations shown in Fig. 5.2c. Expected values from the explicit physical model involving Euler angles (thick blue lines) are depicted for comparison.

Fig. 5.3b presents the normalized Stokes parameters obtained for the bivariate signal $h^I(t) = h_+(t) - ih_\times(t)$ using reconstructed polarizations depicted in Fig. 5.2c. The polarization reconstruction from LIGO/Virgo observations requires solving an inverse problem. Here, this is performed using sparsity-promoting regularization techniques (LASSO) presented in Feng et al. (2018). The reconstructed polarizations are obtained from observations of the black-hole/neutron-star binary system considered in Fig. 5.2c in simulated LIGO/Virgo noise using sensitivity curves comparable to that of the last O2 science run. Stokes parameters are extracted from the ridge of a quaternion continuous wavelet transform presented in Section 4.2.2. This is necessary in order to overcome the remaining noise in reconstructed polarizations in Fig. 5.2c, which hinders the direct use of the quaternion embedding method. On the ridge, one approximately recovers the quaternion embedding of the noiseless signal $h^I(t)$, as explained in Section 4.3. The extracted ridge corresponds to the end of the inspiral ($-1.2 \text{ s} \leq t \leq 0$) since SNR increases and becomes large enough as the binary comes close to the merger. The good agreement between reconstructed normalized Stokes parameters and their explicit physical model involving Euler angles (thick blue lines) demonstrate the relevance of use of Stokes parameters to diagnosis and characterize precession.

5.5 CONCLUSION

We have shown that Stokes parameters estimated from the observed gravitational wave directly connect waveform features to dynamical properties of the source. When applied to the case of coalescing compact binaries, they permit to test the presence of precession of the orbital plane prior to the merger (when the binary collapses). Most importantly these new observables are non parametric and bring robust information to provide a support to more conventional waveform fitting procedures based on a comprehensive and detailed model of the binary dynamics. In some sense, Stokes parameters are a reparametrization that directly encodes orbital properties of the source which are very difficult to obtain individually. In the case of the observation of a simulated simple face-on binary, with dominating $\ell = \pm 2$ modes, our results show a remarkable agreement between theoretical predictions and numerical estimations. They can be extended to arbitrary binary orientations and higher-order modes. This approach could also yield the detailed physical parameters from the Stokes observables by reverting a system of non-linear equations.

These results will be presented at an international conference (Flamant et al., 2018). Together with the reconstruction of polarizations described in Feng et al. (2018), it provides a complete procedure to analyze polarization-related effects in experimental data from LIGO and Virgo detectors. It has the potential of revealing any dynamical effect that affects the gravitational-wave polarization pattern, *i.e.*, not only precession but also *e.g.*, orbital eccentricity.

APPENDICES

5.A HARMONIC ANALYSIS IN SPHERICAL COORDINATES

5.A.1 Spin weighted spherical harmonics

The s -spin-weighted spherical harmonics functions ${}_s Y_{\ell,m}$ form a basis for square integrable signals on the sphere \mathbb{S}^2 . They are defined in *e.g.* Goldberg et al. (1967). For our purpose we only need their expressions for ${}_2 Y_{2,m}$, $m = -2, -1, 0, 1, 2$:

$$\begin{aligned} {}_{-2}Y_{2,-2}(\iota, \varphi_0) &= \frac{1}{8} \sqrt{\frac{5}{\pi}} (1 - \cos \iota)^2 e^{-2i\varphi_0}, & {}_{-2}Y_{2,-1}(\iota, \varphi_0) &= \frac{1}{4} \sqrt{\frac{5}{\pi}} (1 - \cos \iota) \sin \iota e^{-i\varphi_0}, \\ {}_{-2}Y_{2,0}(\iota, \varphi_0) &= \frac{\sqrt{6}}{8} \sqrt{\frac{5}{\pi}} \sin^2 \iota, & & \\ {}_{-2}Y_{2,1}(\iota, \varphi_0) &= \frac{1}{4} \sqrt{\frac{5}{\pi}} (1 + \cos \iota) \sin \iota e^{i\varphi_0}, & {}_{-2}Y_{2,2}(\iota, \varphi_0) &= \frac{1}{8} \sqrt{\frac{5}{\pi}} (1 + \cos \iota)^2 e^{2i\varphi_0} \end{aligned} \quad (5.11)$$

5.A.2 Wigner-D functions

The Wigner-D functions $D_{m'm}^\ell$ form a basis for square integrable functions on the rotation group $\text{SO}(3)$. Their generic expression is given in *e.g.* Rose (1957) or Varshalovich, Moskalev, and Khersonskii (1988). For our purpose, we only need the $D_{m'm}^2$'s functions, with $m' = \pm 2$ and $m = -2, -1, 0, 1, 2$, as given in Table 5.1 below.

		m				
		2	1	0	-1	-2
m'	2	$\left(\frac{1+\cos\beta}{2}\right)^2 e^{-2i(\alpha+\gamma)}$	$-\frac{1+\cos\beta}{2} \sin\beta e^{-i(2\alpha+\gamma)}$	$\sqrt{\frac{3}{8}} \sin^2\beta e^{-i2\alpha}$	$-\frac{1-\cos\beta}{2} \sin\beta e^{i(-2\alpha+\gamma)}$	$\left(\frac{1-\cos\beta}{2}\right)^2 e^{2i(-\alpha+\gamma)}$
	-2	$\left(\frac{1-\cos\beta}{2}\right)^2 e^{2i(\alpha-\gamma)}$	$\frac{1-\cos\beta}{2} \sin\beta e^{i(2\alpha-\gamma)}$	$\sqrt{\frac{3}{8}} \sin^2\beta e^{i2\alpha}$	$\frac{1+\cos\beta}{2} \sin\beta e^{i(2\alpha+\gamma)}$	$\left(\frac{1+\cos\beta}{2}\right)^2 e^{2i(\alpha+\gamma)}$

Table 5.1: Wigner-D functions $D_{m'm}^2(\alpha, \beta, \gamma)$ for $m' = \pm 2$ and $m = -2, -1, 0, 1, 2$.

5.B GRAVITATIONAL WAVEFORM IN THE INERTIAL FRAME

5.B.1 Calculation of the emission modes in the inertial frame

We give explicit expressions for modes h_{2m}^I in the inertial frame using the correspondence (5.3) with modes h_{2m}^P in the precessing frame. Recall that only $m = \pm 2$ modes are assumed to be present in the P frame, such that $h_{2-2}^P = h_{22}^{P,*}$ and

$$h_{2,\pm 2}^P(t) = a_0(t) e^{\mp i\Phi_0(t)}. \quad (5.12)$$

For readability we omit time-dependence in the following calculations.

h_{22}^I -mode

$$\begin{aligned}
 h_{22}^I &= h_{2-2}^P D_{-22}^{2,*}(-\gamma, -\beta, -\alpha) + h_{22}^P D_{22}^{2,*}(-\gamma, -\beta, -\alpha) \\
 &= h_{22}^{P,*} e^{-2i(\alpha-\gamma)} \left[\frac{1 - \cos \beta}{2} \right]^2 + h_{22}^P e^{-2i(\alpha+\gamma)} \left[\frac{1 + \cos \beta}{2} \right]^2 \\
 &= \frac{e^{-2i\alpha}}{2} \left(\text{Re} [h_{22}^P e^{-2i\gamma}] (1 + \cos^2 \beta) + i \text{Im}_i [h_{22}^P e^{-2i\gamma}] 2 \cos \beta \right) \\
 &= \frac{a_0 e^{-2i\alpha}}{2} \left((1 + \cos^2 \beta) \cos(\Phi_0 + 2\gamma) - i 2 \cos \beta \sin(\Phi_0 + 2\gamma) \right) \quad (5.13)
 \end{aligned}$$

h_{21}^I -mode

$$\begin{aligned}
 h_{21}^I &= h_{2-2}^P D_{-21}^{2,*}(-\gamma, -\beta, -\alpha) + h_{22}^P D_{21}^{2,*}(-\gamma, -\beta, -\alpha) \\
 &= -h_{22}^{P,*} e^{i(2\gamma-\alpha)} \sin \beta \frac{1 - \cos(\beta)}{2} + h_{22}^P e^{-i(2\gamma+\alpha)} \sin \beta \frac{1 + \cos(\beta)}{2} \\
 &= e^{-i\alpha} \sin \beta \left(\cos \beta \text{Re} [h_{22}^P e^{-2i\gamma}] + i \text{Im}_i [h_{22}^P e^{-2i\gamma}] \right) \\
 &= a_0 e^{-i\alpha} \sin \beta \left(\cos \beta \cos(\Phi_0 + 2\gamma) - i \sin(\Phi_0 + 2\gamma) \right) \quad (5.14)
 \end{aligned}$$

h_{20}^I -mode

$$\begin{aligned}
 h_{20}^I &= h_{2-2}^P D_{-20}^{2,*}(-\gamma, -\beta, -\alpha) + h_{22}^P D_{20}^{2,*}(-\gamma, -\beta, -\alpha) \\
 &= h_{22}^{P,*} \sqrt{\frac{3}{8}} \sin^2 \beta e^{i2\gamma} + h_{22}^P \sqrt{\frac{3}{8}} \sin^2 \beta e^{-i2\gamma} \\
 &= 2a_0 \sqrt{\frac{3}{8}} \sin^2 \beta \cos(\Phi_0 + 2\gamma) \quad (5.15)
 \end{aligned}$$

h_{2-1}^I -mode

$$\begin{aligned}
 h_{2-1}^I &= h_{2-2}^P D_{-2-1}^{2,*}(-\gamma, -\beta, -\alpha) + h_{22}^P D_{2-1}^{2,*}(-\gamma, -\beta, -\alpha) \\
 &= -h_{22}^{P,*} e^{i(2\gamma+\alpha)} \sin \beta \frac{1 + \cos(\beta)}{2} + h_{22}^P e^{i(-2\gamma+\alpha)} \sin \beta \frac{1 - \cos(\beta)}{2} \\
 &= e^{i\alpha} \sin \beta \left(-\cos \beta \text{Re} [h_{22}^P e^{-2i\gamma}] + i \text{Im}_i [h_{22}^P e^{-2i\gamma}] \right) \\
 &= a_0 e^{i\alpha} \sin \beta \left(-\cos \beta \cos(\Phi_0 + 2\gamma) - i \sin(\Phi_0 + 2\gamma) \right) \quad (5.16)
 \end{aligned}$$

h_{2-2}^I -mode

$$\begin{aligned}
 h_{2-2}^I &= h_{2-2}^P D_{-2-2}^{2,*}(-\gamma, -\beta, -\alpha) + h_{22}^P D_{2-2}^{2,*}(-\gamma, -\beta, -\alpha) \\
 &= h_{22}^{P,*} e^{2i(\alpha+\gamma)} \left[\frac{1 + \cos \beta}{2} \right]^2 + h_{22}^P e^{2i(\alpha-\gamma)} \left[\frac{1 - \cos \beta}{2} \right]^2 \\
 &= \frac{e^{2i\alpha}}{2} \left(\text{Re} [h_{22}^P e^{-2i\gamma}] (1 + \cos^2 \beta) - i \text{Im}_i [h_{22}^P e^{-2i\gamma}] 2 \cos \beta \right) \\
 &= \frac{a_0 e^{2i\alpha}}{2} \left((1 + \cos^2 \beta) \cos(\Phi_0 + 2\gamma) + i 2 \cos \beta \sin(\Phi_0 + 2\gamma) \right) \quad (5.17)
 \end{aligned}$$

5.B.2 Waveform expression

Plugging Eqs. (5.13) – (5.17) into the -2-spin weighted spherical harmonic expansion (5.4) we obtain the waveform $h^I = h_+^I - i h_\times^I$ in the inertial frame for a *fixed* observer specified by angular coordinates (ι, φ_0) . For ease of notation, we introduce $\Phi_\gamma = \Phi_0 + 2\gamma$. Tedious calculations yield to

$$\begin{aligned}
h_+^I - \mathbf{i}h_x^I &= \frac{a_0 e^{2i\alpha}}{2} \left((1 + \cos^2 \beta) \cos(\Phi_\gamma) + \mathbf{i}2 \cos \beta \sin(\Phi_\gamma) \right) \frac{1}{8} \sqrt{\frac{5}{\pi}} (1 - \cos \iota)^2 e^{-2i\varphi_0} \\
&+ a_0 e^{i\alpha} \sin \beta \left(-\cos \beta \cos(\Phi_\gamma) - \mathbf{i} \sin(\Phi_\gamma) \right) \frac{1}{4} \sqrt{\frac{5}{\pi}} (1 - \cos \iota) \sin \iota e^{-i\varphi_0} \\
&+ 2a_0 \sqrt{\frac{3}{8}} \sin^2 \beta \cos(\Phi_\gamma) \frac{\sqrt{6}}{8} \sqrt{\frac{5}{\pi}} \sin^2 \iota \\
&+ a_0 e^{-i\alpha} \sin \beta \left(\cos \beta \cos(\Phi_\gamma) - \mathbf{i} \sin(\Phi_\gamma) \right) \frac{1}{4} \sqrt{\frac{5}{\pi}} (1 + \cos \iota) \sin \iota e^{i\varphi_0} \\
&+ \frac{a_0 e^{-2i\alpha}}{2} \left((1 + \cos^2 \beta) \cos(\Phi_\gamma) - \mathbf{i}2 \cos \beta \sin(\Phi_\gamma) \right) \frac{1}{8} \sqrt{\frac{5}{\pi}} (1 + \cos \iota)^2 e^{2i\varphi_0}.
\end{aligned}$$

Reorganizing terms yields

$$\begin{aligned}
h_+^I - \mathbf{i}h_x^I &= a_0 \frac{1}{8} \sqrt{\frac{5}{\pi}} \left\{ \frac{e^{2i(\alpha-\varphi_0)}}{2} (1 + \cos^2 \beta) (1 - \cos \iota)^2 - 2e^{i(\alpha-\varphi_0)} \sin \beta \cos \beta (1 - \cos \iota) \sin \iota \right. \\
&+ 3 \sin^2 \beta \sin^2 \iota + 2e^{-i(\alpha-\varphi_0)} \sin \beta \cos \beta (1 + \cos \iota) \sin \iota + \left. \frac{e^{-2i(\alpha-\varphi_0)}}{2} (1 + \cos^2 \beta) (1 + \cos \iota)^2 \right\} \cos \Phi_\gamma \\
&+ \mathbf{i}a_0 \frac{1}{8} \sqrt{\frac{5}{\pi}} \left\{ e^{2i(\alpha-\varphi_0)} \cos \beta (1 - \cos \iota)^2 - 2e^{i(\alpha-\varphi_0)} \sin \beta (1 - \cos \iota) \sin \iota \right. \\
&\left. - 2e^{-i(\alpha-\varphi_0)} \sin \beta (1 + \cos \iota) \sin \iota - e^{-2i(\alpha-\varphi_0)} \cos \beta (1 + \cos \iota)^2 \right\} \sin \Phi_\gamma. \tag{5.18}
\end{aligned}$$

5.C INSTANTANEOUS STOKES PARAMETERS

To identify polarization modulation effects in the waveform expression (5.18) for an arbitrary observer described by spherical coordinates (ι, φ_0) we first compute its quaternion embedding $h_{\mathbb{H}}^I(t)$. Then instantaneous Stokes parameters are directly obtained from quantities $|h_{\mathbb{H}}^I|^2$ and $h_{\mathbb{H}}^I \mathbf{j} \overline{h_{\mathbb{H}}^I}$.

5.C.1 Quaternion embedding of the emitted waveform

For simplicity we assume that: (i) Euler angles $[\alpha, \beta, \gamma]$ as well as a_0 vary much slowly that the instantaneous phase Φ_0 , so that Bedrosian theorem's can be applied and (ii) the phase Φ_γ can be factorized as (4.117). The first condition ensures that any sufficiently smooth function f , one has $\mathcal{H}\{f(\alpha, \beta, \gamma, a_0) \cos \Phi_\gamma\} = f(\alpha, \beta, \gamma, a_0) \mathcal{H}\{\cos \Phi_\gamma\}$ where $\mathcal{H}\{\cdot\}$ is the Hilbert transform. The second condition yields $\mathcal{H}\{\cos \Phi_\gamma\} = \sin \Phi_\gamma$.

The quaternion embedding $h_{\mathbb{H}}^I$ of h^I given by (5.18) reads

$$\begin{aligned}
h_{\mathbb{H}} &= a_0 \frac{1}{8} \sqrt{\frac{5}{\pi}} \left\{ \frac{e^{2i(\alpha-\varphi_0)}}{2} (1 + \cos^2 \beta) (1 - \cos \theta)^2 - 2e^{i(\alpha-\varphi_0)} \sin \beta \cos \beta (1 - \cos \iota) \sin \iota \right. \\
&+ 3 \sin^2 \beta \sin^2 \iota + 2e^{-i(\alpha-\varphi_0)} \sin \beta \cos \beta (1 + \cos \iota) \sin \iota + \frac{e^{-2i(\alpha-\varphi_0)}}{2} (1 + \cos^2 \beta) (1 + \cos \iota)^2 \\
&- \mathbf{i}e^{2i(\alpha-\varphi_0)} \mathbf{j} \cos \beta (1 - \cos \iota)^2 + 2\mathbf{i}e^{i(\alpha-\varphi_0)} \mathbf{j} \sin \beta (1 - \cos \iota) \sin \iota \\
&\left. + \mathbf{i}2e^{-i(\alpha-\varphi_0)} \mathbf{j} \sin \beta (1 + \cos \iota) \sin \iota + \mathbf{i}e^{-2i(\alpha-\varphi_0)} \cos \beta (1 + \cos \iota)^2 \mathbf{j} \right\} e^{j\Phi_\gamma} \tag{5.19}
\end{aligned}$$

This can be further simplified as

$$h_{\mathbb{H}} = a_0 \frac{1}{8} \sqrt{\frac{5}{\pi}} (U + \mathbf{i}V) e^{j\Phi_\gamma}$$

where

$$U = \cos[2(\alpha - \varphi_0)](1 + \cos^2 \beta)(1 + \cos^2 \iota) + 3 \sin^2 \beta \sin^2 \iota + \cos(\alpha - \varphi_0) \sin 2\beta \sin 2\iota \\ + j(2 \sin[2(\alpha - \varphi_0)] \cos \beta(1 + \cos^2 \iota) + 2 \sin(\alpha - \varphi_0) \sin \beta \sin 2\iota) \quad (5.20)$$

$$V = -2 \sin[2(\alpha - \varphi_0)](1 + \cos^2 \beta) \cos \iota - 2 \sin(\alpha - \varphi_0) \sin 2\beta \sin \iota \\ + j(4 \cos[2(\alpha - \varphi_0)] \cos \beta \cos \iota + 4 \cos(\alpha - \varphi_0) \sin \beta \sin \iota) . \quad (5.21)$$

5.C.2 Stokes parameters expressions

Stokes parameters are obtained like:

$$S_0 = a_0^2 \frac{1}{64} \frac{5}{\pi} (|U|^2 + |V|^2) \quad (5.22)$$

$$S_1 = a_0^2 \frac{1}{64} \frac{5}{\pi} (|U|^2 - |V|^2) \quad (5.23)$$

$$S_2 = a_0^2 \frac{2}{64} \frac{5}{\pi} \text{Re}\{U\bar{V}\} \quad (5.24)$$

$$S_3 = a_0^2 \frac{2}{64} \frac{5}{\pi} \text{Im}_j\{U\bar{V}\} \quad (5.25)$$

Plugging expressions (5.20)–(5.21) for U and V one gets the following (awful) expressions for Stokes parameters:

$$S_0 = a_0^2 \frac{1}{64} \frac{5}{\pi} \left\{ \left((\cos^2(\beta) + 1) \sin(2\alpha - 2\varphi_0) \cos(\iota) + \sin(2\beta) \sin(\iota) \sin(\alpha - \varphi_0) \right)^2 \right. \\ + 4 \left((\cos^2(\iota) + 1) \sin(2\alpha - 2\varphi_0) \cos(\beta) + \sin(\beta) \sin(2\iota) \sin(\alpha - \varphi_0) \right)^2 \\ + 16 (\sin(\beta) \sin(\iota) \cos(\alpha - \varphi_0) + \cos(\beta) \cos(\iota) \cos(2\alpha - 2\varphi_0))^2 \\ \left. + \left((\cos^2(\beta) + 1) (\cos^2(\iota) + 1) \cos(2\alpha - 2\varphi_0) + 3 \sin^2(\beta) \sin^2(\iota) + \sin(2\beta) \sin(2\iota) \cos(\alpha - \varphi_0) \right)^2 \right\} \quad (5.26)$$

$$S_1 = a_0^2 \frac{1}{64} \frac{5}{\pi} \left\{ -4 \left((\cos^2(\beta) + 1) \sin(2\alpha - 2\varphi_0) \cos(\iota) + \sin(2\beta) \sin(\iota) \sin(\alpha - \varphi_0) \right)^2 \right. \\ + 4 \left((\cos^2(\iota) + 1) \sin(2\alpha - 2\varphi_0) \cos(\beta) + \sin(\beta) \sin(2\iota) \sin(\alpha - \varphi_0) \right)^2 \\ - 16 (\sin(\beta) \sin(\iota) \cos(\alpha - \varphi_0) + \cos(\beta) \cos(\iota) \cos(2\alpha - 2\varphi_0))^2 \\ \left. + \left((\cos^2(\beta) + 1) (\cos^2(\iota) + 1) \cos(2\alpha - 2\varphi_0) + 3 \sin^2(\beta) \sin^2(\iota) + \sin(2\beta) \sin(2\iota) \cos(\alpha - \varphi_0) \right)^2 \right\} \quad (5.27)$$

$$S_2 = a_0^2 \frac{1}{64} \frac{5}{\pi} \left\{ 2 \left(-2 (\cos^2(\beta) + 1) \sin(2\alpha - 2\varphi_0) \cos(\iota) - 2 \sin(2\beta) \sin(\iota) \sin(\alpha - \varphi_0) \right) \right. \\ \times \left((\cos^2(\beta) + 1) (\cos^2(\iota) + 1) \cos(2\alpha - 2\varphi_0) + 3 \sin^2(\beta) \sin^2(\iota) + \sin(2\beta) \sin(2\iota) \cos(\alpha - \varphi_0) \right) \\ + 2 \left(2 (\cos^2(\iota) + 1) \sin(2\alpha - 2\varphi_0) \cos(\beta) + 2 \sin(\beta) \sin(2\iota) \sin(\alpha - \varphi_0) \right) \\ \times \left(4 \sin(\beta) \sin(\iota) \cos(\alpha - \varphi_0) + 4 \cos(\beta) \cos(\iota) \cos(2\alpha - 2\varphi_0) \right) \left. \right\} \quad (5.28)$$

$$S_3 = a_0^2 \frac{1}{64} \frac{5}{\pi} \left\{ 2 \left(-2 (\cos^2(\beta) + 1) \sin(2\alpha - 2\varphi_0) \cos(\iota) - 2 \sin(2\beta) \sin(\iota) \sin(\alpha - \varphi_0) \right) \right. \\ \times \left(2 (\cos^2(\iota) + 1) \sin(2\alpha - 2\varphi_0) \cos(\beta) + 2 \sin(\beta) \sin(2\iota) \sin(\alpha - \varphi_0) \right) \\ - 2 \left(4 \sin(\beta) \sin(\iota) \cos(\alpha - \varphi_0) + 4 \cos(\beta) \cos(\iota) \cos(2\alpha - 2\varphi_0) \right) \\ \times \left((\cos^2(\beta) + 1) (\cos^2(\iota) + 1) \cos(2\alpha - 2\varphi_0) + 3 \sin^2(\beta) \sin^2(\iota) + \sin(2\beta) \sin(2\iota) \cos(\alpha - \varphi_0) \right) \left. \right\} \quad (5.29)$$

In particular, for the case of face-on $(i, \varphi_0) = (0, 0)$ binaries :

$$S_0 = a_0^2 \frac{1}{64} \frac{5}{\pi} (4 \sin^4(\beta) - 32 \sin^2(\beta) + 32) \quad (5.30)$$

$$\frac{S_1}{S_0} = \frac{(-\cos(2\beta) + 1)^2 \cos(4\alpha)}{4 \sin^4(\beta) - 32 \sin^2(\beta) + 32} \quad (5.31)$$

$$\frac{S_2}{S_0} = -\frac{(\cos(2\beta) - 1)^2 \sin(4\alpha)}{(\cos(2\beta) - 1)^2 + 16 \cos(2\beta) + 16} \quad (5.32)$$

$$\frac{S_3}{S_0} = -\frac{4(\cos^2(\beta) + 1) \cos(\beta)}{\cos^4(\beta) + 6 \cos^2(\beta) + 1} \quad (5.33)$$

In particular, remark that S_3/S_0 depend only on the precession angle β .

Conclusion

This thesis has developed a new generic framework for the analysis and filtering of bivariate signals. The proposed approach relies on two key ingredients. Just like univariate or real-valued signals are naturally embedded in the set of complex numbers thanks to the Fourier transform, bivariate signals – viewed as complex-valued signals – are naturally embedded into the set of quaternions \mathbb{H} . Then the definition of a dedicated quaternion Fourier transform enables a meaningful spectral representation of bivariate signals. It permits the definition of many standard signal processing quantities such as spectral densities, linear filters or spectrograms that simultaneously feature: (i) straightforward physical and geometric interpretations, (ii) mathematical guarantees and (iii) computationally fast numerical implementations.

A GENERAL APPROACH FOR THE ANALYSIS AND FILTERING OF BIVARIATE SIGNALS

CHAPTER 1 presented the two key ingredients of the proposed framework: *quaternions* and the *quaternion Fourier transform*. We studied the generic properties of the quaternion Fourier transform (QFT). These are very similar to properties of the usual Fourier transform (FT) (linearity, shifts, differentiation, etc.) but they sometimes require special care due to noncommutativity of the quaternion product. Two fundamental theorems constitute the main contributions of this chapter. The generalized Parseval-Plancherel Theorem 1.1, which states that two quantities are preserved: the usual *energy* and an additional *geometric* quantity. Theorem 1.2 gives the Gabor-Heisenberg uncertainty principle, which shows that the QFT obeys usual time-frequency tradeoffs. The QFT features a computationally efficient numerical implementation using two standard FFTs.

As a first example of the high potential of the approach, we showed that the QFT naturally decomposes bivariate signals into a sum of polarized monochromatic bivariate signals. The use of the Euler polar form of quaternions directly yields natural ellipse parameters. The quaternion-valued spectrum of bivariate signals additionally exhibits Hermitian-like symmetry, a very desirable property which makes it possible to attach physical interpretations to positive frequencies only. The elements presented in this chapter were published as the first part of Flamant, Le Bihan, and Chainais (2017e).

CHAPTER 2 described the spectral characterization of the second-order properties of deterministic and stationary random bivariate signals. The quaternion power spectral density (PSD) of a stationary random bivariate signal is introduced thanks to the quaternion-valued spectral representation of a stationary random bivariate signal (Theorem 2.1). This fundamental quantity enables a straightforward characterization of stationary bivariate signals in terms of

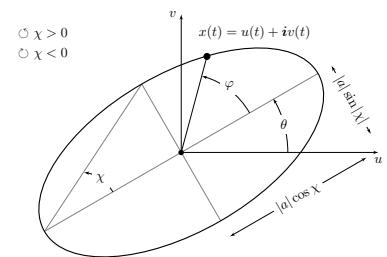


Figure 5.4: A monochromatic bivariate signal $x(t)$ has a direct expression in terms of natural ellipse parameters a , θ , χ and φ , see Section 1.3.

frequency-dependent polarization properties. The quaternion PSD has an elegant expression in terms of Stokes parameters. It also provides an insightful geometric handling of polarization properties thanks to the Poincaré sphere representation and quaternion algebra. The proposed framework naturally separates the quaternion PSD into an unpolarized part and a polarized part, where respective contributions are ruled by the degree of polarization.

To provide a complete and practical characterization of second-order stationary bivariate signals, we also define the notion of quaternion autocovariance, as well as the concepts of quaternion cross-covariances and quaternion cross-PSD. On a practical ground, we investigated the nonparametric spectral density estimation of the quaternion PSD. Standard estimators (periodogram, multitaper) from univariate spectral analysis are readily extended to the proposed framework. We noted that the estimation of polarization parameters (degree of polarization, polarization ellipse) is not straightforward and requires special care. Simple explicit examples and synthetic experiments demonstrated the relevance of the approach. These results have been presented in Flamant, Le Bihan, and Chainais (2017c, 2017a).

CHAPTER 3 addressed one of the most fundamental signal processing tasks: linear time-invariant (LTI) filtering. We provide in this chapter a complete, generic and insightful description of LTI filters for bivariate signals. The proposed framework allows the direct description of linear filters in terms of meaningful physical quantities. We take advantage of an usual decomposition from polarization optics to give a description of any generic LTI filter as the combination of two distinct filters: a unitary and a Hermitian one. These two classes of filters relate to the *birefringence* and *diattenuation* effects in linear media, respectively. The QFT spectral domain filtering relations demonstrate their superiority to standard matrix-based approaches by providing clear and simple expressions featuring eigenproperties. These expressions carry naturally strong physical and geometric interpretations. All together, these remarkable properties make it easy to design, model or prescribe linear filters in the QFT formalism.

The power and generality of the approach has been illustrated on several fundamental applications of signal processing. We introduced a new spectral synthesis method to simulate any Gaussian stationary random bivariate signal with desired spectral and polarization properties. The celebrated Wiener denoising problem can be efficiently designed in the proposed framework. It yields a new insightful perspective on its performances, in particular on the impact of the interplay between polarization properties of the signal and noise. Original decompositions of bivariate signals in two components with specific properties were also provided, which permit *e.g.* the natural decomposition of any stationary bivariate signal into its unpolarized part and its polarized part by hermitian filtering. We also emphasized the potential of unitary filters to model intriguing physical effects specific to the bivariate case such as *polarization mode dispersion*. These results have been described in Flamant, Chainais, and Le Bihan (2018a, 2018b).

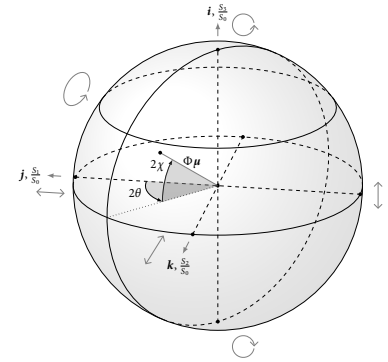


Figure 5.5: The quaternion PSD $\Gamma_{xx}(v)$ of a second-order stationary bivariate signal $x(t)$ has a natural geometric interpretation in terms of the Poincaré sphere of polarization states, see Section 2.3.3.

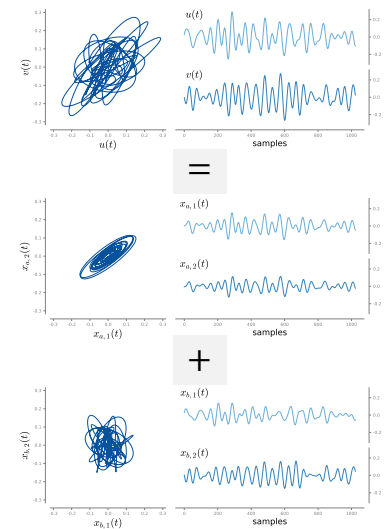


Figure 5.6: Decomposition of a second-order stationary bivariate signal into its polarized and unpolarized parts, see Section 3.3.4.

CHAPTER 4 presented a thorough study of time-frequency representations for bivariate signals. We introduced a bivariate analogue of the analytic signal of univariate signals, called *quaternion embedding*. Its definition builds on the Hermitian-like symmetry property of the QFT of bivariate signals to provide a canonical set of instantaneous attributes in one-to-one correspondence with a bivariate signal. It enables a natural instantaneous polarization ellipse description for narrow-band bivariate signals. It also enables a straightforward and interpretable model for nonstationary bivariate signals, called the bivariate or polarized amplitude modulated-frequency modulated (AM-FM) model. The processing of multicomponent bivariate signals requires, as in the univariate case, to introduce time-frequency representations. For this purpose two linear transforms are introduced, namely the quaternion short-term Fourier transform (Q-STFT) and the quaternion continuous wavelet transform (Q-CWT). Definitions mirror the usual case by using the QFT in place of the Fourier transform. Theorem 4.1 and Theorem 4.2 constitute an important contribution of this chapter. They guarantee the conservation of energy and polarization quantities as well as reconstruction formulas. They directly yield definitions of *energy spectrograms* and *energy scalograms* corresponding to usual time-frequency energy density maps. Remarkably, these theorems also introduce novel graphical representations, namely *polarization spectrograms* and *polarization scalograms*, which characterize the time-frequency-polarization content of bivariate signals.

Just like their univariate counterparts, these novel time-frequency-polarization representations are not perfectly localized. They spread around sets of time-frequency points called *ridges*, which are shown to carry most of the significant information about the signal. The original construction of a generic class of bilinear time-frequency-polarization representations has been presented. This broad class of solutions offers the possibility to tailor the time-frequency representation to the features of the signal. The power and intelligibility of the proposed time-frequency-polarization representations have been demonstrated on both synthetic and real-world data. Most of the findings of this chapter have been published in (Flamant, Le Bihan, and Chainais, 2017e, 2017b, 2017d). The construction of the class of bilinear time-frequency-polarization representations is an original contribution of this manuscript.

CHAPTER 5 presented an applicative contribution to the nonparametric characterization of gravitational waves polarizations. In collaboration with Eric Chassande-Mottin and Fangchen Feng, we have shown that the proposed framework enables to decipher complex dynamical properties of the gravitational wave source. Gravitational waves emitted by coalescing compact binaries are polarized. They form non-stationary bivariate signals that can be characterized using the generic time-frequency analysis methods developed in Chapter 4.

We showed that instantaneous Stokes parameters bring new nonparametric observables that permit to test the precession of the orbital plane of the emitting source. They naturally encode orbital properties that would be cumbersome to obtain individually. Numerical experiments using synthetic noise-free and realistic noises from LIGO and Virgo detectors showed a remarkable agreement between theoretical predictions and numerical estimations. The approach is

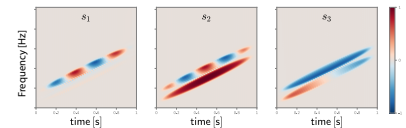


Figure 5.7: The polarization spectrogram of a bivariate signal is a novel time-frequency-polarization representation introduced in Section 4.2.1. It reveals the evolution in the time-frequency plane of the polarization state of the signal (here the two polarized linear chirps example of Fig. 4.4).

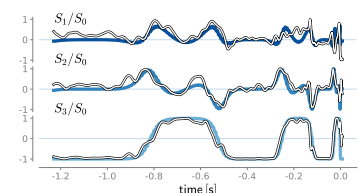


Figure 5.8: Instantaneous normalized Stokes parameters s_1 , s_2 and s_3 encode the dynamical properties of the orbital motion of precessing compact binaries, see Section 5.3.

very generic and can be extended to more challenging scenarios, *e.g.* when higher-order modes have to be considered. By bringing new observables that do not require a specific dynamical model of the source, the proposed approach provides support to current state-of-the-art techniques performing (parametric) waveform fitting. It may also help to reveal any dynamical effect affecting the gravitational-wave polarization, *e.g.* orbital eccentricity. This chapter has been adapted from Flamant et al. (2018).

A COMPANION OPEN-SOURCE Python package called BiSPy: *Bivariate Signal Processing in Python* implements our findings for the sake of reproducible research. Documentation, tutorials and code are available at

 bispy.readthedocs.io/  github.com/jflamant/bispy

PERSPECTIVES

The generality of the proposed approach for the analysis and filtering of bivariate signals allows to consider various prospective works, from methodological aspects to applications involving such signals. However, it triggers this very first natural question.

Can we extend the approach to multivariate signals? The promising results obtained in the case of bivariate signals naturally raise the question of the generalization of this *geometric* approach to the case of n -variate signals. Our approach essentially relies on an embedding argument of bivariate signals into the set of quaternions, which mimics the embedding of real-valued or univariate signals into complex numbers. If one wants to extend this “embedding approach” to n -variate signals, then its “natural” embedding should have at least dimension $2n$, in the sense that each univariate component should be associated to two quantities: an amplitude and a phase. However this naive approach is likely to fail for dimensions greater than $n \geq 5$, since Frobenius Theorem (Baez, 2002) states that any division algebra over the real numbers is isomorphic to either \mathbb{R} (dim = 1), \mathbb{C} (dim = 2), \mathbb{H} (dim = 4) or the set of octonions \mathbb{O} (dim = 8). Note that for octonions \mathbb{O} the multiplication operation is also non-associative, which may hamper the use of octonions in practical Fourier analysis. If one accepts the existence of zero divisors², one could turn to standard geometric embeddings of n -dimensional real-vectors, called Clifford algebras (Hestenes and Sobczyk, 2012). Those algebras have dimension 2^n , but lack apparently some nice interpretable features, such as polar forms. As of today, it remains unclear how far Clifford algebras could be beneficial to the analysis and filtering of multivariate signals.

The non-trivial extension of our approach to the multivariate case also emphasizes the peculiarity of the bivariate case, as well as the central role played by quaternions. For bivariate signals, it is natural to think of a framework where correlation or geometric properties are readily apparent. However, for multivariate signals – perhaps excepted for the case of trivariate signals – one can legitimately wonder which improvements or advantages would arise from the explicit specification of the joint signal structure, compared to *e.g.* a pairwise comparison between the signals components.

² It is unclear how much this condition would affect signal processing practice.

Leaving out the difficult question of multivariate signals for future work, we turn back to the case of bivariate signals. We list below some related perspectives, ranked from short-term to long-term prospects.

Robust estimation of polarization parameters Section 2.4 studied the estimation of the spectral properties of second-order stationary random bivariate signals. Whereas the estimation of the quaternion PSD essentially follows the usual univariate case, the estimation of associated meaningful physical parameters (e.g. polarization axis $\mu_x(v)$ and degree of polarization $\Phi_x(v)$) raises some specific issues. In fact, such parameters require a normalization step. Naive estimates of such quantities can be strongly biased, increasing the difficulty of the estimation problem. The proposed framework still lacks a complete statistical characterization of the properties of estimators of polarization features. Building on previous work in optics (Barakat, 1987; Brosseau, 1995) and spectral analysis (Walden, 2013; Walden and Medkour, 2007), future work should explore the detailed statistical behavior of polarization estimates (bias, variance, confidence intervals, etc.). It should also provide efficient and robust strategies for their estimation. This point is crucial to demonstrate the relevance of polarization parameters to the characterization of generic stationary bivariate random signals.

Identification of LTI systems Chapter 3 demonstrated the relevance of the proposed framework for the description of LTI filters. Appendix 3.B proposed an identification method of unitary and Hermitian filters using unpolarized white Gaussian noise. However a systematic approach to the identification of generic LTI filters is missing. A possible path could be inspired by *ellipsometry* or *polarimetry* techniques in optics (Azzam and Bashara, 1987): a sufficiently large set of outputs obtained from inputs with different polarization states would allow to recover the parameters of filter thanks to filtering relations (3.8) (unitary) and (3.15) (Hermitian) and (3.27) (generic). Another possibility could root in the notion of “impulse response”, which remains to be defined in the proposed framework. The related (time-domain) identification procedures would complete the toolbox for the generic identification of LTI systems involving bivariate signals.

Properties of LTI systems The influence of the parameters of LTI filters on fundamental properties such as *stability* or *causality* has not been investigated yet. In particular, Kramers-Kronig relations ensuring that a bivariate signal x is causal (i.e. $x(t) = 0$ for $t < 0$) could be derived. These relations on the QFT of a signal x essentially encode the dual property of the quaternion embedding and would follow by adapting the discussion presented in Section 4.1.1. The derivation of relations similar to Bayard-Bode equations (Raymond, 1951) for the bivariate case would provide considerable insights on the interplay between causality and the parameters of LTI filters – especially those encoding physical effects such as birefringence or diattenuation. It would also allow to formulate causal solutions to filtering or denoising problems, e.g. a causal solution for the Wiener filter presented in Section 3.3.3.

Optimization in the quaternion domain The Wiener denoising filter described in Section 3.3.3 involves a mean square error criterion. Its resolution thus involves solving an optimization problem in the quaternion domain, which was carried out in Appendix 3.D using the corresponding vector form. This is only partly satisfactory since one could have expected to find the optimal filter directly in the quaternion domain. However, such optimization problems require the notion of quaternion derivatives, *i.e.* derivatives with respect to quaternion variables. To this aim, $\mathbb{H}\mathbb{R}$ -calculus (Mandic, Jahanchahi, and Took, 2011) and the generalized $\mathbb{H}\mathbb{R}$ -calculus (Xu et al., 2015) have been recently introduced. They play the same role as the Wirtinger or $\mathbb{C}\mathbb{R}$ -calculus (see *e.g.* Adali, Schreier, and Scharf (2011) for a review) in the complex case. Just like Wirtinger calculus brings economical and elegant optimization of cost functions of complex variables, one can expect the $\mathbb{H}\mathbb{R}$ -calculus to provide efficient optimization procedures for cost functions appearing in the QFT framework.

Link with data-driven time-frequency approaches Among those methods, the bivariate empirical mode decomposition (EMD) (Tanaka and Mandic, 2007; Rilling et al., 2007) is one of the most popular ones. It aims at decomposing a bivariate signal into a sum of bivariate AM-FM modes called intrinsic mode functions (IMFs). Remarkably, the quaternion embedding offers a straightforward characterization of the instantaneous amplitude, phase and polarization properties of these IMFs. By combining the quaternion embedding method with one of the existing bivariate EMD algorithms, one could directly define a bivariate *Hilbert-Huang transform*³. It has the potential to reveal instantaneous features that would have been complicated to obtain otherwise. Since the bivariate EMD algorithm is used in many applications, the quaternion embedding method could provide robust physical interpretation to the bivariate IMFs extracted from real-world measurements.

Applications Being very generic and essentially nonparametric, the approach permits to consider many potential applications, such as wide-band polarimetric characterization of physical or biological media thanks to LTI filters. Another area where the potential of the framework could be demonstrated is *blind source separation*. For instance, *stereophonic* signals in audio processing can be viewed as bivariate signals. As they provide a geometric perspective on the correlation structure of such signals, the time-frequency-polarization representations introduced in Chapter 4 may provide useful descriptors relevant to source separation or *direction of arrival* estimation (Arberet, Gribonval, and Bimbot, 2010).

Vector field processing using the 2D QFT The extension of the proposed framework to signals $x : \mathbb{R}^2 \rightarrow \mathbb{C}_i$, that is bidimensional bivariate signals or 2D vector fields, requires the introduction of the 2-dimensional QFT. The formal construction of this new tool is expected to closely match the construction of the Fourier analysis of images. Guided by our study in Chapter 1 of the properties of the QFT, its 2D extension should present no particular theoretical difficulty. However, the usefulness and interpretability of the resulting representations remains an open question. Most likely, the 2D QFT should decompose a 2D

3. For univariate signals, the term *Hilbert-Huang transform* relates to two operations: (i) the decomposition of a signal into IMFs thanks to the EMD algorithm and (ii) the extraction of instantaneous features of each IMFs using its analytic signal. For bivariate signals, we simply replace the EMD by the bivariate EMD and use the quaternion embedding method in place of the analytic signal.

vector field into a sum of polarized waves. Still, numerous questions need to be answered. For instance, does the 2D QFT feature interesting decompositions of vector fields in terms of *e.g.* curl-free and divergence-free components? Also, does it permit to build 'à la Gabor' filters for the filtering of 2D vector fields?

Résumé en français

Les signaux bivariés apparaissent dans de nombreuses applications, dès lors que l'analyse jointe de deux signaux à valeurs réelles est nécessaire. Par exemple, citons: l'analyse jointe des vitesses des courants de surface en océanographie (Gonella, 1972; Thomson and Emery, 2014) et météorologie (Hayashi, 1982; Tanaka and Mandic, 2007); l'analyse des ondes polarisées en optique (Brosseau, 1998; Born and Wolf, 1980) et sismologie (Samson, 1983; Pinnegar, 2006); le traitement de signaux EEG enregistrés en deux électrodes différentes (Sakkalis, 2011; Sanei and Chambers, 2013) ou encore l'analyse des ondes gravitationnelles – qui sont elles aussi polarisées.

Un signal bivarié admet deux représentations équivalentes, soit sous la forme d'un signal vectoriel $\mathbf{x} : \mathbb{R} \rightarrow \mathbb{R}^2$, soit sous la forme d'un signal à valeurs complexes $x : \mathbb{R} \rightarrow \mathbb{C}$. Plus précisément, en dénotant par $u(t)$ et $v(t)$ les deux composantes à valeurs réelles correspondant par exemple aux composantes orthogonales d'un champ de vitesse, nous avons

$$\mathbf{x}(t) = \begin{bmatrix} u(t) \\ v(t) \end{bmatrix} \quad \text{ou} \quad x(t) = u(t) + iv(t). \quad (5.34)$$

Indépendamment de la représentation choisie, un signal bivarié décrit une trajectoire dans le plan 2D. L'analyse de la dynamique temporelle et de la géométrie de cette trajectoire définit une première tâche essentielle du traitement des signaux bivariés.

L'application visée impose souvent le choix de l'une ou l'autre représentation. L'approche vectorielle est le plus souvent utilisée en optique et sismologie, tandis qu'en océanographie le choix se porte sur la représentation complexe des signaux bivariés. D'un point de vue traitement du signal, la représentation complexe apparaît comme la plus "naturelle", en raison notamment de la simplification des expressions qu'elle procure, mais aussi de par sa connexion directe avec des notions fondamentales de traitement du signal comme les concepts d'amplitude et de phase.

Toutefois, les approches existantes – fondées sur l'utilisation de la représentation vectorielle ou complexe – présentent des limites inhérentes qui empêchent de les considérer comme des cadres de travail *idéaux* pour le traitement des signaux bivariés. En effet, ces approches ne permettent pas une paramétrisation directe en termes des quantités physiques d'intérêt telles que les paramètres naturels de l'ellipse de polarisation permettant de spécifier, à chaque fréquence, la structure jointe entre les composantes u et v d'un signal bivarié. Par exemple, dans la représentation vectorielle ces paramètres sont estimés à partir des amplitudes et phases de chaque composante via des expressions non-triviales. Une autre limitation propre à la représentation complexe des signaux bivariés concerne la nécessité de considérer à la fois les fréquences positives et négatives. L'absence de symétrie Hermitienne entre le spectre des fréquences positives et négatives empêche, par exemple, de définir directement l'équivalent du

signal analytique pour les signaux bivariés – le premier outil d’analyse du signal non-stationnaire. Mentionnons enfin le problème de l’interprétabilité physique des relations de filtrage. Si dans le cas univarié la notion de gain et phase d’un filtre linéaire temps-invariant est bien connue, la généralisation de telles quantités au cas des filtres pour les signaux bivariés reste une question ouverte.

Ainsi, même si les approches existantes offrent des cadres d’étude bien définis mathématiquement et numériquement efficaces, l’interprétabilité physique directe leur fait défaut. Nous considérons que ce lien avec la physique est particulièrement important. En effet, un formalisme dédié doit permettre la simplification drastique de nombreuses tâches typiques en traitement du signal : analyse, synthèse ou encore filtrage. Nous pensons aussi que l’adaptation du formalisme à la nature physique des signaux bivariés renforce l’intuition, et rend ainsi possible des traitements originaux. En résumé, un cadre idéal pour le traitement des signaux bivariés doit répondre simultanément à trois exigences fondamentales:

- ▶ *interprétabilité physique directe* : les quantités usuelles du traitement du signal telles que densités spectrales de puissance, filtres linéaires ou encore représentations temps-fréquence doivent être définies directement en terme des paramètres physiques d’intérêt. Soulignons aussi, dans ce même but d’interprétabilité, la nécessité d’une correspondance simple entre fréquences positives et négatives.
- ▶ *garanties mathématiques* : l’approche proposée doit rassembler toutes les propriétés mathématiques nécessaires à la définition et l’interprétation rigoureuse des quantités introduites, telles que la conservation des quantités énergétiques ou l’inversibilité des représentations temps-fréquence.
- ▶ *implémentations numériquement efficaces* : les différents outils associés au cadre proposé doivent admettre une implémentation rapide et efficace, n’entraînant pas de surcoût computationnel par rapport aux méthodes existantes.

Cette thèse propose un cadre répondant simultanément aux trois exigences physique, mathématique et computationnelle mentionnées ci-dessus. Au cours des 5 chapitres de ce manuscrit nous décrivons de manière progressive la construction systématique d’un cadre complet pour l’analyse et le filtrage des signaux bivariés. Ce travail répond aux limitations des approches existantes, en proposant un cadre de travail directement interprétable en termes de paramètres physiques pertinents, sans rien sacrifier aux garanties mathématiques ni à l’efficacité numérique des outils proposés.

L’APPROCHE PROPOSÉE repose sur deux éléments essentiels : l’ensemble des quaternions et la notion de transformée de Fourier quaternionique (QFT). Le chapitre 1 est consacré à l’étude de ces deux notions. Nous montrons en particulier qu’en usant de quelques précautions liées à la non-commutativité du produit quaternionique, la QFT se comporte de manière similaire à la transformée de Fourier usuelle. Parmi ses nombreuses propriétés, citons : un théorème de Parseval-Plancherel généralisé montrant la conservation de l’énergie ainsi que d’une quantité quadratique supplémentaire s’interprétant géométriquement; un théorème de Gabor-Heisenberg illustrant la dépendance de la QFT aux compromis temps-fréquence usuels. La fin de ce chapitre pose le cadre

de l'utilisation des quaternions et de la QFT pour le traitement des signaux bivariés. Nous démontrons que la QFT permet une représentation spectrale quaternionique directement interprétable physiquement des signaux bivariés – pris comme signaux à valeurs complexes. Les chapitres suivants étendent ces premiers résultats fondamentaux dans différentes directions afin de développer un formalisme complet et général pour le traitement des signaux bivariés : analyse spectrale au chapitre 2, théorie du filtrage linéaire au chapitre 3 et analyse temps-fréquence au chapitre 4. Le chapitre 5 démontre la pertinence du formalisme proposé par l'étude de la polarisation des ondes gravitationnelles émises lors de la coalescence de systèmes binaires en précession.

Analyse spectrale Le chapitre 2 considère la question importante de la caractérisation spectrale des signaux bivariés. En particulier, nous définissons la notion de densité spectrale quaternionique d'un signal bivarié, dans le cas déterministe et dans le cas stationnaire à l'ordre deux. Dans ce dernier cas, un théorème de représentation spectrale pour la QFT permet d'introduire la notion de densité spectrale de puissance (PSD) quaternionique. Une extension du théorème de Wiener-Khinchine au contexte de la QFT mène à la définition d'une seconde quantité fondamentale appelée auto-covariance quaternionique d'un signal bivarié. Le lien immédiat entre PSD quaternionique et paramètres de Stokes fréquentiels lui confère une interprétation naturelle en termes de paramètres de polarisation. En particulier, nous insistons sur le rôle du degré de polarisation, paramètre naturel qui quantifie la dispersion à chaque fréquence de l'ellipse de polarisation. L'étude détaillée de la question de l'estimation non-paramétrique de la PSD quaternionique montre que celle-ci se comporte de manière similaire au cas univarié, à la différence notable que l'estimation des paramètres de polarisation requiert en général des précautions particulières. Les différents résultats théoriques de ce chapitre sont illustrés par des expériences numériques sur données synthétiques.

Filtrage linéaire temps-invariant (LTI) Le chapitre 3 étudie en détail la notion de filtrage linéaire des signaux bivariés, qui constitue l'une des tâches les plus fondamentales en traitement du signal. Nous empruntons à l'optique une décomposition courante des filtres LTI en deux types, respectivement filtres *unitaire* et *Hermitien*. Chaque classe est liée à une interprétation physique spécifique, liée à une propriété fondamentale des milieux optiques. Les filtres unitaires modélisent un phénomène de *biréfringence*, tandis que les filtres Hermitiens encodent un phénomène de *diatténuation*. Nous démontrons que la formulation quaternionique de ces filtres permet d'écrire les relations de filtrage correspondantes directement en termes des vecteurs et valeurs propres de la matrice associée. Cette propriété remarquable révèle de manière naturelle l'interprétation physique et géométrique de chaque filtre, simplifiant grandement en pratique leur conception. La formulation dans ce cadre de deux tâches standard de traitement du signal, précisément la synthèse spectrale de processus Gaussiens stationnaires et le filtrage de Wiener, renforce l'attractivité de l'approche quaternionique de par sa simplicité et son interprétabilité. De plus, l'approche proposée mène naturellement à des décompositions originales de signaux bivariés en deux parties (non polarisée - polarisée, décorréllées) annonçant des traitements prometteurs.

Analyse temps-fréquence Le chapitre 4 présente nos contributions relatives à la caractérisation des signaux bivariés non-stationnaires. Nous commençons par définir un premier outil analogue au signal analytique appelé plongement quaternionique d'un signal complexe. A l'instar de son homologue univarié, le plongement quaternionique permet une identification directe de l'amplitude et phase instantanée d'un signal bivarié, mais aussi des paramètres de polarisation (orientation, ellipticité) instantanés. Afin de remédier aux limitations de ce premier outil, nous définissons une transformée de Fourier à court terme quaternionique, ainsi qu'une transformée en ondelettes continue quaternionique. Deux théorèmes fondamentaux garantissent leur inversibilité ainsi que l'interprétabilité des représentations temps-fréquence-polarisation associées, respectivement appelées *spectrogramme quaternionique* et *scalogramme quaternionique*. Une étude basée sur une méthode de phase stationnaire montre que ces représentations temps-fréquence-polarisation se concentrent autour de l'information pertinente. Dans une dernière partie, nous montrons comment définir des représentations temps-fréquence-polarisation génériques. La discussion s'articule autour de la définition d'une transformée de Wigner-Ville quaternionique et de l'étude de ses propriétés, avant la construction formelle d'une classe de Cohen pour les signaux bivariés. Des expériences numériques utilisant des données réelles et simulées illustrent les différents résultats théoriques de ce chapitre.

Caractérisation de la polarisation des ondes gravitationnelles Le chapitre 5 présente une étude de la polarisation des ondes gravitationnelles émises lors de la coalescence de systèmes binaires en précession. Cette contribution applicative illustre le fort potentiel du formalisme quaternionique développé lors des chapitres précédents. Ce travail résulte d'une collaboration avec Eric Chassande-Mottin et Fangchen Feng, du laboratoire Astroparticule et Cosmologie à Paris. En présence de précession, l'onde gravitationnelle émise par un système binaire subit une modulation de sa polarisation instantanée. Les techniques d'analyse temps-fréquence-polarisation développées au chapitre 4 permettent alors une caractérisation non-paramétrique de ces effets de précession. Il s'agit à notre connaissance de la première proposition d'une méthode non-paramétrique, c'est à dire ne nécessitant pas de modèle dynamique de la source d'émission. Nous illustrons nos résultats dans des contextes sans bruit et en présence de bruit réaliste simulé. Notons que l'approche proposée est susceptible de révéler, en théorie, tout phénomène affectant la polarisation de l'onde gravitationnelle. Celle-ci s'avère très prometteuse pour le futur de la caractérisation des ondes gravitationnelles.

Perspectives Nous récapitulons enfin les différentes contributions de cette thèse avant de dresser de nombreuses pistes théoriques et applicatives. En particulier, soulignons la question de l'estimation robuste et efficace des paramètres de polarisation ou encore la problématique fondamentale de l'identification systématique des systèmes LTI bivariés à l'aide, par exemple, d'outils empruntés à la polarimétrie.

Recherche reproductible Nous mettons à disposition une implémentation efficace des outils proposés dans ce manuscrit via un package open-source Python dénommé BiSPy⁴.

4. BiSPy: Bivariate Signal Processing in Python.

Documentation, tutoriels et code disponibles

 bispy.readthedocs.io/

 github.com/jflamant/bispy

Bibliography

- A Capella Science. 2016. "William Rowan Hamilton." Youtube. <https://www.youtube.com/watch?v=SZXHoWwBcDc>. (Cited on page 32).
- Abbott, B., et al. 2016a. "Binary Black Hole Mergers in the First Advanced LIGO Observing Run." *Physical Review X* 6 (4): 041015. (Cited on page 133).
- . 2016b. "Observation of Gravitational Waves from a Binary Black Hole Merger." *Physical Review Letters* 116:061102. doi:10.1103/PhysRevLett.116.061102. (Cited on page 133).
- . 2017a. "GW170104: Observation of a 50-Solar-Mass Binary Black Hole Coalescence at Redshift 0.2." *Physical Review Letters* 118 (22): 221101. (Cited on page 133).
- . 2017b. "GW170814: A Three-Detector Observation of Gravitational Waves from a Binary Black Hole Coalescence." *Physical Review Letters* 119 (14): 141101. (Cited on page 133).
- . 2017c. "GW170817: Observation of Gravitational Waves from a Binary Neutron Star Inspiral." *Physical Review Letters* 119 (16): 161101. (Cited on page 133).
- Adalı, T., P. J. Schreier, and L. L. Scharf. 2011. "Complex-valued signal processing: The proper way to deal with impropriety." *IEEE Transactions on Signal Processing* 59 (11): 5101–5125. doi:10.1109/TSP.2011.2162954. (Cited on pages 19, 24, 54, 61, 150).
- Aki, K., and P. G. Richards. 2002. *Quantitative Seismology, 2nd Ed.* University Science Books. (Cited on page 17).
- Altmann, S. L. 2005. *Rotations, quaternions, and double groups.* Courier Corporation. (Cited on pages 35, 72, 79).
- Amblard, P.-O., J.-F. Coeurjolly, F. Lavancier, and A. Philippe. 2012. "Basic properties of the multivariate fractional Brownian motion." *Self-similar processes and their applications* 28 (July): 65–87. (Cited on page 64).
- Amblard, P.-O., M. Gaeta, and J. Lacoume. 1996a. "Statistics for complex variables and signals, part 1: Variables." *Signal Processing* 53 (1): 1–13. (Cited on page 19).
- . 1996b. "Statistics for complex variables and signals, part 2: Signals." *Signal Processing* 53 (1): 15–25. (Cited on page 19).
- Amblard, P.-O., and N. Le Bihan. 2004. "On properness of quaternion valued random variables." In *Proc. IMA Conf. Mathematics in Signal Processing*, 23–26. (Cited on page 72).
- Appel, W., and E. Kowalski. 2007. *Mathematics for physics and physicists.* Princeton University Press Princeton, NJ, USA; Oxford, UK. (Cited on page 36).
- Arberet, S., R. Gribonval, and F. Bimbot. 2010. "A robust method to count and locate audio sources in a multichannel underdetermined mixture." *IEEE Transactions on Signal Processing* 58 (1): 121–133. (Cited on page 150).
- Azzam, R., and N. Bashara. 1987. *Ellipsometry and polarized light.* North Holland. (Cited on page 149).
- Babak, S., A. Taracchini, and A. Buonanno. 2017. "Validating the effective-one-body model of spinning, precessing binary black holes against numerical relativity." *Physical Review D* 95 (2): 024010. doi:10.1103/PhysRevD.95.024010. (Cited on pages 134, 135).

- Baez, J. 2002. "The octonions." *Bulletin of the American Mathematical Society* 39 (2): 145–205. (Cited on pages 32, 148).
- Barakat, R. 1985. "The Statistical Properties of Partially Polarized Light." *Optica Acta: International Journal of Optics* 32 (3): 295–312. doi:10.1080/713821736. (Cited on pages 20, 68).
- . 1987. "Statistics of the Stokes parameters." *Journal of the Optical Society of America A* 4 (7): 1256–1263. doi:10.1364/JOSAA.4.001256. (Cited on page 149).
- Bardenet, R., J. Flamant, and P. Chainais. 2018. "On the zeros of the spectrogram of white noise." *manuscript accepted for publication in Applied and Computational Harmonic Analysis*. eprint: arXiv:1708.00082. (Cited on pages 28, 29, 169).
- Bedrosian, E. 1963. "A product theorem for Hilbert transforms." *Proceedings of the IEEE* 51, no. 5 (May): 868–869. (Cited on page 127).
- Blanc-Lapierre, A., and R. Fortet. 1953. *Théorie des Fonctions Aléatoires*. Paris: Masson. (Cited on pages 15, 53, 74).
- Boashash, B. 1992. "Estimating and interpreting the instantaneous frequency of a signal. I. Fundamentals." *Proceedings of the IEEE* 80 (4): 520–538. doi:10.1109/5.135376. (Cited on page 104).
- Born, M., and E. Wolf. 1980. *Principles of optics: electromagnetic theory of propagation, interference and diffraction of light*. 6th. Pergamon Press. (Cited on pages 15, 17, 18, 57, 59, 60, 91, 153).
- Brosseau, C. 1995. "Statistics of the normalized Stokes parameters for a Gaussian stochastic plane wave field." *Applied Optics* 34 (22): 4788–4793. (Cited on pages 20, 68, 149).
- . 1998. *Fundamentals of polarized light: a statistical optics approach*. Wiley-Interscience. (Cited on pages 15, 18, 58, 60, 80, 91, 153).
- Brown, W., and R. Crane. 1969. "Conjugate linear filtering." *IEEE Transactions on Information Theory* 15 (4): 462–465. (Cited on page 21).
- Bülow, T., and G. Sommer. 2001. "Hypercomplex signals—a novel extension of the analytic signal to the multidimensional case." *IEEE Transactions on Signal Processing* 49 (11): 2844–2852. (Cited on pages 31, 35).
- Carmona, R. A., W. L. Hwang, and B. Torrèsani. 1997. "Characterization of signals by the ridges of their wavelet transforms." *IEEE Transactions on Signal Processing* 45 (10): 2586–2590. doi:10.1109/78.640725. (Cited on page 117).
- Carmona, R. A., W. L. Hwang, and B. Torrèsani. 1999. "Multiridge detection and time-frequency reconstruction." *IEEE Transactions on Signal Processing* 47 (2): 480–492. doi:10.1109/78.740131. (Cited on page 117).
- Chambers, M. J. 1995. "The Simulation of Random Vector Time Series with Given Spectrum." *Mathematical and Computer Modeling* 22 (2): 1–6. (Cited on page 87).
- Chandna, S., and A. T. Walden. 2011. "Statistical properties of the estimator of the rotary coefficient." *IEEE Transactions on Signal Processing* 59 (3): 1298–1303. doi:10.1109/TSP.2010.2092775. (Cited on pages 20, 68).
- . 2013. "Simulation methodology for inference on physical parameters of complex vector-valued signals." *IEEE Transactions on Signal Processing* 61 (21): 5260–5269. doi:10.1109/TSP.2013.2279076. (Cited on page 19).
- Claasen, T., and W. Mecklenbraüker. 1980. "The Wigner distribution - a tool for Time-Frequency signal analysis." *Philips J. Research* 35:217–250. (Cited on page 120).
- Clausel, M., T. Oberlin, and V. Perrier. 2015. "The monogenic synchrosqueezed wavelet transform: a tool for the decomposition/demodulation of AM-FM images." *Applied and Computational Harmonic Analysis* 39 (3): 450–486. (Cited on page 31).

- Cohen, L. 1995. *Time-frequency analysis*. Vol. 299. Prentice hall. (Cited on pages 23, 104).
- Conway, J. H., and D. A. Smith. 2003. *On quaternions and octonions: their geometry, arithmetic, and symmetry*. AK Peters. (Cited on pages 32, 38).
- Crowe, M. J. 1967. *A history of vector analysis*. University of Notre Dame Press, Notre Dame. (Cited on page 32).
- Damask, J. N. 2004. *Polarization Optics in Telecommunications*. Springer-Verlag New York. (Cited on pages 95–97).
- Daubechies, I., and T. Paul. 1988. “Time-frequency localisation operators—a geometric phase space approach: II. The use of dilations.” *Inverse Problems* 4 (3): 661–680. doi:10.1088/0266-5611/4/3/009. (Cited on page 112).
- Daubechies, I. 1992. *Ten lectures on wavelets*. Vol. 61. SIAM. (Cited on page 112).
- Delprat, N., B. Escudie, P. Guillemain, R. Kronland-Martinet, P. Tchamitchian, and B. Torresani. 1992. “Asymptotic wavelet and Gabor analysis: extraction of instantaneous frequencies.” *IEEE Transactions on Information Theory* 38, no. 2 (March): 644–664. doi:10.1109/18.119728. (Cited on pages 115, 117, 128).
- Diallo, M. S., M. Kulesh, M. Holschneider, and F. Scherbaum. 2005. “Instantaneous polarization attributes in the time–frequency domain and wavefield separation.” *Geophysical Prospecting* 53 (5): 723–731. (Cited on pages 22, 25).
- Dimitriadis, D., P. Maragos, and A. Potamianos. 2005. “Robust AM-FM features for speech recognition.” *IEEE Signal Processing Letters* 12 (9): 621–624. (Cited on page 104).
- Dingle, R. B. 1973. *Asymptotic expansions, derivation and interpretation*. Academic Press Inc. (Cited on page 128).
- Ell, T. A., N. Le Bihan, and S. J. Sangwine. 2014. *Quaternion Fourier transforms for signal and image processing*. John Wiley & Sons. (Cited on pages 31, 35, 36).
- Ell, T. A., and S. J. Sangwine. 2007. “Hypercomplex Fourier transforms of color images.” *IEEE Transactions on Image Processing* 16 (1): 22–35. (Cited on page 31).
- Ell, T. A. 2013. “Quaternion Fourier transform: re-tooling image and signal processing analysis.” In *Quaternion and Clifford Fourier Transforms and Wavelets*, 3–14. Springer. (Cited on page 32).
- Ellis, J., and A. Dogariu. 2004. “Differentiation of globally unpolarized complex random fields.” *Journal of the Optical Society of America A* 21 (6): 988–993. (Cited on pages 59, 73, 74).
- Felsberg, M., and G. Sommer. 2001. “The monogenic signal.” *IEEE Transactions on Signal Processing* 49 (12): 3136–3144. (Cited on page 31).
- Feng, F., P. Bacon, E. Chassande-Mottin, and A. Fraysse. 2018. “Structured sparsity regularization for gravitational-wave polarisation reconstruction.” In *26th European Signal Processing Conference (EUSIPCO)*, 1–5. September. (Cited on pages 134, 135, 138, 139).
- Finkelstein, D., J. M. Jauch, S. Schiminovich, and D. Speiser. 1962. “Foundations of quaternion quantum mechanics.” *Journal of Mathematical Physics* 3 (2): 207–220. doi:10.1063/1.1703794. (Cited on page 44).
- Flamant, J., P. Chainais, E. Chassande-Mottin, F. Feng, and N. Le Bihan. 2018. “Non-parametric characterization of gravitational-wave polarizations.” In *26th European Signal Processing Conference (EUSIPCO)*, 2018, 1–5. September. (Cited on pages 28, 29, 133, 139, 148).
- Flamant, J., P. Chainais, and N. Le Bihan. 2018a. “A complete framework for linear filtering of bivariate signals.” *IEEE Transactions on Signal Processing* 66, no. 17 (September): 4541–4552. doi:10.1109/TSP.2018.2855659. (Cited on pages 27, 29, 78, 97, 146).
- . 2018b. “Linear filtering of bivariate signals using quaternions.” In *IEEE Statistical Signal Processing Workshop (SSP)*, 2018, Freiburg, 1–5. Best Student Paper Award. (Cited on pages 27, 29, 78, 97, 146).

- Flamant, J., N. Le Bihan, and P. Chainais. 2017a. "Analyse spectrale des signaux aléatoires bivariés." In *GRETSI 2017*. Juan-les-Pins, France. (Cited on pages 27, 29, 49, 71, 146).
- . 2017b. "Polarization spectrogram of bivariate signals." In *IEEE International Conference on Acoustics, Speech, and Signal Processing (ICASSP), 2017, New Orleans, USA*. (Cited on pages 28, 29, 104, 126, 147).
- . 2017c. "Spectral analysis of stationary random bivariate signals." *IEEE Transactions on Signal Processing* 65 (23): 6135–6145. doi:10.1109/TSP.2017.2736494. (Cited on pages 27, 29, 49, 71, 146).
- . 2017d. "Spectrogramme de polarisation pour l'analyse des signaux bivariés." In *GRETSI 2017*. Juan-les-Pins, France. (Cited on pages 28, 29, 104, 126, 147).
- . 2017e. "Time-frequency analysis of bivariate signals." In Press, *Applied and Computational Harmonic Analysis*. doi:10.1016/j.acha.2017.05.007. (Cited on pages 27–29, 32, 36, 39, 42, 104, 126, 145, 147).
- Flandrin, P. 1998. *Time-frequency/time-scale analysis*. Vol. 10. Academic Press. (Cited on pages 23, 48, 104, 111, 118, 120–123).
- . 2015. "Time–frequency filtering based on spectrogram zeros." *IEEE Signal Processing Letters* 22 (11): 2137–2141. (Cited on page 169).
- . 2016. "The sound of silence: recovering signals from time-frequency zeros." In *50th Asilomar Conference on Signals, Systems and Computers, 2016*, 544–548. IEEE. (Cited on page 169).
- . 2018. "Signal processing: a field at the heart of science and everyday life." Accessed June 7, 2018. <https://theconversation.com/signal-processing-a-field-at-the-heart-of-science-and-everyday-life-89267>. (Cited on page 25).
- Francia, C., F. Bruyère, D. Penninckx, and M. Chbat. 1998. "PMD Second-Order Effects on Pulse Propagation in Single-Mode Optical Fibers." *IEEE Photonics Technology Letters* 10 (12): 1739–1741. doi:10.1109/68.730487. (Cited on page 96).
- Gabor, D. 1946. "Theory of Communication." Part III, *Journal of the Institution of Electrical Engineers* 93 (26): 429–457. (Cited on pages 23, 104).
- Gardner, W. A. 1993. "Cyclic Wiener filtering: theory and method." *IEEE Transactions on Communications* 41, no. 1 (January): 151–163. doi:10.1109/26.212375. (Cited on page 21).
- Gil, J. 2007. "Polarimetric characterization of light and media." *The European Physical Journal Applied Physics* 40:1–47. (Cited on pages 21, 57, 77, 81, 83, 84).
- Gil, J., and R. Ossikovski. 2016. *Polarized Light and the Mueller matrix approach*. CRC Press. (Cited on pages 21, 80–86).
- Goldberg, J. N., A. J. MacFarlane, E. T. Newman, F. Rohrlich, and E. G. Sudarshan. 1967. "Spin-s Spherical Harmonics and δ ." *Journal of Mathematical Physics* 8 (11): 2155–2161. (Cited on page 140).
- Gonella, J. 1972. "A rotary-component method for analysing meteorological and oceanographic vector time series." In *Deep Sea Research and Oceanographic Abstracts*, 19:833–846. 12. Elsevier. (Cited on pages 15, 23, 92, 153).
- Gordon, J. P., and H. Kogelnik. 2000. "PMD fundamentals: Polarization mode dispersion in optical fibers." *Proceedings of the National Academy of Sciences* 97 (9): 4541–4550. doi:10.1073/pnas.97.9.4541. (Cited on pages 95, 96).
- Hamilton, W. R. 1844. "On Quaternions: Letter to John Thomas Graves, 17th October, 1843." *London, Edinburgh and Dublin Philosophical Magazine and Journal of Science* 25:489–95. (Cited on page 26).
- . 1866. *Elements of quaternions*. Longmans, Green, & Company. (Cited on page 32).
- Hannan, E. J. 1970. *Multiple time series*. John Wiley & Sons. (Cited on page 53).

- Hayashi, Y. 1982. "Space-time spectral analysis and its applications to atmospheric waves." *Journal of the Meteorological Society of Japan. Ser. II* 60 (1): 156–171. (Cited on pages 15, 153).
- Hestenes, D., and G. Sobczyk. 2012. *Clifford algebra to geometric calculus: a unified language for mathematics and physics*. Vol. 5. Springer Science & Business Media. (Cited on page 148).
- Hindberg, H., and A. Hanssen. 2007. "Generalized spectral coherences for complex-valued harmonizable processes." *IEEE Transactions on Signal Processing* 55 (6 I): 2407–2413. doi:10.1109/TSP.2007.893932. (Cited on pages 22, 25).
- Hitzer, E. M. S. 2007. "Quaternion Fourier transform on quaternion fields and generalizations." *Advances in Applied Clifford Algebras* 17 (3): 497–517. doi:10.1007/s00006-007-0037-8. (Cited on page 31).
- Holden, H., B. Øksendal, J. Ubøe, and T. Zhang. 2010. *Stochastic partial differential equations*. Second. Springer. (Cited on page 62).
- Huang, N. E., Z. Shen, S. R. Long, M. C. Wu, H. H. Shih, Q. Zheng, N.-C. Yen, C. C. Tung, and H. H. Liu. 1998. "The empirical mode decomposition and the Hilbert spectrum for nonlinear and non-stationary time series analysis." In *Proceedings of the Royal Society of London A: mathematical, physical and engineering sciences*, 454:903–995. 1971. The Royal Society. (Cited on page 22).
- Jamison, J. E. 1970. "Extension of some theorems of complex functional analysis to linear spaces over the quaternions and Cayley numbers." PhD diss., University of Missouri–Rolla. (Cited on pages 31, 35, 36, 38, 44, 45).
- Johnson, G. 1996. "The Complex (and Circular) Argument Continues." *IEEE Signal Processing Magazine* 13, no. 5 (September): 42–. (Cited on page 15).
- Jones, R. C. 1941. "A new calculus for the treatment of optical systems. description and discussion of the calculus." *Journal of the Optical Society of America* 31 (7): 488–493. (Cited on pages 21, 26).
- Karlsson, M. 1998. "Polarization mode dispersion induced pulse broadening in optical fibers." *Optics letters* 23 (9): 688–690. doi:10.1364/OL.23.000688. (Cited on page 95).
- Karlsson, M., and M. Petersson. 2004. "Quaternion approach to PMD and PDL phenomena in optical fiber systems." *Journal of Lightwave Technology* 22 (4): 1137–1146. doi:10.1109/JLT.2004.825330. (Cited on page 26).
- Kikuchi, N. 2001. "Analysis of signal degree of polarization degradation used as control signal for optical polarization mode dispersion compensation." *Lightwave Technology, Journal of* 19 (4): 480–486. doi:10.1109/50.920845. (Cited on pages 58, 67).
- Koopmans, L. H. 1995. *The spectral analysis of time series*. Elsevier. (Cited on page 59).
- Lancaster, P., and M. Tismenetsky. 1985. *The theory of matrices: with applications*. Elsevier. (Cited on pages 79, 86).
- Le Bihan, N. 2017. "The geometry of proper quaternion random variables." *Signal Processing* 138:106–116. (Cited on page 72).
- Le Bihan, N., and J. Mars. 2004. "Singular value decomposition of quaternion matrices: a new tool for vector-sensor signal processing." *Signal processing* 84 (7): 1177–1199. (Cited on page 31).
- Le Bihan, N., S. J. Sangwine, and T. A. Ell. 2014. "Instantaneous frequency and amplitude of orthocomplex modulated signals based on quaternion Fourier transform." *Signal Processing* 94:308–318. (Cited on pages 26, 39, 105).
- Lefèvre, J., N. Le Bihan, and P.-O. Amblard. 2018. "A Geometrical study of the bivariate fractional Gaussian noise." In *2018 IEEE Statistical Signal Processing Workshop (SSP)*, 1–5. June. (Cited on page 64).
- Lilly, J. M. 2016. *JLab: A data analysis package for Matlab, v. 1.6.2*. (Cited on page 124).

- Lilly, J. M., and S. C. Olhede. 2009. "Higher-order properties of analytic wavelets." *IEEE Transactions on Signal Processing* 57 (1): 146–160. doi:10.1109/TSP.2008.2007607. (Cited on pages 112, 114).
- Lilly, J. M., and J. C. Gascard. 2006. "Wavelet ridge diagnosis of time-varying elliptical signals with application to an oceanic eddy." *Nonlinear Processes in Geophysics* 13 (5): 467–483. doi:10.5194/npg-13-467-2006. (Cited on pages 22, 25, 107).
- Lilly, J. M., and S. C. Olhede. 2010a. "Bivariate instantaneous frequency and bandwidth." *IEEE Transactions on Signal Processing* 58 (2): 591–603. (Cited on pages 15, 22, 25, 107).
- . 2010b. "On the analytic wavelet transform." *IEEE Transactions on Information Theory* 56 (8): 4135–4156. (Cited on pages 115, 117).
- . 2012. "Generalized Morse Wavelets as a Superfamily of Analytic Wavelets." *IEEE Transactions on Signal Processing* 60 (11): 6036–6041. (Cited on page 112).
- Lilly, J. M., and J. Park. 1995. "Multiwavelet spectral and polarization analyses of seismic records." *Geophysical Journal International* 122 (3): 1001–1021. (Cited on page 124).
- Loeve, M. 1978. "Probability theory, vol. ii." *Graduate texts in mathematics* 46:0–387. (Cited on pages 53, 74).
- Lu, S.-y., and R. A. Chipman. 1994. "Homogeneous and inhomogeneous Jones matrices." *Journal of the Optical Society of America A* 11 (2): 766–773. doi:10.1364/JOSAA.11.000766. (Cited on page 86).
- Mallat, S. 2008. *A wavelet tour of signal processing: the sparse way*. Academic Press. (Cited on pages 47, 111, 112, 114, 115, 129).
- Mandic, D. P., and V. S. L. Goh. 2009. *Complex Valued Nonlinear Adaptive Filters: Noncircularity, Widely Linear and Neural Models*, 1–324. doi:10.1002/9780470742624. (Cited on page 15).
- Mandic, D. P., C. Jahanchahi, and C. C. Took. 2011. "A quaternion gradient operator and its applications." *IEEE Signal Processing Letters* 18 (1): 47–50. (Cited on page 150).
- Marathay, A. S. 1965. "Operator formalism in the theory of partial polarization." *Journal of the Optical Society of America* 55 (8): 969–980. doi:10.1364/JOSA.55.000969. (Cited on page 26).
- Medkour, T., and A. T. Walden. 2008. "Statistical Properties of the Estimated Degree of Polarization." *IEEE Transactions on Signal Processing* 56 (1): 408–414. (Cited on pages 20, 67, 68).
- Miron, S., N. Le Bihan, and J. I. Mars. 2006. "Quaternion-MUSIC for vector-sensor array processing." *IEEE Transactions on Signal Processing* 54 (4): 1218–1229. (Cited on page 31).
- Misner, C. W., K. S. Thorne, and J. A. Wheeler. 1973. *Gravitation*. W. H. Freeman / Company. (Cited on pages 15, 17).
- Mooers, C. N. 1973. "A technique for the cross spectrum analysis of pairs of complex-valued time series, with emphasis on properties of polarized components and rotational invariants." In *Deep Sea Research and Oceanographic Abstracts*, 20:1129–1141. 12. Elsevier. (Cited on page 15).
- Mueller, H. 1943. "Memorandum on the polarization optics of the photoelastic shutter." *Report of the OSRD project OEMsr-576* 2. (Cited on page 26).
- Olhede, S. C., and A. T. Walden. 2002. "Generalized Morse wavelets." *IEEE Transactions on Signal Processing* 50 (11): 2661–2670. doi:10.1109/TSP.2002.804066. (Cited on page 112).
- . 2003. "Polarization phase relationships via multiple Morse wavelets. II. Data analysis." In *Proceedings of the Royal Society of London A: Mathematical, Physical and Engineering Sciences*, 459:641–657. 2031. The Royal Society. (Cited on page 124).

- Ollila, E. 2008. "On the circularity of a complex random variable." *IEEE Signal Processing Letters* 15:841–844. (Cited on page 19).
- Pan, Y., A. Buonanno, A. Taracchini, L. E. Kidder, A. H. Mroué, H. P. Pfeiffer, M. A. Scheel, and B. Szilágyi. 2014. "Inspiral-merger-ringdown waveforms of spinning, precessing black-hole binaries in the effective-one-body formalism." *Physical Review D* 89 (8): 084006. doi:10.1103/PhysRevD.89.084006. (Cited on page 137).
- Pellat-finet, P. 1984. "Représentation des états et des Opérateurs de Polarisation de la Lumière Par des Quaternions." *Optica Acta : International Journal of Optics* 31:415–434. doi:10.1080/713821517. (Cited on pages 26, 86).
- Percival, D. B. 1992. "Simulating Gaussian Random Processes with Specified Spectra." *Computing Science and Statistics* 24:534–538. (Cited on page 87).
- Percival, D. B., and A. T. Walden. 1993. *Spectral analysis for physical applications*. Cambridge University Press. (Cited on pages 46, 53, 65–67).
- Picinbono, B. 1994. "On circularity." *IEEE Transactions on Signal Processing* 42, no. 12 (December): 3473–3482. (Cited on pages 19, 54, 72).
- . 1996. "Too Complex to be Real." *IEEE Signal Processing Magazine* 13, no. 4 (July): 18–19. (Cited on page 15).
- . 1997. "On instantaneous amplitude and phase of signals." *IEEE Transactions on Signal Processing* 45 (3): 552–560. doi:10.1109/78.558469. (Cited on pages 104, 128).
- Picinbono, B., and P. Bondon. 1997. "Second-order statistics of complex signals." *IEEE Transactions on Signal Processing* 45, no. 2 (February): 411–420. doi:10.1109/78.554305. (Cited on pages 19, 24, 61, 63, 72).
- Picinbono, B., and P. Chevalier. 1995. "Widely Linear Estimation with Complex Data." *IEEE Transactions on Signal Processing* 43 (8): 4–7. (Cited on page 21).
- Pinnegar, C. R. 2006. "Polarization analysis and polarization filtering of three-component signals with the time-frequency." *Geophysical Journal International* 165 (2): 596–606. doi:10.1111/j.1365-246X.2006.02937.x. (Cited on pages 15, 22, 153).
- Poincaré, H. 1892. *Théorie mathématique de la lumière*. (Cited on pages 17, 59).
- Poole, C. D., and R. E. Wagner. 1986. "Phenomenological approach to polarisation dispersion in long single-mode fibres." *Electronics Letters* 22 (19): 19–20. (Cited on pages 95, 96).
- Priestley, M. B. 1981. *Spectral analysis and time series*. Academic press. (Cited on pages 19, 51, 52, 65, 75, 78).
- Raymond, F.-h. 1951. "Transformées de Hilbert et relations de Bayard-Bode." In *Annales Des Télécommunications*, 6:262–272. 10. Springer. (Cited on page 149).
- Réfrégier, P., T. Setälä, and A. T. Friberg. 2011. "Temporal and spectral degrees of polarization of light." In *Physical Optics*, 8171:817102. International Society for Optics and Photonics. (Cited on page 59).
- Rehman, N. ur, and D. P. Mandic. 2010. "Empirical mode decomposition for trivariate signals." *IEEE Transactions on signal processing* 58 (3): 1059–1068. (Cited on page 31).
- Richartz, M., and H.-Y. Hsü. 1949. "Analysis of Elliptical Polarization." *Journal of the Optical Society of America* 39 (2): 136. doi:10.1364/JOSA.39.000136. (Cited on page 26).
- Riedel, K. S., and A. Sidorenko. 1995. "Minimum bias multiple taper spectral estimation." *IEEE Transactions on Signal Processing* 43 (1): 188–195. (Cited on page 66).
- Rilling, G., P. Flandrin, P. Goncalves, and J. M. Lilly. 2007. "Bivariate empirical mode decomposition." *IEEE Signal Processing Letters* 14 (12): 936–939. doi:10.1109/Lsp.2007.904710. (Cited on pages 22, 25, 150).

- Rose, M. E. 1957. *Elementary theory of angular momentum*. New York: John Wiley / sons. (Cited on pages 135, 140).
- Roueff, A., J. Chanussot, and J. Mars. 2006. "Estimation of polarization parameters using time-frequency representations and its application to waves separation." *Signal Processing* 86 (12): 3714–3731. doi:10.1016/j.sigpro.2006.03.019. (Cited on pages 22, 25).
- Rubin-Delanchy, P., and A. T. Walden. 2007. "Simulation of improper complex-valued sequences." *IEEE Transactions on Signal Processing* 55 (11): 5517–5521. doi:10.1109/TSP.2007.898752. (Cited on page 19).
- . 2008. "Kinematics of complex-valued time series." *IEEE Transactions on Signal Processing* 56 (9): 4189–4198. doi:10.1109/TSP.2008.926106. (Cited on pages 20, 68).
- Sakkalis, V. 2011. "Review of advanced techniques for the estimation of brain connectivity measured with EEG/MEG." *Computers in biology and medicine* 41 (12): 1110–1117. (Cited on pages 15, 153).
- Samson, J. 1983. "Pure states, polarized waves, and principal components in the spectra of multiple, geophysical time-series." *Geophysical Journal International* 72 (3): 647–664. (Cited on pages 15, 153).
- Sanei, S., and J. A. Chambers. 2013. *EEG signal processing*. John Wiley & Sons. (Cited on pages 15, 153).
- Sangwine, S. J., and N. Le Bihan. 2010. "Quaternion polar representation with a complex modulus and complex argument inspired by the Cayley-Dickson form." *Advances in applied Clifford algebras* 20 (1): 111–120. (Cited on page 105).
- Sangwine, S. J. 1996. "Fourier transforms of colour images using quaternion or hypercomplex, numbers." *Electronics letters* 32 (21): 1979–1980. (Cited on page 31).
- Santalla del Rio, V., J. M. Pidre Mosquera, M. Vera Isasa, and M. E. de Lorenzo. 2006. "Statistics of the Degree of Polarization." *IEEE Transactions on Antennas and Propagation* 54 (7): 2173–2175. doi:10.1109/TAP.2006.877210. (Cited on pages 67, 68).
- Schreier, P. J. 2008. "Polarization ellipse analysis of nonstationary random signals." *IEEE Transactions on Signal Processing* 56 (9): 4330–4339. doi:10.1109/TSP.2008.925961. (Cited on pages 15, 18, 22, 25).
- Schreier, P. J., and L. L. Scharf. 2003a. "Stochastic Time-Frequency Analysis Using the Analytic Signal: Why the Complementary Distribution Matters." *IEEE Transactions on Signal Processing* 51 (12): 3071–3079. doi:10.1109/TSP.2003.818911. (Cited on page 24).
- Schreier, P. J., and L. L. Scharf. 2003b. "Second-order analysis of improper complex random vectors and processes." *IEEE Transactions on Signal Processing* 51 (3): 714–725. doi:10.1109/TSP.2002.808085. (Cited on pages 20, 21).
- . 2010. *Statistical signal processing of complex-valued data: the theory of improper and noncircular signals*. Cambridge University Press. (Cited on pages 15, 16, 18, 20, 24, 40, 51, 55, 57, 61, 101).
- Segal, S. L. 2014. *Mathematicians under the Nazis*. Princeton University Press. (Cited on page 44).
- Setälä, T., F. Nunziata, and A. T. Friberg. 2010. "Partial polarization of optical beams: temporal and spectral descriptions." In *Information Optics and Photonics*, 207–216. Springer. (Cited on page 59).
- Shirvany, R., M. Chabert, and J. Y. Tournet. 2012. "Ship and oil-spill detection using the degree of polarization in linear and hybrid/compact dual-pol SAR." *IEEE Journal of Selected Topics in Applied Earth Observations and Remote Sensing* 5 (3): 885–892. doi:10.1109/JSTARS.2012.2182760. (Cited on pages 58, 67).
- Silver, P. G., and W. W. Chan. 1991. "Shear wave splitting and subcontinental mantle deformation." *Journal of Geophysical Research* 96 (B10): 16429. doi:10.1029/91JB00899. (Cited on page 94).
- Silver, P. G., and M. K. Savage. 1994. "The Interpretation of shear-wave splitting parameters in the presence of two anisotropic layers." *Geophysical Journal International* 119:949–963. (Cited on page 94).

- Simon, B. 2015. *A comprehensive course in analysis, part I*. American Mathematical Society. (Cited on page 36).
- Simon, R. 1990. “Nondepolarizing and degree polarization.” *Optics Communications* 77 (5): 349–354. (Cited on page 85).
- Slepian, D. 1978. “Prolate spheroidal wave functions, Fourier analysis, and uncertainty—V: The discrete case.” *Bell System Technical Journal* 57 (5): 1371–1430. (Cited on page 66).
- Stokes, G. G. 1852. “On the Change of Refrangibility of Light.” *Philosophical Transactions of the Royal Society of London* 142 (1852): 463–562. (Cited on page 57).
- Sudha and A. V. G. Rao. 2001. “Polarization Elements-A Group Theoretical Study.” *Journal of the Optical Society of America A* 18 (12): 3130. doi:10.1364/JOSAA.18.003130. (Cited on page 86).
- Sykulski, A. M., S. C. Olhede, and J. M. Lilly. 2016. “A Widely Linear Complex Autoregressive Process of Order One.” *IEEE Transactions on Signal Processing* 64 (23): 6200–6210. doi:10.1109/TSP.2016.2599503. (Cited on pages 15, 124).
- Sykulski, A. M., and D. B. Percival. 2016. “Exact simulation of noncircular or improper complex-valued stationary Gaussian processes using circulant embedding.” In *2016 IEEE 26th International Workshop on Machine Learning for Signal Processing (MLSP)*, 1–6. September. doi:10.1109/MLSP.2016.7738840. (Cited on page 19).
- Tanaka, T., and D. P. Mandic. 2007. “Complex Empirical Mode Decomposition.” *IEEE Signal Processing Letters* 14 (2): 101–104. (Cited on pages 15, 22, 25, 150, 153).
- Teichmüller, O. 1936. “Operatoren im Wachsschen Raum.” *Journal für die reine und angewandte Mathematik* 174:73–124. (Cited on page 44).
- Thompson, R. 1973. “Generation of stochastic processes with given spectrum.” *Utilitas Mathematica* 3:127–137. (Cited on page 87).
- Thomson, D. J. 1982. “Spectrum estimation and harmonic analysis.” *Proceedings of the IEEE* 70 (9): 1055–1096. doi:10.1109/PROC.1982.12433. (Cited on page 66).
- Thomson, R. E., and W. J. Emery. 2014. *Data analysis methods in physical oceanography, Third edition*. Elsevier Science. (Cited on pages 15, 153).
- Thorne, K. S. 1987. “Gravitational radiation.” In *Three Hundred Years of Gravitation*, edited by S. W. Hawking and W. Israel, 330–458. (Cited on page 133).
- Took, C. C., and D. P. Mandic. 2009. “The quaternion LMS algorithm for adaptive filtering of hypercomplex processes.” *IEEE Transactions on Signal Processing* 57 (4): 1316–1327. (Cited on page 31).
- . 2010. “A quaternion widely linear adaptive filter.” *IEEE Transactions on Signal Processing* 58 (8): 4427–4431. (Cited on page 31).
- Torrésani, B. 1995. *Analyse continue par ondelettes*. EDP Sciences. (Cited on pages 115, 117).
- Tudor, T. 2010a. “Vectorial Pauli algebraic approach in polarization optics . II . Interaction of light with the canonical polarization devices.” *Optik - International Journal for Light and Electron Optics* 121 (23): 2149–2158. doi:10.1016/j.ijleo.2009.08.001. (Cited on page 26).
- . 2010b. “Vectorial Pauli algebraic approach in polarization optics. I. Device and state operators.” *Optik - International Journal for Light and Electron Optics* 121 (13): 1226–1235. doi:10.1016/j.ijleo.2009.01.004. (Cited on page 26).
- Vakhania, N. N. 1999. “Random vectors with values in quaternion Hilbert spaces.” *Theory of Probability & Its Applications* 43 (1): 99–115. (Cited on page 72).

- Varshalovich, D. A., A. N. Moskalev, and V. K. Khersonskii. 1988. *Quantum Theory of Angular Momentum*. Singapore: World Scientific. (Cited on page 140).
- Vetterli, M., J. Kovačević, and V. K. Goyal. 2014. *Foundations of signal processing*. Cambridge University Press. (Cited on page 46).
- Vía, J., D. Ramírez, and I. Santamaría. 2010. “Properness and widely linear processing of quaternion random vectors.” *IEEE Transactions on Information Theory* 56 (7): 3502–3515. (Cited on pages 31, 72).
- Ville, J. 1948. “Théorie et Applications de la Notion de Signal Analytique.” *Câbles et Transmissions* 2A:61–74. (Cited on pages 23, 104).
- Walden, A. T. 2000. “A unified view of multitaper multivariate spectral estimation.” *Biometrika* 87 (4): 767–788. doi:10.1093/biomet/87.4.767. (Cited on pages 66, 67).
- . 2013. “Rotary components, random ellipses and polarization: a statistical perspective.” *Philosophical Transactions of the Royal Society of London A: Mathematical, Physical and Engineering Sciences* 371 (1984): 20110554. (Cited on pages 15, 18, 20, 92, 149).
- Walden, A. T., and T. Medkour. 2007. “Ensemble estimation of polarization ellipse parameters.” *Proceedings of the Royal Society A: Mathematical, Physical and Engineering Sciences* 463 (2088): 3375–3394. doi:10.1098/rspa.2007.0072. (Cited on pages 20, 68, 149).
- Ward, J. 1997. *Quaternions and Cayley Numbers: Algebra and Applications*. Vol. 403. Springer Science & Business Media. (Cited on page 32).
- Whitney, C. 1971. “Pauli-Algebraic Operators in Polarization Optics.” *Journal of the Optical Society of America* 61 (9): 1207–1213. doi:10.1364/JOSA.61.001207. (Cited on page 26).
- Wigner, E. P. 1971. “Quantum-mechanical distribution functions revisited.” In *Perspectives in Quantum Theory*. Cambridge, MA: MIT Press. (Cited on page 120).
- Wolfe, C. J., and P. G. Silver. 1998. “Seismic anisotropy of oceanic upper mantle: Shear wave splitting methodologies and observations.” *Journal of Geophysical Research: Solid Earth* 103 (B1): 749–771. doi:10.1029/97JB02023. (Cited on page 94).
- Xu, D., C. Jahanchahi, C. C. Took, and D. P. Mandic. 2015. “Enabling quaternion derivatives: the generalized HR calculus.” *Royal Society open science* 2 (8): 150255. (Cited on page 150).


This bibliography contains 184 entries.


Appendix

“On the zeros of the spectrogram of white noise”

R. Bardenet, J. Flamant, P. Chainais

In parallel with the research program of my thesis which has developed a complete framework for the analysis and filtering of bivariate signals, I have been also involved in a collaboration with Rémi Bardenet and Pierre Chainais. The main results of this collaboration are reproduced here in the form of the following paper, accepted for publication in *Applied and Computational Harmonic Analysis*:

 R. Bardenet, J. Flamant, and P. Chainais. 2018. “On the zeros of the spectrogram of white noise.” *manuscript accepted for publication in Applied and Computational Harmonic Analysis*. eprint: [arXiv:1708.00082](https://arxiv.org/abs/1708.00082).

This work studies the distribution of the zeros of the spectrogram of white Gaussian noise when the window is itself Gaussian. Fig. 9 displays such zeros for a realization of real and complex (circular) white Gaussian noise, respectively. Our interest in this topic has been triggered by recent works of Flandrin (2015, 2016) who proposed an heuristic filtering method using spectrogram zeros. We demonstrate in the appended paper that the zeros of spectrograms of white Gaussian noise correspond to zeros of Gaussian analytic functions (GAFs). In particular it appears that the point process formed by the zeros is not a determinantal point process (DPP) as one may have originally expected. Still, its main statistical properties can be investigated. Second, we leverage methods from spatial statistics to implement practical detection and reconstruction of signals corrupted by white Gaussian noise based on the statistics of spectrogram zeros. Numerical experiments demonstrate the feasibility of the approach. Supporting code is made publicly available on GitHub  github.com/jflamant/2018-zeros-spectrogram-white-noise.

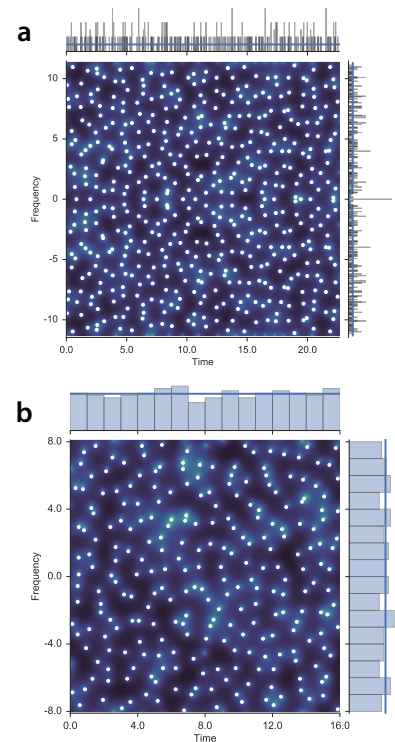


Figure 9: Spectrograms (Gaussian window) of (a) real white Gaussian noise and (b) complex circular white Gaussian noise. White dots show the zeros of spectrograms. See Fig. 1 of the appended paper for details.

On the zeros of the spectrogram of white noise

Rémi Bardenet^{1*}, Julien Flamant¹, Pierre Chainais¹

¹ Univ. Lille, CNRS, Centrale Lille, UMR 9189 — CRIStAL, 59651 Villeneuve d'Ascq, France

Abstract

In a recent paper, [1] proposed filtering based on the zeros of a spectrogram with Gaussian window. His results are based on empirical observations on the distribution of the zeros of the spectrogram of white Gaussian noise. These zeros tend to be uniformly spread over the time-frequency plane, and not to clutter. Our contributions are threefold: we rigorously define the zeros of the spectrogram of continuous white Gaussian noise, we explicitly characterize their statistical distribution, and we investigate the computational and statistical underpinnings of the practical implementation of signal detection based on the statistics of the zeros of the spectrogram. The crux of our analysis is that the zeros of the spectrogram of white Gaussian noise correspond to the zeros of a Gaussian analytic function, a topic of recent independent mathematical interest [2].

1 Introduction

Spectrograms are a cornerstone of time-frequency analysis [3]. They are quadratic time-frequency representations of a signal [4, Chapter 4], associating to each time and frequency a real number that measures the energy content of a signal at that time and frequency, unlike global-in-time tools such as the Fourier transform. Since it is natural to expect that there is more energy where there is more information or signal, most methodologies have focused on detecting and processing the local maxima of the spectrogram [5, 3, 4]. Usual techniques include *ridge extraction*, e.g., to identify chirps, or *reassignment* and *synchrosqueezing*, to better localize the maxima of the spectrogram before further quantitative analysis.

In contrast, recent works have shown that the zeros of a spectrogram play a central role. They appear in the context of reassignment [6] or in the study of the characteristic structure of the phase derivative of the spectrogram around its zeros [7]. Moreover [1] recently observed that the location of zeros of a spectrogram in the time-frequency plane almost completely characterizes the spectrogram. He then proposed filtering and reconstruction procedures based on the point pattern formed by the zeros. This proposition stems from the empirical observation that the zeros of the short-time Fourier transform of white noise are uniformly spread over the time-frequency plane, and tend not to clutter, as if they repelled each other. Without going into details yet, this repulsive behaviour of the zeros can be seen in Figure 1, where we plot the spectrograms of a real and proper complex white noise, respectively. In the presence of a signal, zeros are absent in the time-frequency support of the signal, thus creating large holes that appear to be very rare when observing pure white noise. This leads to testing the presence of a signal by looking at statistics of the point pattern of zeros, and trying to

*Corresponding author: remi.bardenet@gmail.com

identify holes. In this paper, we attempt a formalization of the approach of [1]. To this purpose, we put together notions of signal processing, complex analysis, probability, and spatial statistics.

Our contributions are threefold: we rigorously define the zeros of the spectrogram of continuous Gaussian white noise, we explicitly characterize their statistical distribution, and we investigate the computational and statistical underpinnings of the practical implementation of signal detection and reconstruction. The crux of our analysis is that the zeros of the spectrogram of Gaussian white noise correspond to the zeros of a Gaussian analytic function, a topic of recent independent mathematical interest [2].

In short, our approach starts from the usual definition of white noise as a random tempered distribution. Using a classical equivalence between the short-time Fourier transform with a Gaussian window and the Bargmann transform, we show that the short-time Fourier transform of white noise can be identified with a random analytic function, so that we can give a precise meaning to the zeros of the spectrogram of white noise. It turns out that real and complex Gaussian white noises lead to recently studied random analytic functions, the zeros of which have been completely characterized. We then investigate how to leverage probabilistic information on these zeros to design statistical detection procedures. This includes linking probability and complex analysis results to the discrete implementation of the Fourier transform.

The rest of the paper is organized as follows. In Section 2, we introduce the relevant notions of complex analysis, probability, and spatial statistics. In Section 3, we characterize the zeros of the short-time Fourier transform of real white noise, and we deal with the complex and the analytic case in Section 4. In Section 5, we investigate the relation between our theoretical results for continuous white noise and the usual discrete implementation of the Fourier transform, and we demonstrate the detection and reconstruction of a signal using the zeros of the spectrogram.

2 Spectrograms, complex analysis, and point processes

In this section, we survey the relevant notions from signal processing, probability, and spatial statistics.

2.1 The short-time Fourier transform

Let $f, \gamma \in L^2(\mathbb{R})$, the evaluation at $(u, v) \in \mathbb{R}^2$ of the short-time Fourier transform (STFT) of f with window γ reads

$$V_\gamma f(u, v) = \int f(t) \overline{\gamma(t-u)} e^{-2i\pi tv} dt = \langle f, M_v T_u \gamma \rangle, \quad (1)$$

with $\langle \cdot, \cdot \rangle$ denoting the inner product in $L^2(\mathbb{R})$, $M_v f = e^{2i\pi v \cdot} f(\cdot)$ and $T_u f = f(\cdot - u)$. We copy our notation from [4, Chapter 3], to which we refer for a thorough introduction. The squared modulus of the STFT (1) is called a *spectrogram*, and it is commonly interpreted as a measure of the content of the signal f around time u and frequency v . In contrast, the usual Fourier transform only provides the *global* frequency content of a signal, that is, not localized in time.

The right-hand side of (1) permits a natural extension of the STFT to tempered distributions, see [4, Section 3.1]. This is relevant to us, as white noise will be defined in Sections 3 and 4 as a random tempered distribution.

2.2 The Bargmann transform

Let $a > 0$ and consider the Gaussian window $\gamma_a(x) \propto \exp(-\pi a^2 x^2)$, where \propto means “proportional to” and γ_a is normalized so that $\|\gamma_a\|_2 = 1$. The parameter a measures the inverse of the width of the support of the analysis window γ_a . Equivalently, it measures the width of the support of the Fourier transform of γ_a . When $a = 1$, we drop the subscript and write $\gamma(x) = \gamma_1(x) = 2^{1/4} e^{-\pi x^2}$. We closely follow the textbook by [4], only introducing arbitrary window width, and gather the important results in the following proposition.

Proposition 1. [4, Section 3.4] *Let $f \in L^2(\mathbb{R})$, $u, v \in \mathbb{R}$ and $z = au + i\frac{v}{a}$, then*

$$V_{\gamma_a}(f)(u, -v) \propto e^{-i\pi uv} e^{-\frac{\pi}{2}|z|^2} B(f(\cdot/a))(z), \quad (2)$$

where the Bargmann transform B is defined by

$$Bf(z) = 2^{1/4} \int f(t) e^{2\pi tz - \pi t^2 - \frac{\pi}{2} z^2} dt. \quad (3)$$

Proof. The particular shape of the window allows us to write

$$\begin{aligned} V_{\gamma_a}(f)(u, v) &\propto \int f(t) e^{-\pi a^2 (t-u)^2} e^{-2i\pi tv} dt \\ &= \int f(t) e^{-\pi a^2 t^2} e^{-\pi a^2 u^2} e^{2a^2 \pi tu} e^{-2i\pi vt} dt \\ &= e^{-i\pi uv} e^{-\frac{\pi}{2}(a^2 u^2 + \frac{v^2}{a^2})} \int f(t) e^{-\pi a^2 t^2} e^{2a\pi t(au - i\frac{v}{a})} e^{-\frac{\pi}{2}(au - i\frac{v}{a})^2} dt. \end{aligned} \quad (4)$$

Making the change of variables $s = at$ and denoting

$$z = au + i\frac{v}{a}, \quad (5)$$

we obtain

$$V_{\gamma_a}(f)(u, v) \propto e^{-i\pi uv} e^{-\frac{\pi}{2}|z|^2} \int f\left(\frac{s}{a}\right) e^{-\pi s^2} e^{2\pi s \bar{z}} e^{-\frac{\pi}{2}\bar{z}^2} ds,$$

or equivalently

$$\begin{aligned} V_{\gamma_a}(f)(u, -v) &\propto e^{-i\pi uv} e^{-\frac{\pi}{2}|z|^2} \int f\left(\frac{s}{a}\right) e^{-\pi s^2} e^{2\pi s z} e^{-\frac{\pi}{2}z^2} ds \\ &\propto e^{-i\pi uv} e^{-\frac{\pi}{2}|z|^2} B(f(\cdot/a))(z), \end{aligned} \quad (6)$$

where the Bargmann transform is defined as in (3). \square

Equation (6) means that the zeros of the spectrogram $u, v \mapsto |V_{\gamma_a}(f)(u, v)|^2$ of f are the zeros of the Bargmann transform of $s \mapsto f(s/a)$, up to a symmetry with respect to the real axis. Moreover, Equation (6) also readily extends to tempered distributions.

2.3 Hermite functions

Some functions turn out to have a very simple closed-form Bargmann transform. Informally, if we had an orthonormal basis of $L^2(\mathbb{R})$ formed by such functions, then we could decompose a white noise onto this basis, and easily compute the STFT of white noise using closed-form Bargmann transforms. We now introduce Hermite functions, which will play this exact role in later sections.

Let $(H_n)_{n \in \mathbb{N}}$ be the Hermite orthonormal polynomials with respect to the Gaussian window γ , usually called the Hermite polynomials in the literature [8]. Then, making the change of variables $x' = ax$, it comes

$$\int H_k(ax)H_\ell(ax)\gamma_a(x)dx \propto \int H_k(x')H_\ell(x')\gamma(x')dx' = \delta_{k\ell}.$$

The Hermite functions $h_{a,k} \propto H_k(a\cdot)\sqrt{\gamma_a(\cdot)}$, normed so that $\|h_{a,k}\|_2 = 1$, form an orthonormal basis of $L^2(\mathbb{R})$ [8]. When $a = 1$, we again drop a subscript and denote $h_k = h_{1,k}$. To compute the STFT of an Hermite function using (6), first note that for all s , $h_{a,k}(s/a) \propto h_k(s)$, so that

$$V_{\gamma_a}(h_{a,k})(u, -v) \propto e^{-i\pi uv} e^{-\frac{\pi}{2}|z|^2} B(h_k)(z) \quad (7)$$

$$= e^{-i\pi uv} e^{-\frac{\pi}{2}|z|^2} \frac{\pi^{k/2} z^k}{\sqrt{k!}}, \quad (8)$$

see [4, Section 3.4] for the last equality.

2.4 Point processes on \mathbb{C}

The zeros of the spectrogram of a random signal form a *point process*. Formally, a point process over \mathbb{C} is a probability distribution over configurations of points in \mathbb{C} , i.e., unordered sets of complex numbers. In particular, the cardinality of a point process is random. In this section, we introduce point processes and basic descriptive statistics.

2.4.1 Generalities

One of the most basic point processes over \mathbb{C} is the Poisson point process with constant rate $\lambda \in \mathbb{R}_+$. It is defined as the unique point process such that, for any $B \subset \mathbb{C}$ with finite Lebesgue measure $|B|$, (i) the number of points in B is a Poisson random variable with mean $\lambda|B|$, and (ii) conditionally on the number of points in B , the points are drawn independently from the uniform measure on B . For existence and further properties, see e.g. [9, Chapter 3].

More general point processes can be characterized by their k -point correlation functions $\rho^{(k)}$ for $k \geq 1$, informally defined by

$$\rho^{(k)}(x_1, \dots, x_k) dx_1 \dots dx_k = \mathbb{P} \left(\begin{array}{l} \text{There are at least } k \text{ points, one in each of the} \\ \text{infinitesimal balls } B(x_i, dx_i), i = 1, \dots, k \end{array} \right), \quad (9)$$

for all x_1, \dots, x_k in \mathbb{C} , see [10, Section 5.4] for a rigorous treatment. The interpretation (9) is valid only when the considered point processes are *simple*, that is, the points in each sampled configuration are all distinct. All point processes in this paper will be simple.

Of particular interest to us will be the first and second-order interaction between the points in a realization of a point process, encoded by $\rho^{(1)}$ and $\rho^{(2)}$, respectively. The first order correlation

function $\rho^{(1)}$ is often called the intensity of the point process, for its integral over any Borel set $B \subset \mathbb{C}$ is the average number of points falling in B under the point process distribution. For the Poisson point process with constant rate λ , for instance, the intensity is precisely λ , and thus constant over \mathbb{C} .

The two-point correlation function $\rho^{(2)}$ is often renormalized to obtain the so-called *pair correlation function*

$$g(x, y) = \frac{\rho^{(2)}(x, y)}{\rho^{(1)}(x)\rho^{(1)}(y)}, \quad (10)$$

see [9, Chapter 4]. For a Poisson point process with constant rate, g is identically 1. When $g(x, y) > 1$, (9) indicates that pairs are more likely to occur around (x, y) than under a Poisson process with the same intensity function. Similarly $g(x, y) < 1$ indicates that pairs are less likely to occur. When $g(x, y) < 1$ for all x, y , we speak of a *repulsive* point process. Finally, when the point process is both stationary (i.e., invariant to translations) and isotropic (i.e., invariant to rotations), then g only depends on the distance $r = |x - y|$, and we denote it by $g_0(r) = g(x, y)$. We plot in Figure 2(a) the g_0 of a few point processes, which are introduced later in the paper.

2.4.2 Determinantal point processes and the Ginibre ensemble

We give here another example of a point process on \mathbb{C} , in order to demonstrate a non-constant pair correlation function. If there exists a function $\kappa : \mathbb{C} \times \mathbb{C} \rightarrow \mathbb{C}$ such that the correlation functions (9) defined by

$$\rho^{(k)}(x_1, \dots, x_k) = \det [\kappa(x_i, x_j)]_{1 \leq i, j \leq k} \quad (11)$$

consistently define a point process, then this point process is called a *determinantal* point process (DPP) with kernel κ . DPPs were first introduced by [11], and we refer the reader to [12, 13] for modern introductions and conditions of existence. A classical example of DPP over \mathbb{C} is the infinite Ginibre ensemble. It is defined by its kernel

$$\kappa^{\text{Gin}}(z, w) = e^{-\frac{\pi}{2}|z|^2} e^{\pi z \bar{w}} e^{-\frac{\pi}{2}|w|^2}. \quad (12)$$

The Ginibre ensemble is stationary and isotropic, its intensity is constant equal to 1, and its pair correlation is

$$g_0^{\text{Gin}}(r) = 1 - e^{-\pi r^2},$$

see [2, Section 4.3.7] for these properties, noting that our version is rescaled to have unit intensity. We also plot g_0^{Gin} in Figure 2(a). Importantly for us, $g_0^{\text{Gin}}(r) \leq 1$ for all $r = |x - y|$, which shows that Ginibre is a *repulsive* point process: for any $x, y \in \mathbb{C}$ distant of r , finding a zero in a neighborhood of x and another in a neighborhood of y is less likely than for a Poisson process. Since this happens for all r , we say that Ginibre is repulsive at all scales. Actually, most DPPs are repulsive like Ginibre: by definition (11), if a DPP is stationary and isotropic, and if it has an Hermitian kernel, that is $\kappa(x, y) = \kappa(y, x)$, then $g_0 \leq 1$.

The Ginibre point process is intimately related to the STFT introduced in Section 2.1; indeed, the image of $L^2(\mathbb{R})$ by the STFT with Gaussian window is a reproducing kernel Hilbert space, and κ^{Gin} is its kernel. For this and a generalization to the so-called *Weyl-Heisenberg* ensembles with arbitrary windows, we refer the reader to [14]. Since the zeros of the spectrogram of white noise have been observed to be repulsive by [1], DPPs naturally come to mind as a good candidate for describing the zeros of spectrograms of random processes. However, we shall see in Section 4 that the zeros of the spectrogram of white Gaussian noise are close to Ginibre, but cannot be a DPP, at least not a DPP with a Hermitian kernel.

2.4.3 Zeros of Gaussian analytic functions

Another natural way to obtain point processes on \mathbb{C} is to look at zeros of random analytic functions. Analytic functions indeed have isolated zeros [15, Theorem 2.3.6]. The simplest random analytic functions are those with Gaussian coefficients (GAFs; see the recent monograph [2]). For instance, letting (a_n) be a sequence of i.i.d. complex unit Gaussians, then with probability one

$$\sum a_n \frac{z^n}{\sqrt{n!}} \tag{13}$$

converges uniformly on compact subsets of \mathbb{C} , see e.g. [2, Lemma 2.2.3]. The limit of (13) thus almost surely defines an entire function. The latter function was first investigated in physics under the name of *chaotic analytic* GAF by [16], but in probability it is more commonly known as the *planar* GAF [2]. The zeros of (13) have multiplicity one [2, Lemma 2.4.1], so that the point process of the zeros is simple. Moreover, the correlation functions (9) are known [2, Corollary 3.4.2], and the name *planar* relates to the fact that (13) is the only GAF such that the point process formed by its zeros is invariant to isometries of the complex plane $z \mapsto e^{i\theta}z + b$, $\theta \in \mathbb{R}$, $b \in \mathbb{C}$. In other words, the zero set of (13) is stationary and isotropic, as can be seen in Figure 1(b).

A variant of GAFs are *symmetric* GAFs, which can be defined as GAFs, but with *real* i.i.d. unit Gaussians as coefficients. In particular, the limit of (13) is still almost surely a well-defined analytic function [17], but its zero set now includes real zeros and pairs of conjugate complex zeros, see Figure 1(a). Since they will turn out to be central in our study, more will be said in Section 4 on the zeros of the planar and the symmetric planar GAF, and their relation to the Ginibre point process introduced in Section 2.4.2.

2.4.4 Functional statistics

We will need to investigate how repulsive a stationary and isotropic point process on \mathbb{C} like Ginibre is, given one of its realizations over a compact window of observation. While estimators of g_0 have been investigated [9, Section 4.3], practitioners usually prefer estimating Ripley's K function

$$K(r) = 2\pi \int_0^r t g_0(t) dt, \quad r > 0, \tag{14}$$

and then the so-called *variance-stabilized* L functional statistic

$$L(r) = \sqrt{K(r)/\pi}, \tag{15}$$

which equals r for a unit rate Poisson process. K is proportional to the expected number of points at distance r of the origin, given that there is a point at the origin. Estimating K from data is relatively straightforward and involves counting pairs distant from a collection of values of r . Furthermore, sophisticated edge corrections have been proposed to take into account the fact that the observation window is necessarily bounded [9, Section 4.3]. Estimating L after one has obtained an estimate of K is straightforward. L is not as easy to interpret as K , but is more commonly used in applications, see [18] for a justification.

We plot in Figure 2(b) the $r \mapsto L(r) - r$ statistic of the stationary point processes introduced in this paper, so that a Poisson process corresponds to a constant zero statistic. Visual inspection of such plots allows identification of scales at which the point process is repulsive, in the sense that we can observe a relative lack of pairs within a given distance compared to a Poisson process. For instance,

in Figure 2(b), there is a clear deficit of pairs at small scales for the Ginibre point process introduced in Section 2.4.2, compared to the constant zero of a Poisson process. Note that the cumulative nature of K and L makes large-scale behaviour harder to see on such plots.

There are many more functional statistics for stationary point processes [9, Section 4.2]. In particular, we mention for later reference the so-called *empty space function* F and the *nearest neighbour function* G . For $r > 0$, $F(r)$ is defined as the probability that a ball of radius r centered at 0 contains at least one point. Stationarity implies that the center of the ball can be chosen arbitrarily, so that F encodes the distribution of hole sizes in the point process. Similarly, G is the cumulative distribution function of the distance from a typical random point of the point process to its nearest neighbour in the point process.

3 The spectrogram of real white noise

In this section, we examine the zeros of the spectrogram of a continuous real white noise, and we recognize in Section 3.2 a recently studied point process called *the zeros of the symmetric planar GAF*. To rigorously establish this fact, we first need to review in Section 3.1 how mathematicians define continuous real white noise.

3.1 Definitions

To define white noise, we closely follow [19, Chapter 2.1] through a classical approach that does not require defining Brownian motion first. We denote by $\mathcal{S} = \mathcal{S}(\mathbb{R})$ the Schwartz space of rapidly decaying smooth complex-valued functions of a real variable. The dual $\mathcal{S}' = \mathcal{S}'(\mathbb{R})$, equipped with the weak-star topology, is the space of *tempered distributions*. The topology yields the Borel sigma-algebra $\mathcal{B}(\mathcal{S}')$ on \mathcal{S}' . Now, the Bochner-Minlos theorem [19, Theorem 2.1.1] states that there exists a unique probability measure μ_1 on $(\mathcal{S}', \mathcal{B}(\mathcal{S}'))$ such that

$$\forall \phi \in \mathcal{S}, \quad \mathbb{E}_{\mu_1} e^{i\langle \cdot, \phi \rangle} = e^{-\frac{1}{2}\|\phi\|_2^2}. \quad (16)$$

We call this measure white noise, and $(\mathcal{S}', \mathcal{B}(\mathcal{S}'), \mu_1)$ the white noise probability space. In particular, (16) implies that for a random variable¹ ξ with distribution μ_1 and a set of real-valued orthonormal functions $\varphi_1, \dots, \varphi_p$ in \mathcal{S} , the vector $(\langle \xi, \varphi_1 \rangle, \dots, \langle \xi, \varphi_p \rangle)$ follows a real multivariate Gaussian, with mean zero and identity covariance matrix, see [19, Lemma 2.1.2]. This is in accordance with the usual heuristic of white noise having a Dirac delta covariance function.

Let ξ be a random variable with distribution μ_1 . The Gaussian window $\gamma(x) = 2^{1/4}e^{-\pi x^2}$ is in \mathcal{S} , so that $(u, v) \mapsto M_v T_u \gamma$ is in \mathcal{S} , and we can define the STFT of ξ as the random function

$$u, v \mapsto \langle \xi, M_v T_u \gamma \rangle.$$

We are interested in defining and studying the zeros of the random spectrogram

$$S : u, v \mapsto |\langle \xi, M_v T_u \gamma \rangle|^2. \quad (17)$$

As we shall see in Section 3.2, even if ξ does not have smooth realizations, it turns out that the random spectrogram (17) is almost surely an analytic function, so that its zeros are isolated points and can be defined as the zeros of the spectrogram of ξ .

¹We use the term *random variable* ξ , but it is also customary to call ξ a *generalized random process* in the literature.

3.2 Characterizing the zeros

We work in two steps: in Proposition 2, we identify each value $S(u, v)$ in (17) as a limit in $L^2(\mu_1)$, and we then show in Proposition 3 that the resulting random field defines an entire function, the zeros of which are known.

Proposition 2. *Let $u, v \in \mathbb{R}^2$, and write $z = u + iv \in \mathbb{C}$. Then*

$$\langle \xi, M_v T_u \gamma \rangle = \sqrt{\pi} e^{i\pi uv} e^{-\frac{\pi}{2}|z|^2} \sum_{k=0}^{\infty} \langle \xi, h_k \rangle \frac{\pi^{k/2} z^k}{\sqrt{k!}} \quad (18)$$

where (h_k) denote the orthonormal Hermite functions of Section 2.3, and convergence is in $L^2(\mu_1)$.

Remark 1. Note that in Proposition 2, u and v are fixed, and the equality is a limit in $L^2(\mu_1)$. It is still too early to identify the zeros of the function of the left-hand side to the zeros of the function on the right-hand side.

Remark 2. The proof of Proposition 2, along with Sections 2.2 and 2.3, immediately yield that for a non-unit Gaussian window $\gamma_a(x) \propto \exp(-\pi a^2 x^2)$, Proposition 2 is unchanged, provided that z is defined as $z = au + iv/a$ and a constant is prepended to the RHS of (18). In other words, given a particular value of a , it is always possible to dilate/squeeze the time-frequency axes to obtain the results detailed here for $a = 1$.

Proof. Let $u, v \in \mathbb{R}^2$. Decomposing $M_v T_u \gamma$ in the Hermite basis (h_k) of $L^2(\mathbb{R})$, it comes

$$\begin{aligned} \langle \xi, M_v T_u \gamma \rangle &= \sum_{k=0}^{\infty} \langle \xi, h_k \rangle \langle M_v T_u \gamma, h_k \rangle \\ &= \sum_{k=0}^{\infty} \langle \xi, h_k \rangle \overline{V_\gamma(h_k)(u, v)} \end{aligned} \quad (19)$$

where the limits are in $L^2(\mu_1)$. The STFT of Hermite functions is well-known, see e.g. the proof of [4, Proposition 3.4.4] or our Section 2.2, and it reads

$$V_g(h_k)(u, v) = e^{-i\pi uv} e^{-\frac{\pi}{2}(u^2+v^2)} \frac{\pi^{k/2}}{\sqrt{k!}} (u - iv)^k. \quad (20)$$

Plugging (20) into (19) yields the result. \square

Now we focus on the regularity of the right-hand side of (18) as a function of $z = u + iv$.

Proposition 3. *The random series*

$$\sum_{k=0}^{\infty} \langle \xi, h_k \rangle \frac{\pi^{k/2} z^k}{\sqrt{k!}} \quad (21)$$

μ_1 -almost surely defines an entire function.

Proof. By [19, Lemma 2.1.2], $(\langle \xi, h_k \rangle)_{k \geq 0}$ are i.i.d. unit real Gaussians. We then apply [2, Lemma 2.2.3], which shows that almost surely, the (entire) partial sums of (21) converge uniformly on every compact of \mathbb{C} , so that the limit is entire. \square

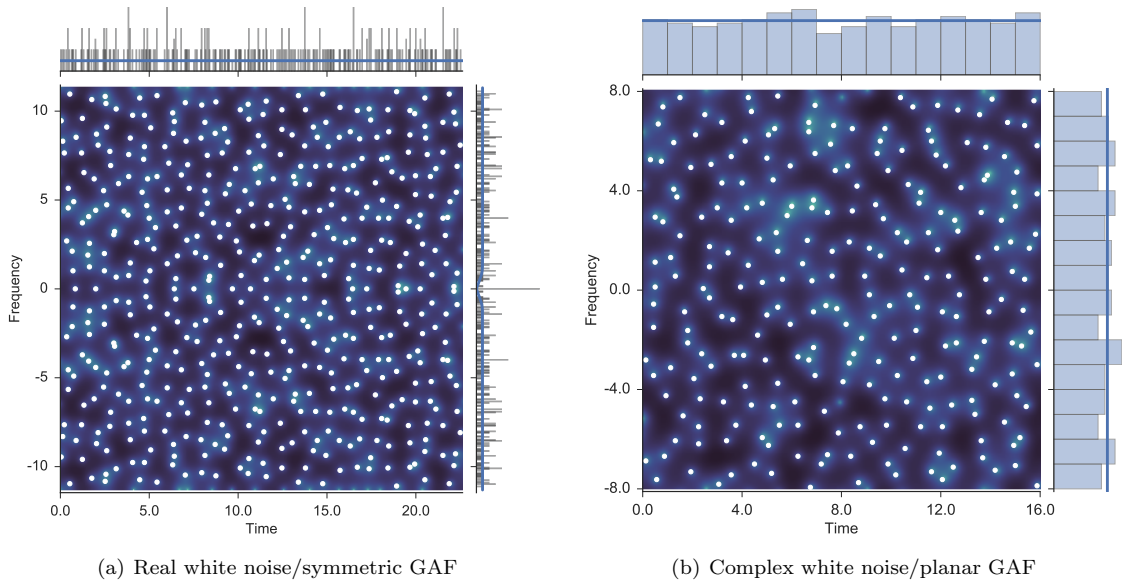


Figure 1: The spectrogram of (a) a realization of real white noise, and (b) a realization of complex white noise. Zeros are in white. The right and top plots on each panel show marginal histograms of the imaginary and real part of the zeros, respectively, superimposed with the theoretical marginal density, see Section 3.2 for details.

Since both L^2 and almost sure convergence imply convergence in probability, L^2 and almost sure limits have to be the same. In particular, Propositions 2 and 3 together yield that the distribution of the zeros of the spectrogram S in (17) is the same as the distribution of the zeros of the random entire function (21). This answers Remark 1. In particular, as noted in Section 2.4.3, the zeros of S are isolated and form a point process known as the zeros of the *symmetric planar Gaussian analytic function* (GAF), and a few of its properties are known [17]. However, its zeros do not define a stationary point process.

Figure 1(a) depicts in blue levels the spectrogram of a realization of real white noise, see later in Section 5.1 for computational details. White dots show the zeros of the spectrogram, or equivalently, a realization of the zeros of the symmetric planar GAF. The marginal distributions of the real and imaginary parts of the zeros are shown on top and on the right, respectively. On these marginal histograms, we have superimposed the theoretical densities from [17]. The non-stationarity is obvious: the pattern of zeros is symmetric with respect to the real axis, and a portion of the zeros actually concentrate on the real axis. Intuitively, one can approximate the zeros of (21) by the zeros of the random polynomial obtained from truncating the series. The resulting polynomial has real coefficients, and it is thus expected to have real zeros as well as pairs of conjugate complex zeros. This explains both the symmetry and the Dirac delta that can be seen at zero in the marginal histogram of the imaginary parts of zeros. As a side note, the number of real zeros is a topic of study on its own, see e.g. [20].

Coming back to the problem of detecting signals, this non-stationarity makes it difficult to approach

via traditional spatial statistics techniques, which often rely on spatial averaging and thus assume some degree of stationarity. However, we shall see in Section 4 that the zeros of the STFT of complex white noise are a stationary point process, and are a good approximation of the zeros of the symmetric planar GAF.

4 The case of complex white noise

In this section, we justify why the zeros of the spectrogram of real white Gaussian noise can be approximated by the zeros of the spectrogram of *complex* white Gaussian noise. The latter are also called *the zeros of the planar GAF* and are a stationary point process. From a practical point of view, this section investigates to what extent we can apply spatial statistics techniques requiring stationarity to the zeros of the spectrogram of real white noise. In Section 4.4, we consider characterizing the zeros of the spectrogram of an analytic white noise.

4.1 The complex white Gaussian noise

Consider the *two-dimensional white noise* of [19, Section 2.1.2], that is, the space $\mathcal{S}' \times \mathcal{S}'$, with the Borel σ -algebra associated to the product weak star topology, and measure $\mu_1 \times \mu_1$. A draw $\boldsymbol{\xi} = (\xi_1, \xi_2) \sim \mu_1 \times \mu_1$ consists of two independent white noises. Following [19, Exercise 2.26], we let $\boldsymbol{\Phi} = (\phi_1, \phi_2)$ in $\mathcal{S} \times \mathcal{S}$, and we *define* the smoothed complex white noise as

$$\boldsymbol{\xi}, \boldsymbol{\Phi} \mapsto \langle \xi_1, \phi_1 \rangle + i \langle \xi_2, \phi_2 \rangle,$$

where $\boldsymbol{\xi} \sim \mu_1 \times \mu_1$. It is called “smoothed” because we define it using a pair of test functions $\boldsymbol{\Phi}$, which will be enough for our purpose. Note also that in signal processing, this is typically called a *proper* or *circular* Gaussian white noise [21].

Now, if we let both test functions be $t \mapsto M_v T_u \gamma$, we recover what can reasonably be called the STFT of complex white noise

$$u, v \mapsto \langle \xi_1, M_v T_u \gamma \rangle + i \langle \xi_2, M_v T_u \gamma \rangle. \quad (22)$$

4.2 Characterizing the zeros

The same arguments as in the proofs of Propositions 2 and 3 lead to

Proposition 4. *With $\mu_1 \times \mu_1$ probability 1, the zeros of the STFT (22) are those of the entire function*

$$\frac{1}{\sqrt{2}} \sum_{k=0}^{\infty} (\langle \xi_1, h_k \rangle + i \langle \xi_2, h_k \rangle) \frac{\pi^{k/2} z^k}{\sqrt{k!}}, \quad (23)$$

where $z = u + iv$.

We note that under $\mu_1 \times \mu_1$, the random variables $2^{-1/2}(\langle \xi_1, h_k \rangle + i \langle \xi_2, h_k \rangle)$ are i.i.d. unit complex Gaussians, and the entire function (23) is the *planar Gaussian analytic function* introduced in Section 2.4.3. In particular, the planar GAF is one of the three fundamental GAFs in the monograph of [2], and more is known about its zeros than for the symmetric planar GAF in Proposition 3. We group some known results in Proposition 5, selecting results that could be of immediate statistical use in signal processing.

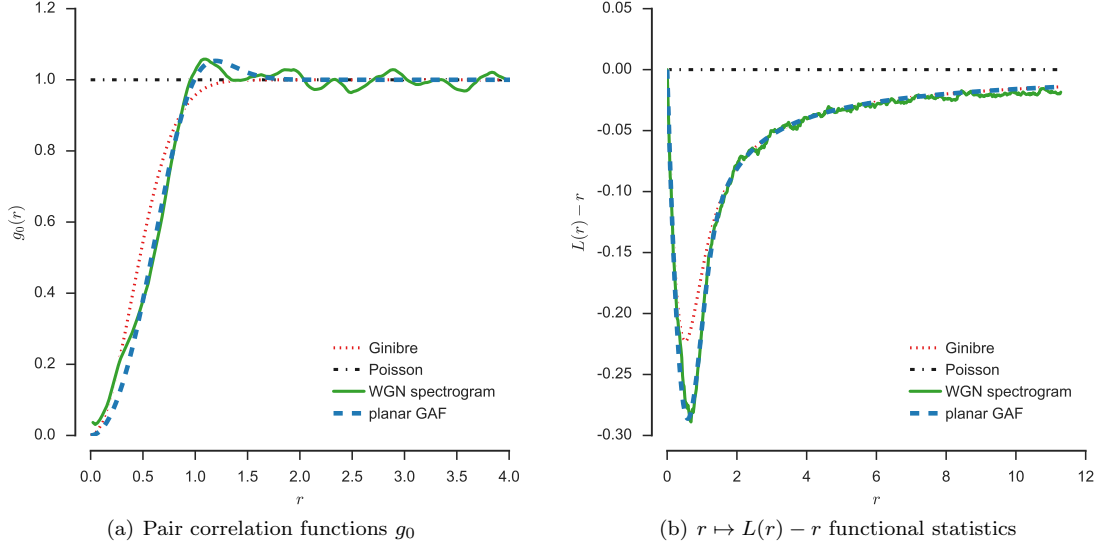


Figure 2: Comparison of the Ginibre point process, the zeros of the planar GAF, and a realization of the spectrogram of complex white noise, using (a) pair correlation functions g_0 , and (b) the L functional statistic, see Section 2.4 for definitions.

Proposition 5 ([2, 22]). *The planar GAF satisfies the following properties:*

1. *The distribution of its zeros is invariant to rotations and translations in the complex plane [2, Proposition 2.3.7]. In particular, it is a stationary point process.*
2. *Its correlation functions are known [2, Corollary 3.4.2]. In particular, the intensity is constant equal to 1, and with the notation of Section 2.4, for $z, w \in \mathbb{C}$ such that $|z - w| = r$, the pair correlation function reads*

$$\rho^{(2)}(z, w) = g_0(r) = \frac{\left[\sinh^2\left(\frac{\pi r^2}{2}\right) + \frac{\pi^2 r^4}{4} \right] \cosh\left(\frac{\pi r^2}{2}\right) - \pi r^2 \sinh\left(\frac{\pi r^2}{2}\right)}{\sinh^3\left(\frac{\pi r^2}{2}\right)}. \quad (24)$$

3. *The hole probability*

$$p_r = \mathbb{P}(\text{no points in the disk of radius } r \text{ centered at } 0)$$

scales as

$$r^{-4} \log p_r \rightarrow -3e^2/4 \quad (25)$$

as $r \rightarrow +\infty$ [22].

Figure 2 illustrates Proposition 5. We plot the pair correlation function (24) of the planar GAF, along with the pair correlation functions of the Poisson and Ginibre point processes introduced in Section 2.4. We also superimpose an estimate of g_0 obtained from the spectrogram of a realization of a complex white noise, see Section 5 for computational procedures. Finally, we also plot the L functional statistic for the same point processes, as introduced in Section 2.4.

Both the zeros of the planar GAF and Ginibre are repulsive at small scales: their g_0 is smaller than 1, and the $r \mapsto L(r) - r$ statistic has a well-marked decrease close to zero. But the planar GAF alone has a small ring of attraction around $r = 1$, well visible in Figure 2(a) where the corresponding ρ_0 is larger than the constant 1 of a Poisson process, as can also be checked from the closed form (24). If we remember that the pair correlation of a DPP with Hermitian kernel cannot exceed 1 by definition (11), this implies that the zeros of the planar GAF cannot be a DPP with Hermitian kernel, unlike what we and [23] may have intuited, see Section 2.4.2. Note that strictly speaking, it is still possible that the zeros of the planar GAF are a DPP with a non-Hermitian kernel.

Even if they are not a DPP with Hermitian kernel, the zeros of the planar GAF are often compared to the Ginibre process introduced in Section 2.4.2, which is a DPP. Both the zeros of the planar GAF and the Ginibre process are invariant to isometries of the plane [2, Section 4.3.7]. Furthermore, the decay of the log hole probability (25) is also in r^4 for the Ginibre process [2, Proposition 7.2.1]. This is to be compared to the slower decay in r^2 of a Poisson process with constant rate. This is an indication that the size of holes in sampled zeros of the planar GAF and samples of the Ginibre ensemble will be similarly distributed, and that both will have significantly fewer large holes than Poisson. There are other intriguing similarities between the two point processes, see [24], where Ginibre is shown to be the zeros of a GAF with a randomized kernel.

4.3 The zeros of the planar GAF approximate those of the symmetric planar GAF

To sum up, the spectrogram of real white noise is described by the symmetric planar GAF, but the zeros of the planar GAF are more amenable to further statistical processing. In this section, we survey results by [17] and [25] that support approximating the zeros of the symmetric planar GAF by those of the planar GAF.

To apply the results in [17], we first need to make the symmetric planar GAF stationary. More precisely, the zeros of the symmetric planar GAF (21) have the same distribution as the zeros of

$$f_{\text{sym}}(z) = e^{-\frac{\pi}{2}z^2} \sum_{k=0}^{\infty} \frac{a_k}{\sqrt{k!}} \pi^{k/2} z^k, \quad (26)$$

where a_k are i.i.d. unit real Gaussians. Note that the covariance kernel of f_{sym} is

$$\begin{aligned} K_{\text{sym}}(z, w) &\triangleq \mathbb{E} f_{\text{sym}}(z) \overline{f_{\text{sym}}(w)} \\ &= e^{-\frac{\pi}{2}z^2} e^{-\frac{\pi}{2}\bar{w}^2} e^{\pi z \bar{w}} \\ &= e^{-\frac{\pi}{2}(z-\bar{w})^2}. \end{aligned} \quad (27)$$

This hints some invariance of f_{sym} to translations along the real axis. By a limiting argument, see e.g. [2, Lemma 2.3.3], (26) is indeed a stationary symmetric GAF in the sense of [17]. Namely, for any $n \geq 1$, any $z_1, \dots, z_n \in \mathbb{C}$, and any $t \in \mathbb{R}$, $(f_{\text{sym}}(z_1 + t), \dots, f_{\text{sym}}(z_n + t))$ has the same distribution as $(f_{\text{sym}}(z_1), \dots, f_{\text{sym}}(z_n))$. Now [17] derives the intensity of the zeros of general stationary symmetric GAFs. In the symmetric planar case, we apply [17, Theorem 1] to (26) and obtain Proposition 6.

Proposition 6 ([17]). *Let $n_{sym}([0, T] \times A)$ be the random number of zeros of f_{sym} in a “vertical” Borel set of \mathbb{C} . Almost surely, the following weak convergence of measures holds as $T \rightarrow \infty$:*

$$\frac{n_{sym}([0, T] \times A)}{T} \rightarrow \int_A [dS(v) + \delta_0], \quad (28)$$

where

$$S(v) = \frac{v}{\sqrt{1 - e^{-4\pi v^2}}}. \quad (29)$$

Equation (28) characterizes the marginal density of zeros along the vertical axis, averaged across the horizontal axis. The Dirac mass in (28) relates to the accumulation of zeros on the real axis discussed in Section 3 and visible in Figure 1(a). The numerator of the continuous part S in (28) is the unnormalized cumulative density of a uniform distribution, and the denominator quickly converges to 1 as v grows.

Now compare (28) to the horizontal counting measure of the zeros of the planar GAF, which is simply the uniform dv , without any atom, see e.g. [17, Theorem 1] again. We observe that the two counting measures are quickly approximately equal, as one goes away from the real axis. More precisely, for $A \subset [1, +\infty)$, the ratio of $S(A)$ to the Lebesgue measure of A is within $2 \cdot 10^{-6}$ of 1. For Gaussian windows of arbitrary width, the change of variables (5) yields that the approximation is tight for $\text{Im}(z) \geq a$. For signal processing, this means the approximation is tight for high frequencies, where “high” means larger than the width a in frequency of the Gaussian window γ_a . Actually, in practice, spectrograms are never considered at low frequencies, that is, within the frequency spread of the observation window from the real axis. This practical habit is in strong agreement with the theoretical results of [17]. Finally, Figure 1 shows a realization of both the symmetric planar GAF and the symmetric GAF. The continuous part of the marginal density (28) can be seen as a thick blue line on the vertical marginal histogram in Figure 1(a). We note the decrease of the continuous part around 0, and the Dirac mass can be seen on the empirical histogram on the right. In comparison, the marginal densities of the zeros of the symmetric GAF are flat, see Figure 1(b).

A natural question is whether the approximation is also accurate for higher-order interactions in the two point processes. This question can be addressed by comparing k -point correlation functions. The case of the planar GAF was derived by [16], and closed-form formulas are derived for the symmetric planar GAF in [25, Equation (12)]. The latter are not easy to interpret as they involve nonstandard combinatorial combinations of matrix coefficients. Still, [25, Equation 25] shows that when $\text{Im}(z) \gg 0$, the k -point correlation functions of the zeros of the symmetric planar GAF are well approximated by those of the zeros of the planar GAF.

To conclude, the distribution of the zeros of the STFT of real white Gaussian noise is well approximated by that of complex white Gaussian noise, as long as the observation window is sufficiently far from the time axis. This is easy to satisfy in practice, by restricting the observation of zeros to frequencies that are larger than the frequency spread a of the observation window.

4.4 On the analytic white noise

A real-valued function $f \in L^2(\mathbb{R})$ has an Hermitian Fourier transform. In signal processing, it is thus common to cancel out the negative frequencies of a real-valued signal $f \in L^2(\mathbb{R})$ by defining another complex-valued function $f^+ \in L^2(\mathbb{R})$ called its *analytic signal*,

$$f^+(x) = 2\mathcal{F}^{-1}(\mathbb{1}_{\mathbb{R}_+}\mathcal{F}f)(x), \forall x \in \mathbb{R}. \quad (30)$$

where \mathcal{F} is the usual Fourier transform. The term “analytic” is related to the alternative definition of f^+ as the boundary function of a particular holomorphic function on the lower half of the complex plane, see e.g. [26, Section 2.1] for a concise and rigorous treatment. In signal processing practice, beyond removing redundant frequencies, the modulus and argument of f^+ have meaningful interpretations for elementary signals [27]. Since our initial goal is to understand the behaviour of the zeros of a real white noise, it is tempting to define and consider an analytic white noise to represent this real white noise. If this approach led to a simple statistical characterization of zeros, then we would avoid the approximation by the complex white noise of Section 4.1.

While folklore has it that the analytic white noise is the circular white noise of Section 4.1, this is not the case for the most natural definition of the analytic signal of a distribution. Following [26, Section 3.3], we define in this paper the analytic white noise by its action on $L^2(\mathbb{R})$: letting $\xi \sim \mu_1$ be a real white noise², we take

$$\langle \xi^+, f \rangle \triangleq 2\langle \xi, \mathcal{F}^{-1}(\mathbb{1}_{\mathbb{R}_+} \mathcal{F}f) \rangle, \quad \forall f \in L^2(\mathbb{R}). \quad (31)$$

For our purpose, it is enough to consider ξ^+ through its action (31). In particular, if we want to follow the lines of Sections 3 and 4 and identify the general term of a random series corresponding to the STFT of ξ^+ , we need an orthonormal basis (ζ_k) of $L^2(\mathbb{R})$ and a window γ such that

$$\langle \zeta_k, \mathcal{F}^{-1}(\mathbb{1}_{\mathbb{R}_+} \mathcal{F}M_v T_u \gamma) \rangle \quad (32)$$

is known in closed-form and simple enough. Hermite functions and the Gaussian window definitely do not satisfy our criteria anymore, and [28] actually prove that the Gaussian is the only window γ such that the range of the STFT is a subset of the space of analytic functions. Consequently, it is not even clear that the STFT of analytic white noise would have isolated zeros in the first place. We leave this as an open question. Still, we have the following heuristic argument: when γ is the unit-norm Gaussian, $\mathcal{F}M_v T_u \gamma = T_v M_{-u} \gamma$, so that (32) becomes

$$\langle \zeta_k, \mathcal{F}^{-1}(\mathbb{1}_{\mathbb{R}_+} T_v M_{-u} \gamma) \rangle. \quad (33)$$

When v is large enough, say a few times the width of the window γ , $T_v M_{-u} \gamma$ puts almost all its mass on \mathbb{R}_+ , and the indicator function in (33) can be dropped. The Hermite basis then satisfies our requirements, giving the planar GAF of Section 4. Intuitively, far from the real axis, the spectrogram of the analytic white noise will look like that of proper complex white noise. This heuristic is to relate to standard time–frequency practice, where one leaves out of the spectrogram a band that is within the width of the window of the lower half plane. This is meant to avoid border effects that result from taking into account both positive and negative frequencies of the signal simultaneously.

5 Practical spatial statistics using the zeros of the STFT

This section aims at using previous theoretical results on the zeros of the spectrogram of white Gaussian noise to design and implement a practical approach to the detection and reconstruction of a signal from its noisy observation. Section 5.1 discusses how to relate the continuous complex plane \mathbb{C} with the practical discrete implementation of the short-term Fourier transform. Sections 5.2 and 5.3 investigate

²As a side note, [26, Section 3] investigates the random field that would be the formal equivalent to the holomorphic continuation of the classical analytic signal of a function in $L^2(\mathbb{R})$. But this time, the limit on the real axis is rather ill-behaved.

simple hypothesis tests for signal detection and signal reconstruction based only on the distribution of the zeros of the spectrogram, in the spirit of [1]. Code to reproduce all experiments is available at <http://github.com/jflamant/2018-zeros-spectrogram-white-noise>.

5.1 Going discrete

To fully bridge the gap with numerical signal processing practice, there is an additional level of approximation that needs to be discussed: continuous integrals are replaced by discrete fast Fourier transforms. We first describe an experimental setting to numerically study the zeros of the spectrogram of Gaussian white noise. In particular, we explain how to reach an asymptotic regime where the noise occupies an arbitrary large range both in time and frequency and the spectrogram is infinitely well resolved. Second, we investigate practical issues related to the detection and reconstruction of a signal in white noise by using its influence on the distribution of zeros of the spectrogram.

5.1.1 Zeros of noise only

Let F_s be the sampling frequency, $\Delta t = 1/F_s$ the time sampling step size. Let N be the number of samples, and we define the duration $T = N\Delta t$.³ Let $\sigma_t = 1/(a\sqrt{2\pi})$ and $\sigma_\nu = 1/(2\pi\sigma_t)$ denote the spreads of the Gaussian analysis window γ_a in time and frequency, respectively. Note that the scale a serves as a fixed reference for scales in the sequel. Let K be the length of the discretized Gaussian analysis window, i.e. its duration is $K\Delta t$; therefore $\Delta\nu = F_s/K = 1/K\Delta t$ is the frequency sampling step. In practice, the spectrogram obtained from a discrete STFT is then an array of size $(N, K/2 + 1)$.

Figure 3(a) illustrates the computation of the STFT of a noisy signal. Figure 3(b) illustrates the relative scales of the duration $T = N\Delta t$, the frequency range $K/2\Delta t$ (for $\nu \geq 0$), the resolution of the time-frequency kernel corresponding to the window $\gamma(t)$ with Gabor spread (σ_t, σ_ν) as well as the time and frequency resolutions Δt and $\Delta\nu$.

We consider the time-frequency domain $[0, T] \times [0, F_s/2]$ only; it corresponds to the analytic signal. This is due to the Hermitian symmetry of the Fourier transform of real signals: negative frequencies do not carry any additional information with respect to positive frequencies, see also Section 4.4. This Hermitian symmetry can also be seen on the zeros of the symmetric GAF in Figure 1(a), where signal processing practitioners would have considered the upper half-plane ($\nu \geq 0$) only.

From [17]’s results, see (28), we know that the expected number of zeros of the continuous spectrogram is close to $TF_s/2$ if we neglect the (asymptotically negligible) region $|\nu| \leq a$ close to the time axis, see Section 4.3. Assuming that we are able to extract every zero, the expected number of zeros in the discrete spectrogram is then $TF_s/2 = N/2$ in very good approximation. We would like to retain the stationary properties of the planar GAF in our discrete STFTs. We thus require that, in the discrete setting, the resolution – in number of points – should be the same in time and frequency, that is

$$\frac{\sigma_t}{\Delta t} = \frac{\sigma_\nu}{\Delta\nu} \iff \sigma_t \cdot F_s = \sigma_\nu \cdot K\Delta t \quad (34)$$

This leads to (recall that $\sigma_t\sigma_\nu = 1/2\pi$)

$$\left(\frac{\sigma_t}{\Delta t}\right)^2 = \frac{K}{2\pi} \iff \sigma_t = \sqrt{\frac{K}{2\pi}}\Delta t. \quad (35)$$

³It is customary to call this T a duration, although strictly speaking it is the period of the discrete signal. The corresponding duration of the continuous signal would be $(N + 1)\Delta t$.

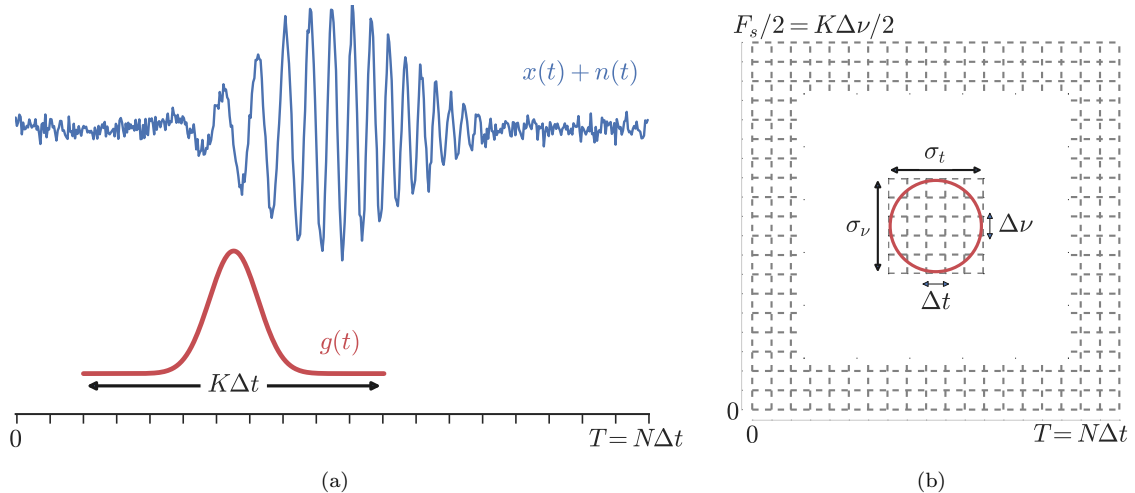


Figure 3: (a) Illustration of the STFT: the noisy signal is projected on a Gaussian analysis window that is translated in time and frequency. (b) discrete time-frequency plane $[0, N\Delta t] \times [0, \frac{K}{2}\Delta\nu]$: the effective resolution of the spectrogram is controlled by the Gabor parameters (σ_t, σ_ν) of the analysis window g .

If we want to study the spectrogram of continuous white noise over an infinite time-frequency domain, numerical simulations must obey two necessary conditions:

$$\left\{ \begin{array}{l} \text{infinite duration} \Leftrightarrow \text{fine frequency resolution:} \\ \text{infinite frequency range} \Leftrightarrow \text{fine time resolution:} \end{array} \right. \quad \begin{array}{l} \frac{\sigma_t}{T} = \frac{\Delta\nu}{2\pi\sigma_\nu} = \frac{1}{N} \sqrt{\frac{K}{2\pi}} \rightarrow 0 \text{ as } N, K \rightarrow \infty, \\ \frac{\sigma_\nu}{F_s} = \frac{\Delta t}{2\pi\sigma_t} = \frac{1}{\sqrt{2\pi K}} \rightarrow 0 \text{ as } N, K \rightarrow \infty. \end{array} \quad (36)$$

These two conditions imply that both $N, K \rightarrow \infty$ and $K \propto N$, where \propto means “proportional to”.

Note that in practice, to avoid border effects, one chooses $N \geq 2K$ and keeps the $N - K$ samples whose time index n is such that $K/2 \leq n \leq N - K/2$. Then, $\sigma_\nu/F_s = 1/\sqrt{2\pi K} \propto 1/\sqrt{N}$, $\sigma_t/T \propto 1/\sqrt{N}$; note that $\Delta t/\sigma_t = \Delta\nu/\sigma_\nu \propto 1/\sqrt{N} \rightarrow 0$ as well. The analysis window is thus more and more finely resolved and the spectrogram gets close to a continuous description. As a result, simulations can asymptotically well approximate the continuous spectrogram of Gaussian white noise over an infinite domain. In parallel, the expected number of zeros in the spectrogram of the white noise is $F_s T/2 = N/2$ and tends to ∞ with N . Therefore, assuming perfect zero detection, statistics such as Ripley’s K function or the variance-stabilized L functional statistic of Section 2.4.4 can be asymptotically perfectly well estimated.

Figure 4 depicts the whole numerical simulation procedure. It represents the simulated spectrogram and the corresponding extracted area when border effects are taken into account. For a given value of a , one has $\sigma_t = 1/(a\sqrt{2\pi})$ and $\Delta t = \sqrt{2\pi/K}\sigma_t$, see (35). For $a = 1$ one has $\Delta t = 1/\sqrt{K}$ so that $u = n/\sqrt{K}$ and $v = k/\sqrt{K}$ are the coordinates of the continuous time-frequency plane corresponding to the discrete time-frequency samples (n, k) . The bound ℓ fixes how many samples close to the zero-frequency axis should be removed. For $a = 1$, we have chosen $\ell = \sqrt{K}$, at it corresponds to $y = 1$

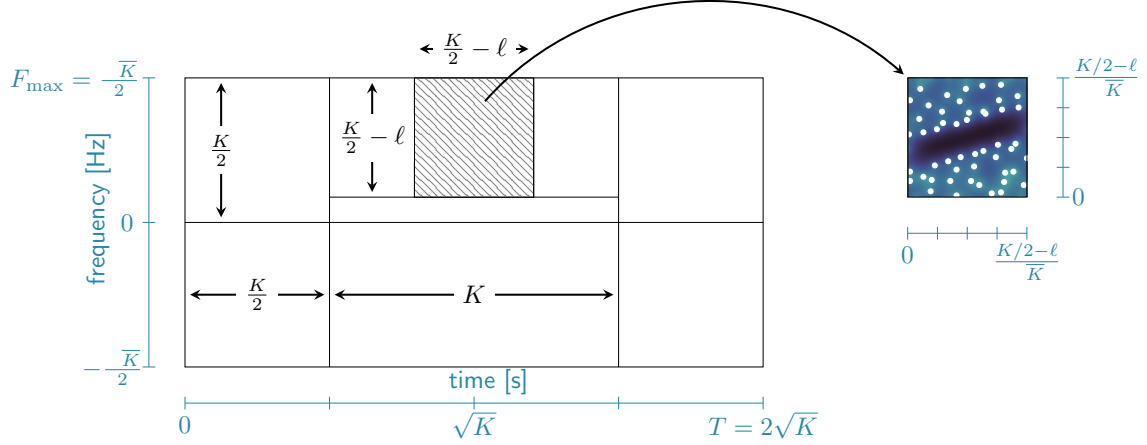


Figure 4: Numerical simulation procedure when $N = 2K$ and $\Delta t = 1/\sqrt{K}$. Black ticks indicate discrete samples, blue ticks show continuous time-frequency units (see text for details). In other words, blue ticks are the coordinates in the complex plane that are implicit in the mathematical results of Sections 3 and 4. The dashed region corresponds to the area used in subsequent simulations.

in (28). Our illustrations will only show a square region of side $K/2 - \ell$ samples both in time and in frequency. Note that one could actually extend the shaded square in Figure 4 horizontally to cover a duration of $K\Delta t$.

Then we need to define a numerical procedure to detect zeros. It appears that zeros are local minima among their eight neighbouring bins: these local minima are very close to zero. Moreover, we found that the number of detected zeros was consistent with what we expected from Proposition 5, even if we did not impose a threshold on the value of the spectrogram at the local minimum.

Remark 3. We have implicitly assumed that the discrete Fourier transforms involved in the computation of the discrete spectrogram converge to their continuous counterpart in the limit of an infinite observation window and an infinite sampling rate. We mathematically justify in what sense this convergence can be expected. Denote by χ_n the indicator of the n th interval $[(n-1)\Delta t, n\Delta t]$. Let $P_{N,T} : \mathcal{S} \rightarrow L^2$ attach to a Schwartz function f the “sampled” simple function $\sum_{n=1}^N f(n)\chi_n$. Then $P_{N,T}f \rightarrow f$ in L^2 as T and N go to infinity and $T/\sqrt{N} \rightarrow \alpha > 0$, which is the setting described above. Moreover,

$$\langle \xi, P_{N,T}M_vT_u g \rangle = \sum_{n=1}^N \langle \xi, \chi_n \rangle e^{-2i\pi v n \Delta t} g(n\Delta t - u) \quad (37)$$

is what we call the discrete STFT at (u, v) of a realization of white noise. Note that in distribution, $(\langle \xi, \chi_n \rangle)_n$ is a sequence of i.i.d. Gaussian variables with variance Δt . To see how (37) is a good approximation to our initial continuous STFT, we note that for all u, v ,

$$\begin{aligned} \mathbb{E}_{\mu_1} |\langle \xi, M_v T_u g \rangle - \langle \xi, P_{N,T} M_v T_u g \rangle|^2 &= \mathbb{E}_{\mu_1} |\langle \xi, M_v T_u g - P_{N,T} M_v T_u g \rangle|^2 \\ &= \|M_v T_u g - P_{N,T} M_v T_u g\|_{L^2}^2 \rightarrow 0. \end{aligned}$$

5.1.2 Zeros of signal plus noise

When a signal is present, its specific scales destroy the scale invariance property of Gaussian white noise and deprives us from any asymptotic regime in our numerical simulations. Let A_S denote the typical time and frequency area occupied by the considered signal. The presence of this signal creates a region of the spectrogram of size A_S where a decrease in the number of zeros is expected due to the positive amount of energy corresponding to the signal. For instance, Figure 5 shows various spectrograms of linear chirps with various A_S and various signal-to-noise ratios (SNRs): there are clearly less zeros where the signal lives. The approach proposed in the next section roots in this intuition to build statistical detection tests based on the distribution of zeros in the spectrogram. To this purpose one needs to quantify how far the presence of a signal can influence the statistics so that we can maximize this influence and the efficiency of the proposed test.

Given a sampling rate F_s and a duration of observation T , the unit intensity in Proposition 5 yields that the expected number of zeros in the spectrogram of a real white noise is $F_s \cdot T/2 = N/2$, neglecting what happens at small frequencies close to the time axis. Note that this number is independent of the width (σ_t, σ_ν) of the Gaussian analysis window γ_a . If one wants to increase the number of zeros in the spectrogram to get better statistics, it is enough to increase either F_s or T . The expected decrease in the number of zeros due to the presence of a signal is of the order of the finite time-frequency area A_S corresponding to the region of the spectrogram describing the signal alone. As a consequence, an excessive increase in either F_s and/or T would result in an asymptotically complete dilution of the influence of the signal on the considered statistics. Thus, our purpose is to build statistics over one or more patches P of the spectrogram of maximal time-frequency area A_P such that $A_S/A_P \simeq 1$.

On one hand, a maximal area A_P is necessary to ensure that the estimate of the chosen statistics is as accurate as possible (in particular in the presence of noise only, to take into account as many zeros as possible and minimize the false positive detection rate). On the other hand, this statistic will be more sensitive if it mostly depends on the influence of the signal on the distribution of zeros in the spectrogram (in particular, in the presence of signal, we maximize the true positive detection rate). In practice, note that one can hope to detect signals such that $A_S \gg \sigma_t \sigma_\nu = 1/2\pi$ only, which means signals with a time-frequency support that affects more than $\sigma_t/\Delta t \cdot \sigma_\nu/\Delta \nu = K/2\pi$ samples of the spectrogram.

5.2 Detecting signals through hypothesis testing

In this section, we present a hypothesis test that checks whether a given pattern of zeros can be attributed to the spectrogram of a realization of Gaussian white noise.

5.2.1 Monte Carlo envelope tests

In Section 2.4.4, we reviewed some popular functional statistics for stationary isotropic point processes. We focus here on L , the variance-stabilized version of Ripley's K function, and the empty space function

$$F(r) = \mathbb{P}(\text{There is at least one point in the ball of radius } r \text{ and center } 0),$$

see Section 2.4. We follow classical Monte Carlo testing methodology based on functional statistics, which we now sketch, see e.g. [29] for a less concise introduction.

The methodology is independent of the test statistic used, so we introduce it for a general functional statistic $r \mapsto S(r)$, which we later instantiate to be L or F . Let \hat{S} denote an empirical estimate obtained from the spectrogram of data, possibly using edge corrections, see [9]. Let S_0 be the theoretical

functional statistic corresponding to complex white noise. For $S = L$, L_0 can be easily computed from (24). Note that our noise is real white noise in the applications, but we approximate the corresponding 2-point correlation function by that of complex white noise far from the real axis, as explained in Section 4.3. Detection of signal over white noise can be formulated as testing the null hypothesis H_0 that \hat{S} was built from a realization of a real white noise, versus the alternate hypothesis H_1 that it was not. Note that we do not put yet any *a priori* knowledge in the design of H_1 , and simply define it by the negation of H_0 . To design our test, we review Monte Carlo envelope-based hypothesis tests, which are popular across applications of spatial statistics.

In a Monte Carlo envelope test, we define a test statistic $T \in \mathbb{R}$ that summarizes the difference $r \mapsto S(r) - S_0(r)$ in a single real number, for instance a norm

$$T_\infty = \sup_{r \in [r_{\min}, r_{\max}]} |S(r) - S_0(r)| \quad \text{or} \quad T_2 = \sqrt{\int_{r_{\min}}^{r_{\max}} |S - S_0|^2}. \quad (38)$$

Let t_{exp} denote the realization of T corresponding to the experimental data to be analyzed. The test consists in 1) simulating m realizations of white noise, 2) computing the corresponding functional statistics estimates S_1, \dots, S_m , 3) computing the realizations t_1, \dots, t_m of the test statistic, and 4) rejecting H_0 whenever the observed t_{exp} is larger than the k -th largest value among t_1, \dots, t_m . Without loss of generality, we assume t_1, \dots, t_m are in decreasing order, so that t_k is the k -th largest. In a nutshell, we reject H_0 if and only if $t_{\text{exp}} \geq t_k$.

Symmetry considerations show that this test has significance level $\alpha = k/(m+1)$. Furthermore, when S_0 is not available in closed form, one can replace it by a pointwise average

$$\bar{S}_0(r) = \frac{1}{m+1} (S_1(r) + \dots + S_m(r) + \hat{S}(r)) \quad (39)$$

while preserving the significance level, see [29].

To illustrate the testing procedure, we consider a synthetic chirp as a signal, to which we add white noise with SNR= 100. Note that we define here SNR to be the ratio of $A^2/2\sigma^2$, where A is the maximum amplitude of the chirp, and σ^2 the variance of the noise. Figure 5 shows vignettes with example spectrograms of such signals, the zeros are depicted as white disks. The rest of Figure 5 shall be explained in Section 5.2.2. Figure 6 illustrates why this test is called an *envelope test*, in the case of $S = L$. The two panels respectively represent the cases $T = T_\infty$ and $T = T_2$ defined in (38). Let $k = 10$ and $m = 199$, so that the significance is $\alpha = 0.05$. We further take $r_{\min} = 0$ and let r_{\max} vary, showing for each r_{\max} the corresponding t_k as the upper limit of the green shaded envelope. The black line shows t_{exp} at each r_{\max} , for the same realizations of the tested signal and the white noise spectrograms. To interpret these plots, imagine the user had fixed r_{\max} to some value, then he would have rejected H_0 if and only if the corresponding intersection of the black line with $r = r_{\max}$ was above the green area. Note that the significance of the test is only guaranteed if r_{\max} is fixed prior to observing data or simulations. Still, Figure 6 gives a heuristic to identify characteristic *scales of interaction* after H_0 is rejected. For instance, characteristic scales could be values of r_{\max} where the data curve in black leaves the green envelope⁴. The user can thus identify regions of the spectrogram that possibly correspond to signal (defined as “different from white noise”). To illustrate this, consider again both plots of Figure 6. There is a hint of an interaction between zeros – an excess or deficit of pairs– between $r_{\max} = 0.5$ and $r_{\max} = 1$ since the data curve in black leaves the green envelope in this region. This interaction cannot be explained by noise only. In Section 5.3, we investigate how

⁴Caveats have been issued against overinterpreting these scales of interaction, see [29].

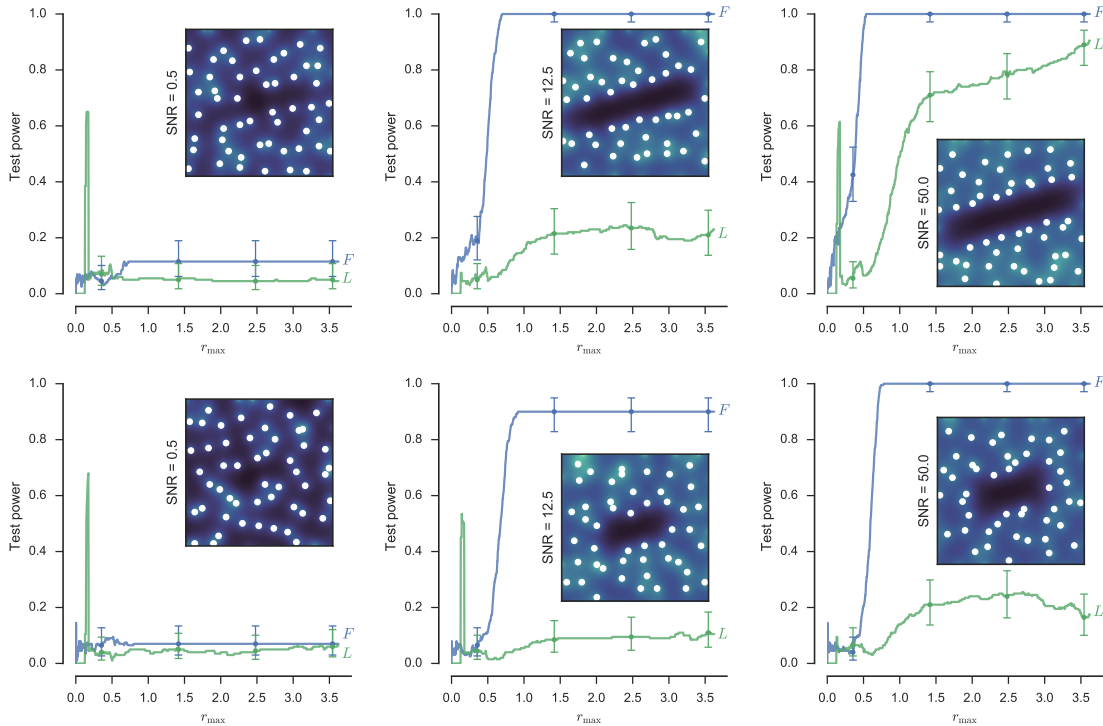


Figure 5: Assessing the power of the test on detecting a linear chirp with various SNRs across columns. The top row corresponds to a support of the chirp that is approximately the width of the observation window, while the bottom row corresponds to a chirp support that is half that. Each panel contains the estimated power for both $S = L$ and $S = F$, using T_2 . We also plot a realization of the corresponding spectrograms for illustration.

the knowledge of such a scale can be used to filter out noise, but before that, we investigate how the power of the test varies with parameters.

5.2.2 Assessing the power of the test

The significance α of the test – the probability of rejecting H_0 while H_0 is true – is fixed by the user as in Section 5.2.1. It remains to investigate the power β of the test, that is, the probability of rejecting H_0 when one should. Following Section 5.1.2, we expect β to increase with SNR, which should be large enough to “push” zeros away from the time-frequency support of the signal to be detected. We also expect the power to be larger when the observation window is not too much larger than the time-frequency support A_S of the signal; in the notation of Section 5.1: if $A_P/A_S \approx 1$.

We back these claims by the experiment in Figure 5. To quantify β , we consider the task of detecting a signal that is a linear chirp. Still taking $m = 199$ and $k = 10$, so that $\alpha = 0.05$, we build each of the six panels as follows: we simulate a mock signal made using a linear chirp plus noise, with SNR indicated on the plot, growing from left to right. We then repeat 200 times: 1) simulate m

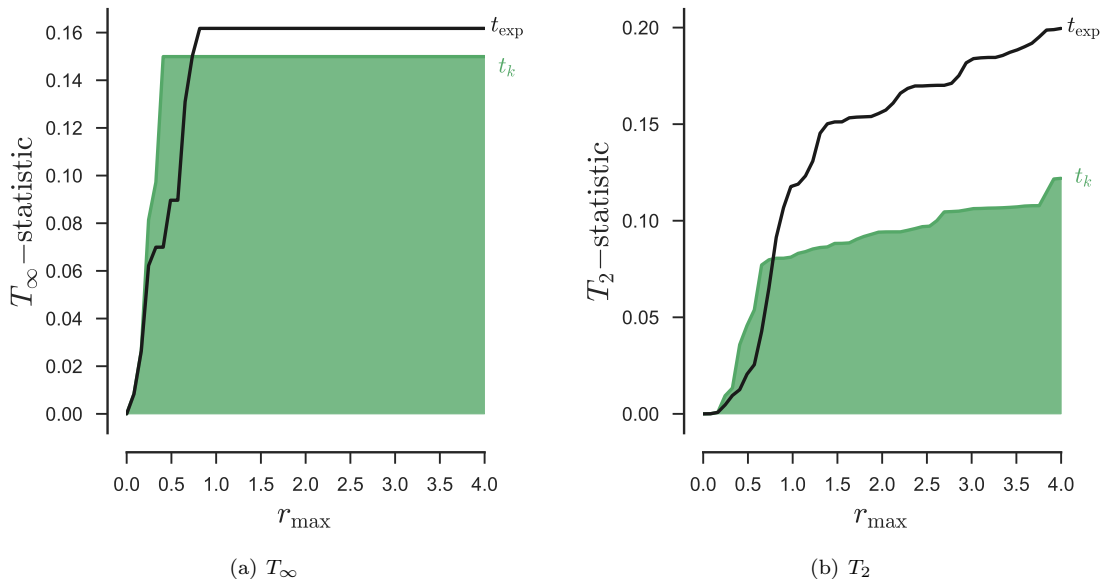


Figure 6: Envelope plots for the detection test of Section 5.2 for the supremum and 2-norm of the deviation of the L functional statistic from its pointwise average (39).

white noise spectrograms, 2) compute the estimates S_1, \dots, S_m , 3) compute the realizations t_1, \dots, t_m , and 4) check whether H_0 is rejected for each value of r_{\max} . We can thus estimate the probability β of rejecting H_0 for various choices of r_{\max} the user could have made. We plot both the power using $S = L$ or $S = F$, choosing the 2-norm in (38) and the empirical average (39). We estimate the functional statistics using the `spatstat` R package⁵. We emphasize that to estimate β , we assumed that signals are linear chirps; however, our testing procedure does not rely on this *a priori* knowledge.

We need to give a confidence interval for the power. We give Clopper-Pearson intervals for four values of r_{\max} in all panels of Figure 5. Note that since we use the same realizations of white noise across 4 different values of r_{\max} and for both L and F , we have to correct for the 8 multiple tests we perform, which we do using Bonferroni correction, see e.g. [30]. Finally, the top row of Figure 5 corresponds to a signal support that matches the size of the observation window, while the bottom row is half that. On each panel, an inlaid plot depicts the spectrogram for one realization of the signal corrupted by white noise. Zeros of spectrograms are in white.

Results confirm our intuitions: power increases with SNR, and decreases as the size of the support of the signal diminishes with respect to the observation window. In all experiments, the best power is obtained by taking r_{\max} to be as large as possible, which here means half of the observation window. This makes sure that as many points/pairs as possible enter the estimation of the functional statistic S . Concerning the choice of functional statistic, the empty space function F performs significantly better for high SNR and large enough r_{\max} . The peaks of power at low r_{\max} for $S = L$ and some combinations of SNR and support are due to the excess of small pairwise distances introduced by the chirp signal. Indeed, zeros tend to clutter on the boundary of the support of the signal, and repulsion

⁵Version 1.51-0, see <http://spatstat.org/>

seems to be lower around this boundary, as can be seen on the depicted spectrograms in Figure 5. The power vanishes quickly once larger pairwise distances are considered, due to the cumulative nature of L . It is dangerous to rely on these peaks for signal detection as they do not appear systematically and would require a careful hand-tuning of r_{\max} that would likely defeat our purpose of automatic detection. Overall, we recommend using F and large r_{\max} , which appears to be a robust best choice. We also found (not shown) first that F is superior or equal to the other functional statistics described in Section 2.4 for chirp detection. Second, we found that the tests using the average (39) are consistently more powerful than those using the closed form L_0 of L . We believe this is due to the edge correction that is implicitly made in (39), while the analytic L_0 corresponds to an infinite observation window. Third, we also observed the 2-norm in (38) to be consistently more powerful than the supremum norm.

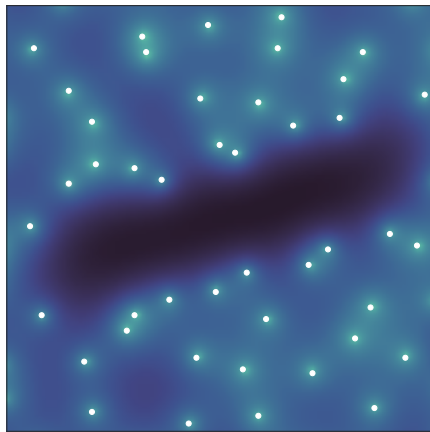
5.3 Reconstruction from the empty space function

We now give a proof of concept that the tests in Section 5.2 can be turned into a reconstruction algorithm, guided by the theory of Section 4. In a nutshell, we look for unlikely holes in the time-frequency plane, where by *hole* we mean a disk containing no zero of the spectrogram.

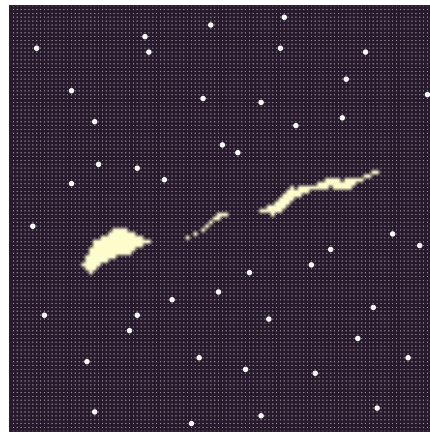
To reconstruct a signal from its time-frequency representation, one often requires a mask gathering the relevant region of the time-frequency plane. One then recovers the signal by inverting the time-frequency representation with this mask. Such masks are usually obtained by thresholding of local maxima called ridges [31]. In contrast, using zeros avoids specifying a model for signals, or parameters like a threshold for the numerical definition of maxima. Furthermore, [1] points out that the geometric rationale behind using the zeros is *rotation-invariant in the time-frequency plane, with a similar ability to deal with impulse-like transients signals (with almost “vertical” time-frequency signatures) and AM-FM-type waveforms (with almost “horizontal” ones)*. The approach described in this paper can be seen as a point process counterpart of the method proposed by [1]. To this aim, we replace the histograms of edge lengths obtained by Delaunay triangulation in [1] by standard tools from spatial statistics.

Consider a linear chirp as in Section 5.2 with SNR= 20. The corresponding spectrogram and its zeros are shown in Figure 7(a). Remember from Section 2.4 that the spatial statistic $r \mapsto F(r)$ used in the tests of Section 5.2 is the probability that a disk of radius r contains at least one zero. If the hypothesis H_0 that the spectrogram is that of a realization of white noise is rejected during a test using F , it is because there are too many holes in the pattern of zeros. To locate these abnormal holes, let us pick a value r_0 such that empty disks with radius larger than r_0 are rare under H_0 . For instance, Figure 2(a) hints that we should pick r_0 around 1, since pairs of zero distant by 1 are very likely – more likely even than in a Poisson point process – while distances smaller than 1 are rare, see Section 2.4. Another method would be to look for characteristic scales in the envelope plots of the test, as done in Section 5.2.1 for the L -statistic. We found both methods to give roughly consistent answers, so we set $r_0 = 1$.

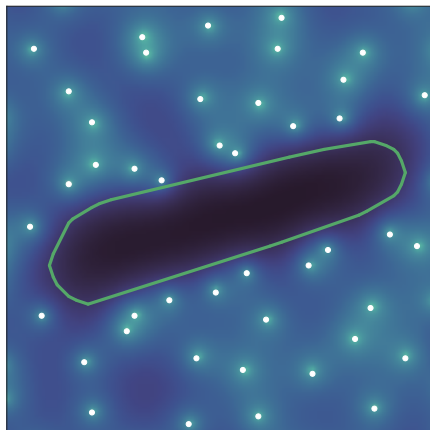
To locate areas of the time-frequency plane that correspond to signal, we sweep through the time-frequency plane, and mark bins of the discrete spectrogram such that there are no zeros in the disk of radius r_0 centered at the bin center. These bin centers are marked in beige in Figure 7(b). Now, to be conservative, we add to the beige area every point of the time-frequency plane that is within $r_0/2 = 0.5$ of it. This value is chosen to be approximately half the typical distance between two zeros and can be interpreted as a resolution, see Figure 2(a). Computing the envelope of this augmented beige area yields the green contour in Figure 7(c), and inverting the STFT with a mask corresponding to this envelope gives us the reconstruction in Figure 7(d), which very accurately picks up the properties of



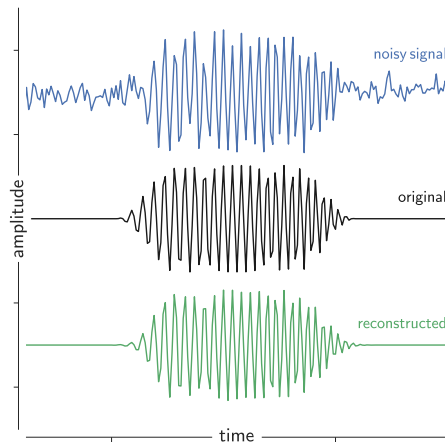
(a) Initial spectrogram



(b) Centers of empty disks



(c) Segmented signal



(d) Reconstruction

Figure 7: Reconstruction of a signal by zero-based segmentation.

the original signal. Finally, we emphasize that while we depicted the spectrogram in Figures 7(a) and 7(c), the whole construction of the mask only relies on the location of the zeros of the spectrogram.

6 Discussion

The main purpose of the present work was to explore the potential of using the zeros of a spectrogram for the detection and reconstruction of a signal in white Gaussian noise. The intuition is based on the duality between maxima and zeros pointed out by [1]: the presence of a signal may be detected as an anomaly in the distribution of zeros in the time-frequency plane. The main idea was to exploit the description of the zeros of the spectrogram of white Gaussian noise as a point process, i.e., a random set of points in the complex plane. In particular, we have shown that determinantal point processes (DPPs) with Hermitian kernels, despite some similarity, do not provide a relevant model for the distribution of the zeros of the spectrogram of white Gaussian noise.

We have also shown how to give a mathematical meaning to the zeros of the spectrogram of white Gaussian noise. We have investigated their statistical distribution for real, complex, and – to a lesser extent – analytic white noise. We have related these zeros to the zeros of Gaussian analytic functions (GAFs), a topic of booming interest in probability. The connection with GAFs puts signal processing algorithms based on the zeros of spectrograms on firm ground, and further progress on GAFs is bound to be fruitful for signal processing. Perhaps less obviously, we believe that signal processing tools can also bring insight into probabilistic questions on GAFs. For instance, the Bargmann transform, zeros of spectrograms, and the fast Fourier transform give a novel way to approximately simulate the zeros of the planar GAF, or even the zeros of random polynomials.

More pragmatically, we have investigated the computational issues raised by implementing statistical tests based on the distribution of the zeros of a spectrogram, the null hypothesis being that there is white Gaussian noise only (no signal). Numerical experiments have demonstrated a simple denoising task that relies on the segmentation of the spectrogram based on zeros only. We have investigated the application of standard frequentist testing tools. They showed good power for sufficiently high SNR and sufficiently large signal support compared to the observation window. For an optimized application, there are various leads to improve on these two points. First, we could transform our global test into several local tests, trying to adapt the tested patch to the support of the signal. Second, if some prior knowledge is available, models for signals could be fed to Bayesian techniques, allowing to explore all signals compatible with a given pattern of zeros. The optimization of practical signal processing procedures based on the proposed approach is the subject of ongoing work.

One limitation of this work is that we have considered spectrograms computed using a Gaussian window only. This choice was motivated by the feasibility of its theoretical study. It remains an open question to determine to what extent our results apply to other analysis windows. A negative result is given by [28], who essentially show that the Gaussian is the only window that makes the STFT map $L^2(\mathbb{R})$ to a set of analytic functions. Yet, it may be that the range of the STFT with some carefully chosen windows is not too different from a space of analytic functions. For instance, Gabor transforms with Hermite windows map to polyanalytic functions [32]; see also [33] for a signal-oriented review of spaces of polyanalytic functions. Polyanalytic functions do not have isolated zeros, but there is still a wealth of analytic tools available to characterize the zero sets [34]. Another lead to generalize the results in this paper is to see the Hermite functions as the eigenfunctions of a particular localization operator [35, 36], and try to explore how much freedom we have on the choice of the localization operator while still controlling the location of the zeros of the associated spectrogram.

Acknowledgments

We thank Patrick Flandrin, Adrien Hardy, Frédéric Lavancier, and two anonymous reviewers for fruitful discussions on various aspects of this paper. RB acknowledges support from ANR BoB (ANR-16-CE23-0003), and all authors acknowledge support from ANR BNPSI (ANR-13-BS03-0006).

References

- [1] P. Flandrin. Time–frequency filtering based on spectrogram zeros. *IEEE Signal Processing Letters*, 22(11):2137–2141, 2015.
- [2] J. B. Hough, M. Krishnapur, Y. Peres, and B. Virág. *Zeros of Gaussian analytic functions and determinantal point processes*, volume 51. American Mathematical Society Providence, RI, 2009.
- [3] P. Flandrin. *Time-frequency/time-scale analysis*, volume 10. Academic press, 1998.
- [4] K. Gröchenig. *Foundations of time-frequency analysis*. Birkhäuser, 2001.
- [5] L. Cohen. *Time-frequency analysis*, volume 778. Prentice Hall PTR Englewood Cliffs, NJ., 1995.
- [6] Timothy J Gardner and Marcelo O Magnasco. Sparse time-frequency representations. *Proceedings of the National Academy of Sciences*, 103(16):6094–6099, 2006.
- [7] Peter Balazs, Dominik Bayer, Florent Jaillet, and Peter Søndergaard. The pole behavior of the phase derivative of the short-time fourier transform. *Applied and Computational Harmonic Analysis*, 40(3):610–621, 2016.
- [8] W. Gautschi. *Orthogonal polynomials: computation and approximation*. Oxford University Press, USA, 2004.
- [9] J. Møller and R. P. Waagepetersen. *Statistical inference and simulation for spatial point processes*. CRC Press, 2003.
- [10] D. J. Daley and D. Vere-Jones. *An Introduction to the Theory of Point Processes*. Springer, 2nd edition, 2003.
- [11] O. Macchi. The coincidence approach to stochastic point processes. *Advances in Applied Probability*, 7:83–122, 1975.
- [12] J. B. Hough, M. Krishnapur, Y. Peres, and B. Virág. Determinantal processes and independence. *Probability surveys*, 2006.
- [13] F. Lavancier, J. Møller, and E. Rubak. Determinantal point process models and statistical inference. *Journal of the Royal Statistical Society*, 2014.
- [14] L. D. Abreu, J. M. Pereira, J. L. Romero, and S. Torquato. The Weyl–Heisenberg ensemble: hyperuniformity and higher Landau levels. *Journal of Statistical Mechanics: Theory and Experiment*, 2017(4), 2017.
- [15] B. Simon. *Basic complex analysis*, volume 2A of *A comprehensive course in analysis*. American Mathematical Society, 2015.

- [16] J. H. Hannay. The chaotic analytic function. *Journal of Physics A: Mathematical and General*, 31(49):L755, 1998.
- [17] N. D. Feldheim. Zeroes of Gaussian analytic functions with translation-invariant distribution. *Israel Journal of Mathematics*, 195(1):317–345, 2013.
- [18] J. E. Besag. Contribution to the discussion on dr. ripley’s paper. *Journal of the Royal Statistical Society, Series B*, 39:193–195, 1977.
- [19] H. Holden, B. Øksendal, J. Ubøe, and T. Zhang. *Stochastic partial differential equations*. Springer, second edition, 2010.
- [20] G. Schehr and S. N. Majumdar. Real roots of random polynomials and zero crossing properties of diffusion equation. *Journal of Statistical Physics*, 132(2):235–273, 2008.
- [21] B. Picinbono and P. Bondon. Second-order statistics of complex signals. *IEEE Transactions on Signal Processing*, 1997.
- [22] A. Nishry. Asymptotics of the hole probability for zeros of random entire functions. *International Mathematics Research Notices*, 2010.
- [23] P. Flandrin. On spectrogram local maxima. In *International Conference on Acoustics, Speech and Signal Processing (ICASSP)*, pages 3979–3983. IEEE, 2017.
- [24] M. Krishnapur and B. Virág. The Ginibre ensemble and Gaussian analytic functions. *International Mathematics Research Notices*, 2014(6):1441–1464, 2014.
- [25] T. Prosen. Exact statistics of complex zeros for Gaussian random polynomials with real coefficients. *Journal of Physics A: Mathematical and General*, 29(15):4417, 1996.
- [26] E. L. Pugh. The generalized analytic signal. *Journal of Mathematical Analysis and Applications*, 89(2):674–699, 1982.
- [27] B. Picinbono. On instantaneous amplitude and phase of signals. *IEEE Transactions on Signal Processing*, 1997.
- [28] G. Ascensi and J. Bruna. Model space results for the Gabor and Wavelet transforms. *IEEE Transactions on Information Theory*, 55(5):2250–2259, 2009.
- [29] A. Baddeley, P. J. Diggle, A. Hardegen, T. Lawrence, R. K. Milne, and G. Nair. On tests of spatial pattern based on simulation envelopes. *Ecological Monographs*, 84(3):477–489, 2014.
- [30] L. Wasserman. *All of statistics: a concise course in statistical inference*. Springer Science & Business Media, 2013.
- [31] Nathalie Delprat, Bernard Escudie, Philippe Guillemain, Richard Kronland-Martinet, Philippe Tchamitchian, and Bruno Torresani. Asymptotic wavelet and gabor analysis: Extraction of instantaneous frequencies. *IEEE transactions on Information Theory*, 38(2):644–664, 1992.
- [32] L. D. Abreu. Sampling and interpolation in Bargmann–Fock spaces of polyanalytic functions. *Applied and Computational Harmonic Analysis*, 29(3):287–302, 2010.

- [33] L. D. Abreu and H. G. Feichtinger. Function spaces of polyanalytic functions. In *Harmonic and complex analysis and its applications*, pages 1–38. Springer, 2014.
- [34] M. B. Balk. Polyanalytic functions. *Mathematical research*, 1991.
- [35] I. Daubechies. Time-frequency localization operators: a geometric phase space approach. *IEEE Transactions on Information Theory*, 34(4):605–612, 1988.
- [36] L. D. Abreu, K. Gröchenig, and J. L. Romero. On accumulated spectrograms. *Transactions of the American Mathematical Society*, 368(5):3629–3649, 2016.

A general approach for the analysis and filtering of bivariate signals

Bivariate signals appear in a broad range of applications where the joint analysis of two real-valued signals is required: polarized waveforms in seismology and optics, eastward and northward current velocities in oceanography, pairs of electrode recordings in EEG or MEG or even gravitational waves emitted by coalescing compact binaries. Simple bivariate signals take the form of an ellipse, whose properties (size, shape, orientation) may evolve with time. This geometric feature of bivariate signals has a natural physical interpretation called polarization. This notion is fundamental to the analysis and understanding of bivariate signals. However, existing approaches do not provide straightforward descriptions of bivariate signals or filtering operations in terms of polarization or ellipse properties. To this purpose, this thesis introduces a new and generic approach for the analysis and filtering of bivariate signals. It essentially relies on two key ingredients: (i) the natural embedding of bivariate signals – viewed as complex-valued signals – into the set of quaternions \mathbb{H} and (ii) the definition of a dedicated quaternion Fourier transform to enable a meaningful spectral representation of bivariate signals. The proposed approach features the definition of standard signal processing quantities such as spectral densities, linear time-invariant filters or spectrograms that are directly interpretable in terms of polarization attributes. These geometric and physical interpretations are made possible by the use of quaternion algebra. More importantly, the framework does not sacrifice any mathematical guarantee and the newly introduced tools admit computationally fast implementations. By revealing the specificity of bivariate signals, the proposed framework greatly simplifies the design of analysis and filtering operations. Numerical experiment support throughout our theoretical developments. We demonstrate the potential of the approach for the characterization of (polarized) gravitational waves emitted by compact coalescing binaries. A companion Python package called BiSPy implements our findings for the sake of reproducibility.

Keywords: bivariate signal, polarization, quaternion Fourier transform, spectral analysis, linear filtering, time-frequency analysis, gravitational waves

Une approche générique pour l'analyse et le filtrage des signaux bivariés

Les signaux bivariés apparaissent dans de nombreuses applications, dès lors que l'analyse jointe de deux signaux réels est nécessaire : ondes polarisées en sismologie et optique, courants marins de surface en océanographie, paires d'enregistrements en EEG et MEG, et même ondes gravitationnelles émises par des binaires coalescentes. Les signaux bivariés simples ont une interprétation naturelle sous la forme d'une ellipse dont les propriétés (taille, forme, orientation) peuvent évoluer dans le temps. Cette propriété géométrique des signaux bivariés correspond à la notion de polarisation en physique. Elle est fondamentale pour la compréhension et l'analyse des signaux bivariés. Les approches existantes n'apportent cependant pas de description directe des signaux bivariés ou des opérations de filtrage en termes de polarisation ou de propriétés géométriques. Cette thèse répond à cette limitation par l'introduction d'une nouvelle approche générique pour l'analyse et le filtrage des signaux bivariés. Celle-ci repose sur deux ingrédients essentiels : (i) le plongement naturel des signaux bivariés – vus comme signaux à valeurs complexes – dans le corps des quaternions \mathbb{H} et (ii) la définition d'une transformée de Fourier quaternionique associée pour une représentation spectrale interprétable de ces signaux. L'approche proposée permet de définir les outils de traitement de signal usuels tels que la notion de densité spectrale, de filtrage linéaire temps-invariant ou encore de spectrogramme ayant une interprétation directe en termes d'attributs de polarisation. Ces multiples interprétations géométriques et physiques sont rendues possibles par l'utilisation de l'algèbre quaternionique. Nous montrons la validité de l'approche grâce à des garanties mathématiques et une implémentation numériquement efficace des outils proposés. En exploitant la spécificité du cas des signaux bivariés, le cadre de travail proposé simplifie grandement la conception d'outils d'analyse et de traitement du signal dédiés. Les développements théoriques présentés dans ce manuscrit sont illustrés par des expériences numériques. En particulier, nous démontrons le potentiel de l'approche pour la caractérisation des ondes gravitationnelles – polarisées – émises par des systèmes binaires en coalescence. Un module Python nommé BiSPy accompagne nos travaux en vue d'une recherche reproductible.

Mots-clés : signal bivarié, polarisation, transformée de Fourier quaternionique, analyse spectrale, filtrage linéaire, analyse temps-fréquence, ondes gravitationnelles